Le Rôle de la myéline dans les maladies dégénératives

Wiebke Knoll

UNIVERSITÉ DE GRENOBLE

THÈSE

Pour obtenir le grade de

DOCTEUR DE L'UNIVERSITÉ DE GRENOBLE

Spécialité : **Physique pour les Sciences du Vivant**

Arrêté ministérial : 7 Août 2006

Présentée par

Wiebke Knoll

Thèse dirigée par **Prof. Dr. Judith Peters**
et codirigée par **Dr. Francesca Natali**

préparée au sein **de l'Institut Laue-Langevin, Grenoble**
et de **l'Ecole Doctorale de Physique**

Reconstituted Myelin Sheaths Investigated by Neutron Scattering: the Role of Myelin Proteins

Thèse soutenue publiquement le **17 Septembre 2012**,
devant le jury composé de :

Dr. Thomas Gutberlet
Helmholtz-Zentrum Berlin für Materialien und Energie GmbH, Berlin, Rapporteur
Prof. Dr. Antonio Deriu
University of Parma, Parma, Rapporteur
Dr. Martin Weik
Institut de Biologie Structurale, Grenoble, Examinateur
Dr. Bruno Franzetti
Institut de Biologie Structurale, Grenoble, Examinateur
Dr. Giorgio Schiro'
University of Palermo, Palermo, Examinateur
Prof. Dr. Judith Peters
Université Joseph-Fourier, Grenoble; Institut de Biologie Structurale, Grenoble;
Institut Laue-Langevin, Grenoble, Directeur de thèse
Dr. Francesca Natali
CNR-IOM-OGG, c/o Institut Laue-Langevin, Grenoble, Co-Directeur de thèse
Dr. Petri Kursula
Department of Biochemistry and Biocenter Oulu, University of Oulu, Oulu;
Department of Chemistry, University of Hamburg, Hamburg;
CSSB-HZI, DESY, Hamburg, Co-Directeur de thèse

Acknowledgments

First of all I wish to express my gratitude to my supervisors Dr. Francesca Natali and Prof. Dr. Judith Peters, who supported, encouraged and guided me throughout my thesis and gave me the opportunity to do this work.

I would like to thank the members of the jury, Prof. Dr. Antonio Deriu and Dr. Thomas Gutberlet, for being the referees of this thesis, and Dr. Martin Weik, Dr. Petri Kursula, Dr. Bruno Franzetti and Dr. Giorgio Schiro', who agreed to be part of the jury.

Another thanks is addressed to Petri, who taught me the expression and purification of the myelin proteins that I used for this work. His support was a great help for me in learning a new scientific field.

I am grateful for Yuri Gerelli, who provided my a fitting program and helped me during the analysis of the quasielastic data.

I am thankful to the DESY, the IBS and the EMBL for using their laboratories and in particular to Colin Jackson, Iulia Blesniac and Juliette Devos, who helped me during the preparation of the samples and to Dr. Martin Weik.

A further thanks goes to the European Commission, which supported the performance of experiments carried out at HZB and to the Science and Technology Facilities Council (STFC), UK, for access to the ISIS Facility and beamtime on the OSIRIS instrument.
I am thanking the team of IN13 with whom I completed my PhD: the local contacts Francesca and Judith, the former PhD student Marcus, the postdoc Nicolas and the technicians Mathieu and Teddy.

I would like to thank the local contacts of the other instruments I used, whose help made my experiments possible: Jacques Olivier, Michael Marek Koza, Bruno Demé, Jérôme Combet, Mark Telling, Ewout Kemner and Nikolas Tsapatsaris.

The responsible scientists for the DSC and the DLS instruments, Isabelle Grillo and Ralf Schweins, also deserve my thanks, especially for using the chemical lab thanks to Isabelle.

I am thanking the ILL, by awarding me a scholarship and providing me with funding for travel, including many conferences and the stay at DESY.

Thanks to Helmut Schober, who supported the performance of my PhD project.

Many thanks to Colin, Yannick, Emilie and Jacques for English and French proofreading.

Furthermore, I would like to thank Yuri, Yannik, Céline, Christoph and Alain for coffee and running breaks.

Ein dicker Dank an Mo, der mich in stressvollen Zeiten mental unterstuetzt, aufgebaut und motiviert hat.

Einen ganz besonderen Dank verdienen meine Eltern Uwe und Bruni, die mich ausnahmslos in Allem unterstützen und immer für mich da sind.

Abbreviations

A	adenine
AFM	atomic force microscopy
C	cytosine
CaM	calmodulin
CH_2	methylene
CH_3	methyl
CNS	central nervous system
CRG	Collaborative Research Group
CSSB	Centre of Structural Systems Biology
C1-lipids	membrane with MBP-C1 (1-fold protein concentration)
C1-P2-lipids	membrane with MBP-C1 and P2 (1-fold protein concentration, respectively)
D	aspartic acid
DESY	Deutsches Elektronen-Synchrotron
DLS	dynamic light scattering
DMPA	dimyristoyl L-aphosphatidic acid
DMPC	1,2-dimyristoyl-*sn*-glycero-3-phosphocholine
DMPS	1,2-dimyristoyl-*sn*-glycero-3-phospho-L-serine
DOPC	1,2-dioleoyl-*sn*-glycero-3-phosphocholine
DOPS	1,2-dioleoyl-*sn*-glycero-3-phospho-L-serine
DPPC	1,2-dipalmitoyl-*sn*-glycero-3-phosphocholine
DSC	differential scanning calorimetry
E	glutamic acid
EAE	autoimmune encephalomyelitis
E. coli	*Escherichia coli*
EINS	elastic incoherent neutron scattering
EISF	elastic incoherent structure factor
EPR	electron paramagnetic resonance
ESS	European Spallation Source
FABP	fatty acid binding protein
FRM II	Forschungsreaktor München
FWHM	full width at half maximum
G	guanine

HEPES	4-(2-hydroxyethyl)-1-piperazineethanesulfonic acid
His	histidine
HWHM	half width at half maximum
HZB	Helmholtz Zentrum Berlin
Ic	cubic ice
IBS	Institut de Biologie Structurale
Ih	hexagonal ice
ILL	Institut Laue-Langevin
IP	interperiod line
IPTG	Isopropyl-β-D-thiogalactopyranoside
J-Parc	Japan Proton Accelerator Research Complex
K	lysine
LB	Luria Broth
lipids	word here used for protein- and buffer-free membrane
LLB	Laboratoire Léon Brillouin
LMV	large multilamellar vesicle
MBP	myelin basic protein
MD	major dense line
mRNA	messenger RNA
MS	multiple sclerosis
MW	molecular weight
N_A	Avogadro's number
NaCl	sodium chloride
Ni-NTA	Nickel-Nitrilotriacetic acid
NMR	nuclear magnetic resonance
PDB	Protein Data Bank
PDI	polydispersity index
PLP	proteolipid protein
PMP-22	peripheral myelin protein-22
PNS	peripheral nervous system
POPC	1-palmitoyl-2-oleoyl-*sn*-glycero-3-phosphocholine
PSI	Paul-Scherrer Institut
PSD	position sensitive detector
P2	myelin protein 2
P2-lipids	membrane with P2 (1-fold protein concentration)
QENS	quasielastic neutron scattering
QSF	quasielastic structure factor
R	arginine
RNA	ribonucleic acid
SAXS	small-angle X-Ray scattering
SDS	sodium dodecyl sulfate
$< R_h >$	hydrodynamic radius

SDSL	site-directed spin-labeling
SDS-PAGE	sodium dodecyl sulfate polyacrylamide gel electrophoresis
SNS	Spallation Neutron Source
U	uracil
ULV	large unilamellar vesicle
wt	weight
w/v	weight/volume
T	thymine
T_c	gel-to-liquid phase transition temperature of the lipids
TEMED	tetramethylethylendiamin
Tris	Tris(hydroxymethyl)-aminomethan
1f-lipids	membrane with 1-fold protein buffer concentration
2f-lipids	membrane with 2-fold protein buffer concentration
4f-C1-lipids	membrane with MBP-C1 (4-fold protein concentration)
4f-C8-lipids	membrane with MBP-C8 (4-fold protein concentration)
4f-lipids	membrane with 4-fold protein buffer concentration
9f-C1-lipids	membrane with MBP-C1 (9-fold protein concentration)
9f-C8-lipids	membrane with MBP-C8 (9-fold protein concentration)
9f-lipids	membrane with 9-fold protein buffer concentration

List of Figures

List of Tables

Contents

General Introduction

The work described in this PhD thesis was carried out at the Institut Laue-Langevin (ILL) in Grenoble, France, under the supervision of Dr. Francesca Natali and Prof. Dr. Judith Peters. The subject deals with the influence of myelin proteins on the structure and dynamics of reconstituted myelin sheaths, investigated by neutron scattering.

The myelin sheath is a tightly packed multilayered membrane wrapped around selected nerve axons in the central (CNS) and the peripheral nervous system (PNS). Myelin is crucial for the proper functioning of the vertebrate nervous system, because of its electrical insulation of the axons, which allows fast, saltatory nerve impulse conduction. The composition [1, 2, 3, 4, 5, 6] and structure [7, 8] of the myelin sheath is well-defined. Myelin is a very lipid-rich membrane, composed of $75 - 80\,\%$ anionic and neutral lipids and $20 - 25\,\%$ proteins [6]. A subset of myelin-specific proteins, which interact closely with the membrane, is well-known [9], but relatively little is known about their influence on the membrane structure and dynamics. In degenerative neurological diseases, for example multiple sclerosis (MS) occurring in the CNS or Guillain-Barré syndrome in the PNS, damage to myelin results in ineffective nerve signal conduction and its dysfunction.
To gain insight into the role of myelin in autoimmune diseases, the influence of two proteins found in myelin, MBP and P2, on the membrane structure and dynamics were investigated using neutron scattering techniques. Reconstituted model membranes were used as a simplified mimic of the highly complex natural myelin membrane. The model membranes were made of a binary mixture of two synthetic lipids (anionic 1,2-dioleoyl-*sn*-glycero-3-phospho-L-serine (DOPS) and neutral 1,2-dioleoyl-*sn*-glycero-3-phosphocholine (DOPC)), which was used to imitate the negatively charged compact myelin, containing several anionic and neutral lipids. In order to study the role of myelin proteins in the PNS, membranes with MBP-C1 (the least modified form of the various MBP isomers) and P2, which are present together only in the PNS, have been investigated and compared to a protein-free membrane. To determine the influence of an MBP mutant MBP-C8, which has properties similar to the highly modified form seen in MS-patients, on the membrane structure and stability, experiments were performed on reconstituted membranes with MBP-C1 and MBP-C8.
This work profited from the neutron scattering technique, which is a powerful tool for the investigation of biological samples. Biological macromolecules contain approximately $50\,\%$ hydrogen atoms, which have a very large incoherent cross section compared to other

elements. Heavy water was used for the hydration of the membranes in order to change the contrast between solvent and lipids, because of a very small incoherent cross section of deuterium. Furthermore, with cold and thermal neutrons, which have energies in the order of $0.1 - 100$ millielectron volts and wavelengths in the order of $1 - 30$ Ångstrom, the study of biomolecular motions occurring on a pico- to nanosecond timescale and on an atomic length-scale, is possible.

Neutron scattering experiments were carried out at the ILL, the Helmholtz Zentrum Berlin (HZB) in Berlin, Germany, and at ISIS at the Rutherford Appleton Laboratory in Oxfordshire, United Kingdom. Recombinant myelin basic proteins MBP-C1 and MBP-C8 and recombinant myelin protein 2 (P2) were expressed and purified during a practical training under the supervision of Dr. Petri Kursula at the Centre of Structural Systems Biology (CSSB) at the Deutsches Elektronen-Synchrotron (DESY) in Hamburg, Germany. Thanks to the experience acquired at DESY, larger quantities of these proteins were independently expressed and purified at the Institut de Biologie Structurale (IBS) in Grenoble, France, in collaboration with Dr. Martin Weik and Dr. Colin Jackson.

In the first chapter of this thesis, the composition and structure of the myelin sheath is introduced, as well as its role in autoimmune neurodegenerative diseases. The myelin proteins MBP and P2 are also described in detail and the phospholipids DOPS and DOPC, used for the modelling of the myelin membranes are presented.

In the second chapter, a general introduction to the theoretical background to neutron scattering and to the properties of a neutron is provided. The difference between elastic incoherent (EINS) and quasielastic neutron scattering (QENS) is highlighted. The concept of the mean square displacements (MSDs), which are extracted from temperature dependent EINS scans, is explained and the models applied to the quasielastic data, which give detailed information about the type of molecular motions occurring in the samples, are presented. Methods for the production of neutrons for scientific applications together with the functioning of the high-flux reactor at the ILL and of the spallation source ISIS are described. Finally, a brief presentation of the neutron scattering instruments used in this work is given.

The third chapter gives a detailed description of the sample preparation, including the expression and purification protocols of the myelin proteins MBP and P2 and of the preparation of the reconstituted membranes. Methods for the sample characterization, which is crucial for the success of the experiments and the reliability of the obtained results, are also reported.

The fourth chapter deals with the results of neutron scattering experiments obtained for the protein-free membrane. Structural properties, investigated with neutron diffraction on D16 and on IN16, and dynamical properties, studied with EINS measurements on the backscattering spectrometers IN13 and IN16 and with QENS experiments on the time-of-

flight spectrometers IN5, Osiris and Neat, are reported. The theoretical model applied to the quasielastic spectra is discussed and the molecular motions performed by the lipids are interpretated in detail. Furthermore, QENS experiments on Neat and IN5, which were performed to investigate any influence of the protein buffer on the membrane dynamics, are presented.

In the fifth chapter, the investigation of the influence of the myelin proteins MBP-C1 and P2 on the structure and dynamics of a reconstituted PNS myelin membrane, using neutron diffraction on D16, EINS on IN13 and QENS on IN5, Osiris and Neat, is discussed. The same model for the quasielastic scattering function as used for the protein-free lipids was applied to the quasielastic spectra and allowed, together with the structural properties, to propose a model for the proteins associated to the membrane.

The influence of the modified form MBP-C8 on myelin membrane structure and stability is described in the sixth chapter. Neutron scattering experiments on membranes containing MBP-C1 and MBP-C8 at higher protein concentrations than previously used for MBP-C1 and P2, are presented and the results are compared to the observations of a protein-free membrane. The effects of MBP-C8 on the structure of the membrane, using neutron diffraction on D16, are described and EINS measurements, performed on IN16 in order to study molecular motions as a function of the temperature, are discussed. QENS experiments on IN5 at two different energy resolutions permitted detailed analysis of molecular dynamics occurring in the membranes, using the same model for the scattering function. The use of different protein concentrations allowed the investigation of any influence of the protein amount on membrane dynamics.

Finally, conclusions of this work and perspectives on future work are provided.

Introduction Générale

Les travaux décrits dans cette thèse ont été effectués à l'Institut Laue-Langevin (ILL) à Grenoble en France, sous la direction du Dr. Francesca Natali et du Prof. Dr. Judith Peters. Le sujet est focalisé sur l'influence des protéines de la myéline sur la dynamique et la structure de la membrane, en effectuant des expériences de diffusion neutronique sur la myéline reconstituée.

La gaine de myéline est une membrane multicouche enroulant les axones dans le système nerveux central (SNC) et le système nerveux périphérique (SNP). La myéline est cruciale pour le fonctionnement du système nerveux des vertébrés car elle permet l'isolation électrique des axones, ce qui conduit à une conduction rapide des impulsions nerveuses. La composition [1, 2, 3, 4, 5, 6] et la structure [7, 8] de la gaine de myéline est connue et bien définie. La myéline est une membrane très riche en lipides, composée de $75 - 80\,\%$ de lipides anioniques et neutres et $20 - 25\,\%$ de protéines [6]. On connaît un sous-ensemble des protéines spécifiques de la myéline interagissant avec la membrane [9], mais on sait peu de choses sur leur influence sur la structure et la dynamique de la membrane. Dans les maladies neuro-dégénératives, comme la sclérose en plaques touchant le SNC ou encore le syndrome de Guillain-Barré touchant le SNP, les dommages sur la myéline conduisent à un dysfonctionnement de la conduction du signal nerveux. Afin de mieux comprendre le rôle de la myéline dans les maladies auto-immunes et dégénératives, l'influence de deux protéines de la myéline (MBP et P2) sur la structure et la dynamique de la membrane a été étudiée par diffusion neutronique. Pour modeler les membranes naturelles, des membranes artificielles ont été utilisées. Ces membranes artificielles sont composées d'un mélange binaire de deux lipides synthétiques (1,2-dioleoyl-*sn*-glycero-3-phospho-L-serine anionique (DOPS) et 1,2-dioleoyl-*sn*-glycero-3-phosphocholine neutre (DOPC)). Ce deux lipides forment des membranes chargées négativement ce qui permet d'imiter les propriétés de la gaine de myéline compacte. Dans le but d'étudier le rôle des protéines de la myéline sur le SNP, des membranes avec MBP-C1 (la forme la moins modifiée des isoformes de MBP) et P2, qui sont présentes ensemble seulement dans le SNP, ont été comparées à des membranes sans protéines. Afin d'étudier l'influence d'un mutant de MBP, MBP-C8 (qui a des propriétés similaires à la forme modifiée vue dans les malade de sclérose en plaque), sur la structure et la stabilité de la membrane, des expériences ont été effectuées avec des membranes reconstituées contenant MBP-C1 et MBP-C8.
L'étude profitera de la diffusion neutronique comme puissante méthode d'investigation de

la matière biologique. Les macromolécules biologiques comportent environ 50 % d'atomes d'hydrogène, qui ont une grande section efficace incohérente comparé aux autres éléments. Grâce à la section efficace incohérente du deutérium, de l'eau lourde a été utilisée pour l'hydratation des membranes afin de varier le contraste entre le solvant et les lipides. L'énergie et la longueur d'onde des neutrons froids et thermiques se situent dans le domaine des $0.1 - 100$ milliélectronvolts et des $1 - 30$ Ångström, ce qui permet d'étudier la dynamique des biomolécules dans la gamme de temps de la picoseconde à la nanoseconde et la gamme de longueur de l'Ångström.

Des expériences neutroniques ont été réalisées à l'ILL, à l'Helmholtz Zentrum Berlin (HZB) à Berlin en Allemagne, et à ISIS au Rutherford Appleton Laboratory au Royaume-Uni. Les protéines basiques de la myéline MBP-C1 et MBP-C8 et la protéine de la myéline 2 (P2) ont été exprimées et purifiées pendant un stage sous la supervision du Dr. Petri Kursula dans les laboratoires du Centre of Structural Systems Biology (CSSB) au Deutsches Elektronen-Synchrotron (DESY) à Hambourg en Allemagne. Grâce à l'expérience acquise au DESY, de grandes quantités de ces protéines ont pu être exprimées et purifiées à l'Institut de Biologie Structurale (IBS) à Grenoble en France, en collaboration avec Dr. Martin Weik et Dr. Colin Jackson.

Dans le premier chapitre de cette thèse, la composition, la structure de la gaine de myéline et son rôle dans les maladies auto-immunes et dégénératives sont introduits. Les protéines de la myéline MBP et P2 sont décrites en détail et les phospholipides DOPS et DOPC, utilisées pour modeler les membranes de la myéline sont présentées.

Dans le chapitre deux, une introduction générale du contexte théorique et des propriétés des neutrons est donnée. La différence entre la diffusion incohérente neutronique élastique et la diffusion quasi-élastique est soulignée. Les concepts de déplacement carré moyen (MSDs), obtenus par diffusion incohérente neutronique élastique (EINS), sont expliqués. Les modèles, qui seront utilisés pour le traitement des données quasi-élastiques et qui donnent de l'information détaillée sur le type des mouvements moléculaires, sont présentés. Une brève introduction des sources de neutrons pour la recherche scientifique et des instruments neutroniques utilisés pour ce travail est donnée.

Le troisième chapitre donne une description detaillée de la préparation des échantillons avec les protocoles de l'expression et de la purification des protéines de la myéline MBP et P2 et avec la préparation des membranes reconstituées. En outre des méthodes de caractérisation des échantillons, cruciale pour le succès des expériences et la fiabilité des résultats obtenus, sont présentées.

Le quatrième chapitre traite des résultats des expériences de diffusion de neutrons obtenus pour la membrane sans protéine. Des propriétés structurelles, étudiées par la diffraction de neutrons sur D16 et IN16, et des propriétés dynamiques, explorées par EINS sur IN13 et IN16 et par des expériences de diffusion quasi-élastique de neutrons (QENS) en utilisant

IN5, Osiris et Neat, sont présentées. Le modèle appliqué à des spectres quasi-élastiques est discuté et les mouvements moléculaires effectués par les lipides sont interprétés en détail.

Dans le cinquième chapitre, l'investigation de l'influence des protéines de la myéline MBP-C1 et P2 sur la structure et la dynamique d'une membrane reconstituée en utilisant la diffraction de neutrons sur D16, de l'EINS sur IN13 et du QENS sur IN5, Osiris et Neat, est discutée. Le même modèle pour la fonction de diffusion quasi-élastique utilisée pour les lipides, a été appliquée aux spectres quasi-élastiques. Avec les propriétés structurelles, cela a permis de proposer un modèle pour les protéines associées à la membrane.

Dans le sixième chapitre, l'influence de la forme modifiée MBP-C8 sur la structure et la stabilité est décrite. Des expériences de diffusion de neutrons sur des membranes contenant MBP-C1 et MBP-C8 avec une concentration plus élevée comme utilisée pour les membranes avec MBP-C1 et P2, sont présentées. Les résultats sont comparés avec une membrane sans protéine. L'effet du MBP-C8 sur la structure de la membrane, utilisant de la diffraction sur D16, sont décrits. Des mesures EINS sur IN16, afin d'étudier les mouvements moléculaires en fonction de la température, sont discutés. Les mesures QENS sur IN5 à deux résolutions différentes ont permis une analyse détaillée des mouvements moléculaires dans la membrane en utilisant le même modèle pour la fonction de diffusion quasi-élastique. L'utilisation des concentrations de protéines différentes ont permis d'étudier une influence possible de la quantité de protéine sur la dynamique de la membrane.

Finalement, des conclusions sur la présente étude et des perspectives pour de futurs travaux sont données.

Chapter 1

Myelin in the Vertebrate Nervous System

The myelin sheath is the insulating, multi-lamellar membrane structure wrapped around selected nerve axons in the CNS and the PNS. The composition and structure of this membrane, which is crucial for the proper functioning of the vertebrate nervous system, is described in this chapter, as well as its role in degenerative neurological disease, for example MS or Guillain-Barré syndrome. Two myelin proteins, MBP and P2, whose influence on structure and dynamics on model myelin membranes is studied in this work, are described in detail. Finally, an introduction to reconstituted bilayers, used to mimic natural membranes, is given and characteristics of the phospholipids DOPS and DOPC are presented.

1.1 The Myelin Sheath: Composition and Structure

The vertebrate nervous system controls and coordinates all activities of the body by sending electrical signals from the brain through a network of nerve cells. It is separated into the CNS and the PNS. The CNS consists of the brain (cerebrum and cerebellum) and the spinal cord, in which the latter transfers messages between the brain and the PNS. Figure 1.1 illustrates the human nervous system schematically. The CNS is shown in red (brain and spinal cord) and the PNS in blue.

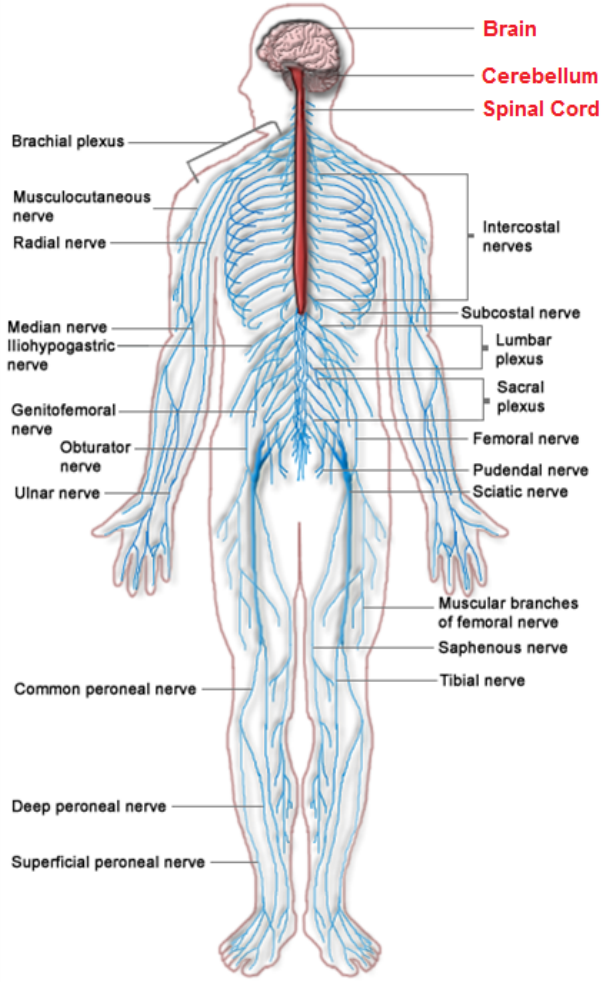

Figure 1.1: Schematic view of the human nervous system with the CNS in red (brain and spinal cord) and the PNS in blue.

Nerve cells (or neurons) not belonging to the CNS comprise the PNS, including cranial, spinal and intramural nerves, with the main function being the connection of the CNS to the limbs and organs. The PNS does not exist as an autonomous system, since neurons responsible for body motion and function of the organs have their soma located in the CNS and neurons related to sensations have their soma in the PNS, but nearly all dendrites in the CNS.
A neuron possesses a cell body (soma) with its nucleus, dendrites, and an axon. The dendrites connect nerve cells to each other and axons build nerve fibers in the form of nerve bundles. The membrane surrounding the nerve axons in both the CNS and the PNS is called myelin, which acts as an electrical insulator and accelerator of nerve impulse conduction (Fig. 1.2). In the white matter of the brain, myelin accounts for approximately

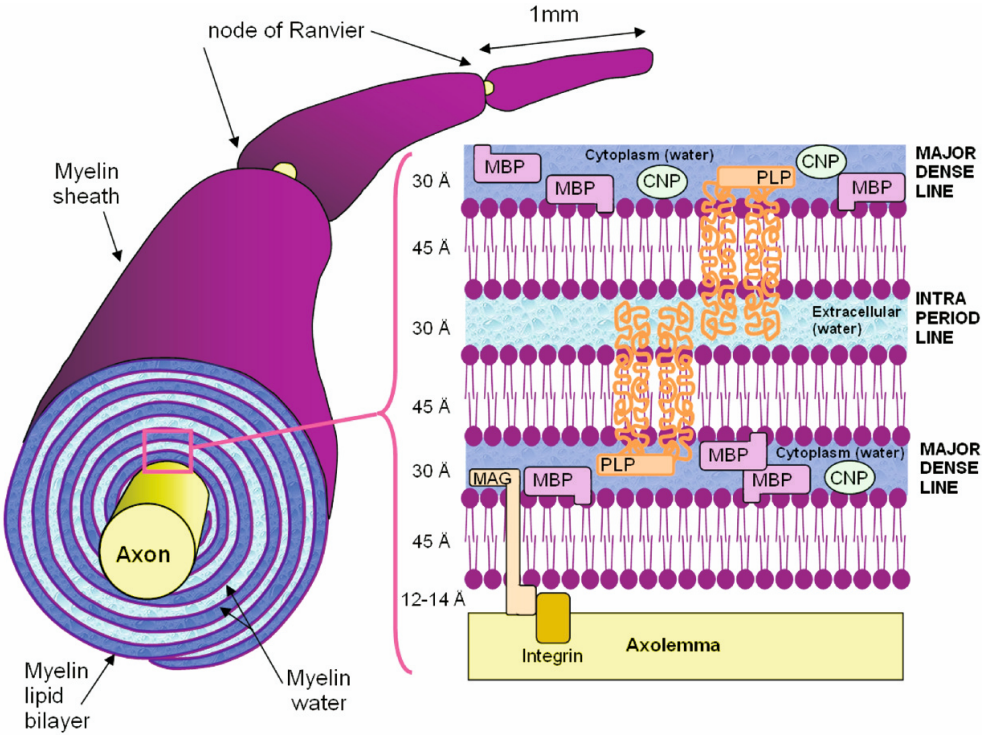

Figure 1.2: The CNS myelin sheath of an axon. The magnified part depicts the membrane with its specific proteins and structural spacings [10].

50 % of the dry weight, giving the white matter its characteristic color [1]. However, the grey matter contains much smaller myelin quantities. The myelin sheath is generated from glial cells, which are the main component of cells belonging to the nervous system [3]. In the PNS, one Schwann cell myelinates only one single segment of one axon [11, 12]. Figure 1.3 shows a schematic view of the peripheral myelination process [1]. First of all, a Schwann cell surrounds the axon and the plasma membrane of the cell joins to form a double membrane structure, the so-called mesaxon (Fig. 1.3 a). Then, the mesaxon fuses into a five-layered structure and wraps the axon in a spiral fashion (Fig. 1.3 b). The formation

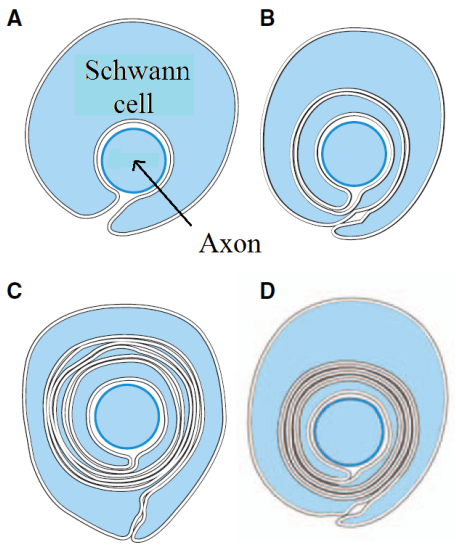

Figure 1.3: Schematic illustration of the myelination process in the PNS (taken from [1]): (a) A Schwann cell surrounds the axon and its plasma membrane forms a double membrane structure (mesaxon). (b) The mesaxon forms a five-layered membrane spiraling around the axon. (c) Formation of membrane layers, which start to compact. (d) Condensation of the cytoplasmic surfaces into a compact myelin sheath.

of layers around the axon continues and the membrane layers start to compact (Fig. 1.3 c). Finally, the cytoplasmic surfaces condense into a compact myelin sheath forming the major dense line (MD) and the extracellular surfaces that adhere to each other to form the intraperiod line (IP) (see Fig. 1.3 d and 1.4 b). The MD and the IP differ not only in their structure, but also in their protein composition. In the CNS, each oligodendrocyte may myelinate segments of not only one, but several axons (40 or more) [14, 1]. During myelination, the surface area of these segments varies between 5000 μm^2 and 50000 μm^2 per day [2]. CNS myelin has also a spiral structure, similar to PNS myelin: it has an inner and outer mesaxon, which ends in an outer loop of glial cytoplasm (illustrated in Fig. 1.4). This cytoplasmic loop presents only a small fraction of the myelin sheath, in contrast to peripheral myelin, where the sheath is surrounded by Schwann cell cytoplasm on the inside and outside (Fig. 1.3).
Myelinated segments are called internodes and the periodic interruptions where no myelin is present are the so-called nodes of Ranvier, which are locations for sodium channels (see Fig. 1.4). Due to this unique segmental structure of the myelin sheath, nerve impulses are not transmitted slowly along the axon as in un- or demyelinated fibers, but they jump from node to node: ion exchange during nerve conduction is prevented at the internodes and occurs only at the nodes of Ranvier [15]. This process is named saltatory conduction and results in increasing the speed of the nerve impulse conduction of up to 100-fold (100 m/s in a healthy person) compared to the conduction rate in axons without myelin.

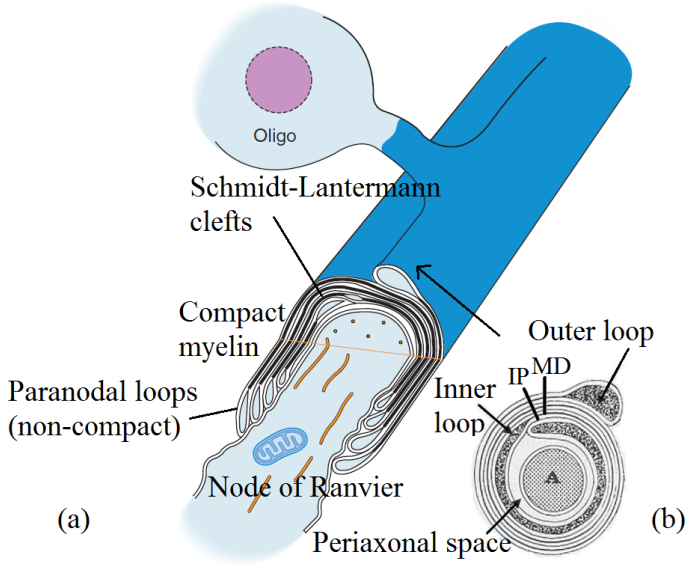

Figure 1.4: (a) Side-view (taken from [1]) and (b) cross section of the myelin sheath in the CNS surrounding an axon (A), taken and readapted from [13]. The MD is formed by the cytosolic surfaces of two unit membranes and the IP by the extracellular surfaces.

Figure 1.4 illustrates the myelin sheath in the CNS schematically. The sheath contains regions of compacted, i. e. very tightly packed, and non-compacted myelin. The non-compacted myelin is found at the para-nodal loops adjacent the nodes of Ranvier, the inner- and outer loops and Schmidt-Lanterman clefts running through the internodes [4]. The non-compacted regions include Schwann cell or oligodendrocyte cytoplasm. The periodicity of the spiraled myelin sheath varies between 150 and 180 Å [7, 8], the extracellular spacing in myelin (IP) is $30 - 50$ Å and the intra cellular spacing (MD) is $30 - 40$ Å (see Fig. 1.2).
The composition of myelin is well defined, due to the ability to isolate myelin at a high degree of purity by sucrose gradient centrifugation [5]. Myelin is very lipid-rich, containing $75 - 80$ % lipids (anionic and neutral) and $20 - 25$ % proteins [6]. Its water content is approximately 40 % of the total weight. The water is located in the intra- (cytoplasm) and extracellular spaces between the bilayers, as sketched in Fig. 1.2. Lipids found in CNS myelin are not "myelin-specific" [1, 2]: the most abundant lipids are phospholipids, which account for 40 % of the total dry weight and are important for the membrane structure. Galactolipids, preferentially localized at the IP, and cholesterol, enriched likewise at the IP and essential for myelin assembly, constitute approximately 30 % of the total dry weight. Regarding the molecular weights of these lipids in CNS myelin, the ratio of cholesterol, phospholipids and galactolipids varies between 4:3:2 and 4:2:2. Despite some quantitative differences in lipid composition, PNS myelin is quite similar to CNS myelin. Nevertheless, the differences of myelin proteins present in the PNS and the CNS are significant and discussed in the following Section 1.2.
In demyelinating degenerative diseases, such as MS, which occurs in the CNS, or Guillain-

Barré syndrome, which occurs in the PNS, damage to the myelin sheath results in ineffective nerve signal conduction by the axons.
MS is the most commonly occurring chronic inflammatory disease of the CNS in Europe and has a prevalence of 150 per 100 000 citizen. It is characterized by disseminated multiple patches of demyelination in the white matter of the brain and in the spinal cord. Typical symptoms are primary sight disorders or visual loss and impairment of body movements when the illness is progressing. Primary demyelination of the axons occurs in the early stages of MS and results in myelin destruction, whereas in the later chronic stage even axonal loss occurs, which is responsible for permanent disability [16]. The etiology of the disease is still not clarified. However, it is assumed that the myelin sheath is damaged by autologous antibodes.
Guillain-Barré syndrome is, with 1 to 2 cases per 100 000 people per year, a more rare neurologic disease. It is a polyneuropathy (neurological disorder) characterized by inflammatory changes of PNS myelin found at nerve roots in the spinal cord and results in demyelination and possible axonal damage. Typical symptoms include weakness beginning in the feet and hands and migrating towards the body as well as increasing paralysis.
Like MS, the etiology of this and other neuropathic diseases remains unknown. These diseases share the common trait of demyelination, obstructing the neuronal transmission, and constitute a serious medical and social problem in the world.

1.2 Myelin Proteins

The myelin sheath contains a well characterized subset of myelin-specific proteins [9], which have unique biochemical properties and interact closely with the membrane. The major CNS proteins are MBP and the proteolipid protein (PLP), which constitute 80 % of the total protein fraction [12]. PNS myelin contains MBP, the P0 glycoprotein, the peripheral myelin P2, and the peripheral myelin protein-22 (PMP-22). Figure 1.5 illustrates CNS and PNS compact myelin with its specific protein compositions. In this work, we focus on the two peripheral myelin proteins MBP, present in the CNS and PNS, and P2, present only in the PNS, both located in the compacted regions of myelin.

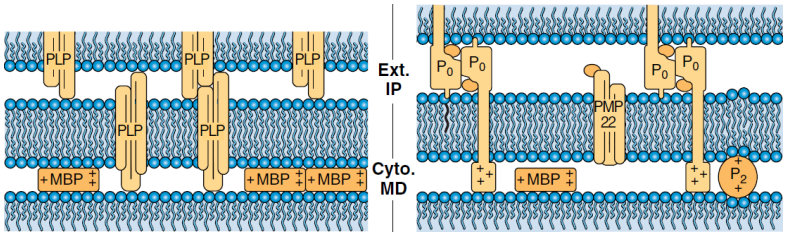

Figure 1.5: Schematic illustration of the compact myelin membrane of the CNS (left) and the PNS (right) containing a different composition of myelin-specific proteins [1].

1.2.1 Myelin Basic Protein (MBP)

The MBP is located between the cytoplasmic leaflets in the MD of the multi-lamellar myelin sheath in both the CNS and the PNS, where it constitutes approximately 30 % [17] and $5-18$ % [4] of the total protein fraction, respectively. It comprises numerous isoforms, of which the 18.5-kDa protein is the most abundant in adult human myelin. MBP is one of the main agents responsible for formation and compaction of CNS myelin [18, 19] and plays a structural role in maintaining myelin stability by providing the adhesiveness of the cytosolic surfaces of the membrane [13, 20, 21, 22]. However, in the PNS, it is assumed that MBP plays a less important role in myelin structure, probably because P_0 is crucial for stabilizing the MD of PNS myelin [1]. Due to the high positive charge of MBP, it binds to mixtures of neutral and negatively charged lipids, preferentially to the latter [23, 24]. The surface adhesion of the cytoplasmic surfaces of myelin lipid bilayers is maximal, with minimum cytoplasmic spacing, when each anionic lipid binds to a cationic argine or lysine group of the MBP protein [25]. Polverini *et al.* [26] have shown with ellipsometric techniques that lipid-free bovine MBP interacts differently with neutral and negatively charged phospholipid monolayers: MBP in the presence of neutral lipids seems to penetrate among the lipid domains with a nonspecific interaction, whereas MBP binds to the headgroups of anionic lipids due to electrostatic interactions, building a lipid-protein complex. Sedzik *et al.* [27] have discovered that bovine MBP, when added to single-bilayer vesicles, which are made of bovine myelin lipids, causes aggregation of the vesicles within seconds. The aggregated vesicles form to multilayers within minutes at a protein concentration of ≥ 2 wt%. X-Ray diffraction patterns indicated that the inter-bilayer spaces in the multilayers are comparable to the cytoplasmic spaces in CNS myelin. It has been discovered that myelin monolayers exhibit two phases at low surface pressure: a cholesterol-enriched, liquid-ordered phase and a protein-enriched, liquid-expanded phase. MBP was present in the latter and squeezed out of the layer at higher surface pressures that result in gel-phase formation [28, 29, 30]. This suggests that MBP causes a phase separation of lipids into gel and liquid phase and binds preferentially to liquid-disordered domains. With neutron scattering experiments it was demonstrated that MBP, purified from mammalian CNS, affects the mobility of lipids when bound to bilayers made of dimyristoyl L-aphosphatidic acid (DMPA) [31]. Membrane dynamics perpendicular to the membrane plane in the order of 1 ns, characterized by spatially restricted diffusive motions of the lipids, were significantly enhanced by MBP in the liquid phase of the lipids.
MBP does not only associate with cytosolic lipids, but also with different cytosolic proteins, suggesting that it might function as a binding agent and a scaffolding protein [22]. One of the proteins bound by MBP is for example calmodulin (CaM), which is a highly negatively charged calcium-binding protein. By affinity chromatography it has been confirmed that the C-terminal segment of MBP interacts mainly with the C-terminal of calmodulin [32].
The 18.5-kDa isoform of MBP exists *in vivo* as a series of charged isomers denoted as MBP-C1 to MBP-C8 [33]. MBP-C1 is the least modified and most cationic form, with a net charge of +20 at neutral pH [34]. The amino acid sequence of murine MBP-C1 is [35]

MASQKRPSQRSKYLATASTMDHARHGfIPRHRDTGILD
SIGRffSGDRGAPKRGSGKDSHTRTTHYGSLP QKSQHG
RTQDENPVVHffKNIVTPRTPPPSQGKGRGLSLSRFSWG
AEGQKPGFGYGGRASDYKSAHKGFKGAYDAQGTLSKI
FKLGGRDSRSGSPMARR,

where the positively charged amino acids lysine (K) and arginine (R) are marked in blue and the negatively charged aspartic acid (D) and glutamic acid (E) in red, in order to demonstrate the charge distribution, which is quite homogeneous. MBP-C8 harbors six point post-translational modifications of arginine and lysine residues converted to uncharged citrulline side chains, which results in a net charge of +14 at neutral pH [21]. This form has properties similar to the highly modified form seen in MS-patients [36]. Due to a less compact protein structure and disruption of its interactions with negatively charged lipids, MBP-C8 exhibits a limited ability to maintain a compact myelin sheath [37, 38]. MBP is one of the auto-antigens in MS [39, 40] and in autoimmune encephalomyelitis (EAE), which is a model for MS [41]. Collectively, these results imply that changes to the biophysical properties of MBP might cause or result from the changes to myelin observed in some neurodegenerative diseases.

A detailed three-dimensional structure of MBP is still not known. Since MBP is highly charged and hydrophilic, which leads to intramolecular electrostatic repulsion, it exists in an extended, intrinsically disordered, conformation in solution [42, 43, 44]. In contrast, in the presence of lipids, MBP adopts a more ordered structure with β-sheets and α-helical regions [45, 46]. In the mid 1980's Stoner [47] and Martenson [48] predicted regions with a β-sheet-backbone and α-helical segments in MBP. By ^{1}H-NMR (nuclear magnetic resonance) spectroscopy and CD spectropolarimetry, Mendz *et al.* have found discrete interaction sites in MBP-peptides in the presence of micelles, one of which could be an α-helix between residues 87 and 97. In 1997, Beniac and Ridsale [49, 50] suggested a "C"-shape for lipid-bound bovine MBP. They reconstructed a three-dimensional model based on electron microscopy studies of single MBP particles on a lipid-monolayer. Built on this and on the model of Stoner and Martenson, molecular dynamics simulations have been performed, resulting in a "C"-shape with a β-sheet backbone (Protein Data Bank (PDB) entry 1QLC). A picture of the MBP structure is shown in Fig. 1.6 a, made by using the software PyMol (The PyMOL Molecular Graphics System, Version 1.3, Schrodinger, LLC). The dimensions of this form are 55 Å for the outer and 30 Å for the inner diameter, an circumference of 150 Å and a height of 47 Å. MBP is supposed to lie flat on the MD of the myelin membrane, i.e. the cavity of the "C"-shape in plane with the membrane. Since the MD has a width of approximately 17 Å, the protein would have to penetrate deeply into the apposing bilayers. Bates *et al.* [21] have performed molecular modeling simulations with this MBP-model (using the PDB-entry 1QCL) in water with, and without, added counter ions to simulate also the less cationic mutant MBP-C8. They have discovered the formation of α-helices resulting in an extended protein structure, which could readily fit into the MD of the myelin sheath. MBP-C8 had an even less compact structure, indicating that the tertiary structure of MBP is affected by its net charge.

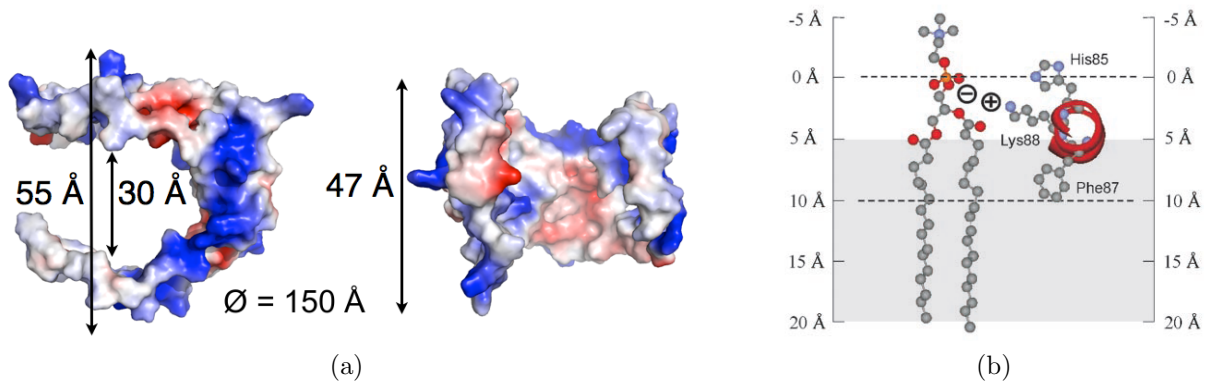

(a) (b)

Figure 1.6: (a) "C"-shape of bovine MBP determined by electron microscopy and molecular modeling [49, 50], PDB-entry 1QLC. (b) Schematic representation of the region 83-92 of recombinant murine MBP bound to an anionic phospholipid, forming an α-helix. The lysine group of these residues Lys-88 interacts with the negatively charged lipid headgroup. (Figure referred in [51].)

Site-directed spin-labeling (SDSL) and electron paramagnetic resonance (EPR) spectroscopy, complemented with molecular modeling simulations and CD spectroscopy have shown that the region of residues 83-92 of recombinant murine MBP (corresponding to residues 86-95 of human MBP) formed an α-helix, when bound to myelin-like vesicles [51]. This α-helix penetrated up to 12 Å into the bilayer and was tilted at 9° with respect to the membrane plane surface (Fig. 1.6 b). The central lysine of this segment was in such a position that the positively charged side chains interact with the negatively charged lipid headgroups. Polverini *et al.* [52] have studied the α-helical peptide Glu80-Glu103 associated with a bilayer made of 1,2-dimyristoyl-*sn*-glycero-3-phosphocholine (DMPC) lipids. This segment consists of two successive structural motifs: a membrane-bound amphiphatic α-helix including the residues 83-92, followed by a proline-rich segment. Since one strand of the β-sheet backbone of the original "C"-shape model contains exactly the residues 83-92, the "C"-shape model has been challenged. In contrast, at the same time, Haas *et al.* [53] performed small-angle X-Ray scattering (SAXS) studies on lipid-bound bovine MBP and discovered by model-free fitting of the SAXS-data an extended "C"-shape for the protein, consistent with the structure available in the PDB (entry 1QLC). The precise MBP three-dimensional structure is therefore still unclear and requires further analysis.

1.2.2 Myelin Protein 2 (P2)

The peripheral myelin protein P2 is a 14.8-kDa protein and only present in the PNS, where it constitutes $1-15\,\%$ of the protein fraction, depending on the species [1, 54]. P2 is located on the cytoplasmic side of compact myelin [55]. In this fluid zone with a high amount of phospholipids, the pH might be low [56], which could induce the interactions of the negatively charged headgroups with the basic P2 protein and cause a flexible and partial

unfolded protein-structure, due to the loss of hydrogen bonds. Further, computational docking experiments have shown, that cholesterol, one of the most abundant myelin-lipids (see Section 1.1), might be a ligand for P2, and therefore P2 probably binds to cholesterol-rich micro-domains in compact myelin [43].
Due to the electrostatic potential of the P2 surface (net charge +10 at neutral pH), with two highly positively charged large, opposed regions, separated by a neutral central rim (Fig. 1.7, right), it is thought to play a similar structural role in PNS myelin as MBP does in CNS myelin, by the interplay of the protein with two opposing myelin membrane leaflets [43]. Similar to MBP, P2 causes single bilayer vesicles to transform into stable

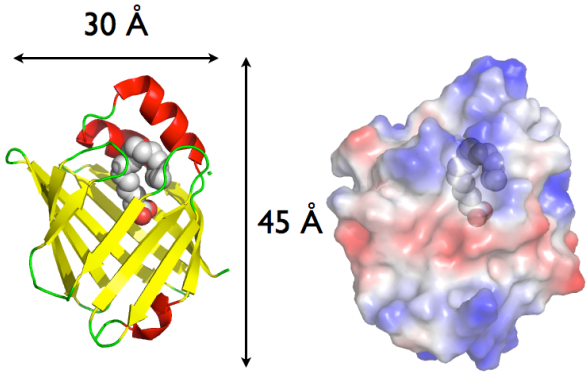

Figure 1.7: Left: Crystal structure of the human myelin protein P2. The 10-stranded up- and down-β-barrel is linked by two anti-parallel $\alpha-$ helices on the top open end of the barrel. The fatty acid bound inside the cavity is shown in grey. Right: Electrostatic potential of the P2 surface: Positively charged opposite regions and an almost neutral center (blue: positive charge; red: negative charge; grey: neutral). The figures were made using PyMOL with the PDB-entry 2WUT (human P2).

stacked multilayers, but only at an adequate protein concentration [57]. Compared to MBP, which created multilayers at a smallest amount of 2 wt% [27], for P2 at least 4 wt% were needed, indicating that P2 is not as strong an agent as MBP for the formation of multilayers. Protein-lipid-binding was saturated at 15 wt%, corresponding to the amount of P2 in the PNS. Recent studies on P2 (1.25 wt%) bound to myelin-like vesicles made of DMPA and vesicles made of DOPS and DOPC, respectively, have shown that P2 stabilizes them by reducing their dynamics [58].
Atomic force microscopy (AFM) experiments on MBP and P2 bound to a myelin-like membrane, have shown that both myelin proteins act synergistically to induce stacking of the bilayers, at concentrations of 1.8 μM MBP-C1 (corresponding to 1.64 wt%) and 0.338 μM P2 (corresponding to 0.24 wt%) [59]. This stacking effect was also caused by MBP and P2 alone, but less strongly than in combination. P2 induced stacking at lower concentrations than MBP (0.338 μM of P2 was needed to detect stacking, but 1.8 μM was the minimum concentration for MBP). This effect could be caused by the local positive charge on the globular P2-surface, and thus charge alone seems to be not the driving factor

for membrane stacking (the electrostatic potential of MBP is higher).
Unlike MBP, no modified variants of P2 have been identified with links to autoimmune diseases. However, P2 is supposed to be an auto-antigen in Guillain-Barré syndrome, which is an autoimmune disease of the PNS [60, 61].
P2 belongs structurally to the family of cytoplasmic fatty acid binding proteins (FABPs), which are characterized by a β-barrel and an internal single-ligand-binding cavity, and are able to transport fatty acids into the cytoplasm [62]. The crystal structures of bovine and equine P2 have been established by X-Ray crystallography [63, 61], revealing a compact β-barrel, which consists of 10 antiparallel β-sheets surrounding an internal ligand-binding cavity (see Fig. 1.7, left). Two α-helices are located on one open end of the β-barrel, linking the first two β-strands and closing the barrel on the top. When the binding cavity interacts with lipids, the α-helices open like a "lid" and possibly penetrate partially into the hydrophobic headgroups [43].
Recently, Majava *et al.* [43] have identified the structure of recombinant human P2 (PDB-entry 2WUT), which shared the same structural features as the bovine and equine forms. X-Ray studies indicated a mainly β-sheet structure, with 48 % β-sheets, 17 % α-helices and 35 % other structures. The shape of P2 in solution was found to be similar to its crystal structure with dimensions of 30 Å for the length, 20 Å for the width and 45 Å for the height, including the helical lid. The β-barrel without the lid has a height of approximately 30 Å. The structure of P2 is influenced when bound to lipids, which causes a decrease in the α-helical and an increase in the β-sheet content compared to lipid-free P2 [64]. Steele *et al.* [65] have shown an increase of the binding-ability to fatty acids of a FABP-mutant with less α-helical and higher β-sheet content. The lack of α-helices allowed a wider opening of the lid and therefore a more efficient binding between the internal cavity and the external fatty acids. Sedzik *et al.* [66] have performed X-Ray diffraction on P2 crystals bound to myelin lipids, resulting in slightly larger unit-cell dimensions of the crystal. Mass spectrometry measurements indicated that the myelin lipids were intrinsic components of the crystal.

1.3 Model Myelin Membranes

Since natural myelin membranes are highly complex and consist of several types of lipids, proteins and carbohydrates (glycolipids and glycoproteins), model membranes were used to mimic these complex systems. To gain insight into the role of myelin proteins in degenerative diseases, reconstituted myelin-like membranes with two myelin proteins MBP and P2 were investigated with neutron scattering techniques, as a first approach. Therefore, the influence of MBP-C1, MBP-C8 and P2 on the structure and dynamics of those membranes was of great interest. In the future, other myelin components will be added gradually, in order to study more complex systems, and natural tissue containing myelin, suffering, or not, from neurodegenerative diseases, will be investigated as well. The model membranes, studied in this work, consist of a binary mixture of two synthetic lipids (anionic DOPS and neutral DOPC) with, and without, the recombinant myelin proteins MBP-C1, MBP-C8 and P2. This synthetic neutral-anionic lipid mixture was used to mimic the properties of

the inner leaflet of the bilayers in myelin, which is negatively charged (containing several anionic and neutral lipids). To study the role of myelin proteins in the PNS, membranes with two PNS myelin proteins MBP-C1 and P2, have been investigated and compared to a protein-free membrane. To determine the structure and dynamics of diseased and healthy myelin, a second membrane sample set with both MBP-C1 and the mutated form MBP-C8 (which has properties similar to the highly modified form seen in MS-patients), have been prepared and measured to investigate the influence of the mutant on membrane stability. In the following, an introduction to reconstituted bilayers, mimicking natural membranes, is given and characteristics of the phospholipids DOPS and DOPC are described.

1.3.1 Phospholipids DOPS and DOPC

Phospholipids are phosphoric, amphiphilic molecules, which consist of a hydrophilic headgroup and two hydrophobic hydrocarbon chains. They spontaneously form different structures when inserted into aqueous solution, such as micelles, liposomes and bilayers (Fig. 1.8). A phospholipid bilayer can adopt different phases as function of temperature, which

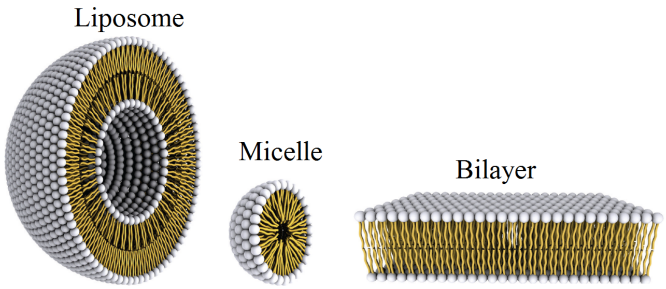

Figure 1.8: Different structures formed by phospholipids: liposomes (left) are constructed by a lipidic bilayer (right) and micelles by one lipid layer (middle). Taken from [67].

has a significant effect on the lipid mobility; namely, the lamellar gel phase $L_{\beta'}$ (ordered) and the lamellar liquid crystalline phase L_{α} (disordered). Figure 1.9 shows a schematic drawing of a bilayer in the gel (left) and in the liquid phase (right). In the gel phase, the

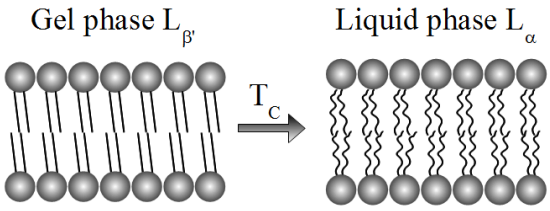

Figure 1.9: Schematic drawing of a bilayer in the gel (left) and in the liquid phase (right).

lipid chains are organized in an ordered state, whereas in the liquid phase the chain order

vanishes. The transition from the ordered gel phase to the disordered liquid phase is called main phase transition and occurs at a temperature T_c, specific for each lipid type. Some saturated phospholipids, wich have chains of carbon atoms linked together by single bonds, exhibit minor phase transitions prior to the main phase transition, such as the ripple phase P'_β, characterized by one dimensional ripples on the membrane surface and tilted chains [68]. Since DOPS and DOPC lipids are unsaturated lipids, with a carbon-carbon double bond in each chain, a pre-transition does not exist.
To mimic the properties of the inner leaflet of the negatively charged multi-lamellar myelin sheath, the synthetic phospholipids DOPS and DOPC were used to model myelin membranes. Figure 1.10 illustrates the chemical structure of DOPS and DOPC. Both

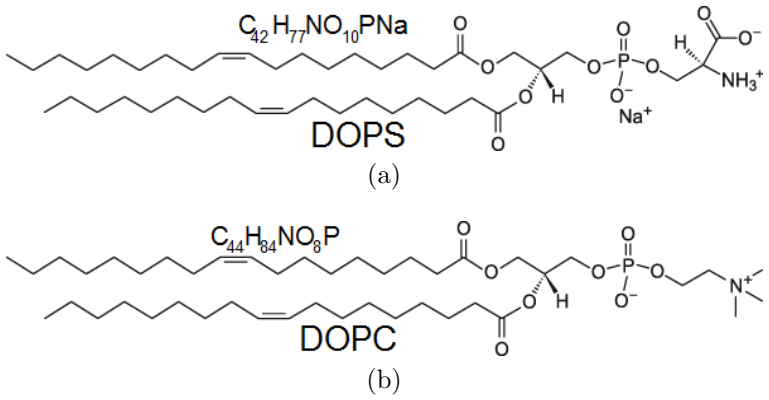

Figure 1.10: Chemical structures of (a) DOPS with an added counterion Na^+ and (b) neutral DOPC [69, 70].

lipids possess the same tails containing 17 carbon molecules in each chain, but they differ in their headgroups. DOPS has an anionic lipid head and a molecular weight of MW = 810 Da, whereas DOPC has an electrically neutral headgroup and a molecular weight of MW = 786 Da. Their main phase transition temperature is T_c = 262 K for DOPS and T_c = 253 K for DOPC. Since the melting temperature of human P2, where the protein unfolds, is T_M = 335 K [43], and the purpose of the neutron experiments was to investigate the model membranes in their gel and in their liquid phases, DOPS and DOPC lipids were chosen, since they are very suitable due to their lower phase transition temperatures.
Biological systems, such as membranes, are always in an aqueous environment and its function is primarly associated with the fully hydrated form, i. e. 100 % humidity. The level of hydration has a strong influence on membrane dynamics [71, 72]. The hydration water is located in the interbilayer space and between the headgroups. The structural parameters of fully hydrated DOPS and DOPC bilayers in the fluid phase have been investigated in detail using X-Ray scattering techniques [68, 73]. The molecular volume of the lipid heads was found to be $V_H^{DOPS} = V_L^{DOPS} - V_C = 244\,\text{Å}^3$ for DOPS, where V_L is the molecular volume of the lipid and V_C of the lipid chain, and $V_H^{DOPC} = 319\,\text{Å}^3$ for DOPC, respectively. Despite the electrostatic repulsion expected for PS headgroups, DOPS has a

smaller lipid cross-section area of $A^{DOPS} = 65\,\text{Å}^2$ than DOPC, which has a cross-section area of $A^{DOPC} = 73\,\text{Å}^2$. This suggests hydrogen bonding between the negatively charged PS headgroups. The cross-section area for the lipid heads of DOPC was found to be $46\,\text{Å}^2$ [74]. Figure 1.11 shows a sketch of a fully hydrated phospholipid membrane. D_B is the

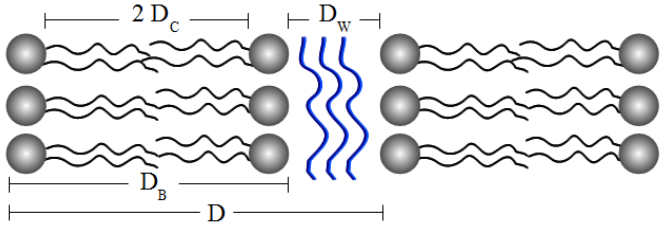

Figure 1.11: Sketch of a fully hydrated phospholipid membrane. D_B: bilayer thickness, D_W: thickness of water layer between two bilayers, D_C: chain length, $D = D_B + D_W$: repeat distance of the bilayers.

bilayer thickness, D_W the thickness of the water layer between two bilayers, D_C the chain length and $D = D_B + D_W$ the repeat distance of the bilayers. In Table 1.1 these values are listed for DOPS and DOPC.

	D [Å]	D_B [Å]	D_W [Å]	$2\,D_C$ [Å]	V_L [Å^3]	V_C [Å^3]	V_H [Å^3]	A [Å^2]
DOPS	53	38	15	31	1228	984	244	65
DOPC	63	36	27	27	1303	984	319	73

Table 1.1: Structural parameters for DOPS and DOPC bilayers in the fluid phase of the lipids (303 K) [68, 73].

Chapter 2

Neutron Scattering to Study Structure and Dynamics of Biological Membranes

The neutron was discovered by James Chadwick in 1932 [75, 76]. Together with the proton it builds the nuclei of atoms, with the exception of hydrogen. It has a mass of $m_n = 1.675 \cdot 10^{-27}$ kg, a spin of 1/2 and a magnetic moment of $\mu_n = -9.66236 \cdot 10^{-27}\mathrm{TJ}^{-1}$. Due to its electric neutral charge it penetrates deeply into matter and interacts strongly with the nuclei of a scatterer. Therefore, neutrons are scattered by nuclear forces depending on the element. Elastic scattering occurs, when no energy transfer between the neutron and the scatterers occurs. Besides elastic scattering, there are inelastic and quasielastic scattering processes, allowing the investigation of dynamical processes in the sample. Inelastic scattering gives information about lattice vibrations (phonons) and quasielastic scattering permits the study of diffusive or rotational motions, which occur in a time scale ranging from pico- to nanoseconds and in a spatial range from about 1 to 20 Å.
In this chapter, the theoretical background to neutron scattering is introduced. Furthermore, the difference between EINS and QENS is emphasized and models for QENS used for data analysis (see Chapters 4, 5 and 6) are specified. In later sections, the production of neutrons for scientific applications is described and the functioning of the high-flux reactor at the ILL and of the spallation source ISIS, as well as of neutron instruments used in this work, are reported.

2.1 Neutron Scattering Theory and Models

Since a detailed description of the neutron scattering theory can be found in textbooks [77, 78], only a short overview is given in the following section. Fundamental quantities and relations necessary for the understanding of neutron scattering are explained. The difference between coherent and incoherent scattering is illustrated in order to clarify the investigation of structural and of dynamical processes.

2.1.1 Properties of a Neutron

A neutron features both wave and particle properties. It can be described as a particle with a kinetic energy of

$$E = \frac{1}{2}\, m_n\, v^2, \tag{2.1}$$

where m_n is the neutron mass and v its velocity. The de Broglie wavelength of a neutron is

$$\lambda = \frac{h}{m_n\, v} = \frac{2\,\pi}{|\vec{k}|} \tag{2.2}$$

with Planck's constant h and $|\vec{k}|$ being the modulus of the wave vector

$$\vec{k} = \frac{m_n}{\hbar}\,\vec{v}, \tag{2.3}$$

where $\hbar = h/(2\,\pi)$. Hence, it follows for the neutron energy:

$$E = \frac{\hbar^2\, k^2}{2\, m_n} = \frac{h^2}{2\, m_n\, \lambda^2} \tag{2.4}$$

and it holds for the relation between neutron energy and wavelength

$$\lambda \;\propto\; \frac{1}{\sqrt{E}}. \tag{2.5}$$

2.1.2 The Scattering Event

Figure 2.1 illustrates the geometry of a neutron scattering experiment. The incident neutron with an energy E_i and a wave vector $\vec{k}_i$ has an incident angle of Θ and is scattered at the sample position with a scattering angle 2Θ in direction $\vec{k}_f$. The energy transfer is thus

$$\Delta E = \hbar\omega = E_f - E_i = \frac{\hbar^2}{2m_n}(k_f^2 - k_i^2). \tag{2.6}$$

with the frequency ω. $E_f > E_i$ implies energy gain of the neutron and therefore energy loss of the sample, while $E_f < E_i$ implies energy loss of the neutron and energy gain of the sample. Scattering processes with $E_f \neq E_i$ are called inelastic or quasielastic scattering and processes with $E_f = E_i$ elastic scattering. The momentum transfer is defined as

$$\hbar\vec{Q} = \hbar\vec{k}_f - \hbar\vec{k}_i \tag{2.7}$$

with the scattering vector or momentum transfer

$$\vec{Q} = \vec{k}_f - \vec{k}_i. \tag{2.8}$$

For inelastic processes with with $\vec{k}_i \neq \vec{k}_f$, it has to be taken into account that $\vec{Q}$ changes with the energy transfer ΔE. It holds for the scattering vector $\vec{Q}$:

$$Q^2 = {k_i}^2 + {k_f}^2 - 2\, k_i\, k_f\, \cos 2\Theta \tag{2.9}$$

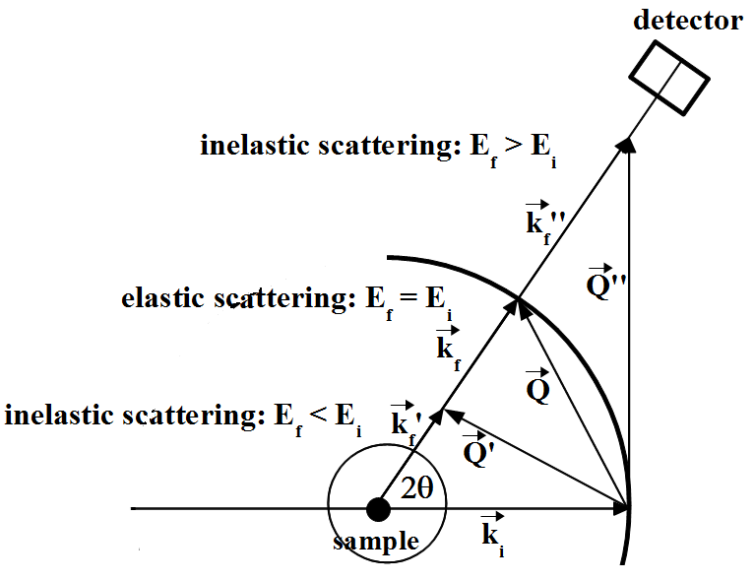

Figure 2.1: Sketch of the geometry in a neutron scattering experiment. Energy transfer $\Delta E = E_f - E_i$ and scattering vector $\vec{Q}$ are illustrated schematically. $\vec{k}_i$ is the wave vector of the incident neutron and $\vec{k}_f$ the wave vector of elastic scattered neutrons. $\vec{k}'_f$ and $\vec{k}''_f$ illustrate the wave vectors of inelastic scattered neutrons.

For elastic scattering, $|\vec{k}_i| = |\vec{k}_f|$ and the modulus of the scattering vector can be written as

$$|\vec{Q}| = \frac{4\pi}{\lambda} \sin\Theta. \tag{2.10}$$

With Eq. 2.4 it follows the relation between the energy dependent scattering vector $\vec{Q}$, incident wave vector $\vec{k}_i$ and scattering angle $2\,\Theta$ for inelastic scattering

$$Q^2(\Delta E) = 2\,{k_i}^2 - \frac{2\,m_n\,\Delta E}{\hbar} - 2\,k_i\,\cos 2\Theta\sqrt{{k_i}^2 - \frac{2\,m_n\,\Delta E}{\hbar}}. \tag{2.11}$$

In a neutron scattering experiment the double differential scattering cross section

$$\frac{d^2\sigma}{d\Omega\,dE} \tag{2.12}$$

is measured. It indicates the number of neutrons, normalized to the incident neutron flux ϕ, of an incident energy E_i with final energy in the interval between E_i and $E_f = E_i + dE$, that are scattered per second into a solid angle element $d\Omega$ in direction of vector $\vec{k}_f$. Integration of the double differential cross section gives the total cross section

$$\sigma = \int dE \int \frac{d^2\sigma}{d\Omega\,dE}\,d\Omega, \tag{2.13}$$

which is defined as the total number of neutrons scattered per second in all directions and has the unit barn with $1\,\text{barn} = 10^{-28}\text{m}^2$.
The interaction between a neutron and a nucleus is caused by short-ranged nuclear forces. For cold and thermal neutrons, this interaction can be described in a first approximation by the isotropically diffusing Fermi pseudopotential:

$$V_i(\vec{r}) = \frac{2\pi\hbar^2}{m_n}\, b_i\, \delta(\vec{r} - \vec{R}_i), \tag{2.14}$$

where $\vec{r}$ is the position of the neutron and $\vec{R}_i$ the position of the i-th nucleus. b_i is the scattering length of the i-th nucleus, which is dependent on the isotope as well as on the orientation of the total nuclear spin. The so-called coherent scattering length b_{coh} is defined as the average of all scattering lengths b_i of all the isotopes in a sample

$$b_{coh} = \langle b_i \rangle \tag{2.15}$$

and the incoherent scattering length b_{inc} as the square root of the variance of the mean average value b_i

$$b_{inc} = \sqrt{\langle b_i^2 \rangle - \langle b_i \rangle^2}. \tag{2.16}$$

Since every sample consists of several elements with different isotopes having an appropriate nuclear spin I, in which the total spin is either $I + \frac{1}{2}$ or $I - \frac{1}{2}$, the corresponding scattering length is b^+ or b^-. Considering an individual isotope ($i = 1$), it follows for the coherent and the incoherent scattering length

$$b_{coh} = \langle b \rangle = \frac{1}{2I+1}[(I+1)b^+ + I\, b^-] \tag{2.17}$$

and

$$b_{inc} = \sqrt{\langle b^2 \rangle - \langle b \rangle^2} = \frac{\sqrt{I(I+1)}}{2I+1}[b^+ - b^-]. \tag{2.18}$$

The relation between b_{coh} and b_{inc} and the scattering cross section is the following [78]:

$$\sigma_{coh} = 4\pi \langle b \rangle^2 = 4\pi\, b_{coh}^2 \tag{2.19}$$

and

$$\sigma_{inc} = 4\pi\, (\langle b^2 \rangle - \langle b \rangle^2) = 4\pi\, b_{inc}^2. \tag{2.20}$$

Therefore the total cross section can be written as

$$\sigma = \sigma_{coh} + \sigma_{inc} = 4\pi\, b_{coh}^2 + 4\pi\, b_{inc}^2. \tag{2.21}$$

2.1.3 The Scattering Law

A further evaluation of the double differential cross section is based on the classical approximation according to van Hove [79], in which a sufficient high sample temperature is required such that $|\hbar\omega| \ll k_B T/2$ has to be valid. A quantum mechanical demonstration for low temperatures can be found in [77] and is not discussed here.
In the first order Born approximation, the double differential cross section is proportional to the so-called scattering function $S(\vec{Q},\omega)$:

$$\left(\frac{d^2\sigma}{d\Omega\, dE}\right) = \frac{1}{4\pi}\frac{k_f}{k_i}\sigma S(\vec{Q},\omega), \tag{2.22}$$

which can be also written as

$$\left(\frac{d^2\sigma}{d\Omega\, dE}\right) = \frac{N}{4\pi}\frac{k_f}{k_i}\left[\sigma_{coh}S_{coh}(\vec{Q},\omega) + \sigma_{inc}S_{inc}(\vec{Q},\omega)\right] \tag{2.23}$$

with the number of scatterers N of one type of isotopes.
The so-called coherent and incoherent scattering functions $S_{coh}(\vec{Q},\omega)$ and $S_{inc}(\vec{Q},\omega)$ are the Fourier transforms in time and space of the classical pair correlation function $G(\vec{r},t)$ and the self correlation function $G_s(\vec{r},t)$, respectively:

$$S_{coh}(\vec{Q},\omega) = \frac{1}{2\pi}\int_{-\infty}^{\infty}\int_{-\infty}^{\infty} G(\vec{r},t)\, e^{-i\,\omega t}\, e^{i\,\vec{Q}\cdot\vec{r}}\, d\vec{r}\, dt \tag{2.24}$$

with

$$G(\vec{r},t) = \frac{1}{N}\sum_{i,j=1}^{N}\langle\delta(\vec{r} + \vec{R}_i(0) - \vec{R}_j(t))\rangle \tag{2.25}$$

and

$$S_{inc}(\vec{Q},\omega) = \frac{1}{2\pi}\int_{-\infty}^{\infty}\int_{-\infty}^{\infty} G_s(\vec{r},t)\, e^{-i\omega t}\, e^{i\,\vec{Q}\cdot\vec{r}} d\vec{r}\, dt \tag{2.26}$$

with

$$G_s(\vec{r},t) = \frac{1}{N}\sum_{j=1}^{N}\langle\delta(\vec{r} + \vec{R}_j(0) - \vec{R}_j(t))\rangle. \tag{2.27}$$

The pair correlation function contains the probability to find any scattering particle (index j) at the position $\vec{r}$ at time t, if another particle (index i) was at the position $\vec{r} = 0$ at time $t = 0$. The self correlation function is the probability to find the same particle, that was at $\vec{r} = 0$ at time $t = 0$, at the position $\vec{r}$ at time t.
With these definitions coherent and incoherent scattering, which occur simultaneously in every neutron scattering experiment, can be explained. Coherent scattering results from interference of neutron waves scattered at different particles and gives information about structure and collective excitations (phonons) in the sample. Incoherent scattering is defined as the superposition of waves, which have been scattered by the same nucleus,

Isotope	σ_{coh} [barn]	σ_{inc} [barn]
H	1.76	80.27
^{2}H (D)	5.59	2.05
^{3}H (T)	2.89	0.14
He	1.34	0.0
^{3}He	4.42	1.53
C	5.55	0.00
N	11.05	0.50
O	4.23	0.0
Na	1.66	1.62
Al	1.50	0.01
Si	2.16	0.0
P	3.01	0.01
V	0.02	5.09
Cd	3.05	6.50

Table 2.1: Coherent and incoherent cross sections σ_{coh} and σ_{inc} for some elements common in biological samples and used for neutron scattering experiments [80].

but at different times. The scattered intensities of individual nuclei are then summed, which gives information about dynamics of single atoms in the sample. The coherent and the incoherent scattering cross sections of an element can differ significantly and are given in Table 2.1 for several elements. The incoherent cross section of hydrogen dominates with $\sigma_{inc}(\mathrm{H}) = 80.27\,\mathrm{barn}$ compared to the one of other elements, for example deuterium with $\sigma_{inc}(\mathrm{D}) = 2.05\,\mathrm{barn}$, carbon with $\sigma_{inc}(\mathrm{C}) = 0\,\mathrm{barn}$ or nitrogen with $\sigma_{inc}(\mathrm{N}) = 0.5\,\mathrm{barn}$ (Table 2.1). Since biological macromolecules contain approximately 50 % hydrogen atoms, which are homogeneously distributed, neutrons are a powerful probe to investigate the dynamics of biological matter. In contrast, the incoherent cross section of deuterium is very little. Hence, selective deuteration can be used to change the contrast between different parts of the sample or between the sample and the buffer.
Another quantity related to the scattering law is the so-called intermediate scattering function $I(\vec{Q},t)$. It is the Fourier transform in time of $S(\vec{Q},\omega)$ and it holds:

$$S_{coh}(\vec{Q},\omega) = \frac{1}{2\pi}\int_{-\infty}^{\infty} I_{coh}(\vec{Q},t)\, e^{-i\,\omega\, t} dt \tag{2.28}$$

and

$$S_{inc}(\vec{Q},\omega) = \frac{1}{2\pi}\int_{-\infty}^{\infty} I_{inc}(\vec{Q},t)\, e^{-i\,\omega\, t} dt \tag{2.29}$$

with

$$S(\vec{Q},\omega) = S_{coh}(\vec{Q},\omega) + S_{inc}(\vec{Q},\omega). \tag{2.30}$$

The coherent intermediate scattering function $I_{coh}(\vec{Q},t)$ and the incoherent intermediate scattering function $I_{inc}(\vec{Q},t)$ are given by the Fourier transform in space of the pair corre-

lation function $G(\vec{r},t)$ and of the self correlation function $G_s(\vec{r},t)$, which results in

$$I_{coh}(\vec{Q},t) = \frac{1}{N}\sum_{i,j=1}^{N}\langle\, e^{i\,\vec{Q}\cdot\vec{r}_i(0)}\, e^{-i\,\vec{Q}\cdot\vec{r}_j(t)}\rangle \tag{2.31}$$

and

$$I_{inc}(\vec{Q},t) = \frac{1}{N}\sum_{j=1}^{N}\langle\, e^{i\,\vec{Q}\cdot\vec{r}_j(0)}\, e^{-i\,\vec{Q}\cdot\vec{r}_j(t)}\rangle. \tag{2.32}$$

2.2 Inelastic Neutron Scattering

Inelastic neutron scattering gives information about motions of individual atoms in the sample, which occur on a timescale depending on the energy resolution of the neutron instrument. The variety of these motions is represented by numerous possible interactions between neutron and sample atoms, in which the energy transfer may be either zero (elastic scattering) or non-zero values (inelastic scattering), at different scattering vectors $\vec{Q}$. Figure 2.2 represents a typical incoherent neutron scattering spectrum. Elastic scat-

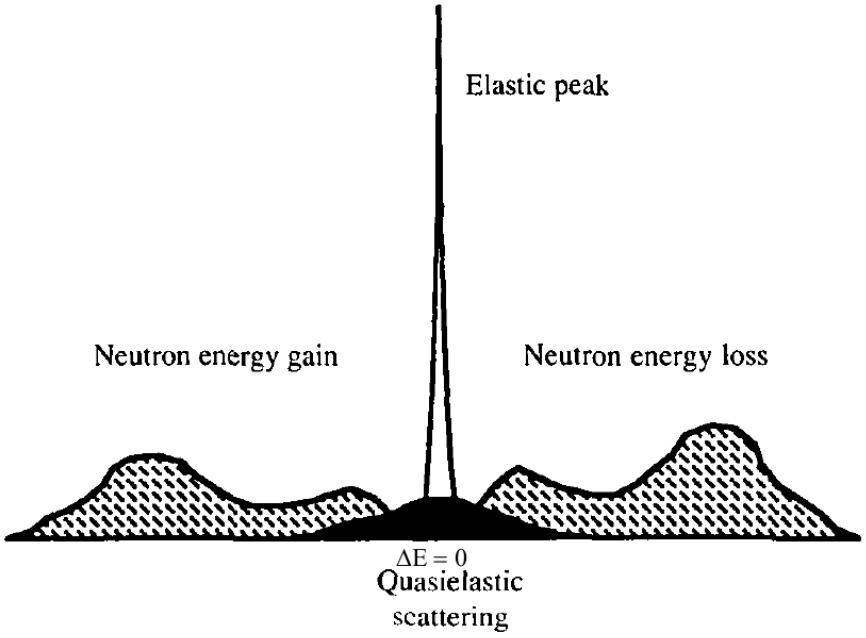

Figure 2.2: A typical incoherent scattering spectrum: The black part indicates the quasielastic broadening of the elastic peak and the dotted part inelastic scattering (taken from [81]).

tering refers to the signal of neutrons that are scattered by atoms without transferring

energy. It appears as an elastic peak at $\Delta E = 0$ with a finite full width at half maximum (FWHM), which is given by the instrumental energy resolution ΔE, more precisely by the convolution of a delta function $\delta(\hbar\omega)$ convoluted with the instrumental resolution function $R(\hbar\omega)$. The elastic intensity as a function of Q gives information about the amplitude of local molecular motions.
QENS is visible as a broadening of the elastic peak centered at $\Delta E = 0$, which is caused by diffusive and rotational molecular motions occurring in a timescale from pico- to nanoseconds. The energy transfer between quasielastically scattered neutrons and nuclei performing these types of motions is $|\Delta E| = \hbar\omega \leq 1.5\,\mathrm{meV}$. The quasielastic broadening is described by a sum of Lorentzian functions, each of which has a characteristic intensity and half width at half maximum (HWHM) and describes the type of motion occurring in the sample [77]. Depending on the model, quantities characteristic for the type of motion can be extracted.
Inelastic neutron scattering arises at $\Delta E \neq 0$ and is caused by vibrational excitations generated, for example, by phonons.

2.2.1 Elastic Incoherent Neutron Scattering and Mean Square Displacement

The extraction of average intra-molecular dynamics via the temperature dependent MSD $\langle u^2 \rangle$ is realized through EINS scans as a function of the temperature. The determination of the MSD is described in the following.
The incoherent intermediate scattering function 2.32 averaged over all N atoms in the system is

$$I_{inc}(\vec{Q},t) = \langle\, e^{i\,\vec{Q}\cdot[\vec{r}(0)-\vec{r}(t)]} \rangle. \tag{2.33}$$

The incoherent intermediate scattering function can be divided into an elastic part, which is defined as the time independent part of the scattering function with $I_{inc}(\vec{Q},t \to \infty)$, and an inelastic part $I'_{inc}(\vec{Q},t)$ [77]:

$$I_{inc}(\vec{Q},t) = I^{el}_{inc}(\vec{Q},t \to \infty) + I'_{inc}(\vec{Q},t), \tag{2.34}$$

with

$$I^{el}_{inc}(\vec{Q},t \to \infty) = \langle e^{i\,\vec{Q}\cdot\vec{r}(0)}\, e^{-i\,\vec{Q}\rangle\,\langle\vec{r}(t\to\infty)} \rangle. \tag{2.35}$$

After a long time $t \to \infty$, the position of the atoms in the sample are uncorrelated to their initial position. Hence, the phase factors in Eq. 2.35 are decorrelated and their average can be written as [82]

$$I^{el}_{inc}(\vec{Q},t \to \infty) = \langle e^{i\,\vec{Q}\cdot\vec{r}(0)} \rangle\, \langle e^{-i\,\vec{Q}\cdot\vec{r}(t\to\infty)} \rangle = \langle e^{i\,\vec{Q}\cdot\vec{r}} \rangle^2. \tag{2.36}$$

In the Gaussian approximation [82], implying that the fluctuations of the atoms around there rest position $\vec{r}(0)$ are Gaussian distributed, Eq. 2.36 can be written as

$$I^{el}_{inc}(Q,t \to \infty) = e^{-\frac{1}{6}Q^2\,\langle u^2 \rangle}. \tag{2.37}$$

$\langle u^2 \rangle$ is the MSD averaged over all atoms and directions, where $\vec{u}(t) = \vec{r}(t) - \vec{r}(0)$ are the fluctuations.
With Eq. 2.34 the incoherent scattering function is

$$S_{inc}(\vec{Q},\omega) = S_{inc}(\vec{Q},t \to \infty)\, \delta(\omega) + S'_{inc}(\vec{Q},\omega). \tag{2.38}$$

It follows for the elastic part of the incoherent scattering function

$$S_{inc}(Q,\omega = 0) \propto e^{-\frac{1}{6}Q^2\langle u^2 \rangle}, \tag{2.39}$$

which is valid for the product $Q^2\langle u^2 \rangle \leq 2$ [83]. This formulation is similar to the Guinier approximation in small angle scattering [84], with $\langle u^2 \rangle/2$ being equivalent to the squared radius of gyration. The MSD $\langle u^2 \rangle$ is obtained by linear regression in a semi-logarithmic plot of the elastic scattered intensities as a function of Q^2, following

$$\langle u^2 \rangle = -6\, \frac{d \ln S(Q,0)}{dQ^2}. \tag{2.40}$$

2.2.2 Quasielastic Neutron Scattering

Quasielastic neutron scattering experiments give detailed information about the type of molecular motions. The quasielastic scattering function is distributed symmetrically around the elastic line $\Delta E = 0$. Since this type of scattering is a broadening of the elastic line, it is called quasielastic scattering [85]. As already mentioned, in experiments on hydrogenous samples, like biological molecules, the incoherent scattering of the hydrogen atoms, dominates other scattering contributions. Therefore, the word hydrogen atoms instead of protons is used for the scatterers in this work. The total incoherent scattering function includes terms for lattice vibrations, intramolecular vibrations and molecular reorientations. It has the form

$$S_{inc}(\vec{Q},\omega) = e^{-\langle u^2 \rangle Q^2} \left[S^R_{inc}(\vec{Q},\omega) + S^I_{inc}(\vec{Q},\omega) \right], \tag{2.41}$$

where $e^{-\langle u^2 \rangle Q^2}$ is the Debye Waller factor, which describes the average vibrational motions of all the atoms and contains their MSD (see Section 2.2.1). The term $S^I_{inc}(\vec{Q},\omega)$ contains inelastic contributions, which result from phonons, and internal excitations, which are never in the energy region of the quasielastic spectrum. The term $S^R_{inc}(\vec{Q},\omega)$ describes molecular reorientations contributing to the quasielastic spectrum.
The theoretical scattering function describing a quasielastic spectrum can be written as [77]

$$S_{theo}(\vec{Q},\omega) = e^{-\langle u^2 \rangle Q^2} \left[f\, A_0(\vec{Q})\delta(\omega) + (1-f) \sum_n A_n(\vec{Q}) \mathcal{L}_n(\vec{Q},\omega) \right]. \tag{2.42}$$

The last term is the quasielastic component of the scattering function, which consists of a sum of Lorentzians with

$$\mathcal{L}(\vec{Q}) = \frac{1}{\pi}\, \frac{\Gamma(\vec{Q})}{\omega^2 + \Gamma(\vec{Q})^2}. \tag{2.43}$$

$\Gamma(\vec{Q})$ is the HWHM of each Lorentzian. The $\vec{Q}$-dependent functions $A_n(\vec{Q})$ are called quasielastic structure factors (QSF) and give the relative intensities of quasielastic contributions. The delta function $\delta(\omega)$ takes into account atoms performing motions that cannot be resolved by the instrumental energy resolution and which thus appear immobile (fraction f). Its prefactor $A_0(\vec{Q})$ is the so-called elastic incoherent scattering factor (EISF), which is the fraction of the elastic contribution contained in the total scattering intensity. It comprises information about the amplitude and geometry of the molecular motions and can be evaluated from the ratio

$$A_0(Q) = \frac{I^{el}(Q)}{I^{el}(Q) \; + \; I^{q}(Q)}, \tag{2.44}$$

where I^{el} is the elastic and I^q the quasielastic intensity of the spectra. Between the EISF and the QSF it holds the coherency EISF + QSF = 1.
The measured quasielastic spectrum is then modeled by the theoretical model function $S_{theo}(\vec{Q},\omega)$ and a background $B(\vec{Q},\omega)$, convoluted with the resolution function $S_{Res}(\vec{Q},\omega)$ of the instrument:

$$S_{meas}(\vec{Q},\omega) = \Big[S_{theo}(\vec{Q},\omega) + B(\vec{Q},\omega)\Big] \otimes S_{Res}(\vec{Q},\omega). \tag{2.45}$$

The resolution function is usually measured by vanadium, whereas the vanadium spectrum is either directly used or fitted by a Gaussian or a Lorentzian, depending on the shape of the instrument resolution.

2.2.3 Introduction of the Scattering Function for Model Myelin Membranes

In order to investigate the dynamics of hydrogens belonging to the lipids in reconstituted myelin membranes, quasielastic measurements were performed on membranes containing MBP-C1, MBP-C8 and P2 proteins, using the time-of-flight spectrometers IN5, IN6 (ILL), Osiris (ISIS) and Neat (HZB). Due to very different energy resolutions and Q-ranges of the instruments (described in detail in Chapter 4), the investigation of motions occurring on a different time- and length-scale was possible. To describe these motions, a model function $S_{theo}(\vec{Q},\omega)$ has been fitted to the measured scattering function described by Eq. 2.45. The resolution function $S_{res}(\vec{Q},\omega)$ was given by a vanadium spectrum. The shape of $S_{theo}(\vec{Q},\omega)$ depends on the type of motions, which are very diverse in biological samples. For the data obtained at 300 K, the liquid phase of the lipids, a model for $S_{theo}(\vec{Q},\omega)$, which describes the following four hydrogen atom populations, executing different kind of motions, as described in the following subsections, has been adopted:

(i) A population performing only vibrational motions described by a Debye-Waller factor $e^{-\langle u^2\rangle Q^2}$ and that appears immobile within the instrumental resolution.

(ii) A population undergoing free-diffusion in a confined spherical volume of radius R_{V1} with diffusion constant D_{V1}, described by a scattering law $S_V(\vec{Q},\omega)$ (Volino-model, see Subsection 2.2.3).

(iii) A population undergoing the same motions as population (ii), with a radius of confinement R_{V2} and a larger diffusion constant $D_{V2} > D_{V1}$.

(iv) A population that performs 2-site jump diffusion among two equivalent sites (see Subsection 2.2.3) described by a scattering law $S_{Jump}(\vec{Q},\omega)$, with jump distance d and mean residence time τ. This motion is faster than the free-diffusion in confinement and causes a much broader quasielastic contribution to the spectrum.

An additional Lorentzian had to be added for data obtained on instruments with a large energy resolution (Neat with $\Delta E \approx 216\,\mu$eV, FWHM, and IN5 with $\Delta E \approx 75\,\mu$eV, FWHM), for $Q \leq 0.76\,\text{Å}^{-1}$, which is constant in Q and describes a motion occurring on a picosecond timescale and on a length-scale of $\approx 10\,$Å, but whose meaning is not clear yet. Experiments on instruments with a similar energy resolution and a higher spatial resolution for low Q-values would be needed for a better understanding.
The fractions of hydrogen atoms belonging to these populations are indicated with f (i), p_{V1} (ii), p_{V2} (iii), p_{Jump} (iv) and p_{Lor} (for the additional Lorentzian) with $f + p_{V1} + p_{V2} + p_{Jump} + p_{Lor} = 1$. Hence, the resulting model scattering function is

$$\begin{aligned} S^{300K}_{theo}(\vec{Q},\omega) = \; e^{-\langle u^2\rangle Q^2} \, [\, f\,\delta(\omega) + p_{V1}\, S_{V1}(\vec{Q},\omega) + p_{V2}\, S_{V2}(\vec{Q},\omega) \\ + p_{Jump}\, S_{Jump}(\vec{Q},\omega) + p_{Lor}\, \mathcal{L}(\vec{Q},\omega)\,]. \end{aligned} \tag{2.46}$$

It is important to note that the Debye-Waller factor is an overall factor common to all of these hydrogen populations.
For data obtained at 230 K, the gel phase of the lipids, a slightly different model for the quasielastic scattering function has been applied, due to the reduced dynamics. This model describes two hydrogen populations performing three different motions:

(i) A population f executing only vibrational motions described by a Debye-Waller factor $e^{-\langle u^2\rangle Q^2}$.

(ii) A population $p_{V\otimes Rot}$ that diffuses in a confined spherical volume of radius R_V with diffusion constant D_V described by the Volino-model $S_V(\vec{Q},\omega)$, and that also rotates isotropically following the scattering law $S_{Rot}(\vec{Q},\omega)$ (see Subsection 2.2.3).

The resulting total scattering function describing data obtained at 230 K is thus

$$S^{230K}_{theo}(\vec{Q},\omega) = \; e^{-\langle u^2\rangle Q^2} \, \left[f\,\delta(\omega) + p_{V\otimes Rot} \, \Big(S_V(\vec{Q},\omega) \otimes S_{Rot}(\vec{Q},\omega) \Big) \right], \tag{2.47}$$

with $f + p_{V\otimes Rot} = 1$.
Instead of fitting each quasielastic spectrum obtained on different instruments individually,

a program developed by Gerelli *et al.* [86] has been used in this work, which is based on the *Minuit non-linear minimization routine* [87] and which is able to fit simultaneously all spectra of different Q-values obtained on two instruments.
In the following paragraphs, the formulation of the theoretical models applied to quasielastic data analyzed for this work, is described.

Volino Model

Volino and Dianoux [88] developed a model to describe molecules undergoing diffusion in a confined spherical volume of radius R_V with a diffusion constant D, for example hydrogens in lipids or proteins. The corresponding scattering function reads

$$S_V(Q,\omega) = A_0^0(Q)\,\delta(\omega) + \frac{1}{\pi}\sum_{(l,n)\neq(0,0)} (2l+1) A_n^l(Q)\,\frac{(x_n^l)^2\,D_V/R_V^2}{\left[(x_n^l)^2\,D_V/R_V^2\right]^2 + \omega^2}, \tag{2.48}$$

with the EISF

$$A_0^0(Q) = \left[\frac{3\,j_1(QR_V)}{Q\,R_V}\right]^2, \tag{2.49}$$

from which the radius R_V can be obtained using the first order Bessel function $j_1(x)$. The factors A_n^l are the QSFs of the l-th order and the x_n^l are numerical coefficients of the series 2.48. Following Volino *et al.* [88], the first 99 x_n^l have been used for the data analysis.
For the limit $Q \to \infty$ the $D_V\,Q^2$ scattering law for free continous diffusion is recovered:

$$S_V(Q,\omega)\big|_{Q\to\infty} = \frac{1}{\pi}\frac{D_V\,Q^2}{(D_V\,Q^2) + \omega^2}, \tag{2.50}$$

with Fick's law for the HWHM: $\Gamma(Q) = D_V\,Q^2$.
Figure 2.3 shows the HWHM of such a scattering law as a function of $Q^2\,R_V^2$.

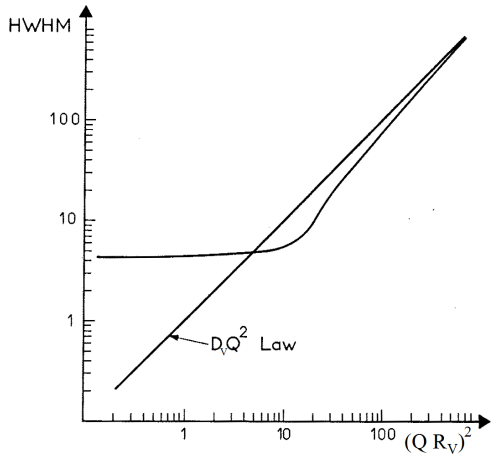

Figure 2.3: The HWHM as a function of $Q^2 R_V^2$ of the quasielastic scattering function for a molecule that diffuses in a confined spherical volume with radius R_V (Volino model) [88]. For $Q \to \infty$ the $D_V\, Q^2$ law for free diffusion is valid.

For $QR_V \to \infty$ it holds Fick's law, which is illustrated by a straight line in the graph. For small Q-values with $Q \leq \pi/R_V$ the HWHM Γ approaches a constant value Γ_0, which gives the radius of confinement via

$$R_V = \frac{\pi}{Q}. \tag{2.51}$$

Jump Model Among Two Equivalent Sites

Rotational motions of a molecule around 180 ° can be described by the jump model among two sites (also named as 2-site jump diffusion) [85], as illustrated in Fig. 2.4. This motion can be performed, for example, by the hydrogen atoms of CH_2 molecules of lipid or protein side chains, where the hydrogens change their position. The intermediate scattering

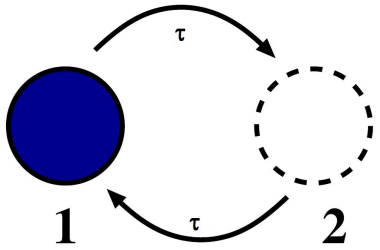

Figure 2.4: Jump model among two sites. τ is the mean residence time at position 1 or 2 (assumed to be equal at both positions) and the corresponding jump rate probability from 1 to 2 and back is given by τ^{-1}.

function can be determined with an ansatz of rate equations:

$$I_{Jump}(\vec{Q},t) = A_0(\vec{Q}) + \left[1 - A_0(\vec{Q})\right] e^{-2t/\tau} \tag{2.52}$$

with the EISF

$$A_0(\vec{Q}) = \frac{1}{2}\left[1 + \cos\left(\vec{Q}\cdot(\vec{r_2} - \vec{r_1})\right)\right], \tag{2.53}$$

where τ is the mean residence time of an atom at one of the equilibrium positions $\vec{r}_1$ or $\vec{r}_2$ and $1/\tau$ the jump rate probability of the atom. τ is assumed to be equal for both positions. Fourier transform in time leads to the scattering law

$$S_{Jump}(\vec{Q},\omega) = A_0(\vec{Q})\,\delta(\omega) + \left[1 - A_0(\vec{Q})\right] \frac{1}{\pi}\frac{2\tau}{4+\omega^2\tau^2}. \tag{2.54}$$

The quasielastic term is thus a Lorentzian with the HWHM $\Gamma = 2/\tau$, which is independent of the scattering vector $\vec{Q}$. In the case of isotropic samples, $S_{Jump}(\vec{Q},\omega)$ has to be averaged over all possible orientations of $\vec{Q}$, which leads to

$$S_{Jump}(Q,\omega) = A_0(Q)\,\delta(\omega) + [1 - A_0(Q)] \frac{1}{\pi}\frac{2\tau}{4+\omega^2\tau^2} \tag{2.55}$$

with

$$A_0(Q) = \frac{1}{2}\left[1 + j_0(Qd)\right], \tag{2.56}$$

where $d = |\vec{r}_2 - \vec{r}_1|$ is the jump distance between the two sites.

Model for Isotropic Rotational Diffusion

The model for isotropic rotational diffusion describes a reorientational motion of a molecule, which rotates randomly on a spherical surface. In this model, it is assumed that every possible orientation is equiprobable in time average. A detailed derivation of this model can be found in [89].
The scattering function describing this isotropic motion can be written as

$$S_{Rot}(Q,\omega) = A_0(Q)\,\delta(\omega) + \sum_{l=1}^{\infty} A_l(Q)\,\frac{1}{\pi}\,\frac{\tau_l}{1+\omega^2\tau^2}, \tag{2.57}$$

where

$$A_0(Q) = j_0^2(QR) \tag{2.58}$$

is the EISF and

$$A_l(Q) = (2l+1)j_l^2(QR) \tag{2.59}$$

is the QSF. $j_0(x)$ is a spherical Bessel function of zero order and $j_l(x)$ of l-th order. R is the radius of the spherical rotation and

$$\tau_l = l(l+1)D_R \tag{2.60}$$

the correlation time for $j_l(x)$ with the isotropic rotational diffusion constant D_R. The sum in Eq. 2.57 ranges from 1 to 3 in this work, since more orders did not change the convergence of the function.

2.3 Production of Neutrons

Neutrons bound to the nuclei of atoms comprise more than 50 % of the matter. Unbound neutrons are unstable and have a half-life of approximately 15 minutes. So called β^--decay results in the conversion of a neutron to a proton by the emission of an electron and an electron-antineutrino. In neutron research facilities, free neutrons are either produced by fission or by spallation.
Fission occurs in neutron reactors by absorption of a slow neutron by an uranium nucleus U^{235}, which is thereby excited to U^{236} and then fissions into at least two lighter elements (on the left in Fig. 2.5). During the fission, some γ rays and averaged three neutrons are emit-

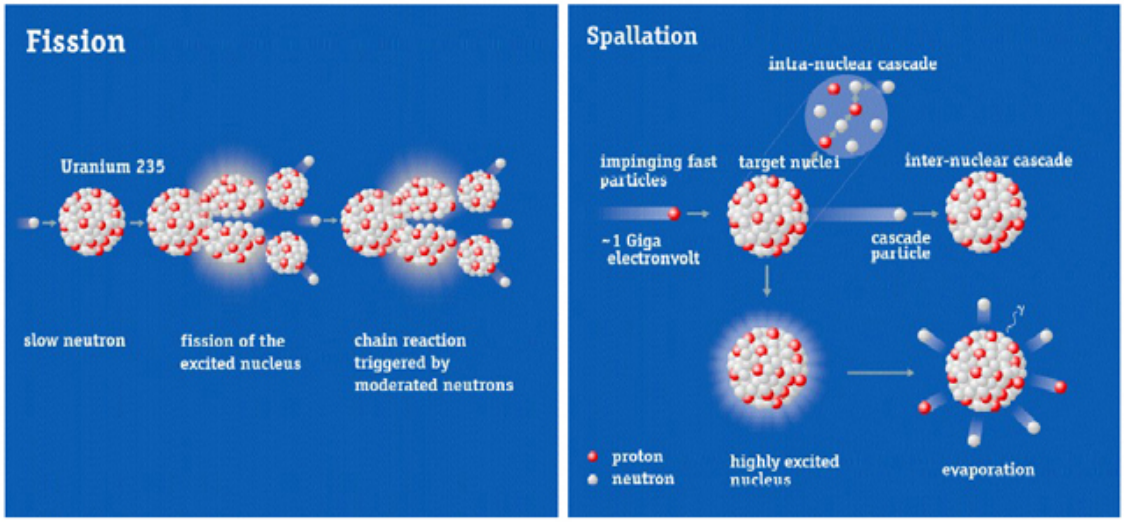

Figure 2.5: Schematic illustration of the two main methods of neutron production: fission (left) and spallation (right) [90].

ted. Research neutron reactors in Europe include the ILL in Grenoble, France, the HZB in Berlin, Germany, the Forschungs-Neutronenquelle Heinz Maier-Leibnitz (Forschungsreaktor München, FRM II) in Munich, Germany or the Laboratoire Léon Brillouin (LLB) in Saclay, France. The high-flux reactor at the ILL has with a flux of $1.2 \cdot 10^{15}$ neutrons per cm^2 and second ($n/cm^2/s$) and a thermal power of 58.3 MW, the highest neutron flux world-wide.
Nuclear spallation occurs when a fast proton collides with a heavy metal target, for example lead, which heats up and evaporates neutrons (on the right in Fig. 2.5). This heating process originates from an interaction between the proton and the individual nucleons of the target and subsequent interactions between the nucleons themselves and other nucleons, such that a particle cascade is generated in the target. The excitation of the target leads to evaporation of about 20-30 neutrons per event. Spallation sources in Europe include ISIS, at the Rutherford Appleton Laboratory in Oxfordshire, United Kingdom, and the Paul-Scherrer Institut (PSI) in Villigen (Switzerland). The European Spallation Source (ESS)

in Lund (Sweden) is under construction and aims to be the brightest source of neutrons in the world. At the moment, the Spallation Neutron Source (SNS) in Oak Ridge (Tennessee, USA) provides the most intense pulsed neutron beams world-wide for scientific research and industrial development in the future.
As examples for the functioning of a neutron reactor and of a spallation source, the principle of operation of the high-flux reactor at the ILL and of the European spallation source ISIS will be explained.

2.4 Functioning of the High-flux Reactor at the ILL

The reactor at the ILL has the most intense neutron flux in the world. A flux of $1.5 \cdot 10^{15}$ n/s/cm^2 is produced by nuclear fission occurring in a 8.57 kg fuel element of 93 % U^{235}, which is placed in a tank of 2.5 m diameter. The produced neutrons have energies in the order of magnitude of some MeV. Since for neutron scattering experiments the required energy to study interatomic distances in solids or liquids is in the range of meV, the kinetic energy of the neutrons has to be reduced. This is realized by moderators kept at a certain temperature. The neutrons are slowed down by collisions with the atoms of the cooling medium. In thermal equilibrium with the moderator, they have a temperature dependent Maxwell energy distribution with the maximum corresponding to the moderator temperature. For the ILL reactor, D_2O, contained in the tank, acts as a cooling medium and moderator at 300 K. The thermal neutron flux has a Maxwell distribution with a maximum at 1.2 Å. A pool made of dense concrete and filled with H_2O, surrounds the tank, in order to provide biological shielding. The moderated neutrons can be further modified by special moderators, which is needed for the use of hot and cold neutrons: the hot source, consisting of a graphite block (volume of 10 liters), is placed near the uranium core and reaches a temperature of 2400 K to reduce the neutron wavelength below 0.8 Å. A vertical and a horizontal cold source consist of liquid deuterium (20 and six liters, respectively) kept at 25 K and enhances the neutron flux at wavelength above 3 Å.
Table 2.2 shows temperature, energy and wavelength ranges of cold, thermal and hot neutrons and Figure 2.6 the corresponding Maxwell distributions for the ILL reactor.

	Temperature [K]	Energy [meV]	Wavelength [Å]
Cold Neutrons	1 - 120	0.1 - 10	30 - 3
Thermal Neutrons	120 - 1200	10 - 100	3 - 1
Hot Neutrons	1200 - 6000	100 - 500	1 - 0.4

Table 2.2: Temperature, energy and wavelength ranges of cold, thermal and hot neutrons, calculated according to $E = (m_n\, v)/2 = h^2/(2\, m_n\, \lambda^2) = k_B\, T$, where k_B is the Boltzmann constant.

Instruments that are operated with hot neutrons are located close by the reactor, whereas cold and thermal neutrons are extracted to the experimental hall using neutron guides. Since neutrons have no electrical charge, they cannot be deflected with an electromagnetic

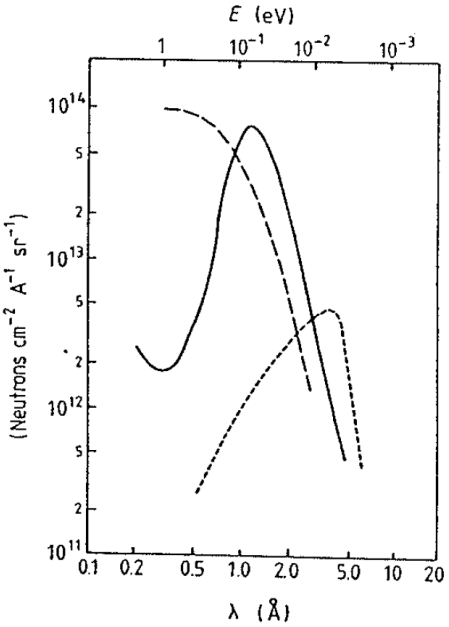

Figure 2.6: Neutron flux as a function of the energy and wavelength for thermal neutrons (solid curve), hot neutrons (dashed curve) and cold neutrons (dotted curve) for the ILL-reactor [77].

field. Hence, they are transported by the principle of total reflection, which occurs below a critical angle of $\Theta_c = \lambda[\text{Å}] \times 0.1^\circ$, and which is achieved by evacuated, rectangular glass tubes having an inner surface coated by hundreds of layers of nickel, which have a high refraction index n [91]. Neutron beam loss is thus less than 1 %. The critical angle Θ_c can be doubled by the use of neutron guides equipped with supermirror coatings, consisting of 100 Ni/Ti double layers of varying thickness. However, neutron beam loss is about 10 %.

2.5 Functioning of the Spallation Source ISIS

The ISIS pulsed neutron spallation source is a world-leading research-center, which accelerates protons to 84 % of the speed of light to produce neutrons and muons [92]. Compared to a neutron reactor, more neutrons per spallation event are produced. In order to maintain a good time-of-flight resolution at a pulsed spallation source, such as ISIS, a small neutron pulse is important. For this purpose, moderators are kept small, which results in undermoderated neutrons. Compared to neutrons produced at a reactor, they have a spectrum that is a Maxwell distribution for low energies, but a $1/E$ distribution for energies larger than 100 meV. This yields a neutron flux that is approximately an order of magnitude larger than the neutron flux in a reactor.
The ISIS facility consists of a 70 Mev linear accelerator, the Linac, an 800 MeV Synchrotron and two target stations, one of them optimized for low energy neutrons, where several neutron instruments are located. In the Linac, the so-called injector, H^- ions (a proton with

two electrons) are produced and accelerated. The production is performed by the use of an electric discharge and the ions are separated into bunches by a radio frequency quadrupole accelerator. The bunches are further accelerated by 10 m long tanks, containing copper drift electrodes, up to 37 % of the speed of light at the end of the Linac. The acceleration continues in the synchrotron, a ring of a 163 m circumference and powerful magnets, which bend the beam on a circle. A thin aluminum foil at the entrance of the synchrotron removes the electrons of the H^- ions to produce a proton beam. The protons are accelerated by radio frequency electric fields. After $\approx$ 10 000 rotations around the synchrotron ring, the protons have separated into two bunches of 84 % of the speed of light. The bunches are extracted by magnets, in which the current rises from zero to 5 000 amps in 100 ns, from the synchrotron into two targets, respectively. Passing through a thin graphite target provides the production of $\approx$ 3 % muons of the proton beam for the use in muon spin spectrometry. The collision of the protons with the targets yields neutron production by a spallation process, as described above (Section 2.3). Finally, the neutrons are decelerated to speeds needed for condensed matter research by an array of hydrogenous moderators around the target, and are guided to the neutron instruments.

2.6 Neutron Scattering Instruments

There is a large variety of different types of neutron scattering instruments at neutron research facilities, covering a large range of energy resolutions and momentum transfers. While neutron scattering spectrometers give information about different types of molecular motions occurring in a sample, the use of diffractometers and reflectometers allows the study of the structure of materials. From a diffraction pattern, which shows the elastic scattered intensities as a function of the momentum transfer Q, the repeat-distance, characteristic for the sample, can be derived, using the relation

$$Q = \frac{2\,\pi}{d}. \tag{2.61}$$

There are different types of diffractometers: powder diffractometers, operating with short wavelengths ($0.3 - 2.0$ Å), are used to resolve the structure of powders or liquids to atomic resolution. For single crystal diffractometers, hot neutrons are used to study nuclear positions in condensed matter. Large scale diffractometers, using cold neutrons with long wavelengths, give information about larger structures of 1 to 100 nm by measuring at low Q-values. In this work, the large scale diffractrometer D16 was used to investigate the structure of myelin model membranes.
The use of spectrometers with different energy resolutions and Q-ranges gives access to different types of motions occurring on a characteristic time- and length-scale. The timescale is defined by the energy resolution ΔE of the spectrometer via Heisenberg's uncertainty principle

$$\Delta E\,\Delta t \geqq \frac{\hbar}{2}. \tag{2.62}$$

The detectable length scale of the motions is given by the momentum transfer range (Q-range), which depends on the wavelength of the incident neutron beam, using the relation 2.61. Neutron spin echo instruments have the highest energy resolution, in the order of magnitude of neV. Backscattering spectrometers have also a very high energy resolution ranging from 0.9 μeV to 10 μeV. Time-of-flight spectrometers feature choppers, whose speed can be adjusted, resulting in a variation of the incident neutron wavelength or rather of the energy resolution between 10 μeV to 3 meV. Three-axis spectrometers are primarily designed for solid state physics to investigate collective motions of atoms (phonons) and are not treated here.
In backscattering spectrometers, crystal reflections are used to select a wavelength given by Bragg's law

$$n\,\lambda = 2\,d\,\sin\Theta_B, \tag{2.63}$$

where n is the order of the Bragg reflection, d is the d-spacing of the crystal and Θ_B is the Bragg angle. The perfect backscattering at the analyzers with a scattering angle of $2\,\Theta = \Theta_B = 180^\circ$, or rather $\Theta = 90^\circ$, yield a very high energy resolution. This can easily be derived from the expression for the resolution, which is the differentiation of Eq. 2.63:

$$\frac{\Delta E}{E} = \frac{2\,\Delta\,\lambda}{\lambda} = 2\cot\Theta\,\Delta\,\Theta + \frac{2\Delta\,d}{d}. \tag{2.64}$$

The first term of the right hand side is zero for $2\,\Theta = 180^\circ$ and the second term is only dependent on the crystal quality, where $\Delta\,d/d$ is the mosaicity, which is the degree of the long-range order of the unit cells within the crystal. The backscattering is realized at the analyzer crystals, which are mounted in perfect backscattering geometry, such that only neutrons with the corresponding wavelength are reflected to the neutron detectors. This principle, where the final neutron energy is fixed, by selection at the analyzers, is called inverse geometry. The incident energy is either varied at the monochromator for inelastic scans or kept fixed for elastic measurements.
In contrast, time-of-flight spectromters for example, have a direct geometry: the incident neutron energy is given by the choppers and the final energy of the neutrons is varied due to their energy transfer at the sample and recorded at the detectors. The technique of time-of-flight spectroscopy uses the time-of-flight of the scattered neutrons to determine their energy transfer. The neutron beam is pulsed by a chopper system. A chopper is a rotating disk coated with a neutron absorbing material, except for a small fraction where the neutrons can pass. Hence, neutron pulses with a given velocity distribution, depending on the chopper speed, are created. Neutrons that are scattered inelastically at the sample change their initial velocities, and thus they reach the detector with a time difference relative to elastically scattered neutrons. This time difference $\Delta t = t - t_0$ between neutrons that have gained or lost energy when scattered at the sample (time t), and elastically scattered neutrons (time t_0), is recorded. The energy transfer ΔE is determined via:

$$\Delta E = \frac{m_n}{2}\left(v_0 - v\right)^2 = \frac{m_n}{2}L^2\left(\frac{1}{t_0} - \frac{1}{t}\right)^2 = \frac{m_n}{2}L^2\left(\frac{1}{t_0} - \frac{1}{\Delta t + t_0}\right)^2, \tag{2.65}$$

where L is the distance between sample and detector bank.
In this work the time-of-flight spectrometers IN5, IN6 (ILL), Osiris (ISIS) and Neat (HZB) and the backscattering spectrometers IN13 and IN16 (ILL) were used, in order to investigate dynamics of model myelin membranes. Their characteristic parameters, including the wavelength λ, the instrumental energy resolution ΔE, the energy domain and the accessible Q-range are given in Table 2.3. A detailed description of the backscattering

Spectrometer	λ [Å]	ΔE [μeV]	Energy domain [μeV]	Q-range [Å^{-1}]
IN5	10.00	12.0	-30000...500	0.23...1.14
	5.00	75.0	-30000...2000	0.27...2.23
IN6	5.12	78.0	-200...2	0.24...2.20
IN13	2.23	8.0	-125...300	0.20...4.90
IN16	6.27	0.9	-15...15	0.19...1.89
Osiris	3.30	99.0	-4000...4000	0.60...3.52
Neat	5.10	216.0	-1200...1200	0.37...2.26

Table 2.3: Characteristic parameters of neutron spectrometers used in this work. λ is the wavelength used during experiments (variable for time-of-flight spectrometers) and ΔE the instrumental energy resolution. The time-of-flight spectrometers IN5 and IN6 and the backscattering spectrometers IN13 and IN16 are situated at the ILL and the time-of-flight spectrometers Osiris and Neat at ISIS and at the HZB, respectively.

spectrometers IN13 and IN16, the time-of-flight spectrometers IN5, IN6, Osiris and Neat and the diffractometer D16 follows.

2.6.1 Backscattering Spectrometer IN13

The thermal backscattering spectrometer IN13 [93, 77] at the ILL, which is operated by a Collaborative Research Group (CRG), is located at the thermal guide H24. The instrument is characterized by the relatively high energy of the incident neutron beam $E_i \approx 16.45\,\mathrm{meV}$, which spans a wide momentum transfer range of $0.2\,\mathrm{Å}^{-1} \leq Q \leq 4.9\,\mathrm{Å}^{-1}$. With this Q-range and an energy resolution of $\Delta E \approx 8\,\mu\mathrm{eV}$ (FWHM), molecular motions of an amplitude from 1.3 Å to 31.4 Å occurring in a time scale of $\approx 100\,\mathrm{ps}$ can be investigated. Due to the extremely large Q-range, together with the high energy resolution, IN13 is particularly useful for the study of single particle motions occurring in biological samples like jump reorientation as well as rotational and translational diffusion. The applications of the instrument lie mainly in the field of life sciences, but also in areas of material science, solid-state physics, geophysics and chemistry. Figure 2.7 shows a schematic representation of IN13: the thermal neutron beam is scattered at a monochromator, which are three CaF_2 crystals in (4 2 2) orientation mounted in a cryofurnace. The energy resolution, which is optimal for a scattering angle of $2\Theta = 180^\circ$ at the monochromator (perfect backscattering), is with $\Delta E \approx 8\,\mu\mathrm{eV}$ very high. In fact, perfect backscattering with $2\Theta = 180^\circ$ cannot be

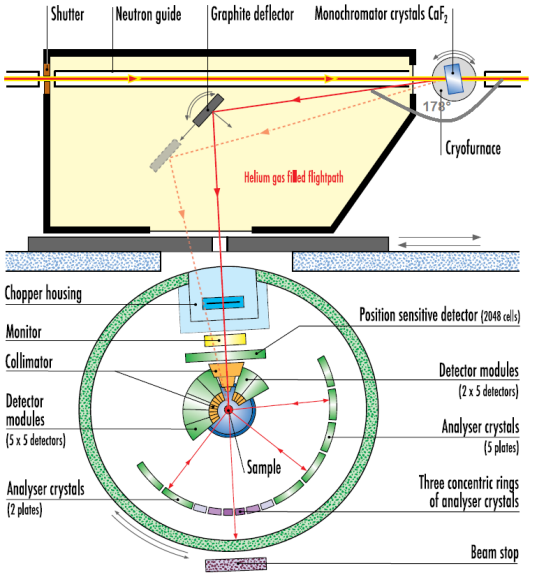

Figure 2.7: Schematic representation of the backscattering spectrometer IN13 [93].

reached, because 2Θ must be smaller than 178° due to the neutron guide positioned in backscattering direction (see Fig. 2.7). For elastic scans, the monochromator temperature T_M is kept constant and thus the incident energy is fixed. By variation of T_M, the energy of the incident neutrons can be scanned due to the changing of the d-spacing of the CaF_2 crystals, and inelastic scans can be performed, whereas the final energy is always kept fixed thanks to the analyzers. The wavelength of the resulting monochromatic neutron beam is $\lambda = 2.23\,\text{Å}$, which is given by Eq. 2.63, and the neutron flux at the sample is $\phi \approx 2 \cdot 10^4$ n/cm^2/s. The beam is then deflected by a vertically bent graphite deflector and focused on the sample. Seven spherically curved analyzers and a small-angle setup of concentric rings, composed of (4 2 2) CaF_2 crystals, are arranged such that they reflect the scattered neutrons in perfect backscattering, providing the selection of the right final energy of the neutrons. Finally the scattered neutrons are detected by 35 cylindrical ^{3}He gas counter detectors, placed behind the sample, and by a position sensitive detector (PSD), which is made of 35 ^{3}He tubes and used to detect neutrons coming from the small-angle analyzers. A chopper, rotating at 6756 rpm, pulses the neutron beam and is used to avoid the detection of neutrons scattered directly from the sample into the detectors, since those neutrons do not fulfill the backscattering condition, and to shield higher orders of the incoming neutron beam (factors of $\lambda/2$). The incoming neutron flux is measured by a monitor placed between the chopper and the sample. A second monitor can be placed behind the sample in order to determine the sample transmission.

2.6.2 Backscattering Spectrometer IN16

The cold neutron backscattering spectrometer IN16 at the ILL has applications in rotational tunneling spectroscopy, glass relaxation processes, diffusion processes in metals or conductors, in soft matter science and in biology. The instrument setup is illustrated in Fig. 2.8. The beam is extracted from the cold neutron guide H53 by a deflector and

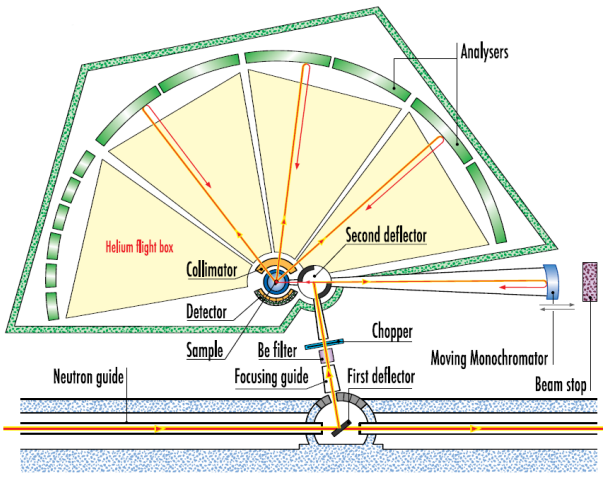

Figure 2.8: Instrument setup of the cold neutron backscattering spectrometer IN16 [94].

passes a focusing guide, which leads to a 5-fold increase of the neutron flux. A second graphite (0 0 2) double deflector, mounted on a chopper device, diffracts the beam to a Doppler monochromator (silicium (1 1 1)), which backscatters highly monochromatic neutrons with a wavelength of $\lambda = 6.27\,\text{Å}$ to the sample. Neutrons scattered at the sample are reflected with perfect backscattering at spherically shaped silicium (1 1 1) analyzers and finally detected behind the sample. With an energy resolution of $\Delta E = 0.9\,\mu\text{eV}$ (FWHM), molecular motions in a time scale of $\approx 1\,\text{ns}$ can be investigated. The accessible Q-range is $0.20\,\text{Å}^{-1} \leq Q \leq 1.9\,\text{Å}^{-1}$ and the neutron flux at the sample is $\phi \approx 1 \cdot 10^5$ n/cm^2/s.
In addition to the standard setup, the instrument can be operated in a high resolution setup of $\Delta E = 0.32 - 0.44\,\mu\text{eV}$ (FWHM) for a Q-range of $1.0\,\text{Å}^{-1} < Q \leq 1.9\,\text{Å}^{-1}$. This setup consists of three large-angle analyzer plates ($0.8\,\text{m}^2$ each), which are covered with small, polished, single crystals (4 x 4 mm^2). The neutron flux at the sample is $\phi \approx 2 \cdot 10^4$ n/cm^2/s.
320 ^{3}He diffraction single detector tubes, which are grouped by hardware to 160 pairs, are installed to simultaneously measure diffraction during elastic window scans, quasielastic and inelastic spectroscopy, which is a special feature of IN16.

2.6.3 Time-of-flight Spectrometer IN5

IN5 at the ILL is a disk chopper time-of-flight spectrometer. These kinds of spectrometers contain a chopper system in the primary spectrometer with a flexible chopper speed selec-

tion, in order to span a wide range of incident wavelengths and energy resolutions. Hence, IN5 is used in several fields of research, including physics, chemistry and biology. It is currently the highest-flux cold neutron time-of-flight instrument world-wide. A schematic representation of the instrument is shown in Fig. 2.9: the neutron beam, coming from the cold neutron guide H16, with a wavelength distribution centered around an average wavelength of 4.5 Å, first passes the primary spectrometer. This consists of a chopper

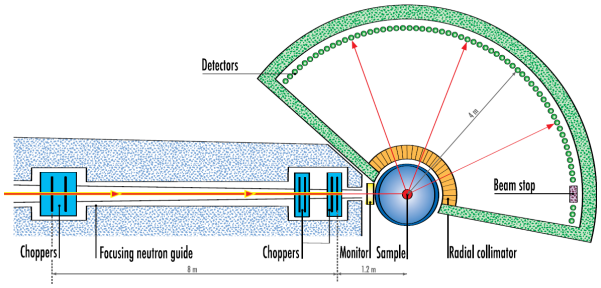

Figure 2.9: Schematic layout of the disk chopper time-of-flight spectrometer IN5 [95].

system with two counter-rotating disks, a focusing guide, which allows a significant gain in neutron flux, and finally choppers with four disks. The speed of the choppers varies from 2000 to 17000 rpm, resulting in neutron wavelengths between 1.8 Å and 20 Å and energy resolutions from 1 to 1000 μeV (FWHM). The monochromatic beam reaches the secondary spectrometer, consisting of an evacuated sample chamber and an oscillating radial collimator, which reduces reflections from the sample environment. Neutrons, scattered at the sample, are detected at 4 m distance by 259 spherically ordered ^{3}He detectors of the height of 3 m, covering an angular range of 14.5° to 132.5°. A PSD counts neutrons in the small angle region between 2° and 8°.
The higher the wavelength the higher (or narrower) is the energy resolution and the smaller is the accessible Q-range and the neutron flux at the sample. For experiments performed for this work, incident wavelengths of 5 Å and of 10 Å were used: at an incident neutron wavelength of 5 Å, the energy resolution is 75 μeV, the momentum transfer range is $0.27\,\text{Å}^{-1} \leq Q \leq 2.23\,\text{Å}^{-1}$ and the neutron flux at the sample is $\phi \approx 6.83 \cdot 10^5\,\text{n/cm}^2\text{/s}$. At an incident wavelength of 10 Å, the energy resolution is 12 μeV and the momentum transfer range is $0.23\,\text{Å}^{-1} \leq Q \leq 1.14\,\text{Å}^{-1}$. The corresponding time scales for those configurations are ≈ 10 ps and ≈ 100 ps, respectively.

2.6.4 Time-of-flight Spectrometer IN6

The time-focusing time-of-flight spectrometer IN6 [96, 77] is situated at the neutron guide H15 at the ILL. The neutrons are extracted from the guide by passing a triple monochromator, each made of seven pyrolytic graphite crystals. Figure 2.10 illustrates a scheme of the spectrometer and its beam path. The monochromators can be fixed at four different positions, resulting in incident neutron wavelengths of 4.1, 4.6, 5.1 and 5.9 Å. At 4.1 Å the

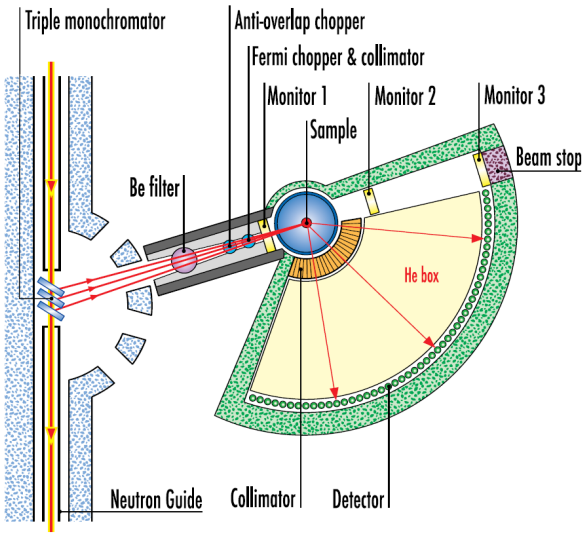

Figure 2.10: Schematic view of the time-of-flight spectrometer IN6 [96].

incident neutron flux is $\phi \approx 8.9 \cdot 10^4\,\mathrm{n/cm^2/s}$. Using a wavelength of 5.1 Å, as chosen for this work, the accessible Q-range is $0.4\,\text{Å}^{-1} \leq Q \leq 2.2\,\text{Å}^{-1}$ and the energy resolution approximately 78 μeV (FWHM). The neutron beam passes a beryllium filter, which removes the second order reflection from the graphite monochromator, an anti-overlap chopper and a Fermi chopper. The Fermi chopper allows the best possible energy resolution, due to the so-called time-focusing principle. This time-focussing principle is achieved in the following way. At the triple monochromator, the incident neutron beam is divided into three beams, each having slightly different directions and thus different wavelengths and velocities. After being focused on the sample in a helium filled sample area, the elastically scattered neutrons are detected at different times. Hence, the energy resolution is reduced. To avoid this, a Fermi chopper is placed between triple monochromator and sample, in order to pulse the neutrons with a rotational speed ranging from 3000 to 15000 rpm. To prevent frame-overlap of two subsequent neutron pulses, an anti-overlap chopper, which rotates in phase with the Fermi chopper, is placed in front of the Fermi chopper. The scattered neutrons are finally detected by 337 ^{3}He detectors, which cover an angular range of 10° to 115°. The energy transfer of the scattered neutrons is related to their time-of-flight from the Fermi chopper to the detectors.

2.6.5 Time-of-flight Spectrometer Neat

The cold neutron multichopper time-of-flight spectrometer Neat is located at the neutron guide NL2 of the HZB. It has a broad spectrum of applications due to an energy resolution ranging from $\Delta E = 6\,\mu$eV to $\Delta E = 5400\,\mu$eV (FWHM) and a neutron wavelength from 1.8 Å to 19 Å. Dynamics in a time domain from 0.1 ps to 1 ns on a length-scale ranging

from 0.5 Å up to 500 Å can be probed. A setup of the spectrometer is shown in Fig. 2.11. The incoming white neutron beam passes a multichopper system, containing seven phased

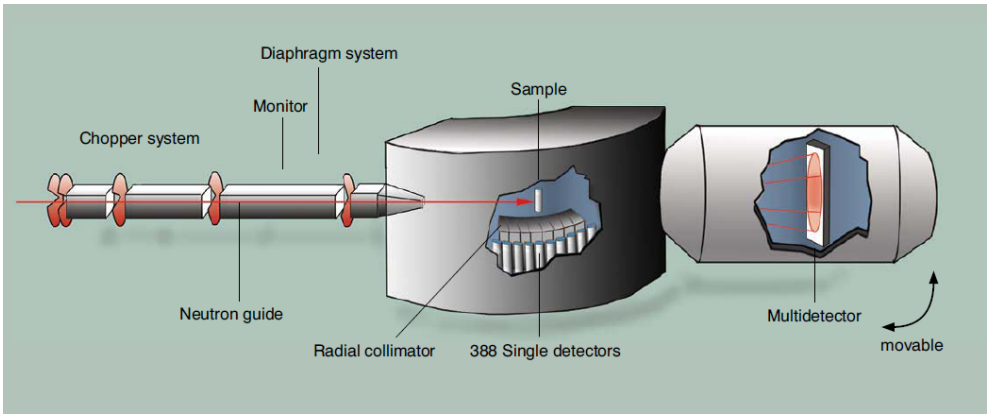

Figure 2.11: Setup of the time-of-flight spectrometer Neat [97].

disks. The choppers operate either at a speed of 750 rpm, 1000 rpm or 20000 rpm, resulting in different time and energy widths of the neutron pulses. This leads to a variation of the energy resolution. The pulsed monochromatic beam is guided through a monitor and a diaphragm system and then scattered at the sample. Neutrons are counted by 388 ^{3}He single detectors, situated at 2.5 m distance from the sample. A PSD-multidetector is used either for small angle scattering or inelastic scattering. For the experiments carried out for this work, the incident neutron wavelength was 5.1 Å, corresponding to an energy resolution of $\Delta E = 216\,\mu$eV, the accessible Q-range was $0.37\,\text{Å}^{-1} \leq Q \leq 2.26\,\text{Å}^{-1}$ and the incident neutron flux $\phi \approx 2 \cdot 10^4\,\text{n/cm}^2\text{/s}$.

2.6.6 Time-of-flight Spectrometer Osiris

Osiris is situated at the N6 (B) line at ISIS [98, 99]. As a time-of-flight spectrometer with backscattering analyzer crystals, it can be used as a high-resolution, long-wavelength diffractometer or as a high-resolution, quasi- and inelastic spectrometer. It consists of a primary spectrometer, in which the neutron beam passes from the moderator to the sample position, and a secondary spectrometer. In the primary spectrometer, the neutrons are guided from a liquid nitrogen moderator, operated at 25 K, to the sample, using a curved super-mirror neutron guide. A tapered guide piece in the end allows the focusing of the beam to the sample position. The incident neutron energy is defined by two disk-choppers, which are synchronized to the ISIS operating frequency of 50 Hz and rotate either at 50, 25, 16.6 or 10 Hz.
The secondary spectrometer, illustrated in Fig. 2.12, consists of a vacuum box with pyrolytic graphite crystal analyzers, which reflect the neutrons scattered at the sample to the detector bank. The detectors consist of 42 ^{3}He detectors and a diffraction detector bank consisting of 962 ZnS tubes, oriented at $2\Theta \approx 170^\circ$. The latter allows simultaneous

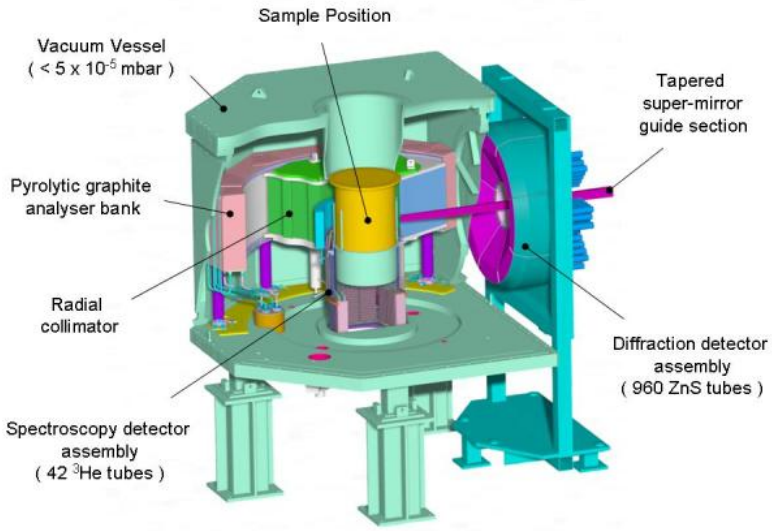

Figure 2.12: The secondary spectrometer of the time-of-flight spectrometer Osiris [100].

measurements of dynamics and structure by quasi- or inelastic scattering and diffraction. By measuring the time of arrival of each analyzed neutron at the detectors, energy gain or loss of a neutron scattered at the sample is investigated. Using pyrolytic analyzers, analyzing reflections of (0 0 2) and (0 0 4) are possible, corresponding to energy resolutions of $\Delta E = 24.5\,\mu$eV and $\Delta E = 99\,\mu$eV (FWHM). For experiments carried out for this work, the latter energy resolution was used, corresponding to a wavelength of the incident neutron beam of $\lambda = 3.3\,$Å with an accessible Q-range of $0.60\,\text{Å}^{-1} \leq Q \leq 3.52\,\text{Å}^{-1}$. The flux at the sample was $\phi \approx 2.7 \cdot 10^7\,\text{n/cm}^2\text{/s}$.

2.6.7 Diffractometer D16

D16 is a small momentum transfer diffractometer and is situated at the H53 guide at the ILL. It is useful for the study of a large field of systems in physics, physical chemistry and biology, particularly for the investigation of partially ordered structures, such as stacked membranes. Figure 2.13 demonstrates a sketch of the diffractometer: a focussing pyrolytic graphite monochromator with two beam holes at angles of 90° and 115° permits the selection of a neutron beam with either a wavelength of 4.7 Å or 5.6 Å, which can be changed by rotating the diffractometer. The monochromatic beam is focussed on the sample, after passing a diaphragm, a Beryllium filter, eliminating higher order reflections, a monitor and a second diaphragm. The diaphragms are supposed to adapt the beam size to the size of the sample. After scattered at the sample, neutrons are detected by a multidetector with a very good angular resolution, which can be rotated in the horizontal axis in an

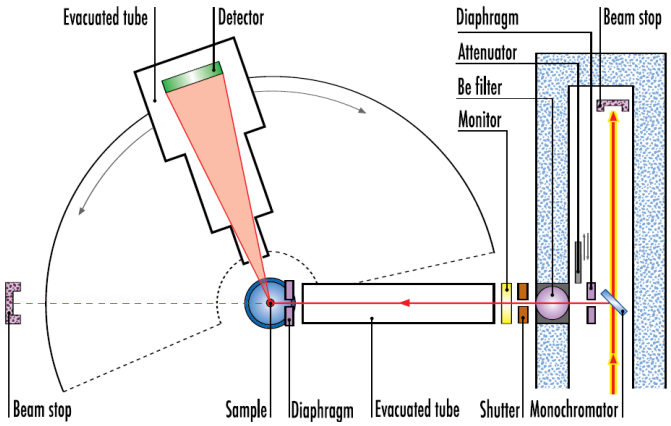

Figure 2.13: Design of the small momentum transfer diffractometer D16 [101].

angular scattering range from Θ to $2\,\Theta$. For neutron scattering experiments, a wavelength of 4.7 Å was used, with an accessible Q-range of $0.12\,\text{Å}^{-1} \leq Q \leq 0.42\,\text{Å}^{-1}$ and a maximal neutron flux at the sample of $\phi \approx 10^7\,\text{n/cm}^2/\text{s}$.

Chapter 3

Sample Preparation

In this chapter, first of all the sample preparation including expression and purification of the myelin proteins MBP and P2 and the preparation of the reconstituted membranes for neutron scattering experiments are described. Furthermore, the characterization of the membrane samples, which is crucial for the success of the experiment and for the reliability of the obtained results, is reported.

3.1 Expression and Purification of the Myelin Proteins MBP and P2

Recombinant myelin basic protein (MBP) and recombinant myelin protein 2 (P2) were expressed and purified during a practical training of four weeks under the supervision of Dr. Petri Kursula at the Centre of Structural Systems Biology (CSSB) at the Deutsches Elektronen-Synchrotron (DESY) in Hamburg, Germany, in October 2009. A second stay of two weeks took place in August 2010 for the purification of the proteins MBP-C1 and MBP-C8. Thanks to the experience acquired at DESY, larger quantities of these proteins were independently expressed and purified at the Institut de Biologie Structurale (IBS) in Grenoble, France, in collaboration with Dr. Martin Weik and Dr. Colin Jackson in September 2010.

For recombinant protein expression, His_6-tagged MBP-C1 and MBP-C8 isomers of murine 18.5-kDa MBP were expressed by using the pET-22b vector [20, 102] and His_6-tagged human P2 by using the pTH27 vector [103]. A plasmid vector is a circular double-stranded DNA molecule, which replicates independently. The plasmids used in this work both contain an origin of replication and antibiotic (ampicillin) resistance genes and a His_6-tag, to which the protein is attached, as shown in Fig. 3.1. The His_6-tag, an affinity purification tag is a sequence of six histidine residues placed on the N- (or C-) terminus of the protein to be purified. Its tight coordination of nickel ions, immobilized on a chromatography resin, allows the proteins to be purified from other cell proteins that do not bind to the resin. During gene transcription, a ribonucleic acid (RNA) polymerase copies the DNA template

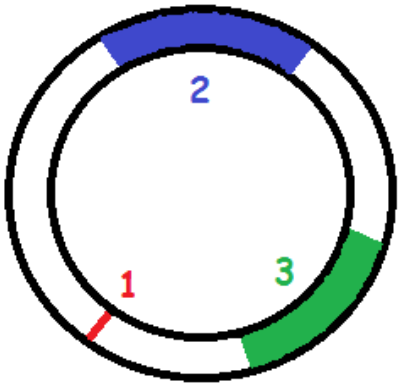

Figure 3.1: Schematic illustration of a plasmid. 1: Origin of replication, the sequence where the replication of DNA begins. 2, 3: Antibiotic resistance genes.

into a messenger RNA (mRNA) molecule, with the exception that nucleobase uracil (U) replaces nucleobase thymine (T) (DNA nucleobases adenine (A), T, guanine (G), cytosine (C) are transcribed as RNA nucleobases A, U, G, C). This mRNA transcript is then read by the ribosome, which carries out protein synthesis based on the nucleotide sequence.

For the heat-shock transformation of the MBP-plasmids into *Escherichia coli* (*E. coli*) BL21(DE-3) cells, 1 μl of plasmid solution (50 ng/μl) was added to 50 μl of *E. coli* competent cells. After incubating the solution on ice for 20 minutes, it was heated at 42 °C for two minutes and cooled again on ice for further two minutes. 400 μl of Luria Broth (LB)-medium was added and the cells were incubated at 37 °C for one hour with constant shaking at 500 rpm. The cells were then plated onto LB-medium-agar plates, containing 100 μg/ml ampicillin. This antibiotic ensures the growth of only *E. coli* cells with antibiotic resistant pET-22 plasmids inside. Bacterial colonies were obtained on the plates after overnight incubation at 37 °C. For small scale bacteria growth, single bacterial colonies of MBP-C1 and MBP-C8 were transferred into 10 ml volumes of LB-medium, respectively, supplemented with 100 μg/ml ampicillin. The cultures were grown overnight at 37 °C, with constant shaking at 200 rpm. 3 ml of each culture were then diluted into 1 l LB-medium (100 μg/ml ampicillin) and grown under the same conditions. Protein expression was induced once cells reached an optical density (OD) $A(600\,nm) = 0.4 - 0.5$ by addition of Isopropyl-β-D-thiogalactopyranoside (IPTG) to a final concentration of 1 mM and growth was allowed to proceed for a further 8 hours. IPTG is a synthetic inductor (a chemically modified lactose), which induces the transcription and is used to produce the requested recombinant proteins by expression of cloned genes. The OD was measured using an Eppendorf Biophotometer and data were normalized to a measurement of LB-medium, used as a blank. The bacterial cells were pelleted by centrifugation at 4200 rpm (JA-12 rotor, Beckmann, USA) for 15 minutes. The cell pellet was resuspended in 20-40 ml lysis

buffer(6 M urea, 300 mM NaCl, 10 mM imidazole pH 8.0, 50 mM Tris, pH 8.0) and frozen at -20 °C. Cell lysis was achieved by sonication (15-20 30-second-pulses with 30 seconds interval) in an ice-water bath, centrifuged at 15000 rpm for 20 minutes (JA-20 rotor, Beckmann, USA), before the supernant was finally filtered through a 0.44 μm membrane.
To purify the proteins by nickel affinity chromatography, 10 ml Nickel-Nitrilotriacetic acid (Ni-NTA) agarose (QIAGEN) columns were used (Fig. 3.2). Initially the columns were

Figure 3.2: Picture of a Ni-NTA agarose (QIAGEN) column used for nickel affinity chromatography to purify MBP and P2 proteins. Protein-buffer-solutions are loaded onto a column with 10 ml of Ni-NTA matrix and the buffer can flow through the closable hole on the bottom (yellow seal).

equilibrated with lysis buffer (10 times the column volume) and the supernatant of each protein (MBP-C1 and MBP-C8, respectively) was applied onto the column. At the pH of the lysis buffer (8.0), the His-tag on the N-terminal of the proteins is negatively charged and therefore able to bind to Ni^{2+}-ions of the Ni-NTA matrix. Unbound proteins were removed by washing with washing buffer (6 M urea, 300 mM NaCl, 20 mM imidazole pH 8.0, 50 mM Tris, pH 8.0) to remove all molecules from the matrix except the desired proteins. Bound proteins were finally eluted using elution buffer (6 M urea, 300 mM NaCl, 250 mM imidazole pH 8.0, 50 mM Tris, pH 8.0), containing a high amount of imidazole, which binds to the nickel ions of the matrix and thus displaces the proteins.

The expression and purification of P2 were slightly different and carried out essentially as described in Majava *et al.* [104]. Autoinduction was used for the expression, by the use of glucose and lactose instead of IPTG, in order to optimize protein production (10 - 100

more P2 proteins than with IPTG). The P2 expression vector pTH27 was transformed into *E. coli* BL21(DE3) cells. The heat-shock transformation was performed as described above for MBP proteins. The plasmid solution was then plated onto LB-medium-agar plates, containing 100 μg/ml ampicillin and 34 g/ml chloramphenicol. Overnight cultures were grown in 10 ml volumes of ZYM-5052 autoinduction medium [105] with the same concentrations of the antibiotics. After shaking at 200 rpm at 37 °C overnight, 1 l of autoinduction medium was inoculated with the small scale cultures. Large scale bacteria growth continued at 37 °C for four hours and then at 18 °C for further 48 hours with constant shaking at 200 rpm. Cells were collected by centrifugation at 5000 rpm (JLA-9.1000 rotor, Beckmann, USA) for 10 minutes. The bacteria cell pellets were resuspended in 20-40 ml lysis buffer (50 mM sodium phosphate, 300 mM NaCl, 10 mM imidazole pH 8.0, 50 mM Tris, pH 8.0), sonicated and centrifuged as described above, and finally filtered through a 0.44 μm membrane. The purification of P2 proteins was performed without urea, which was used for the unfolded MBP proteins to remove impurities by the denaturation of other proteins. Therefore, the washing buffer contained 50 mM sodium phosphate, 300 mM NaCl and 20 mM imidazole pH 8.0 and the elution buffer 50 mM sodium phosphate, 300 mM NaCl and 250 mM imidazole pH 8.0.
Sodium dodecyl sulfate polyacrylamide gel electrophoresis (SDS-PAGE) was used to identify elution fractions containing MBP-C1, MBP-C8 or P2 (a detailed description of SDS-PAGE is provided in Section 3.3.2). Pictures of the gels are shown in Fig. 3.3. On the

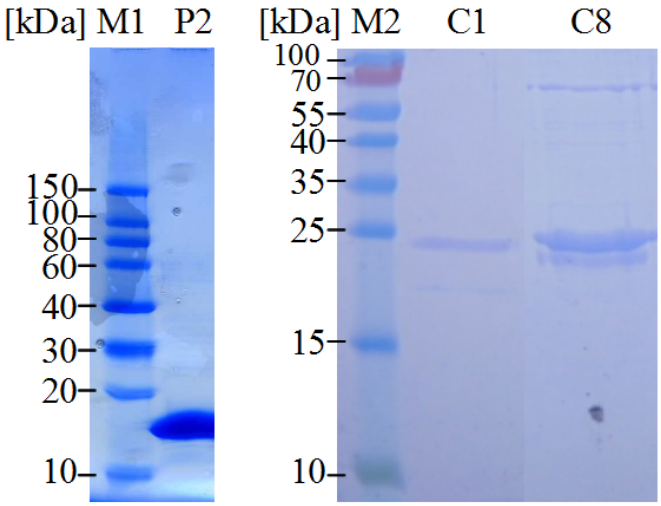

Figure 3.3: SDS-PAGE for purified myelin proteins P2 (left, 14.8 kDa), MBP-C1 and MBP-C8 (right, 18.5 kDa). Protein markers M1 *Roti^{TM}-Mark 10-150 PLUS* and M2 *PageRuler^{TM} Prestained Protein Ladder #SM0671* were used.

left, a gel with P2 and protein marker M1 *Roti^{TM}-Mark 10-150 PLUS* is shown and on the right-handside the gel with MBP-C1, MBP-C8 and protein marker M2 *PageRuler^{TM} Prestained Protein Ladder #SM0671* (Fermentas International Inc., Canada). Both MBP

proteins exhibited anomalously large molecular weights as judged by SDS-PAGE. A molecular weight of approximately 20 kDa instead of 18.5 kDa was found, respectively. This could be caused by the His_6-tag, which could increase the molecular weight by approximeately 10 %.
For the MBP proteins, urea was removed by dialysis against buffer containing 20 mM HEPES (2-(4-(2-Hydroxyethyl)-1-piperazinyl)-ethansulfonsäure, ph 7.5) and 150 mM NaCl (sodium chloride), at 4 °C. ZelluTrans/Roth dialysis tubes with a molecular weight cutoff of 3500 kDa and a wall thickness of 25 μm were used. For P2 proteins, which were purified without urea, 45 mM HEPES (pH 7.5) and 150 mM NaCl were added to the protein solution, without dialysing. NaCl was necessary to enhance the stability of the proteins and to prevent them from precipitation and HEPES buffer is commonly used in order to keep a constant pH of 7 to 8. Subsequent centrifugation at 3000 rpm in a Beckman Allegra 6 benchtop centrifuge with GH 4.7 swinging bucket rotor and filtration through a 0.2 μm membrane yielded the final protein solution, which was again verified by a SDS-PAGE. Finally, the proteins were lyophilized, in order to store them until the sample preparation for neutron scattering experiments.

3.2 Preparation of Reconstituted Membranes

The lipids DOPS and DOPC were purchased from Avanti® Polar Lipids (Alabaster, AL, USA) and used without further purification (the supplier certified a purity of at least 99 %). Liposomes (or lipid vesicles) are formed, when thin lipid films are hydrated and stacks of lipid bilayers become fluid and swell. Hydrated lipid sheets detach and create large multilamellar vesicles (LMVs) due to their amphiphilic behaviour. For this purpose, the lipid-powders were dissolved and mixed in chloroform with a 1:1 mass ratio, in order to assure a homogenous mixture of both lipids. Chloroform was removed to yield a thin lipid film by evaporation of the solvent, using a dry nitrogen stream. The glass vessel containing the lipid solution was rotated, such that the nitrogen flux formed a thin lipid film on the sides of the vessel. The lipids were further dried under vacuum overnight. Hydration of the dried lipid-film was provided by dissolving the lipids in D_2O to a concentration of 50 mg/ml with subsequent gentle vortexing, resulting in LMVs. Before large unilamellar vesicles (ULVs) were obtained by extrusion of the lipid solution through a 100 nm pore-sized membrane using the Avanti® Mini- Extruder (Fig. 3.4), the LMV suspension has been disrupted by 5 cycles of freezing and thawing. This procedure prevents from membrane fouling and improves the homogeneity of the size distribution of the final ULVs. The LMV solution was frozen one minute in liquid nitrogen (70 K) and thawed another minute in a warm water bath of 60°C (above the lipid phase transition temperature). Extrusion allows the preparation of ULVs in an efficient rapid manner in the liquid phase of the lipids. Therefore, the temperature during extrusion was kept constant at approximately 60°C, using a heating block. A pore size of 100 nm yields usually large ULVs with the same diameter. In order to achieve a homogeneous, ULV solution, lipids were extruded 31 times. Appropriate amounts of protein solution, at a concentration respecting the ratio of MBP and P2 in the

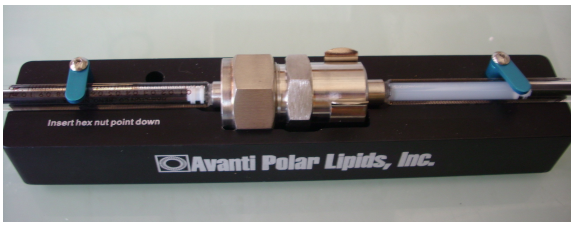

Figure 3.4: The Avanti® Mini-Extruder to obtain large unilamellar vesicles.

PNS, were added to the ULV solution. For the first membrane sample set with MBP-C1 and P2 proteins, this concentration was 4.6 mg/ml for MBP-C1 and 2.3 mg/ml for P2 in D_2O. Since for MBP-C1 the amount of HEPES buffer and NaCl was 34 wt% and 63 wt %, with respect to the lyophilized protein powders, respectively, and thus the protein amount 3 wt%, the concentration of the MBP-C1 itself was 0.14 mg/ml, resulting in 0.07 wt % with respect to the reconstituted membrane. For P2, the amount of HEPES was 47.5 wt %, the amount of NaCl 38.9 wt % and the amount of protein 13.6 wt % (in the lyophilized protein powder) and hence the protein concentration 0.31 mg/ml, which corresponds to 0.16 wt %, in the final sample. The following samples were prepared: protein-free lipids (lipids), lipids with MBP-C1 (C1-lipids), lipids with P2 (P2-lipids) and lipids with MBP-C1 and P2 (C1-P2-lipids). The protein component of the membrane sample was very little, which allowed us to neglect the scattering signal arising from the proteins and to investigate only the dynamics of the membrane in presence of the proteins. In order to investigate the influence of the protein concentration, this concentration was increased 4- and 9-fold for the second membrane sample set with MBP-C1 and MBP-C8 proteins. Concentration tests indicated that the maximum protein concentration that could be achieved was 1.28 mg/ml (9-fold) before protein aggregation, which was measured by absorption measurements using an Eppendorf Biophotometer. 4-fold samples contained 0.47 mg/ml protein concentration. The same amount of protein buffer (150 mM HEPES and 20 mM NaCl used for dialysis, see Section 3.1) was added to protein-free lipids as a control sample. The following samples were prepared: protein-free lipids with 4-fold buffer (28.8 mM HEPES, 216.8 mM NaCl, 4f-lipids), protein-free lipids with 9-fold buffer (65.0 mM HEPES, 487.5 mM NaCl, 9f-lipids), lipids with 4-fold MBP-C1 (0.47 mg/ml, 4f-C1-lipids), lipids with 9-fold MBP-C1 (1.28 mg/ml, 9f-C1-lipids), lipids with 4-fold MBP-C8 (0.47 mg/ml, 4f-C8-lipids) and lipids with 9-fold MBP-C8 (1.28 mg/ml, 9f-C8-lipids). In order to determine a possible influence of the protein buffer, especially of the high amount of NaCl, further samples, containing 1-fold (1f-lipids) and 2-fold buffer (2f-lipids) were prepared. Each sample contained 2 ml of lipid solution and 0.5 ml of protein and buffer solution, respectively. The size distribution of the ULVs was measured by dynamic light scattering (DLS) experiments and monodispersity of the samples was verified (see Subsection 3.3.1). For an overview, all samples are listed in Table 3.1. Oriented bilayers were obtained by spreading the samples on monocrystalline SiO_2 (1 1 1) wafers, which had a thickness of 375 μm and n-doping (phosphor) (purchased from Silchem Handelsgesellschaft mbH, Freiberg, Germany). Circular wafers

	protein concentration [mg/ml]	amount HEPES [mM]	amount NaCl [mM]
lipids			
C1-lipids	0.14	7.2	54.2
P2-lipids	0.31	7.2	54.2
C1-P2-lipids	0.14 MBP-C1, 0.31 P2	7.2	54.2
4f-lipids		28.8	216.8
4f-C1-lipids	0.47		
4f-C8-lipids	0.47		
9f-lipids		65.0	487.5
9f-C1-lipids	1.28	65.0	487.5
9f-C8-lipids	1.28	65.0	487.5
1f-lipids		7.2	54.2
2f-lipids		14.4	108.4

Table 3.1: Samples prepared for neutron scattering experiments.

with a diameter of 76.2 mm were cut to a rectangle of the dimension 2.8 cm × 3.8 cm, in order to fit in a slab shaped aluminum sample holder (3 cm × 4 cm) for neutron experiments. Figure 3.5 a shows three wafers containing oriented bilayers. The samples were dried in a vacuum oven with a gentle nitrogen stream at 40 °C for 24 hours and re-hydrated in a desiccator with a D_2O atmosphere for 36 hours. The relative humidity was 95 % due to a saturated $CaSO_4$-D_2O solution. For neutron scattering experiments, three such wafers were stacked in a sample holder with an empty wafer on the top (Fig. 3.5 b). Each wafer contained 33.3 mg lipids and approximately 6600 bilayers (and accordingly 13200 monolayers). The number of monolayers was calculated from the fraction of the total number of lipids in a sample ($n^{total} = N_A(m/MW) = 7.55 \cdot 10^{19}$, where N_A is Avogadro's number, $m = 100$ mg the amount of the lipids and $MW = 798$ g/mol the average molecular weight of both lipids) over the number of lipids in a monolayer ($n^{mono} = A^{mem}/A^{head}$, where $A^{mem} = 8{,}75 \cdot 10^{16}$ Å^2 is the surface area of the membrane or rather a wafer and $A^{head} = 46$ Å^2 the area of a lipid head), which results in approximately 39600 monolayers, divided by three (number of wafers containing multilayers). The total number of bilayers is accordingly about $n_{bi} = 19800$. To make the sample holder vacuum tight an indium seal was used when closing it.

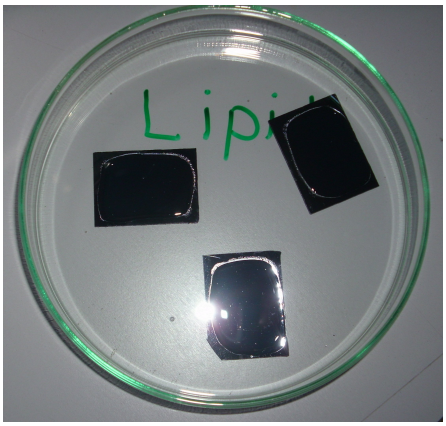

(a) Oriented bilayers spread on monocrystalline SiO_2 (1 1 1) wafers.

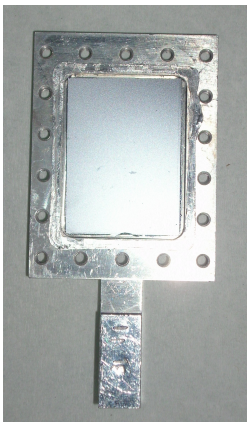

(b) Reconstituted myelin membrane on wafers stacked in a slab shaped aluminum sample holder.

Figure 3.5: A membrane sample for neutron scattering experiments.

3.3 Sample Characterization

Correct sample preparation is essential for the reliability of the obtained results. Therefore, samples were characterized by several methods, which will be presented within the next subsections. Dynamic light scattering (DLS) experiments were performed to determine the particle size distribution of the ULVs in solution with and without proteins (before spreading them on wafers). Therefore, their average hydrodynamic radius $\langle R_h \rangle$ and the polydispersity index PDI were estimated. Correct lipid-protein binding was verified by sucrose gradient centrifugation followed by SDS-PAGE. To confirm the gel to liquid phase transitions of DOPS and DOPC, differential scanning calorimetry (DSC) measurements were carried out on both, ULVs in D_2O and deuterated lipid membranes on SiO_2 wafers. In order to study the repeat distance and the mosaic spread of the final membrane-samples, neutron diffraction experiments were performed on the diffractometer D16 (ILL).

3.3.1 Dynamic Light Scattering Experiments

To estimate $\langle R_h \rangle$ and the PDI of the ULVs in solution with and without proteins DLS measurements were performed, using the ALV CGS-3 Compact Goniometer (ALV-GmbH, Germany) at the ILL. The lipid concentration was very low (0.001 mg/ml), in order to avoid multiple scattering. In DLS measurements the time-dependent correlation function

$$G(t) = \langle I(t)\, I\,(t+\tau) \rangle \tag{3.1}$$

for particles in Brownian motion is obtained, where τ is the delay time and $I(t)$ the time-dependent scattered intensity. This was fitted to a stretched exponential decay function:

$$G(t) = A \exp\left[-\left(\frac{2\,t}{\tau}\right)^{\beta}\right] \tag{3.2}$$

with the stretching parameter β. From the fit parameters τ and β, $\langle R_h \rangle$ and PDI have been calculated as described in the following. The average decay time is given by

$$\tau = \int dt \, \exp\left[-\left(\frac{t}{\tau}\right)^{\beta}\right], \tag{3.3}$$

which is equal to [106]

$$\tau = \frac{\tau}{\beta}\,\Gamma\left(\frac{1}{\beta}\right), \tag{3.4}$$

where $\Gamma(x)$ is the Gamma function.
Since the radius of a particle measured with DLS is a value that is related to the particle diffusion within the solvent, the radius is called hydrodynamic radius [107]. It is the radius of a sphere which has the same translational diffusion coefficient as the particle. The average hydrodynamic radius $\langle R_h \rangle$ of all particles is given by the Stokes-Einstein equation:

$$\langle R_h \rangle = \frac{k_B\,T}{6\,\pi\,\eta\,\langle D \rangle}, \tag{3.5}$$

where η is the viscosity of the solvent and $\langle D \rangle$ the average diffusion coefficient:

$$\langle D \rangle = \frac{1}{\langle \tau \rangle Q^2}. \tag{3.6}$$

Q is the modulus of the scattering vector, with

$$|\vec{Q}| = \frac{4\,\pi\,n_0}{\lambda}\sin\Theta, \tag{3.7}$$

where λ is the wavelength, 2Θ the scattering angle and n_0 the refraction index of the sample. The polydispersity index PDI is the width of the particle size distribution. It is defined by the ratio between the standard deviation σ of the decay time τ and the average value $\langle \tau \rangle$, namely

$$PDI = \frac{\sqrt{|\langle \tau \rangle^2 - \langle \tau^2 \rangle|}}{\langle \tau \rangle} = \sqrt{\left(\frac{\tau^2}{\beta}\left[\frac{1}{\beta}\,\Gamma\left(\frac{1}{\beta}\right)^2 - \Gamma\left(\frac{2}{\beta}\right)\right]\right)}. \tag{3.8}$$

Figure 3.6 shows the data obtained for the protein-free lipids with the fitted correlation function $G(t)$. The hydrodynamic radius $\langle R_h \rangle = (50 \pm 1)\,\mathrm{nm}$ of a single ULV population corresponds to the pore-size of the membrane used for extrusion (pore-diameter of 100 nm), whereas $\langle R_h \rangle$ of ULVs with added proteins are slightly larger. The hydrodynamic radii and the polydispersity index PDI are shown in Table 3.2. The PDI is very small, indicating that the samples are monodisperse.

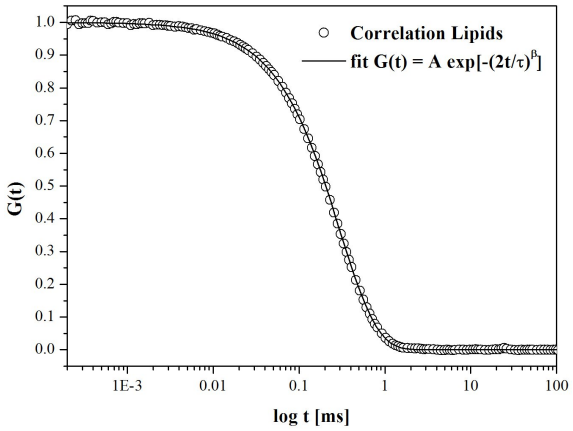

Figure 3.6: Correlation function $G(t)$ for the protein-free lipids obtained by DLS. Data were fitted with a stretched exponential function, leading to a mono-disperse population with a hydrodynamic radius of $\langle R_h \rangle = (50 \pm 1)\,\mathrm{nm}$.

	lipids	C1-lipids	P2-lipids	C1-P2-lipids
$\langle R_h \rangle$ [nm]	50 ± 1	56 ± 1	57 ± 2	58 ± 2
PDI	$0.1162 \pm 3 \cdot 10^{-4}$	$0.1558 \pm 9 \cdot 10^{-4}$	$0.1096 \pm 7 \cdot 10^{-4}$	$0.145 \pm 1 \cdot 10^{-3}$
	9f-lipids	9f-C1-lipids	9f-C8-lipids	
$\langle R_h \rangle$ [nm]	58 ± 1	57 ± 1	57 ± 1	
PDI	$0.1560 \pm 6 \cdot 10^{-4}$	$0.0533 \pm 3 \cdot 10^{-4}$	$0.0950 \pm 5 \cdot 10^{-4}$	

Table 3.2: $\langle R_h \rangle$ and PDI for ULVs with, and without, myelin proteins MBP-C1, MBP-C8 and P2, obtained by DLS.

3.3.2 Sucrose Gradient Centrifugation and SDS-PAGE

Correct lipid-protein binding was checked and verified by sucrose gradient centrifugation, followed by SDS-PAGE. A sucrose gradient is created by stacking lower concentrations on higher concentrations of sucrose in a centrifuge tube. The sample of each protein-ULV-solution is applied on the top and the gradient is ultracentrifuged. The particles of the sample travel through the gradient until they reach the point at which the sucrose density is similar to the density of the particles. With this method, possible lipid or protein aggregates, which are not bound to the lipids, can be identified, since those have a high density and would travel to the bottom of the tube. Each sucrose layer, including the sample, was further analyzed by SDS-PAGE, which is a separating process for proteins based on their size. This allowed to determine, if proteins were present only in the lipid-protein sample (and not in the sucrose layers), indicating that they are bound to the lipids. For the sucrose gradient, 10 ml polycarbonate tubes were prepared for each lipid-protein sample. The sucrose gradients consisted of 1 ml layers with 65 %, 45 %, 35 %, 28 %, 23 %, 18 %, 13 %, 8 % and 3 % (w/v) sucrose solution, from the bottom to the top of the tube. After putting each sucrose layer, the gradient was frozen in liquid nitrogen in order to avoid mixing of the separate layers. Thawing occurred at 4 °C overnight. 0.5 ml of each protein-ULV solution was carefully applied onto the top layer with 3 % (w/v) sucrose solution of each tube, followed by another 3 % (w/v) sucrose layer. The tubes were then filled with H_2O until the bezel. After centrifugation with a Beckman ultracentrifuge using an SW41 rotor (15 hours at 3500 rpm), a band of lipids with proteins was clearly visible (see inset in Fig. 3.7), and no protein or lipid aggregates were found at the bottom of the tube.

A small aliquot of each sucrose layer was analyzed by SDS-PAGE. 3 μl of threefold sample loading buffer (containing 2.4 ml 1 M Tris-HCl (pH 6.8), 3 ml 20 % sodium dodecyl sulfate (SDS), 3 ml 100 % glycerol, 1.6 ml B-mercaptoethanol and 0.006 g bromophenol blue) was added to 6 μl of each layer. This buffer contains SDS, which is an anionic detergent and denaturates the protein. SDS-protein binding and further unfolding was promoted by additionally heating of the samples at 95 °C for 3-5 minutes. The anionic charge of SDS-molecules overlaps the intrinsic charge of proteins, when bound to them. Hence, the proteins exhibit a high negative charge, which is proportional to the length of their polypeptide chains. Therefore, the velocity with which the proteins migrate through the gel, is dependent exclusively on their molecular weight and not on their charge. Samples were loaded onto a polyacrylamide-gel surrounded by a so-called running buffer, which is an electrolyte (a 10-fold running buffer stock was made of 30.3 g Tris base, 144 g glycine, 10 g SDS and distilled water to make 1 l). The polyacrylamide-gel is built up of pores acting like a sieve: when a voltage is applied, small proteins migrate easily through the gel from the cathode (above) towards the anode (below), whereas larger proteins are migrating more slowly. An additional protein marker is typically loaded, containing proteins of a known size, allowing the estimation of the size of the protein-samples (here protein marker *Broad Range Protein Marker P7702* New England Biolabs, USA was used). The polyacrylamide-gel usually consists of two parts: a stacking gel near the cathode, in which the proteins are collected, and a running gel in which the size separation occurs. These gels differ in

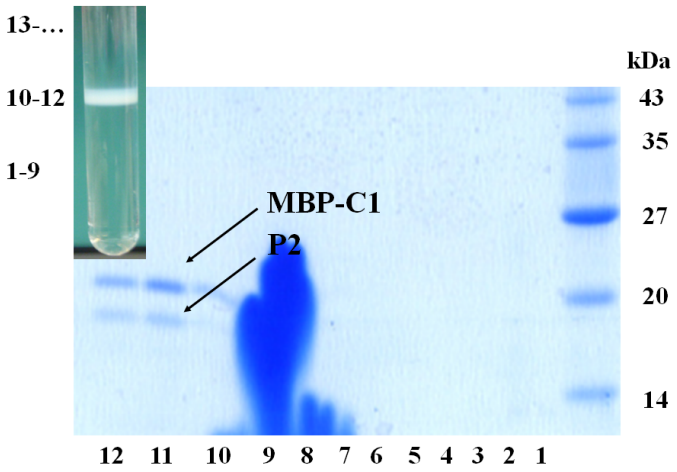

Figure 3.7: SDS-PAGE for samples of each 1 ml-layer of the sucrose gradient with lipid-band and myelin proteins MBP-C1 and P2 after centrifugation (inset). The numbers indicate each sucrose layer. Protein bands of MBP-C1 (18.5 kDa) and P2 (14.8 kDa) are clearly visible in gel-columns with the lipid-protein band of the gradient, indicating correct lipid-protein binding. The "flower" at the bottom of the gel is a feature typical assigned to lipids.

their pH and in their pore size: the stacking gel is macropored with a pH of 8.8 and the running gel is fine pored with a pH of 6.8. The concentration of acrylamide used for the running gel depends on the size of the proteins to be analyzed. The higher is the acrylamide concentration, the smaller are the pores of the gel. Small proteins are therefore separated using higher acrylamide concentrations - otherwise they would migrate through the gel with maximum speed. Since MBP has a size of 18.5 kDa and P2 of 14.8 kDa, a gel containing acrylamide of 15 % concentration was prepared. This gel can be used for protein sizes ranging from 12 to 43 kDa and was made of 2.3 ml H_2O, 5 ml 30 % acrylamide mix, 2.5 ml 1.5 M Tris (pH 8.8), 0.1 ml 10 % SDS, 0.1 ml 10 % ammonium persulfate and 4 μl TEMED, for the use of two gels. The solution was filled into a gel cassette and became solidified after $15 - 20$ minutes. Then stacking gel was added, consisting of 2.72 ml H_2O, 0.68 ml 30 % acrylamide mix, 0.52 ml 1.0 M Tris (pH 6.8), 0.04 ml 10 % SDS, 0.04 ml 10 % ammonium persulfate and 4 μl TEMED (also for two gels). A voltage of $U = 200$ V was applied for one hour. MBP and P2 proteins were found in sucrose fractions containing lipids, which verified correct lipid-protein binding, as shown in Fig. 3.7. Both proteins exhibited anomalously large molecular weights, which could be caused by a slower migration in SDS-PAGE of membrane bound proteins, such as those, than of soluble, globular proteins [108].

3.3.3 Differential Scanning Calorimetry

DSC measurements were carried out on DOPS-DOPC ULVs in D_2O as well as on deuterated DOPS-DOPC membranes on silica wafers after neutron scattering experiments. The purpose was to confirm the gel to liquid phase transitions of the lipids and to investigate,

if two distinct phase transitions occur in the system (one for DOPS and one for DOPC), or one intermediate phase transition. Therefore, the Micro DSC III instrument (Setaram Instrumentation, France) at the ILL was utilized. The thermoanalytic technique is used to determine physical transformations of a system, such as phase transitions. Therefore, the sample to be analyzed and a reference sample are heated at a similar heating rate. The difference between the amount of heat that flows into the sample and into the reference, maintaining both at the same temperature, is measured as a function of temperature and time. When no transformation of the sample occurs, the heat flow behaves linearly with the temperature. If the temperature increases and the sample undergoes an endothermic reaction, such as a gel-to-liquid phase transition of lipids, the differential temperature signal is not equal to zero, resulting in a positive peak: more heat is required to increase the sample temperature at the same rate as the reference. If the temperature decreases and the reaction is exothermic (transition from liquid to gel phase), the signal shows a negative peak. A more detailed description can be found in [109].
To cover the lipid phase transitions and the phase transition of the surrounding water, the samples were heated from 225 K to 290 K at a heating rate of 2 K/min. An empty aluminum sample holder (cylindrical with a diameter and a height of approximately 5 mm, respectively) was used as a reference for the ULV sample, whereas for the oriented membrane sample a wafer was added. Figure 3.8 shows DSC data obtained for an oriented DOPS-DOPC membrane sample during heating (an aliquot of a sample used for neutron scattering experiments). Phase transitions are clearly visible at 254 K, 259 K and 274 K.

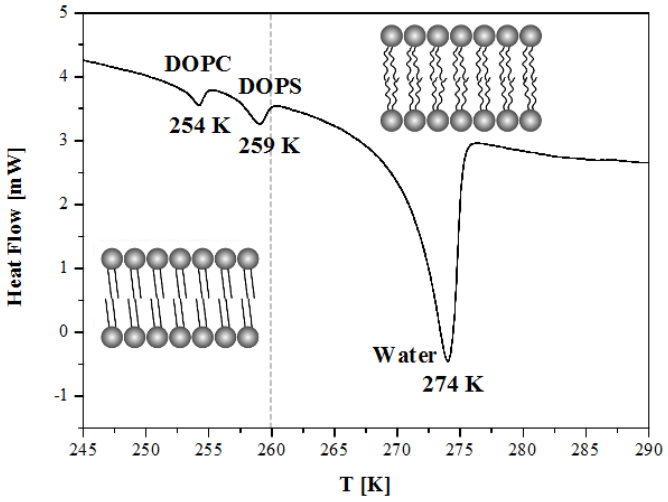

Figure 3.8: DSC data obtained for an oriented DOPS-DOPC membrane. The gel to liquid phase transitions for the lipids are clearly visible at 254 K and 259 K, slightly shifted to the literature values. The peak at 274 K agrees with the water phase transition.

The first peak most likely corresponds to the phase transition of DOPC and the second to the transition of DOPS. The temperature values are slightly shifted with respect to

values found in the literature (+1 K for DOPC and −3 K for DOPS), which could be due to the interaction between both lipids resulting in an influence of one phase transition to the other. The peak at almost 274 K is caused by the water phase transition. DSC measurements on H_2O and D_2O have confirmed phase transition temperatures of 273 K and 277 K, respectively. Since the membrane sample was removed from a sample holder used for neutron experiments, the amounts, needed for DSC experiments, are very little and the DSC-sample holders are not vacuum-tight, H-D exchange in the solvent cannot be excluded, resulting in a measured water phase transition at 274 K. Similar values for the phase transition temperatures for heating were obtained for the DOPS-DOPC ULV sample.

3.3.4 Diffraction on D16

Further characterization of the final membrane samples was performed with neutron diffraction experiments using the small momentum transfer diffractometer D16 at the ILL [101] at a wavelength of 4.7 Å. The purpose of the measurements was to investigate the characteristic repeat distance and the mosaic spread of the membranes and thus the quality of the bilayer orientation. Diffraction measurements for the first sample set (lipids, C1-lipids, P2-lipids and C1-P2-lipids) were carried out in parallel to the elastic and quasielastic measurements (described in Chapter 5). In order to measure the membranes in the gel and in the liquid phase, data was recorded at 230 and 300 K. In contrast, for the characterization of the second sample set (9f-lipids, 9f-C1-lipids and 9f-C8-lipids), diffraction measurements were only possible after quasielastic neutron experiments (see Chapter 6). Due to a lack of time, experiments were carried out only at 300 K on 9f-C1-lipids and 9f-C8-lipids. To obtain the repeat distances of the membranes, the scattering angle 2Θ was scanned by rotation of the detectors. From the scattering intensity as a function of 2Θ the corresponding Q-values can be calculated using Eq. 2.10 and the characteristic repeat distance of the bilayers corresponding to a given Q-value is given by Eq. 2.61. Figure 3.9 presents a diffraction pattern obtained for the lipids at 242 K (gel phase, blue curve) and at 300 K (liquid phase, red curve). Both curves show a first order Bragg peak at $Q = 0.109\,\text{Å}^{-1}$ (resulting in a repeat distance of $d = 58$ Å, respectively), indicating the same structure for the lipids in the gel and in the liquid phase. With repeat distances of 53 Å for a DOPS-bilayer and of 63 Å for a DOPC-bilayer, respectively, a distance of 58 Å is the mean value of both. This suggests that DOPS and DOPC lipids are homogeneously distributed in a protein-free membrane.
The mosaic spread $\Delta\omega$, which is an indication for the parallel orientation of the multilayer, was achieved by rotation of the sample with respect to the incoming neutron beam (so-called rocking curve). This rotational axis is called the ω-axis, with $\omega = \Theta$ (half of the scattering vector 2Θ). The mosaic spread was calculated from the FWHM of the first order Bragg peak as a function of ω. However, it has to be remarked that a narrow and a broad Lorentzian had to be used to fit the data points. The narrow Lorentzian describes the mosaic spread $\Delta\omega$ and the broad one describes probably fluctuations like disorder in directions parallel to the membrane plane. $\Delta\omega$ was obtained from the FWHM of the nar-

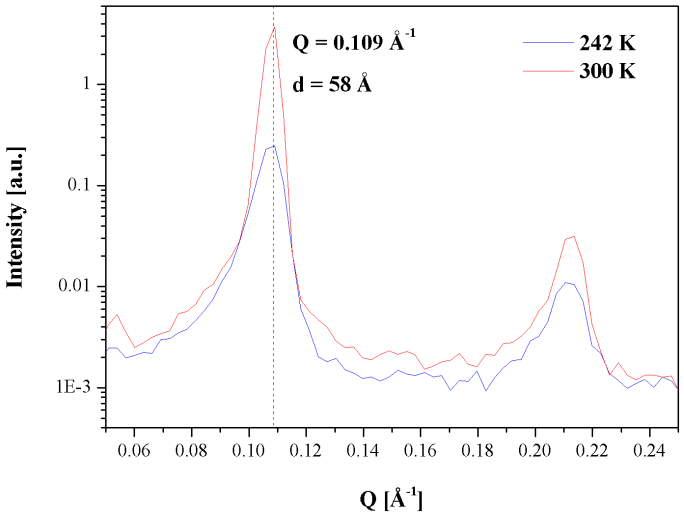

Figure 3.9: Diffraction pattern obtained for the lipids at 242 K (blue curve) and at 300 K (red curve). Both curves exhibit a first order Bragg peak at $Q = 0.109\,\text{Å}^{-1}$ and a corresponding second order Bragg peak, according to a characteristic repeat distance of $d = 58\,\text{Å}$ in the gel and in the liquid phase of the lipids.

row Lorentzian, which is given in Table 3.3 for all membrane samples. The mosaic spread was found to be less than 0.6° for all samples. Considering approximately 6600 bilayers per wafer, this low mosaicity confirms that the bilayers are oriented in a highly parallel manner, which is an important indication of the quality of the reconstituted membranes. As an example, Fig. 3.10 shows the mosaicity $\Delta\,\omega = (0.33 \pm 0.01)^{\circ}$ for the lipids at 300 K (calculated from first order Bragg peak at $Q = 0.109\,\text{Å}^{-1}$). The results of these diffraction measurements performed on D16, giving informations about the structure of myelin-like membranes, will be discussed in Section 5.1 in more detail.

Sample	$\Delta\omega$ [°]
lipids 230 K	0.28 ± 0.04
lipids 300 K	0.33 ± 0.01
C1-lipids 230 K	0.25 ± 0.02
C1-lipids 300 K	0.33 ± 0.03
P2-lipids 230 K	0.16 ± 0.03
P2-lipids 300 K	0.46 ± 0.03
C1-P2-lipids 300 K	0.51 ± 0.09
9f-C1-lipids 300 K	0.38 ± 0.05
9f-C8-lipids 300 K	0.40 ± 0.10

Table 3.3: Mosaic spreads $\Delta\omega$ for oriented reconstituted membranes with and without myelin proteins obtained on the diffractometer D16.

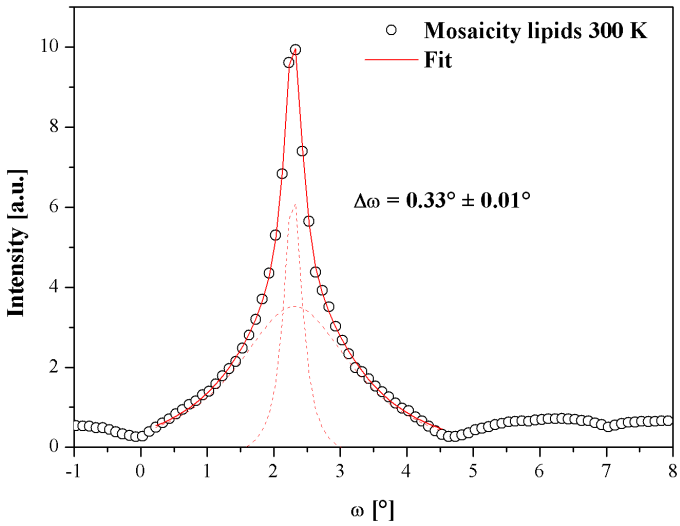

Figure 3.10: Rocking curve for the lipids at 300 K measured on D16. Two Lorentzians (red dashed curves) were used to model the data, where the FWHM of the narrow Lorentzian gives a mosaic spread of $\Delta\omega = 0.33^\circ \pm 0.01^\circ$. The broad Lorentzian describes probably disorder in directions parallel to the membrane plane.

Chapter 4

Characterization of the Structural and Dynamical Properties of Protein-Free Model Myelin Membranes

In order to introduce experimental methods used for the characterization of the structure and dynamics of model myelin membranes, the results of neutron scattering experiments on a protein-free DOPS-DOPC membrane are described in this chapter. Diffraction data obtained on the diffractometer D16 and on the backscattering spectrometer IN16 (ILL) are shown together with EINS measurements obtained on the backscattering spectrometers IN13 (ILL) and IN16. Furthermore, quasielastic measurements on the time-of-flight spectrometers IN5 (ILL), Osiris (ISIS) and Neat (HZB) are presented. In order to interpretate the effect of myelin proteins on membrane dynamics, described in the following chapters, the influence of the protein buffer (HEPES and NaCl, which prevent the protein from degradation) on membrane dynamics will be discussed.
The experimental conditions for each instrument and the data correction protocols, described in this chapter, stay the same for the experiments presented in the following chapters.

4.1 Structural Properties

Neutron diffraction measurements were performed on D16 and IN16, which allowed the investigation of the membrane structure in a very large Q-range. Since the Q-region explored on D16 was $0.039\,\text{Å}^{-1} \leq \text{Q} \leq 0.424\,\text{Å}^{-1}$ with a resolution of $\Delta\text{Q} = 0.003\,\text{Å}^{-1}$, repeat distances characteristic for reconstituted DOPS-DOPC bilayers were studied. Moreover, with an accessible Q-range on IN16 of $0.356\,\text{Å}^{-1} \leq \text{Q} \leq 1.838\,\text{Å}^{-1}$ with $\Delta\text{Q} = 0.005\,\text{Å}^{-1}$, Bragg peaks characteristic for ice, which was present in the fully hydrated membranes,

were visible. The diffraction measurements on IN16 were carried out simultaneously with temperature dependent EINS experiments, presented in the end of this chapter.
As already mentioned in Subsection 3.3.4 (sample characterization using neutron diffraction), the diffractometer D16 was used to determine the structure of model myelin membranes. Covering the gel-to-liquid phase transitions of the lipids, temperature scans ranging from 240 K to 300 K and back were performed. First order Bragg peaks at $Q = 0.109\,\text{Å}^{-1}$, which results in a repeat distance of the lipid membrane of $E_1 = 58\,\text{Å}$, were observed at 240 K (gel phase) and at 300 K (liquid phase) (see Fig. 3.9). Since a repeat distance of 58 Å is the mean value of the characteristic repeat distance of DOPS and DOPC bilayers, respectively, ($D^{DOPC} = 63\,\text{Å}$ and $D^{DOPS} = 53\,\text{Å}$, see Subsection 1.3.1), it was assumed that DOPS and DOPC lipids are homogeneously distributed in the membrane.
In order to investigate the d-spacings of the membranes in the liquid phase in more detail, the first order Bragg peak measured in the liquid phase was fitted by Gaussian functions (Fig. 4.1). Three Gaussian functions were required to properly reproduce the data,

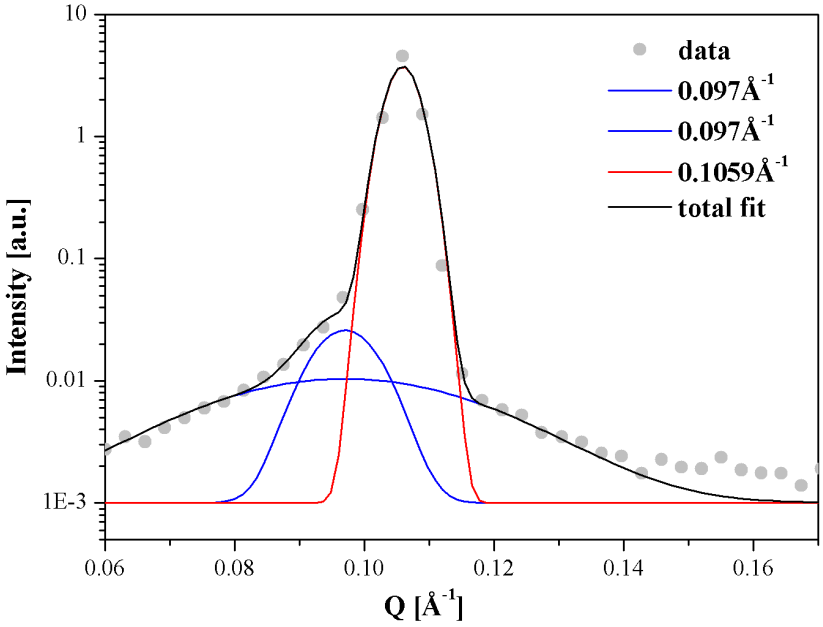

Figure 4.1: First order Bragg peaks in the liquid phase of the lipids (285 K). Data were fitted by three Gaussian functions.

resulting in three different membrane domains with a particular repeat distance, which corresponds to the center of the fitted Gaussian. The fraction of membrane domains with a particular repeat distance with respect to the whole membrane, is given by the fraction of the area of the corresponding Gaussian with respect to the total area (of all fitted Gaussian functions). The fitting parameters are listed in Table 4.1. A main repeat distances has been found with $D_1 = 59.3\,\text{Å}$, accounting for 96.8 %. Two other Gaussian functions with the same centers indicate further membrane domains with a repeat distance of $C_1 = 65\,\text{Å}$

Bragg peak [Å^{-1}]	0.1059 ± 0.0004	0.0970 ± 0.0004
repeat distance d [Å]	59.3 ± 0.1	65 ± 0.1
labeling	D_1	C_1
lipids		
fraction [%]	96.8	1.9 ; 1.3
FWHM [Å^{-1}]	0.005	0.04 ; 0.01

Table 4.1: Results for the fitting of Gaussian functions to the first order Bragg peaks of the lipids at 285 K. The Q-values of the Bragg peaks are given by the center of the Gaussians and the corresponding repeat distances d were calculated using Eq. 2.61. The relative weight of each contribution (in %) is given by the fraction of the area of the corresponding Gaussian with respect to the total area.

and a relatively large FWHM of 0.04 Å^{-1} and 0.01 Å^{-1}, respectively. This suggests that the lipids are still highly ordered in the liquid phase, with a minor fraction ($< 2\,\%$) of less ordered domains. Considering a mean value for the bilayer thickness D_B of a DOPS-DOPC membrane $\langle D_B \rangle = (36\,\text{Å} + 38\,\text{Å})\,/\,2 = 37\,\text{Å}$ (see Subsection 1.3.1), the spacing between the two bilayers is $D_W = E_1 - \langle D_B \rangle = 58\,\text{Å} - 37\,\text{Å} = 21\,\text{Å}$.
Figure 4.2 illustrates a sketch of a protein-free DOPS-DOPC membrane for the liquid phase of the lipids. In Fig. 4.3 three-dimensional plots of heating (Fig. 4.3 a) and cooling

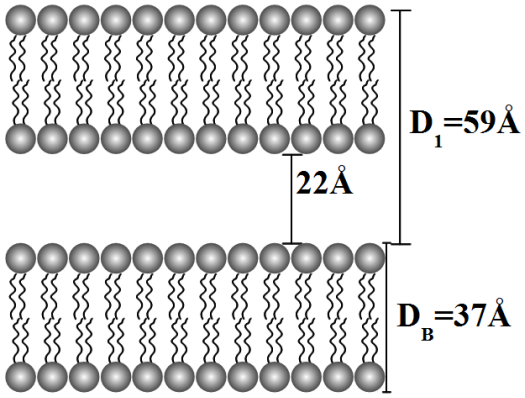

Figure 4.2: Illustration of a protein-free DOPS-DOPC membrane. The same repeat distance was obtained on D16 in both the gel and the liquid phases of the lipids. The average bilayer thickness of a DOPS-DOPC membrane is $\langle D_B \rangle = 37\,\text{Å}$.

(Fig. 4.3 b) temperature scans are shown, recorded with a rate of $\approx 1\,\text{K/min}$, in which the color represents the radially summed scattering intensity as function of Q (x-axis) and

of the temperature (y-axis). When heating the sample (Fig. 4.3 a), the repeat distance

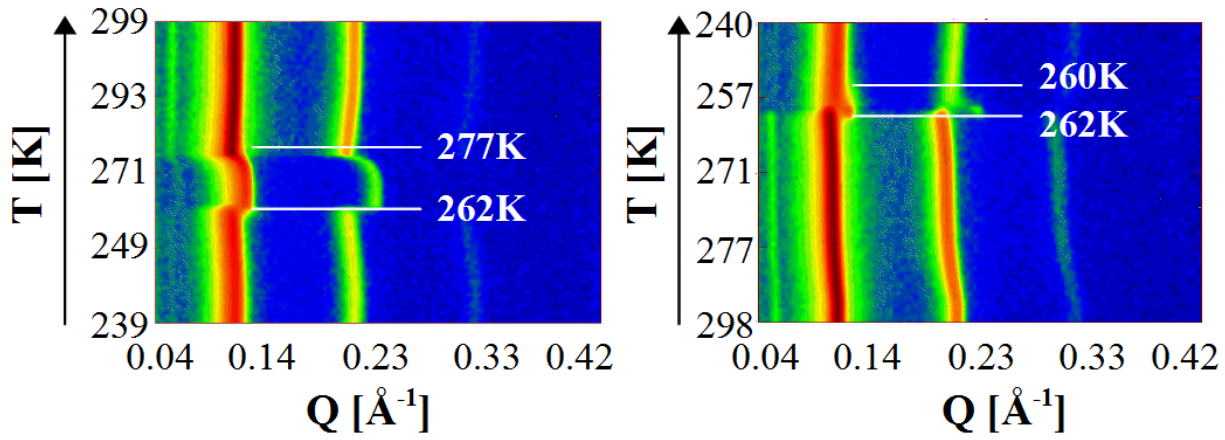

Figure 4.3: Diffraction patterns obtained on D16 for the protein-free lipids during heating (left) and cooling (right). The color represents the radially summed scattering intensity as function of Q (x-axis) and of the temperature (y-axis). A shift of the repeat distance of the bilayers is visible with increasing and decreasing the temperature.

shifts at $\approx 262\,\mathrm{K}$ to smaller values and shifts back to its initial value at $\approx 277\,\mathrm{K}$. During cooling from 300 K to 240 K, a shift of the repeat distance is also visible (Fig. 4.3 b), but at slightly different temperatures.
In order to study the changes of the repeat distance in more detail, the elastic intensity as a function of Q at temperatures of 242 K, 264 K, 274 K, 285 K and 299 K, during heating, is illustrated in Fig. 4.4 a and the intensities at the Q-values of these Bragg peaks as a function of the temperature is shown in Fig. 4.4 b. The repeat distance of the lipid membrane at $\approx 242\,\mathrm{K}$ is $E_1 = 58\,\text{Å}$, corresponding to $Q = 0.109\,\text{Å}^{-1}$, in the lipid gel phase. When heating the sample, this repeat distance shifts at $\approx 262\,\mathrm{K}$ to smaller values (peak $G_1 = 53\,\text{Å}$ in Fig. 4.4 a), back to $F_1 = 55\,\text{Å}$ at $\approx 274\,\mathrm{K}$ and finally to slightly larger values (peak $D_1 = 59\,\text{Å}$ at $\approx 285\,\mathrm{K}$) and at $\approx 299\,\mathrm{K}$ the repeat distance is again $E_1 = 58\,\text{Å}$. However, the peaks D_1 and E_1, and F_1 and G_1, are shifted only by one data point, which corresponds to approximately 1 Å (Fig. 4.4 a), and thus it is not clear if they can be distinguished. For clarity, the Bragg peaks occurring in this temperature region are listed in Table 4.2. The system seems to change its structure when both lipids have transformed from the ordered gel to the disordered liquid phase. These structural changes continue until the phase transition of the water between the bilayers also occurs ($\approx 277\,\mathrm{K}$). When the entire system is in the liquid state, including the water, it shows the same structural properties as in the gel state. However, the Bragg peak E_1 is more intense at 299 K than at 242 K, indicating a more ordered structure in the liquid phase (see Fig. 3.9). Regarding the intensity maxima of these Bragg peaks (Fig. 4.4 b) a transient Bragg peak at $G_1 = 0.118\text{Å}^{-1}$ arises at approximately 259 K and is disappeared at around 277 K. DSC measurements (Subsection 3.3.3) have indicated, that the gel-to-liquid phase

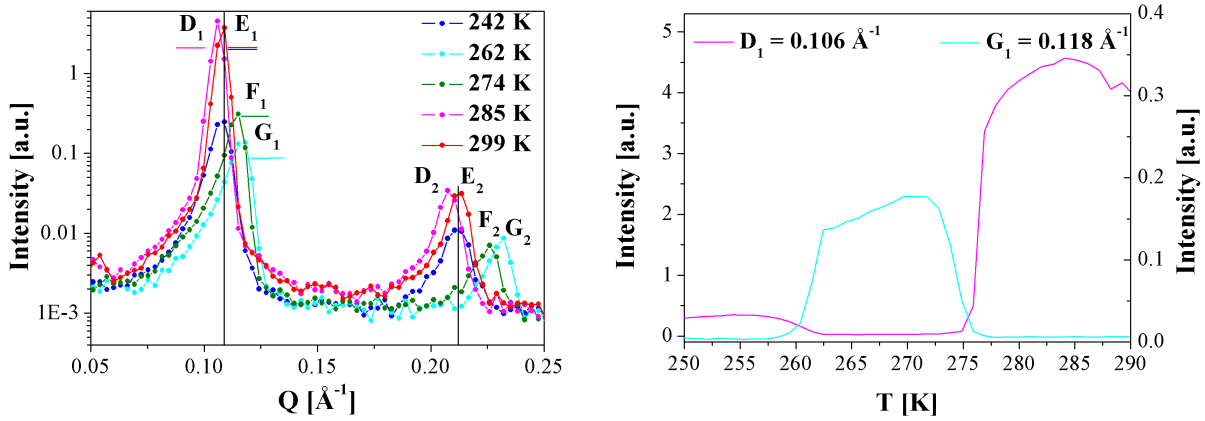

(a) (b)

Figure 4.4: (a) Diffraction patterns for the protein-free lipids at several temperatures during heating. First order Bragg peaks are indicated with index 1 and second order Bragg peaks with index 2. The repeat distance shifts with increasing temperature. (b) Intensities at the Q-values $0.106\,\text{Å}^{-1}$ and $0.118\,\text{Å}^{-1}$ of the Bragg peaks D_1 and G_1, respectively, are plotted as a function of the temperature.

1^{st} order Bragg peak	repeat distance [Å]	Q-value [Å^{-1}]	temperature [K]
D_1	59	0.106	285
E_1	58	0.109	242, 299
F_1	55	0.115	274
G_1	53	0.118	262

Table 4.2: Bragg peaks obtained by diffraction for the lipids during heating. The peaks D_1, E_1, and F_1, G_1, respectively, are very close and thus might be caused by the same d-spacings.

transitions of DOPC and DOPS occur at 254 K and at 259 K (which are slightly shifted to the literature values of 253 K and 262 K), respectively. Obviously, this transient repeat distance of G_1 is present, when both lipids are in their liquid phase and the water is still crystalline (until 277 K, which is approximately the freezing point of D_2O). It seems that the phase transition of DOPC alone is not sufficient to vary the membrane structure, and that the structure does not change until the anionic DOPS lipids also transform from the gel to the liquid phase. When both lipids are in the liquid disordered phase and the water is still crystalline, the repeat distance decreases, which could be caused by compression of the, now highly flexible, bilayers by the crystalline ice between them.
In order to investigate the structure of a protein-free membrane for higher Q-values, diffraction measurements were performed on IN16. Figure 4.5 a shows a diffraction pattern as function of the temperature and the momentum transfer Q. Three Bragg peaks occur at

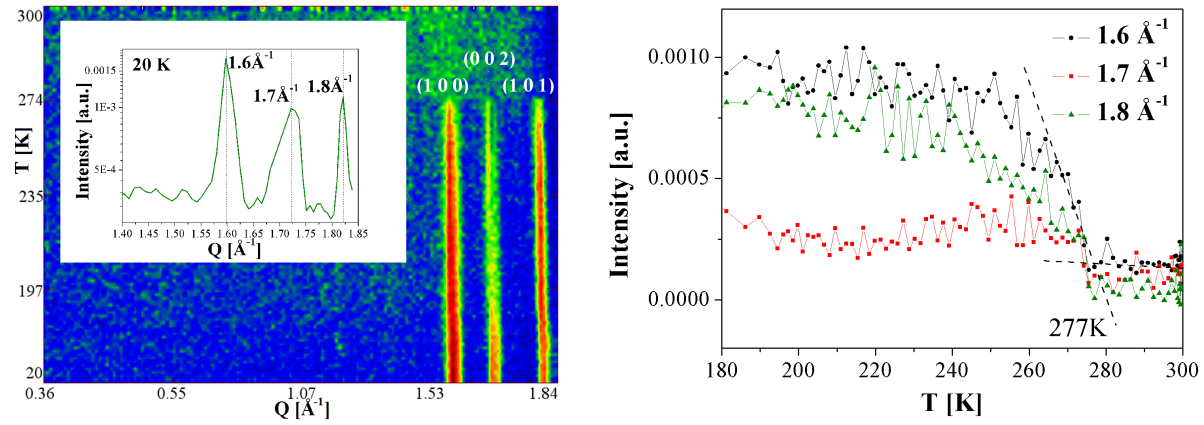

(a) (b)

Figure 4.5: (a) Diffraction patterns obtained on IN16 for a protein-free membrane during heating from 20 K to 300 K. The inset shows the three Bragg peaks obtained at 1.6 $Å^{-1}$, 1.7 $Å^{-1}$ and 1.8 $Å^{-1}$ at 20 K, assigned to crystalline water. (b) Intensity maxima of these ice Bragg peaks as a function of temperature, during heating: at approximately 277 K they are disappeared.

approximately 1.6 $Å^{-1}$, 1.7 $Å^{-1}$ and 1.8 $Å^{-1}$. In Fig. 4.5 b the intensity maxima of these Bragg peaks are plotted as a function of the temperature from 180 K to 300 K. The Bragg peak at 1.6 $Å^{-1}$ is the most pronounced, whereas the Bragg peak at 1.7 $Å^{-1}$ is the least intense. All Bragg peaks are disappeared at the melting point of heavy water at $\approx$ 277 K (the literature value is 276.82 K), which was used to hydrate the membrane. The three peaks can respectively be assigned to the (1 0 0), the (0 0 2) and (1 0 1) orientations of hexagonal ice (ice Ih) which disappear at the water melting point [110, 111, 112, 113]. Since a hexagonal structure is characteristic for bulk water, these findings suggest that not only confined, but also bulk water is present in the membrane [114], which was hydrated at 95 % (see Section 3.2). Crystalline water in confinement would form so-called "cubic ice" (ice Ic) which exhibit the same (1 0 0), (0 0 2) and (1 0 1) reflexes, at 1.6 $Å^{-1}$, 1.7 $Å^{-1}$ and

$1.8\,\text{Å}^{-1}$, respectively, but the second reflex is much more intense than the third, caused by stacking faults, but which is not visible here.
Since structural changes occurring in a protein-free membrane were different during heating and cooling, all temperature dependent EINS measurements, described in the following, were performed using the same temperature protocol, particularly with increasing the temperature. This permitted the measurement of data for all samples under the same experimental conditions.

4.2 Dynamical Properties

In order to determine characteristic molecular dynamics of protein-free lipids, EINS temperature scans and quasielastic measurements were performed. First of all, the general treatment for the data corrections, as performed for such measurements, will be described. In neutron scattering experiments the double differential cross section (Eq. 2.12) is not measured directly, but a quantity related to it. Hence, for the data treatment, some reductions have to be done. First of all, the obtained data has to be normalized to the incident neutron flux, which is measured by the monitor, a low-efficiency detector placed in front of the sample. Furthermore, the experimentally measured spectra have to be corrected for the scattering absorption effects of an empty aluminum sample cell. Therefore, additionally to the sample in a sample cell, a spectrum of an empty aluminum cell has to be measured. Neglecting multiple scattering processes, which is justified by a high transmission of the sample, the theoretical scattering from the sample can be obtained by [77]

$$I^S = \frac{1}{A^S_{S+C}} \left(I^S_{S+C} - \frac{A^C_{S+C}}{A^C_C} I^C_C \right), \tag{4.1}$$

where I^S_{S+C} is the scattering intensity from the sample in the presence of the sample cell and I^C_C is the intensity from the sample cell alone. They can be written as

$$I^S_{S+C} = A^S_{S+C}\, I^C, \tag{4.2}$$

whereas A^S_{S+C} is the attenuation coefficient and I^C the scattering of the cell without attenuation, and

$$I^C_C = A^C_C\, I^C, \tag{4.3}$$

with the attenuation coefficient A^C_C. A^C_{S+C} in Eq. 4.1 is the attenuation factor of the scattering intensity from the cell in presence of the sample, where

$$I^C_{S+C} = A^C_{S+C}\, I^C. \tag{4.4}$$

The evaluation of the three attenuation coefficients can be found in Bée [77].
In addition, the relative detector efficiency has to be provided. This is in general realized by normalization to a spectrum of vanadium, which gives the instrumental resolution function, since its scattering is almost completely incoherent and isotropic, and therefore

Q-independent. For EINS experiments, the scattering signal of the lowest temperature run (20 K) provided this normalization factor and for QENS experiments, the spectra were normalized to a vanadium spectrum. For background corrections, the signal of a cell with four SiO_2 wafers was subtracted from the raw data. All spectra were normalized to the incident neutron flux. Transmission measurements on IN13 indicated a transmission of $\approx 95\,\%$. Therefore, multiple scattering effects could be neglected. The data corrections were performed using the ILL software LAMP [115].
During all EINS and QENS experiments, the membrane samples was oriented at 135° and 45° with respect to the incoming neutron beam, which allowed the study of motions predominantly parallel (in-plane, 135°) and perpendicular (out-of-plane, 45°) to the membrane plane, as illustrated in Fig. 4.6. EINS measurements on the backscattering spectrometer

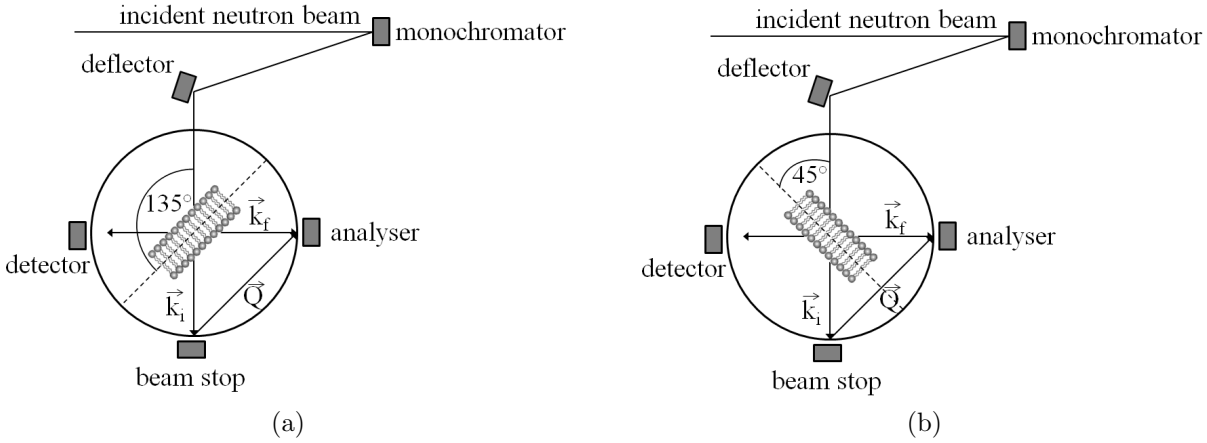

Figure 4.6: Scheme for the two orientations of the membrane samples: (a) In-plane configuration for a bilayer: the sample is oriented at 135° with respect to the incoming beam, the scattering vector $\vec{Q}$ is parallel to the membrane plane and perpendicular to the lipid chains. (b) Out-of-plane configuration: the sample is oriented at 45° and the scattering vector $\vec{Q}$ is perpendicular to the membrane plane and parallel to the lipid chains.

IN13 were performed, varying the temperature across a range of 20 to 300 K with steps of 10 K, in order to cover the gel to liquid phase transitions of the lipids DOPS and DOPC. With an energy resolution of $\Delta E \approx 8\,\mu$eV (FWHM) and an accessible momentum transfer range of $0.2\,\text{Å}^{-1} \leq Q \leq 4.9\,\text{Å}^{-1}$, IN13 allows the investigation of molecular motions in the time-scale of 100 ps and an amplitude from 1.3 Å to 31.4 Å and is thus particularly useful to study molecular motions occurring in biological samples, such as membranes. Each temperature point was measured for two hours in order to obtain a high signal to noise ratio. Figure 4.7 shows an example of the elastic incoherent intensities as a function of the squared momentum transfer for every measured temperature for the lipids. The elastically scattered intensities decrease with increasing temperature and Q-values, as described by the Debye-Waller factor. For low temperatures, the membrane sample behaves harmonically, i. e. thermal motions of the hydrogen atoms are characterized by harmonic vibrations

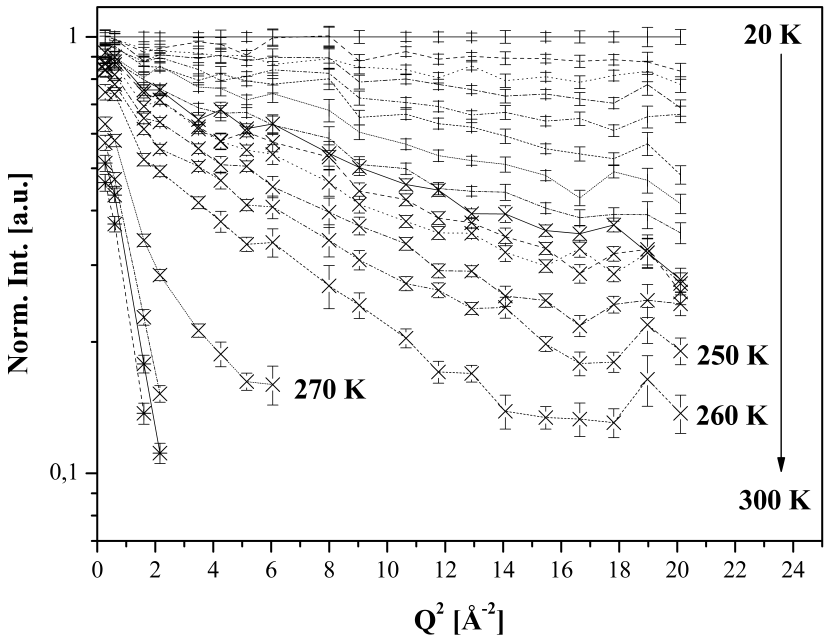

Figure 4.7: Normalized elastic intensities of lipids in out-of-plane configuration as a function of Q^2, obtained on IN13, for every measured temperature point. The temperature was varied from 20 K to 300 K (from top to bottom), with steps of 10 K.

around their equilibrium positions, resulting in a nearly linear decrease of the temperature dependent intensities, due to the enhancement of vibrations. For higher temperatures anharmonic distributions arise. The decrease in the elastic intensity with increasing Q-values (corresponding to smaller distances in the sample, see Eq. 2.61) is caused by the increasing quasielastic contribution, which is typical for non-liquid samples. For small Q-values, the probed distance is much larger than the length-scale in which a proton of the sample moves, and thus the proton appears immobile, resulting in only elastically scattered neutrons at $Q = 0$. With increasing Q-values, the probed distances decrease and the proton appears mobile, yielding quasielastic contributions arising. From 20 K to approximately 260 K the intensity decreases almost regularly. Between 260 K and 270 K, there is a gap due to a very fast decay of the elastic intensity, caused by an abrupt increase of lipid dynamics in the membrane. This increase may be assigned to the completion of the gel-to-liquid phase transitions of DOPS and DOPC lipids (measured by DSC, see Subsection 3.3.3), since the dynamics of lipids in the disordered liquid phase are much higher than in the ordered gel phase. A second gap occurs between 270 K and 280 K, which could be caused by the melting point of the D_2O in the sample. For temperatures higher than 280 K, the slope of the intensities is very high, demonstrating that the dynamics occurring in the sample are too far from the timescale defined by the instrumental resolution of IN13 to be resolved, which is given by the accessible Q-range of IN13 (there are only few detectors at low Q). For clarity, the data points at high Q-values for temperatures larger than 270 K are not

shown, owing to very high experimental noise due to the low scattering intensity.
In Fig. 4.8 a the normalized elastic intensities as function of the temperature, integrated over a Q-range of $0.522\,\text{Å}^{-1} \leq Q \leq 4.485\,\text{Å}^{-1}$, is illustrated for the in-plane configuration of the lipids.

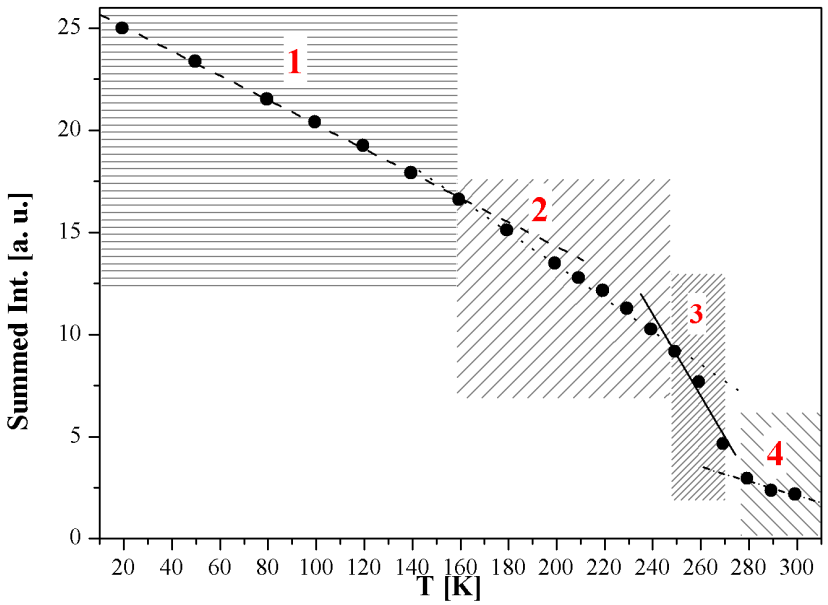

(a)

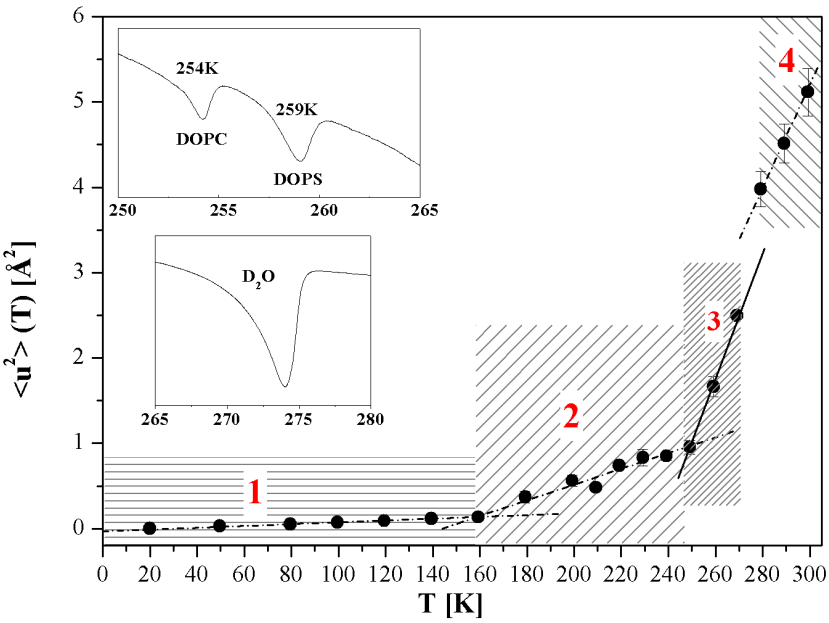

(b)

Figure 4.8: (a) Temperature dependent normalized elastic intensities of the lipids in the in-plane configuration integrated over a Q-range of $0.522\,\text{Å}^{-1} \leq Q \leq 4.485\,\text{Å}^{-1}$. (b) The corresponding MSDs as function of the temperature. Insets: DSC spectra showing the phase transitions of the lipids (top) and of the water between the bilayers (bottom) (see Subsection 3.3.3).

The Q-range was chosen in order to eliminate the Bragg peaks caused by the repeat distance characteristic for a DOPS-DOPC membrane, occurring between $Q = 0.106\,\text{Å}^{-1}$ and $Q = 0.118\,\text{Å}^{-1}$ during heating, as measured on D16 by diffraction (see Table 4.2). Although the ice Bragg peaks were detected on IN16 at $Q = 1.6\,\text{Å}^{-1}$, $Q = 1.7\,\text{Å}^{-1}$ and $Q = 1.8\,\text{Å}^{-1}$, they were not visible on IN13, which could be caused by their relatively low intensities with respect to the Bragg peaks of the bilayers (see Figs. 4.5 and 4.4). To describe the intra-molecular dynamics, the MSDs $\langle u^2 \rangle(T)$ have been calculated for every measured temperature by linear regression in a semi-logarithmic plot of the scattering intensities as a function of Q^2, using Eq. 2.39. For high temperatures the Gaussian approximation was not valid using the first Q-values. A Q-range of $0.27\,\text{Å}^{-2} \leq \text{Q}^2 \leq 2.17\,\text{Å}^{-2}$ was chosen for the fitting, where the Gaussian approximation was valid below the phase transitions of the lipids. The resulting MSDs for the in-plane configuration of the lipids are shown in Fig. 4.8 b. A deviation of the linear trend of the elastic intensity and of the corresponding MSDs indicates a change in the membrane dynamics. Therefore, the curve of the elastic intensity and of the MSDs were characterized by four different regions, enumerated in the figures from 1 to 4.

In region 1, at low temperature from about 20 K to 160 K, the system shows a harmonic behavior, where thermal motions of the hydrogen atoms are characterized by harmonic vibrations around their equilibrium positions. This leads to a nearly linear dependence of the elastic scattering intensity to the temperature. At approximately 160 K, the slope of the elastic intensity and the MSDs increases, indicating that a transition from the harmonic regime (1) to a anharmonic regime (2) occurs. In contrast, for data obtained in out-of-plane configuration, the lipids show a harmonic behavior up to ≈ 200 K (shown in Chapter 5).

In region 2, ranging from about 160 K to 250 K, the protons in the sample are no longer vibrating harmonically around single equilibrium positions, but new degrees of freedom are acquired [116, 117]. Similar behavior has previously been found by other research groups by EINS measurements on purple membranes [118, 119, 120] and proteins [121, 122] at ≈ 150 K. This transition has been attributed to methyl group (CH_3-molecules) rotations entering in the experimental time-window of the instrument, which was independent of the hydration level of the samples.

At approximately 250 K a second, more distinct, inflection arises, yielding region 3 from about 250 K to 270 K. In this regime, the intensities decrease and the MSDs increase strongly, indicating a fast enhancement of the membrane dynamics. DSC measurements (see Subsection 3.3.3), shown in the upper inset in Fig. 4.8 b, suggest that this transition is caused by the gel-to-liquid phase transitions of the lipids DOPC ($T_c = 254$ K) and DOPS ($T_c = 259$ K). These phase transitions occur in a very restricted temperature region between 250 K and 270 K and, due to the lack of experimental points in this temperature range, they cannot be separated in this EINS study. The transition of the heavy water molecules between the bilayers (the hydration of the membranes is 95% using D_2O, see Section 3.2) is outside this regime at approximately 277 K, as seen with IN16 (in the DSC spectrum in the lower inset in Fig. 4.8 b, the melting point is shifted to 274 K, due to

H-D-exchange, as described in Subsection 3.3.3). Since between around 270 K and 280 K no data was recorded, the water phase transition cannot be resolved.
For temperatures above 280 K (region 4), the temperature dependent elastic intensity (Fig. 4.8 a) is almost flat, which corresponds to the very fast decrease of the elastic intensities as a function of Q in Fig. 4.7 and to the high error bars in the MSDs. Due to the liquid D_2O the dynamics are too far from the timescale defined by the instrumental resolution to be visible in the accessible length-scale. Therefore, complementary neutron scattering experiments on instruments with a smaller energy resolution and accessible smaller Q-values would be necessary, in order to investigate membrane dynamics at temperatures higher than 280 K.
In order to investigate characteristic molecular motions of DOPS-DOPC lipids occurring in the interesting temperature region between 250 K and 280 K (region 3) in more detail, an elastic temperature scan was carried out on the backscattering spectrometer IN16. A Q-range from $0.19\,\text{Å}^{-1}$ to $1.89\,\text{Å}^{-1}$ and an energy resolution of $0.9\,\mu$eV allowed the investigation of motions occurring on a length-scale from approximately 3.3 Å to 33 Å and on a timescale of about 1 ns. The temperature was increased with a rate of 0.3 K/min, which allowed an accurate investigation of the temperature region between 250 K and 280 K, and the data was stored every 5 minutes.
Figure 4.9 a illustrates the incoherent elastic intensity as function of the temperature.

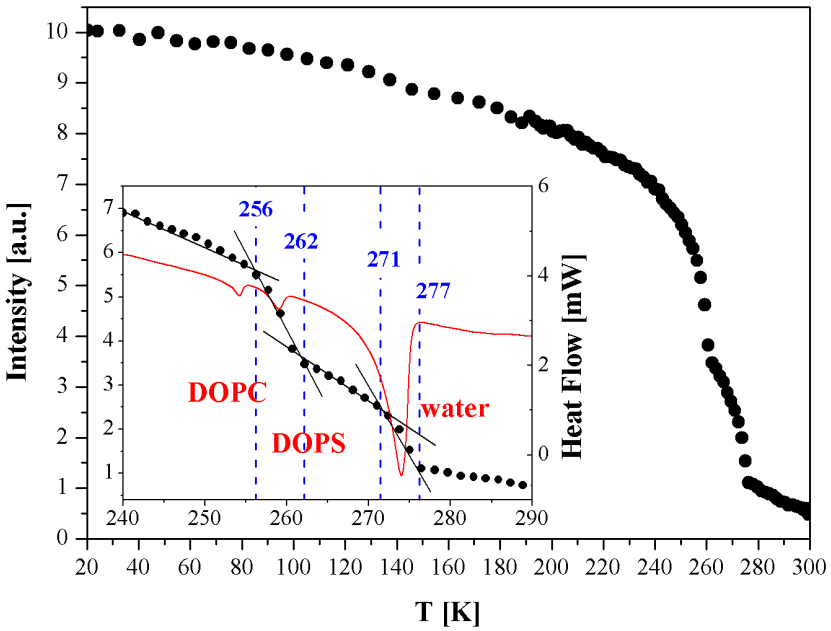

(a)

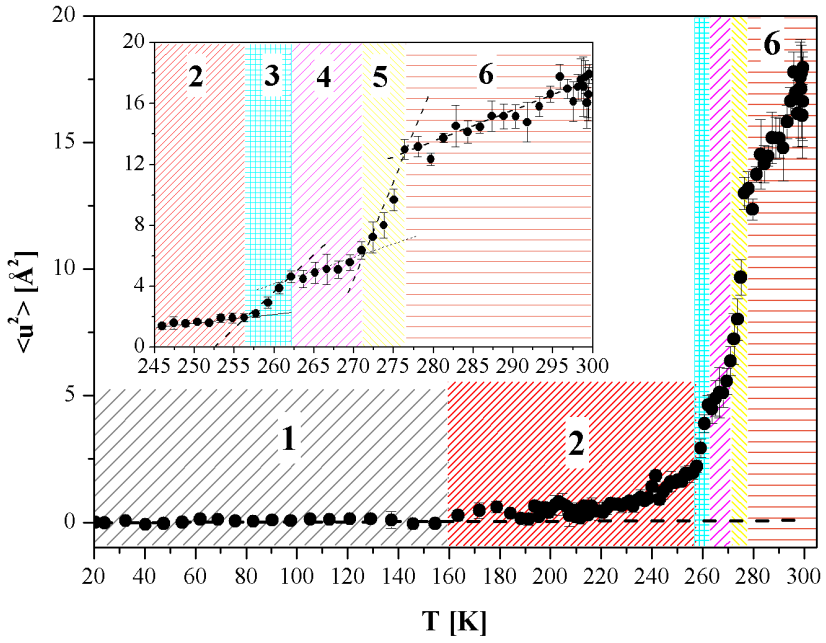

(b)

Figure 4.9: (a) Temperature dependent normalized elastic intensities of the lipids integrated over a Q-range of $0.45\,\text{Å}^{-1} \leq Q \leq 1.49\,\text{Å}^{-1}$ for the in-plane configuration. A magnification of the intensities for a temperature ranging from about 240 K to 290 K is shown in the inset and compared to a DSC spectrum. (b) The corresponding MSDs with a magnification for the regions 3 to 6 shown in the inset.

The intensity was summed over a Q-range of $0.45\,\text{Å}^{-1} \leq Q \leq 1.49\,\text{Å}^{-1}$, which excludes the Q-value of the first detector, in order to avoid Bragg peaks from the membrane, and the Q-values of the Bragg peaks at $1.6\,\text{Å}^{-1}$, $1.7\,\text{Å}^{-1}$ and $1.8\,\text{Å}^{-1}$, arising from crystalline ice. The inset shows a magnification of the plot in the temperature region from approximately 240 K to 290 K, together with a DSC spectrum measured for this sample. The number of data points in this temperature region are much higher for this EINS study on IN16 than for the previous experiment performed on IN13. Hence, the main phase transitions of the lipids DOPC and DOPS, respectively, and the phase transition of the water in the bilayers can be separated. The MSDs $\langle u^2 \rangle(T)$ have been calculated for every measured temperature by fitting Eq. 2.39 to the scattering intensities as a function of Q^2, using a Q-range of $0.19\,\text{Å}^{-2} \leq \text{Q}^2 \leq 0.91\,\text{Å}^{-2}$. In Fig. 4.9 b the MSDs as function of the temperature are shown. The curve can be divided into six different regimes (numbered 1 to 6), in which changes in the membrane dynamics occur, indicated by deviation of the linear trend of the MSDs (and of the elastic intensity as function of the temperature). The inset illustrates a magnification of the regions 3 to 6, in order to clarify the changes in membrane dynamics in this temperature range.

In the low temperature region, from approximately 20 K to 160 K (regime 1), the membrane shows a harmonic behavior, as previously observed on IN13. A first kink in the MSDs occurs at ≈ 160 K, indicating a transition from the harmonic to an anharmonic regime (2), which was also found by EINS measurements on IN13 and which was attributed to rotational motions of the methyl groups in the lipid chains and in the proteins. A further transition from region 2 to region 3 occurs at ≈ 256 K, which is the temperature at which the gel-to-liquid phase transition of DOPC lipids is completed, indicated by the DSC spectrum (shown in the inset in Fig. 4.9). Regime 3 ranges from ≈ 256 K to ≈ 262 K, in which the phase transition of DOPS lipids occurs, as shown by the DSC data. At ≈ 262 K, where this phase transition is completed, the slope of the MSDs declines (regime 4), indicating that the system relaxes in an equilibrium state in the liquid-disordered phase. At ≈ 271 K the slope of the curve increases again, which is probably caused by the melting of the ice within the bilayers. This coherency is shown with the DSC spectrum, which indicates that the water peak is very large and that the heat flow already starts to decrease at this temperature. As mentioned above, D_2O was used for the hydration of the bilayers, whose freezing point is slightly larger than the freezing point of H_2O, namely ≈ 276 K, but which was slightly shifted in the DSC spectrum. Region 5 ranges from ≈ 271 K to ≈ 277 K, which seems to be the temperature region, in which all of the ice contained in the multilayers melt. For $T \geq 277$ K, this phase transition is complete, as already shown with diffraction data, and all membrane components are in their liquid, disordered phase (region 6).

With these EINS measurements performed on IN16 and recorded with a temperature rate of 0.3 K/min, the temperature region 3 of the measurements obtained on IN13 (see Fig. 4.8), in which the phase transitions of the lipids and of the water occur, could now be described by three regions (3 to 5, see Fig. 4.9) and studied in further detail.

A scientific paper about further studies performed on IN16, including EINS scans with decreasing temperature and simultaneous diffraction, indicating a hysteresis of the elastically

scattered intensities, is under progress, but will not be discussed in this work.
In order to investigate molecular motions of the lipids occurring in a very broad time domain, QENS experiments were carried out on the time-of-flight spectrometers IN5, Osiris and Neat with energy resolutions of 12 (corresponding to $\Delta t = 30\,\mathrm{ps}$), 100 ($\Delta t = 10\,\mathrm{ps}$) and 216 μeV ($\Delta t = 1\,\mathrm{ps}$), respectively. With Q-regions ranging from $0.24\,\mathrm{\AA}^{-1}$ to $1.14\,\mathrm{\AA}^{-1}$ for IN5, from $0.60\,\mathrm{\AA}^{-1}$ to $3.52\,\mathrm{\AA}^{-1}$ for Osiris and from $0.37\,\mathrm{\AA}^{-1}$ to $2.26\,\mathrm{\AA}^{-1}$ for Neat, it was possible to identify membrane dynamics of different length scales. Measurements were performed at 230 K and 300 K, which correspond to the gel and to the liquid phase of the phospholipids, and the samples were oriented in the in-plane and the out-of-plane configuration. For correction purposes, a cell with four SiO_2 wafers, a vanadium sample and an empty cell were measured at 300 K.
Data corrections were performed using ILL software LAMP for IN5 data [115], ISIS software MODES for Osiris data [123] and HZB software FITMO [124] for Neat data, taking into account the transmission of each sample (measured on IN13, see above). The time-of-flight spectra were normalized to the scattering signal of vanadium and the time-of-flight was transformed into energy transfer, using Eq. 2.65. The Q-values for the membrane Bragg peaks, as well as the Q-values containing the shadow of the sample holder present at the out-of-plane configuration, were excluded. Ice Bragg peaks were not visible.
With D_2O as the solvent and a low protein content in the membrane, this quasielastic study gives information about the dynamics of hydrogen atoms belonging to the lipids. To investigate these dynamics, a model function, described by Eq. 2.46 for data obtained at 300 K and by Eq. 2.47 for data obtained at 230 K, was used to fit the measured scattering functions. A detailed description of this model can be found in Section 2.2.3. In the following, $S_{V1}(\vec{Q},\omega)$ will be called Volino 1, $S_{V2}(\vec{Q},\omega)$ Volino 2 and $S_{Jump}(\vec{Q},\omega)$ 2-site jump diffusion. The resolution function $S_{Res}(\vec{Q},\omega)$ was given by the vanadium spectrum, where a Gaussian function was used to fit the vanadium data of IN5 and Neat and both a Gaussian and a Lorentzian function were needed to fit the vanadium data of Osiris, due to a very asymmetric resolution function.
The fitting of the spectra was performed using a program developed by Gerelli *et al.* [86], as described in Subsection 2.2.3. Since this routine was written for the use of two instruments, the fitting procedure was performed as follows: for 300 K data, IN5 and Osiris data were first fitted. Then, Osiris and Neat data were fitted with fixed parameters of Volino 1, which were obtained from the first fit. At the last step, IN5 and Osiris data were re-fitted, fixing parameters of Volino 1, Volino 2 and the 2-sites jump diffusion. The additional Lorentzian was adjusted in the last step by fitting the first four Q-groups of Neat-data with fixed parameters for Volino 1, Volino 2 and the 2-site jump diffusion. Since the resulting values of the HWHM of this Lorentzian Γ were very similar to the HWHM of the jump diffusion (which is $2/\tau$), Γ was finally fixed to $2/\tau$. Therefore, the Lorentzian could describe a rotational motion that is not included within this model. The pre-factors f, p_{V1}, p_{V2} and p_{Jump} were not the same for all instruments, since the model is an average description of the main motions, but does not contain information about all components present in the system, for example water. Hence, scattering intensities arising from some

of these components are considered negligible when analyzing the data of the single instruments, but they lead to differences when fitting all the instruments together.
In the case of data obtained at 230 K it was possible to fit the spectra obtained on all three instruments simultaneously. Since at 230 K some molecular motions are frozen, and considered elastic for all the instruments, it was possible to use the same weights f and $p_{V\otimes Rot}$ for all instruments, and thus the free parameters were reduced.
Figure 4.10 shows quasielastic spectra of the lipids measured on IN5 at 230 K (blue symbols) and at 300 K (red symbols) for the in-plane configuration. The intensities are normalized

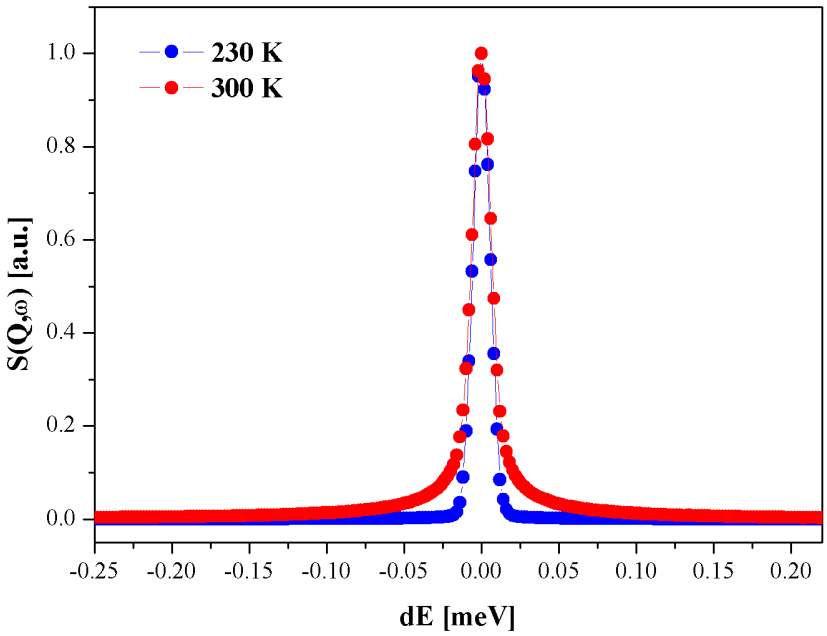

Figure 4.10: QENS spectra of the lipids measured on IN5. Data are shown for 230 K (blue symbols) and 300 K (red symbols) for the in-plane configuration. The normalized intensities were integrated over the whole accessible Q-range.

and integrated over the whole accessible Q-range. It is clearly visible that the quasielastic contribution for data obtained at 300 K is much larger with respect to data recorded at 230 K, indicating a highly dynamic membrane in the liquid phase.
An example for the fitting of the model function, described above, to spectra obtained at 300 K in the out-of-plane configuration for the three instruments at similar Q-values is illustrated in Fig. 4.11.

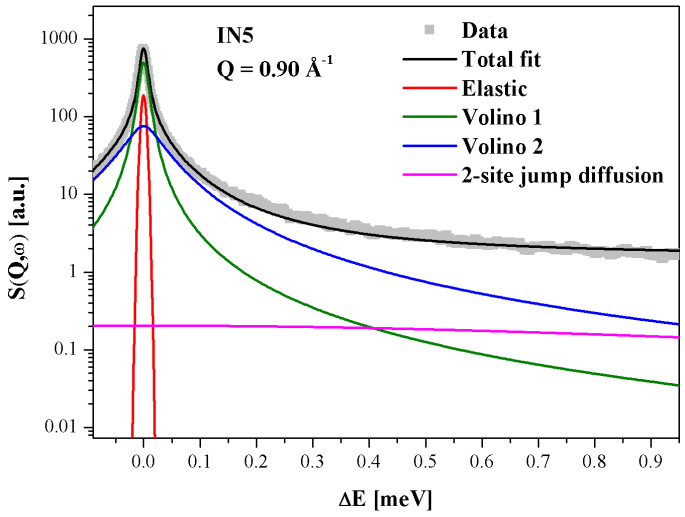

(a)

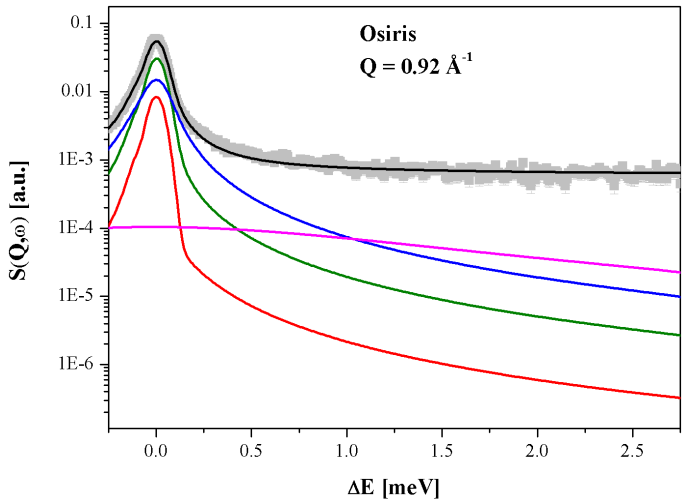

(b)

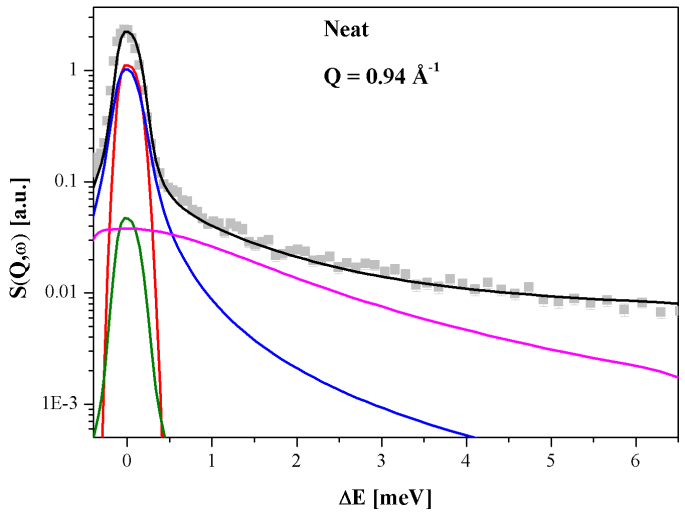

(c)

Figure 4.11: Normalized QENS data for the lipids in out-of-plane configuration at 300 K, fitted using a model containing two Volino functions and a function describing 2-sites jump diffusion for $Q \approx 0.9\,\text{Å}^{-1}$. Top: IN5-data; middle: Osiris-data; bottom: Neat-data.

The hydrogen fraction p_{Jump} performing 2-sites jump diffusion (represented by the pink curve) was visible only on Neat with a large energy resolution of $\Delta E = 216\mu$eV and occurred as background on IN5 and Osiris. In contrast, the fraction p_{V1}, which diffuses in a confined spherical volume of radius R_{V1} was detectable on IN5 and Osiris, but moves too slowly to be resolved by the energy resolution of Neat, where it appears inside the elastic peak.
Figure 4.12 shows an example for the fitting of the first spectra obtained for the lipids in the out-of-plane configuration on Neat, in order to show the importance of the additional Lorentzian. The additional Lorentzian (light blue curve), which has the same shape as the

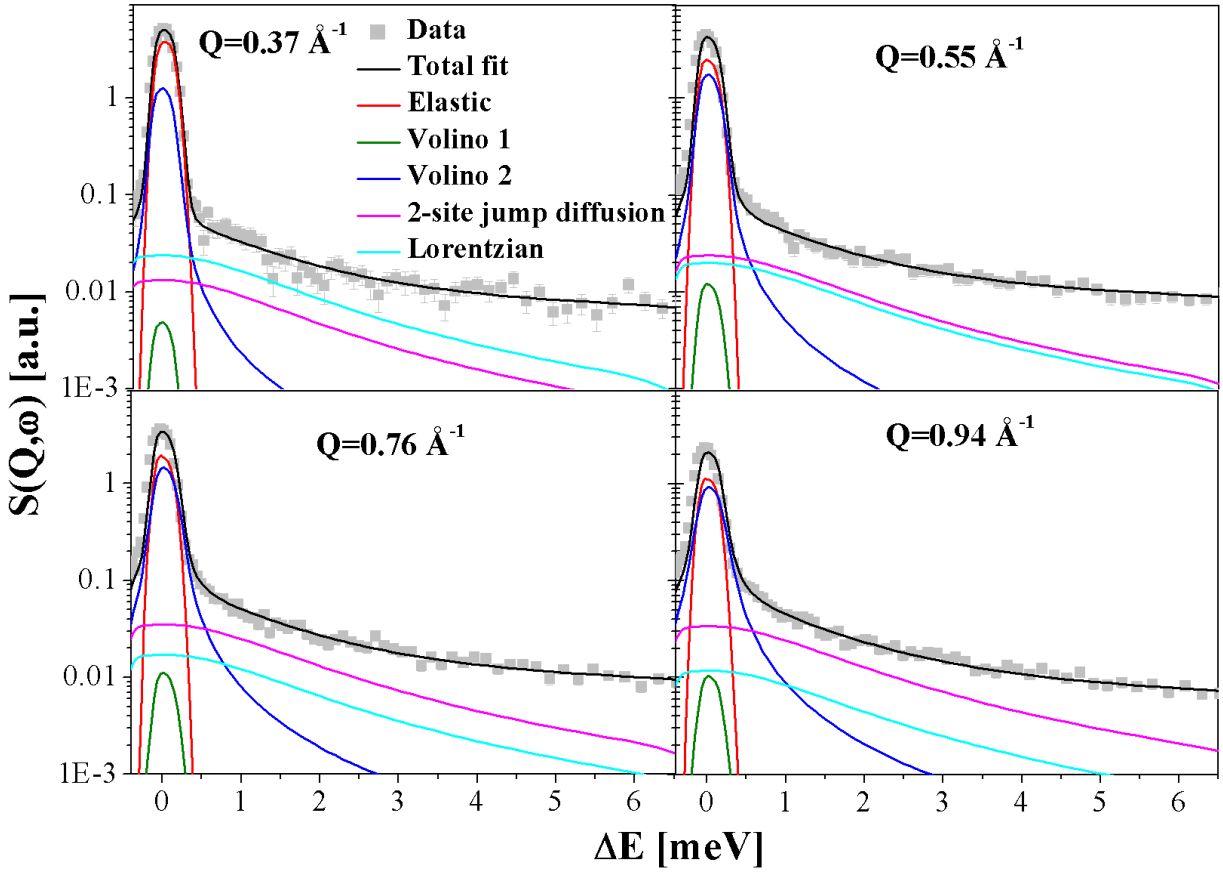

Figure 4.12: Normalized QENS data for the lipids in out-of-plane configuration obtained on Neat. Data were fitted to a model containing two Volino functions, a function describing 2-sites jump diffusion and a Lorentzian, which is constant in Q and has the same HWHM as the jump diffusion component, for $Q = 0.37\,\text{Å}^{-1}$ (top left), $Q = 0.55\,\text{Å}^{-1}$ (top right), $Q = 0.76\,\text{Å}^{-1}$ (bottom left) and $Q = 0.94\,\text{Å}^{-1}$ (bottom right).

2-site jump diffusion component $S_{Jump}(\vec{Q},\omega)$ (pink curve), is present in the first spectra for $Q = 0.37\,\text{Å}^{-1}$ to $Q = 0.76\,\text{Å}^{-1}$. For Q-values larger than $0.76\,\text{Å}^{-1}$, the Lorentzian is smaller than $S_{Jump}(\vec{Q},\omega)$ and becomes negligible. It seems that the Lorentzian describes

a motion occurring on a picosecond timescale and on a length-scale of $\approx 10\,\text{Å}$, which is similar to the 2-sites jump diffusion $S_{Jump}(\vec{Q},\omega)$. The model, applied here to describe the data, is a very good approximation. The meaning of the Lorentzian, which contributes only a little, is not clear yet. To investigate this motion occurring on a large length-scale (and a small Q-range), experiments on instruments with a similar energy resolution ($\approx 216\,\mu$eV) and a higher spatial resolution for low Q-values would have to be performed.
The type of dynamics described by the model has already been found in lipid-membranes using quasielastic neutron scattering [125, 86, 71, 126, 127, 128], NMR studies [129] and molecular dynamics simulations [130]. Brown *et al.* [129] have carried out NMR studies on 1,2-dipalmitoyl-*sn*-glycero-3-phosphocholine (DPPC) and DOPC multilayers as well as on DPPC vesicles, to investigate spin lattice relaxation rates $1\,/\,T_1$. The relaxation time T_1 is the time for the return of the spin from the excited to the equilibrium state and characterizes internal lipid chain dynamics and molecular reorientations of the chain methylenes, occurring on a pico- to nanosecond timescale. These reorientations arise from molecular rotational diffusion or from internal dynamics as torsional isomerization between *gauche* and *trans* conformation. Molecular dynamics simulations indicate that the *trans-gauche* isomerizations occur on a timescale of tens of picoseconds in the lipid chains and slow down closer towards the lipid headgroups (timescale of a few 100 picoseconds) [131]. $1\,/\,T_1$ relaxation rates as a function of the position along the DPPC lipid chains were found to be constant for the third to the 9th carbon with a frequency of $\approx 10^{10}\,\text{Hz}$ and to increase from the 9th to the 15th carbon. This effect was the same for DPPC multilayers and vesicles. Pitman *et al.* [130] have performed molecular dynamics simulations for $1\,/\,T_1$ relaxation rates as function of the carbon positions along the oleic chain of DOPC, based on the results of Brown *et al.*, which confirmed those results: the relaxation rate was found to be constant from the first to the 8th carbon and to increase from the 11th to the 17th carbon. At the double bond of the vinyl group, which is between the 9th and 10th carbon for DOPC, the relaxation was slower. This indicated that the spin lattice relaxation rates are strongly affected by unsaturation.
Based on these observations, it appears that the first part of oleic lipid chains in a bilayer undergoes motions with approximately constant relaxation times, which become faster in the terminal part of the chains. The slow confined diffusion carried out by p_{V1} (Volino 1) is assigned to the upper part of the lipids (including the lipid head groups and the double bond of the vinyl group) and the fast confined diffusion executed by p_{V2} (Volino 2) to the terminal part of the lipids, from the last methylene group until the double bond. The resulting fitting parameters are listed in Tables 4.3 and 4.4.
The fraction of immobile hydrogen atoms is zero, within the errors, for both the in-plane and the out-of-plane configurations (for all instruments), indicating that the membrane is highly dynamic. The hydrogen fraction p_{V1}, belonging to the upper part of the lipids, is with 0.59 (obtained on IN5, which is the most sensible for this contribution) approximately 10 % larger for the in-plane configuration than for the out-of-plane configuration, suggesting that more hydrogen atoms diffuse in a confinement perpendicular to the lipid chains than parallel. The hydrogen fraction p_{V2}, undergoing confined diffusion in the terminal part of the lipid chains, is nearly the same for both configurations. The corresponding

Sample 300 K	R_{V1} [Å]	D_{V1} [cm^2/s 10^{-5}]	R_{V2} [Å]	D_{V2} [cm^2/s 10^{-5}]	d [Å]	τ [meV^{-1}]	Γ [meV]
lipids, out-of-plane	6	0.15	7	1.1	2.5	1.36	1.47
lipids, in-plane	4	0.16	5	1.8	2.5	0.93	2.15

Table 4.3: Fitting parameters for data obtained at 300 K with the following absolute errors: $\Delta D_{V1} \approx \pm 0.01\,10^{-5}$cm^2/s, $\Delta D_{V2} \approx \pm 0.1\,10^{-5}$cm^2/s, $\Delta R_{V1} \approx \Delta R_{V2} \approx \pm 1$ Å, $\Delta d \approx \pm 0.5$ Å, $\Delta\tau \approx \pm 0.01$ meV^{-1} and $\Delta\Gamma \approx \pm 0.05$ meV.

Sample 300 K	p_{V1}	p_{V2}	p_{Jump}	f	p_{Lor}
lipids, out-of-plane	0.49;0.45;0.03	0.40;0.40;0.44	0.11;0.15;0.53	0;0;0	0;0;0.09
lipids, in-plane	0.59;0.37;0.15	0.41;0.35;0.42	0.00;0.22;0.43	0;0.06;0	0;0;0.08

Table 4.4: Fitting parameters obtained for hydrogen populations p_{V1} , p_{V2}, p_{Jump} and f and for fraction of the Lorentzian p_{Lor} for data measured at 300 K for all instruments. The absolute errors are ≈ 0.05 for all parameters. The first values are for parameters obtained for IN5, the second values for parameters obtained for Osiris and the third values for parameters obtained for Neat, respectively.

diffusion constants D_{V1} and D_{V2} differ by one order of magnitude for all membrane samples. This tendency has also been observed from QENS studies by Gerelli and co-workers [86] for slow and fast diffusive motions in confinement, occurring in liposomes made of 1-palmitoyl-2-oleoyl-*sn*-glycero-3-phosphocholine (POPC) and 1,2-dimyristoyl-*sn*-glycero-3-phospho-L-serine (DMPS) in the liquid phase of the lipids (300 K). The slow motion has been attributed to hydrogens in the lipid headgroups and the initial part of the lipid chains and the fast motion to hydrogens belonging to the end part of the chains. However, the diffusion constants were both one order of magnitude smaller than the diffusion constants D_{V1} and D_{V2}. Regarding the membrane orientations, both confined diffusions are faster in the in-plane configuration, i.e. perpendicular to the lipid chains, than in the out-of–plane configuration, i.e. parallel to the lipid chains.
The radii of confinement R_{V1} and R_{V2} are approximately 5 Å, according to the radii found by the work of Gerelli and co-workers. Similar values were determined by Doxastakis *et al.* [128] using QENS techniques and molecular simulations on freeze-dried head-deuterated DPPC liposomes at different temperatures in the liquid phase of the lipids.
For the 2-site jump diffusion, jump distances d of approximately (2.5 ± 0.5) Å were obtained. Since the distance between the hydrogen atoms of CH_2 groups (methylene) in the lipid chains is ≈ 1.8 Å (with a C-H bond length of ≈ 1.1 Å and a bond angle of 102°), the fraction p_{Jump} can be assigned to these hydrogens. This 2-site jump process of the methylene groups was already found by others using quasielastic neutron scattering on oriented membranes and was explained by isomerization between *gauche* and *trans* conformations of CH_2 [86]. In contrast to the hydrogen populations p_{V1} and p_{V2}, which are larger in the

in-plane configuration, the contribution p_{Jump} is, with approximately 10 %, larger in the out-of-plane configuration than in the in-plane configuration, obtained on Neat and IN5. For Osiris the contribution is the same, within the error bars, for both configurations. A schematical representation of the model describing data of a DOPS-DOPC membrane in the liquid phase is shown in Fig. 4.13.

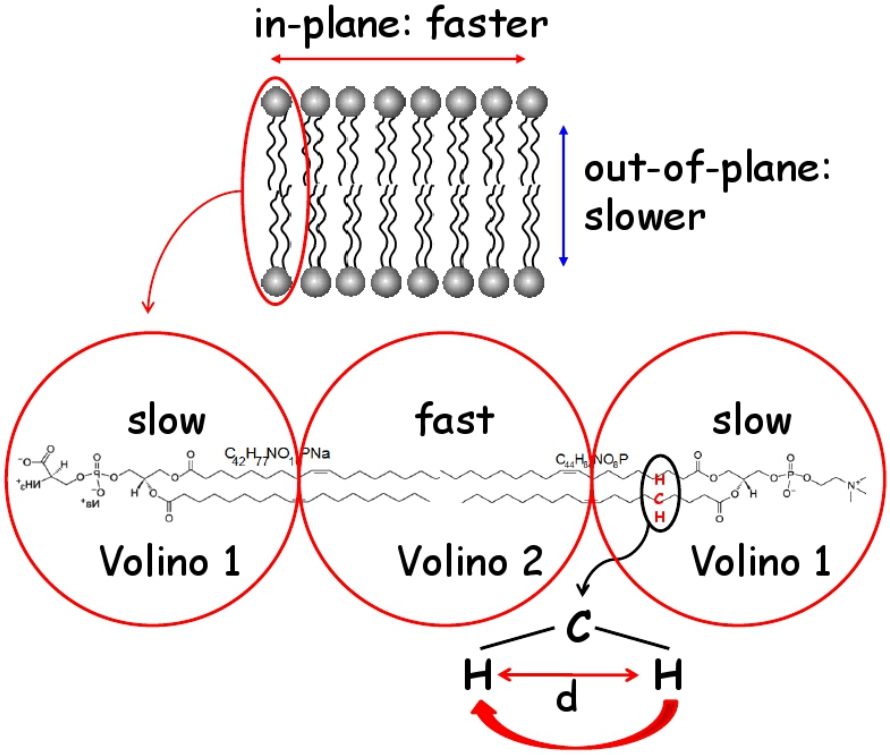

Figure 4.13: Schematic illustration of the model applied to quasielastic data of a DOPS-DOPC membrane in the liquid phase. Based on NMR studies and molecular dynamics simulations, Volino 1 could be assigned to the first part of the lipid chains, including the lipid headgroups and the double bond, and Volino 2 to the terminal part of the chains, both with a radius of confinement of $R_V \approx 5\,\text{Å}$. The 2-site jump diffusion could be attributed to the H-atoms of the methylene groups, with jump distances of $d \approx 1.8\,\text{Å}$.

When regarding now the resulting fitting parameters for data obtained at 230 K (see Table 4.5), it is obvious that, in contrast to the data obtained at 300 K, the elastic contribution f of the scattering function is very high and the quasielastic contribution $p_{V\otimes Rot}$ accounts for only $\approx 10\,\%$. Nevertheless, within the 10 % of the hydrogen fraction that performs diffusion

Sample 230 K	R_V [Å]	D_V [$\mathrm{cm^2/s}$ 10^{-5}]	R [Å]	τ [$\mathrm{meV^{-1}}$]	f	$p_{V\otimes Rot}$
lipids, out-of-plane	6	0.10	1.1	6.65	0.91	0.10
lipids, in-plane	3	0.68	1.2	2.03	0.92	0.08

Table 4.5: Fitting parameters for data obtained at 230 K for the lipids in in-plane and out-of-plane configuration. The absolute errors are $\Delta R_{V1} \approx \pm 1$ Å, $\Delta D_V \approx \pm 0.01\,\mathrm{cm^2/s}$, $\Delta R \approx \pm 0.5$ Å, $\Delta\tau \approx \pm 0.01\,\mathrm{meV^{-1}}$ and $\Delta f \approx \Delta p_{V1\otimes Rot} \approx 0.05$.

in confinement and simultaneously rotates isotropically, the radius of confinement is in the out-of-plane configuration with 6 Å larger than in the in-plane configuration (3 Å). The radii of rotation are approximately 1.1 Å, for both configurations, and can be attributed the the C-H bond length of the methylene groups in the lipid chains. This suggests that in the gel phase of the lipids, the energy for the methylene groups is probably not high enough to perform jumps around two sides, but sufficient to rotate isotropically.

4.3 Influence of the Protein Buffer

Due to the sample preparation protocol (see Section 3.2), the protein buffer (HEPES and NaCl) concentration is relatively high with respect to the protein concentration in the membrane samples, containing MBP-C1 and P2 proteins, in particular the concentration of NaCl. Detailed buffer concentrations are listed in Table 3.1 in Chapter 3. Therefore, any possible influence of the buffer on membrane dynamics was investigated. Quasielastic measurements were performed on DOPS-DOPC-membranes containing 1-fold (1f-lipids) and 2-fold buffer (2f-lipids) and a buffer-free membrane (lipids) on the time-of-flight spectrometer Neat and the spectra of all samples for each configuration and temperature are compared. The experiments were carried out with an energy resolution of 216 μeV and a Q-range from 0.37 $\mathrm{Å^{-1}}$ to 2.26 $\mathrm{Å^{-1}}$. The lipids, the 1f-lipids and the 2f-lipids were measured at 230 K and 300 K for the in-plane and for the out-of-plane configuration. For data obtained in the liquid phase (300 K) and in the gel phase (230 K) of the lipids no significant differences between the spectra are visible at this energy resolution, for both configurations. Fig. 4.14 shows the quasielastic spectra of all samples measured at 300 K and at 45° configuration, normalized and integrated over the whole accessible $Q-$range. Any effect of the protein buffer on the membrane dynamics at these buffer concentrations and at this instrumental resolution or rather on this timescale, can be excluded and the results of experiments on membranes containing MBP-C1 and P2 proteins can be compared to the results of the protein- and buffer-free lipids. Since only Neat was sensitive to 2-site jump

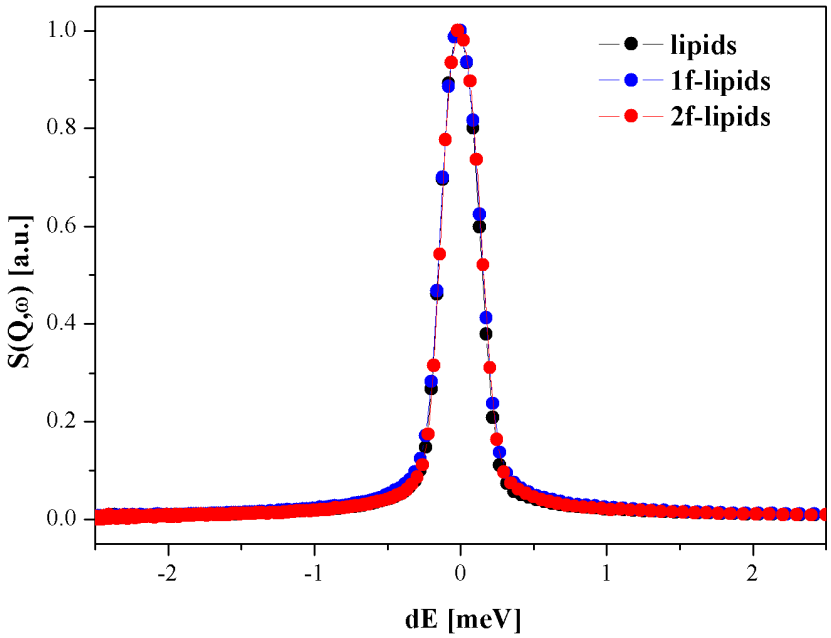

Figure 4.14: QENS spectra of lipids (black circles), 1f-lipids (blue circles) and 2f-lipids (red circles) measured on Neat at 300 K for the out-of-plane configuration. The intensities were normalized and integrated over the whole accessible Q-range.

diffusion, as shown in Fig. 4.11, this type of molecular motion will not be influenced by the buffer. However, this does not exclude neither any influence of the buffer on membrane dynamics occurring on other timescales nor any influence of the protein buffer at higher concentrations. Since DOPS-DOPC membranes containing MBP-C1 and MBP-C8, at a 4-fold and a 9-fold protein (and therefore protein buffer-) concentration, respectively, are investigated using quasielastic neutron scattering techniques (see Chapter 6), the same experiments were performed on protein-free membranes containing 4-fold (4f-lipids) and 9-fold (9f-lipids) protein buffer concentrations and will be used as references. The results obtained for the 4f-lipids and the 9f-lipids will be compared with the results obtained for the lipids, described in Section 4.2, in order to investigate any influence of the protein buffer at those high concentrations. The experiments were caried out on IN5, at energy resolutions Δ E of $\approx 12\,\mu$eV (corresponding to a wavelength of 10 Å) and $75\,\mu$eV (corresponding to a wavelength of 5 Å), in order to investigate membrane dynamics on timescales of ≈ 20 ps and ≈ 4 ps, respectively (ΔE is here FWHM). Since the momentum transfer Q ranged from 0.23 Å^{-1} to 1.14 Å^{-1} for IN5 at ΔE $\approx 12\,\mu$eV and from 0.27 Å^{-1} to 2.23 Å^{-1} for IN5 at ΔE $\approx 75\,\mu$eV, dynamics occurring on different length-scales were studied. The samples were measured in the liquid phase of the lipids, at 300 K, in the in-plane and in the out-of-plane configuration. Since the membranes were measured at 300 K, any Bragg peaks arising from crystalline ice were not present.
In order to verify the reproducibility of the data, further experiments were performed on

IN6 with approximately the same energy resolution and wavelength as on IN5 (Δ E was $\approx 78\,\mu$eV, FWHM, and the wavelength 5.12 Å). The analysis of those data gave the same results, which confirmed their reproducibility and which guaranteed the absence of any experimental artifacts. Hence, only results obtained on IN5 will be discussed here.
The same model scattering function, $S^{300K}_{theo}(\vec{Q},\omega)$, Eq. 2.46, as applied to the lipids measured on IN5, Osiris and Neat, was used to describe the quasielastic spectra. Also an additional Lorentzian, which was constant in Q and describes a motion occurring in a timescale of ≈ 20 ps and a length-scale of ≈ 10 Å, had to be added for data obtained on IN5 with the larger energy resolution (ΔE $\approx 75\,\mu$eV), for Q-values up to ≈ 0.75 Å^{-1}. The model $S^{300K}_{theo}(\vec{Q},\omega)$ was used to simultaneously fit all spectra of different Q-values obtained on IN5 at the two different energy resolutions. First, all spectra besides the first four spectra of IN5 data with ΔE $\approx 75\,\mu$eV, were fitted, without using the additional Lorentzian. Then, these four spectra, where the additional Lorentzian was needed, were fitted individually with fixed fitting parameters for Volino 1, Volino 2 and the 2-site-jump diffusion obtained from the first fitting, and with free parameters for the Lorentzian. The resulting fitting parameters for the HWHM Γ of the Lorentzian were very similar to the HWHM of the 2-site jump diffusion component $S_{Jump}(\vec{Q},\omega)$, as already been found for the lipids. Therefore, Γ was fixed to the HWMH of $S_{Jump}(\vec{Q},\omega)$, and all spectra were finally fitted, for verification, with fixed parameters R_{V1}, D_{V1}, R_{V2}, D_{V2}, d, τ and Γ.
Since the same model function was applied to quasielastic spectra of the lipids, the 4f-lipids and the 9f-lipids, at 300 K, the resulting fitting parameters of all lipid samples are listed in Table 4.6 for comparison. In Table 4.7 the fitting parameters obtained for hydrogen

Sample	R_{V1} [Å]	D_{V1} [cm^2/s 10^{-5}]	R_{V2} [Å]	D_{V2} [cm^2/s 10^{-5}]	d [Å]	τ [meV^{-1}]	Γ [meV]
lipids, out-of-plane	6	0.15	7	1.1	2.5	1.36	1.47
4f-lipids, out-of-plane	5	0.44	7	3.1	2.0	1.78	1.12
9f-lipids, out-of-plane	4	0.65	6	3.7	1.9	2.13	0.94
lipids, in-plane	4	0.16	5	1.8	2.5	0.93	2.15
4f-lipids, in-plane	4	0.48	7	3.0	1.8	1.31	1.53
9f-lipids, in-plane	7	0.54	6	2.9	2.0	1.22	1.64

Table 4.6: Fitting parameters for the lipids, the 4f-lipids and the 9f-lipids, with the following absolute errors: $\Delta D_{V1} \approx \pm 0.01\,10^{-5}$cm^2/s, $\Delta D_{V2} \approx \pm 0.1\,10^{-5}$cm^2/s, $\Delta R_{V1} \approx \Delta R_{V2} \approx \pm 1$ Å, $\Delta d \approx \pm 0.5$ Å and $\Delta\tau \approx \pm 0.01$ meV^{-1}.

populations p_{V1} , p_{V2}, p_{Jump} and f and for the fraction of the Lorentzian p_{Lor} for IN5 at the two different energy resolutions are shown. As obtained for the lipids, the fraction of immobile hydrogen atoms is zero for all samples at both configurations, indicating a highly dynamic membrane. Regarding the other contributions, it is remarkable that the fraction p_{V2} changes significantly when the protein-buffer is present: for the lipids, this fraction accounts for approximately 0.4, whereas for the 4f-lipids and the 9f-lipids, it accounts for

Sample	p_{V1}	p_{V2}	p_{Jump}	f	p_{Lor}
lipids, out-of-plane	0.49;0.45;0.03	0.40;0.40;0.44	0.11;0.15;0.53	0;0;0	0;0;0.09
4f-lipids, out-of-plane	0.60 ; 0.53	0.17 ; 0.20	0.20 ; 0.23	0 ; 0	0 ; 0.04
9f-lipids, out-of-plane	0.60 ; 0.52	0.20 ; 0.19	0.15 ; 0.21	0.02 ; 0	0 ; 0.09
lipids, in-plane	0.59;0.37;0.15	0.41;0.35;0.42	0.00;0.22;0.43	0;0.06;0	0;0;0.08
4f-lipids, in-plane	0.58 ; 0.43	0.18 ; 0.24	0.19 ; 0.24	0 ; 0	0 ; 0.07
9f-lipids, in-plane	0.44 ; 0.39	0.27 ; 0.28	0.23 ; 0.20	0 ; 0	0 ; 0.20

Table 4.7: Fitting parameters obtained for hydrogen populations p_{V1} , p_{V2}, p_{Jump} and f and for the fraction of the Lorentzian p_{Lor}. The absolute errors are ≈ 0.05 for all parameters. For the 4f-lipids and the 9f-lipids, the first values are for parameters obtained on IN5 at $\Delta E = 12\,\mu eV$ and the second values for parameters obtained at $\Delta E = 75\,\mu eV$, respectively. For the lipids, the first values are for parameters obtained for IN5 ($\Delta E = 12\,\mu eV$), the second values for parameters obtained for Osiris ($\Delta E = 100\,\mu eV$) and the third values for parameters obtained for Neat ($\Delta E = 216\,\mu eV$), respectively.

0.2 to 0.3, indicating that the hydrogen population, undergoing confined diffusion in the final parts of the lipid chains, is smaller when the protein buffer is present. As mentioned above, the 2-site jump diffusion component can be attributed to jumps of the hydrogen atoms belonging to the CH_2 groups in the lipid chains, with jump distances of 2.0 Å to 2.5 Å. No significant differences between the membrane samples were obtained, neither for the populations p_{Jump}, nor for the jump distances d. The diffusion constant D_{V1} is approximately one order of magnitude smaller than the diffusion constant D_{V2}, for all samples. Comparing the values for the diffusion constants D_{V1} and D_{V2}, respectively, for membranes containing different buffer concentrations, differences are observed. Indeed, the radii of confinement do not change remarkably, with values between 4 Å and 7 Å, but the differences between the diffusion constants D_{V1} and D_{V2} are not negligible. Fig. 4.15 illustrates schematically the diffusion constants of Volino 1 obtained for the three different samples for the out-of-plane (shown in blue) and the in-plane configuration (shown in red). Although p_{V2} is smaller for the 4f-lipids and the 9f-lipids, the diffusion constant D_{V1} obtained for the in-plane and for the out-of-plane configurations increases with higher amounts of protein buffer. Fig. 4.16 shows the differences between the diffusion constants for the 4f-lipids (D_{V1}^{4f-lip}) and the 9f-lipids (D_{V1}^{9f-lip}), respectively, and the diffusion constant for the buffer-free lipids (D_{V1}^{lipids}), used as reference, with

$$dD_{V1}^{4f-lip} = D_{V1}^{4f-lip} - D_{V1}^{lipids} \tag{4.5}$$

for the 4f-lipids and

$$dD_{V1}^{9f-lip} = D_{V1}^{9f-lip} - D_{V1}^{lipids} \tag{4.6}$$

for the 9f-lipids. The out-of-plane configuration is illustrated in Fig. 4.16 a and the in-plane configuration in Fig. 4.16 b. It is clear that the differences of the diffusion constants with respect to the lipids increase with the buffer concentration, while p_{V1} and p_{V2} are the

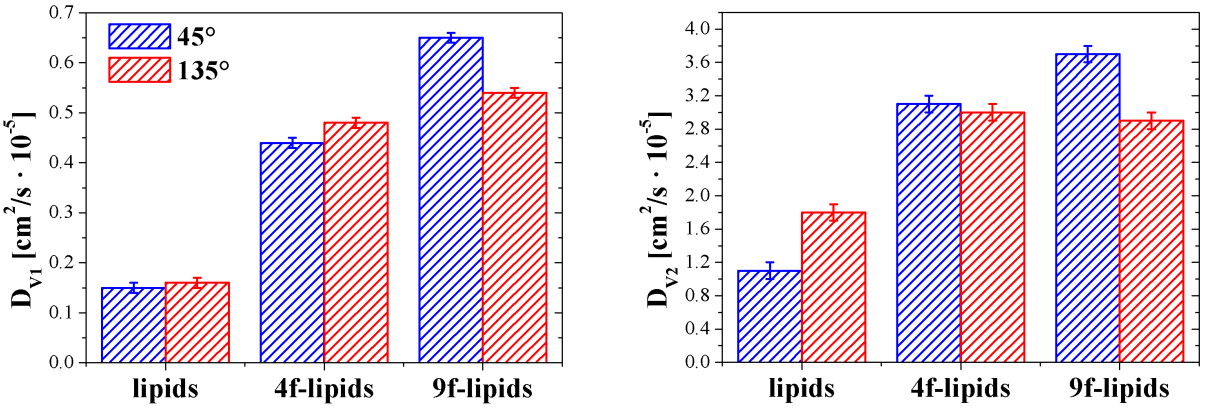

(a) (b)

Figure 4.15: Diffusion constants D_{V1} of hydrogen population p_{V1}, described by Volino 1 (a), and D_{V2} of population p_{V2}, described by Volino 2 (b), for protein-free lipids with different buffer concentrations (lipids: without any buffer; 4f-lipids: with 4-fold buffer amount; 9f-lipids: with 9-fold buffer amount). Blue: parameters obtained for data in out-of-plane configuration (45°); red: in-plane configuration (135°).

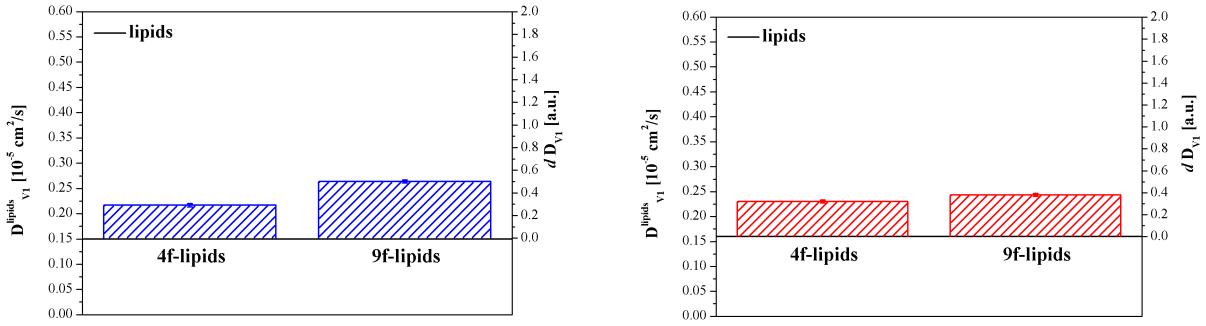

(a) (b)

Figure 4.16: Differences dD_{V1}^{4f-lip} and dD_{V1}^{9f-lip} between the diffusion constants for the 4f-lipids (D_{V1}^{4f-lip}) and the 9f-lipids (D_{V1}^{9f-lip}), respectively, and the D_{V1}^{lipids} for the buffer-free lipids, which is shown as a black constant line. The absolute errors are $\Delta dD_{V1}^{4f-lip} = \Delta dD_{V1}^{9f-lip} = 0.014\,10^{-5}\,\mathrm{cm}^2/\mathrm{s}$. (a) out-of-plane configuration and (b) in-plane configuration.

same for the 4f-lipids and the 9f-lipids for both configurations, and p_{V2} is $\approx 10\,\%$ smaller than for the lipids. For the diffusion constant D_{V2}, the same tendency is obtained for all samples and in both configurations, besides the nearly similar values of D_{V2} for the 4f-lipids and the 9f-lipids in the in-plane orientation. In order to show the relative increase of both diffusion constants with respect to the diffusion constant of the lipids, dD_V/D_V^{lipids}, this coherency is illustrated in Fig. 4.17 for all samples. It is suggested that the diffusive

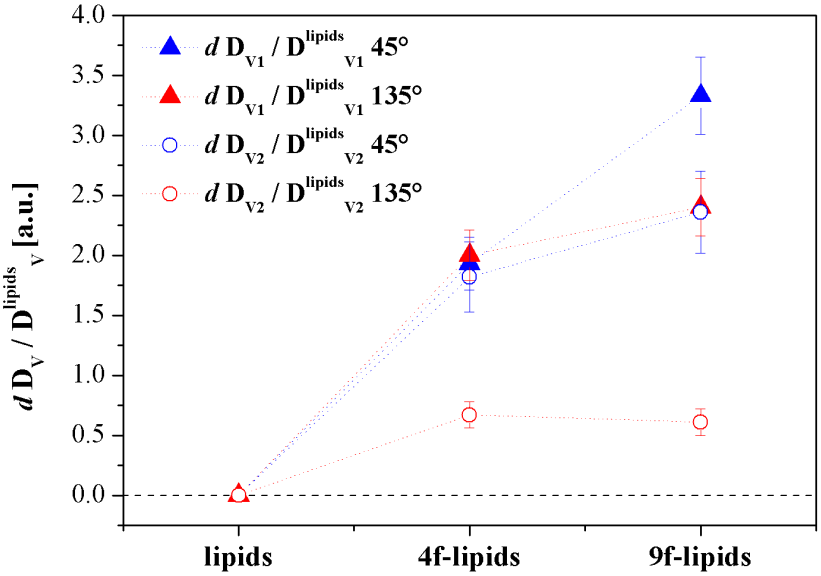

Figure 4.17: Increase of both diffusion constants D_{V1} (filled symbols) and D_{V2} (empty symbols) with respect to the diffusion constant of the lipids: dD_V/D_V^{lipids} for the out-of-plane (red symbols) and the in-plane configuration (blue symbols).

motions in confinement performed by both hydrogen populations p_{V1} and p_{V2}, belonging to the upper and the lower parts of the lipid chains, respectively, are faster by the higher concentration of protein buffer in the samples. In contrast, the population p_{V2} is smaller for the membranes containing buffer. However, the relative increase does not behave linearly, but becomes smaller, indicating a saturation effect at higher buffer concentration.
In order to understand the effect of the protein buffer on the confined diffusion, the number of HEPES and NaCl molecules with respect to the number of lipid molecules in a membrane sample (see Section 3.2), was calculated for the membrane sample with highest buffer concentration. As described in Section 3.2, each sample contained 2 ml of lipid solution and 0.5 ml of buffer solution, respectively. The absolute number of molecules in a sample is

$$n = N_A\, V\, c, \tag{4.7}$$

where N_A is Avogadro's number, $V = 0.5\,\text{ml}$ is the volume and c the molar concentration (in M or mol/l). In Table 4.8 the absolute and the relative number of molecules are listed for membranes containing 1-, 2-, 4- and 9-fold buffer concentrations (for HEPES and

NaCl concentrations see Table 3.1). For the 4f-lipid sample and the 9f-lipid sample, the

no. molecules	1f-lipids	2f-lipids	4f-lipids	9f-lipids
lipids				
absolute	$7.55 \cdot 10^{19}$	$7.55 \cdot 10^{19}$	$7.55 \cdot 10^{19}$	$7.55 \cdot 10^{19}$
relative [%]	80	67	50	31
NaCl				
absolute	$1.63 \cdot 10^{19}$	$3.26 \cdot 10^{19}$	$6.53 \cdot 10^{19}$	$1.47 \cdot 10^{20}$
relative [%]	17	29	44	61
HEPES				
absolute	$2.17 \cdot 10^{18}$	$4.34 \cdot 10^{18}$	$8.67 \cdot 10^{18}$	$1.96 \cdot 10^{19}$
relative [%]	3	4	6	8
total				
absolute	$9.40 \cdot 10^{19}$	$1.12 \cdot 10^{20}$	$1.49 \cdot 10^{20}$	$2.42 \cdot 10^{20}$
relative [%]	100	100	100	100

Table 4.8: Absolute and relative number (no.) of lipid-, NaCl- and HEPES-molecules present in membrane samples containg 1-fold, 2-fold, 4-fold and 9-fold protein buffer (NaCl and HEPES) concentrations.

number of NaCl molecules in a membrane sample is very high, accounting for 44 % and 61 %, respectively. Molecular dynamics simulations on hydrated DPPC bilayers with, and without, NaCl [132] have shown that Na^+ and Cl^- ions bind to the membrane and the latter slightly weaker. This could explain the effect of the protein buffer concentration: when distributed homogeneously, Na+ and Cl− molecules could cause more space between each lipid molecule and thus, increase the lipid flexibility.
Regarding the total scattering cross sections $\sigma_{scatt} = \sigma_{inc} + \sigma_{coh}$ of the membrane components DOPS-DOPC lipids, NaCl and HEPES, the scattering of the protein buffer can be excluded, even at such high buffer concentrations, as shown in Table 4.9. Hereby, the scattering cross sections of each molecule were multiplied with the corresponding number of molecules, and the percentage was calculated. The scattering cross sections of each molecule are: $\sigma_{scatt} = 20.01$ barn for NaCl, $\sigma_{scatt} = 1555.00$ barn for HEPES with its chemical formula of $C_8H_18N_2O_4S$ and $\sigma_{scatt} = 6867.74$ barn for a lipid molecule, considering an average cross section for DOPS ($C_42H_77NO_10PNa$) and DOPC ($C_44H_84NO_8P$). Since the scattering cross section of the lipids is between 94 % and 99 % for all samples, it can be guaranteed that molecular dynamics of only the lipid-multilayers, and not of the protein buffer molecules, are visible with neutron scattering techniques and were characterized with our model. Hence, the large number of NaCl molecules in membrane samples containing the highest protein buffer concentration (9-fold) seems to be responsible for the enhancement of membrane flexibility.
However, for an accurate interpretation of the results described in the following chapters,

σ_{scatt} [barn]	1f-lipids	2f-lipids	4f-lipids	9f-lipids
lipids				
absolute	$5.19 \cdot 10^{23}$	$5.19 \cdot 10^{23}$	$5.19 \cdot 10^{23}$	$5.19 \cdot 10^{23}$
relative [%]	99.24	98.60	97.20	94.00
NaCl				
absolute	$3.26 \cdot 10^{20}$	$6.52 \cdot 10^{20}$	$1.31 \cdot 10^{21}$	$2.94 \cdot 10^{21}$
relative [%]	0.06	0.12	0.26	0.50
HEPES				
absolute	$3.37 \cdot 10^{21}$	$6.75 \cdot 10^{21}$	$1.35 \cdot 10^{22}$	$3.04 \cdot 10^{22}$
relative [%]	0.70	1.28	2.54	5.50
total σ_{scatt}				
absolute	$5.23 \cdot 10^{23}$	$5.26 \cdot 10^{23}$	$5.34 \cdot 10^{23}$	$5.52 \cdot 10^{23}$
relative [%]	100	100	100	100

Table 4.9: Scattering cross sections $\sigma_{scatt} = \sigma_{inc} + \sigma_{coh}$ for the membrane components (lipids, NaCl and HEPES) of membranes containing 1-fold, 2-fold, 4-fold and 9-fold protein buffer (NaCl and HEPES) concentrations.

each data set will be compared to the protein-free lipids measured at the same conditions, i. e. membranes containing 4- and 9-fold protein concentrations (and correspondingly the same amount of protein buffer) will be compared to protein-free membranes with the same amount of buffer, in order to avoid any contribution arising from the buffer.

4.4 Conclusions

To introduce experimental methods used for the characterization of the structure and dynamics of reconstituted myelin membranes, the results for a protein-free membrane (lipids) were presented in this chapter.
Diffraction measurements on D16 and IN16 revealed structural properties characteristic for the lipids. The diffraction on D16 allowed the investigation of the bilayer structure. In the lipid gel phase, a repeat distance of $E_1 = 58\,\text{Å}$ occurred, which shifted to smaller values during increasing the temperature in the temperature region of the lipid phase transitions, and shifted back to the initial value when the whole system was in the liquid phase. The behavior of the temperature dependence of the intensities at the Q-values of the Bragg peaks, which occurred during heating, indicates that a transient Bragg peak is present after the phase transition temperatures of the lipids. This Bragg peak arises not before also the anionic DOPS lipids transform into the liquid-disordered phase ($\approx 259\,\text{K}$). Diffraction measurements on IN16, permitted to identify three Bragg peaks at approximately $1.6\,\text{Å}^{-1}$, $1.7\,\text{Å}^{-1}$ and $1.8\,\text{Å}^{-1}$, which can be assigned to the (1 0 0), the (0 0 2) and (1 0 1) orientations of hexagonal ice. This crystal structures disappeared at the melting point of heavy water,

suggesting the presence of bulk water in the bilayers.
The elastic temperature scan on IN13 indicated that oriented protein-free DOPS-DOPC multilayers behave harmonically at low temperature. A transition to an anharmonic regime occurs at $\approx 160\,\mathrm{K}$. This transition, which occurs below the phase transition of the lipids, could be attributed to rotation of the methyl groups (CH_3 molecules) in the lipid chains. A further transition was found at $\approx 250\,\mathrm{K}$, which seems to be caused by the gel-to-liquid phase transition of the lipids, as indicated by DSC measurements. Also the melting of the surrounding D_2O, which initiates between $\approx 270\,\mathrm{K}$ and $280\,\mathrm{K}$, but could not be resolved due to the absence of data points, could affect the membrane dynamics. Since only few temperature points were measured in the temperature region between $250\,\mathrm{K}$ and $270\,\mathrm{K}$, a separation of the phase transitions of the lipids was not possible. Therefore, EINS measurements with a temperature rate of $0.3\,\mathrm{K/min}$, ranging from $20\,\mathrm{K}$ to $300\,\mathrm{K}$, were performed on IN16, which allowed the investigation of characteristic molecular motions of DOPS-DOPC lipids. The results indicated that the lipid dynamics increase at $\approx 256\,\mathrm{K}$, when the gel-to-liquid phase of the DOPC lipids ($T_c = 254\mathrm{K}$) was completed. The lipid system seemed to relax into an equilibrium state when the DOPS lipids also transformed to the liquid phase, and the lipid dynamics are enhanced further at the water melting point. In summary, structural and dynamical changes of a reconstituted protein-free membrane occur in the temperature region of the lipid phase transitions.
The results of the QENS studies on lipids in the liquid phase, performed on IN5, Osiris and Neat, have revealed four different hydrogen populations: f describes the fraction performing only vibrational motions, p_{V1} represents the fraction that belongs to the upper part of the lipid molecules, from the headgroups until the vinyl group, and diffuses in a confined, spherical volume, p_{V2} the fraction belonging to the terminal part of the lipids that diffuses faster than p_{V1} in a confined volume and finally p_{Jump}, which is a population belonging to the methylene groups (CH_2) of the lipid chains, which undergoes 2-site jump diffusion. Both diffusive motions have been found to be faster in the in-plane configuration, probably due to more degrees of freedom of the lipid chains in this direction.
QENS experiments on Neat have shown that any effect of the protein buffer at concentrations present in model myelin membranes containing MBP-C1 and P2 proteins (1-fold and 2-fold concentrations), on the membrane dynamics, can be excluded on a timescale of $\approx 20\,\mathrm{ps}$. Since neither any influence of the buffer on membrane dynamics occurring on other timescales nor any influence of the protein buffer at higher concentrations could be excluded with this study, QENS experiments on IN5 at two different energy resolutions ($\Delta E \approx 12\,\mu\mathrm{eV}$ and $\Delta E \approx 75\,\mu\mathrm{eV}$) were performed on 4f-lipids and on 9f-lipids. This allowed to compare the results obtained for model membranes containing MBP-C1 and MBP-C8 proteins at a 4-fold and a 9-fold concentration, respectively, with such reference membranes (see Chapter 6). The results indicated that the diffusive motions in confinement as performed by hydrogen populations p_{V1} and p_{V2} are enhanced the higher the buffer concentration. Indeed, the total scattering cross sections of the buffer molecules (HEPES and NaCl) are negligibly small, but the number of NaCl molecules in the 4f-lipids and the 9f-lipids accounts for 44 % and 61 %, respectively. Hence it is possible, that Na^+ and Cl^- ions may cause more space between each lipid and therefore increase the flexibility of the

multilayers. For an accurate interpretation of the influence of myelin proteins on both the structure and dynamics of myelin-like membranes, which is presented and discussed in the following chapters, each data set will be compared to the protein-free lipids measured at the same conditions, which will be used as references.

Chapter 5

Influence of MBP-C1 and P2 Proteins on the Structure and Dynamics of Model Myelin Membranes

To investigate the influence of myelin proteins MBP-C1 and P2 on the structure and dynamics of a reconstituted PNS-myelin membrane, neutron diffraction, elastic and quasielastic neutron scattering experiments have been performed. In the first part of this chapter, the results of diffraction measurements carried out on the diffractometer D16 at the ILL are presented. The second part deals with elastic mesurements performed on the backscattering spectrometer IN13 (ILL). Finally, quasielastic measurements on the time-of-flight spectrometers IN5 (ILL), Osiris (ISIS) and Neat (HZB) are discussed.

5.1 Influence on Structural Properties

Neutron diffraction measurements were carried out on the diffractometer D16. In order to cover the gel to liquid phase transitions of the lipids, temperature scans ranging from 240 K to 300 K and back were performed.
Figure 5.1 shows the Q-dependent elastic intensities for lipids, C1-lipids, P2-lipids and C1-P2-lipids at 242 K (below the lipid phase transitions) and at 285 K (above the lipid phase transitions).

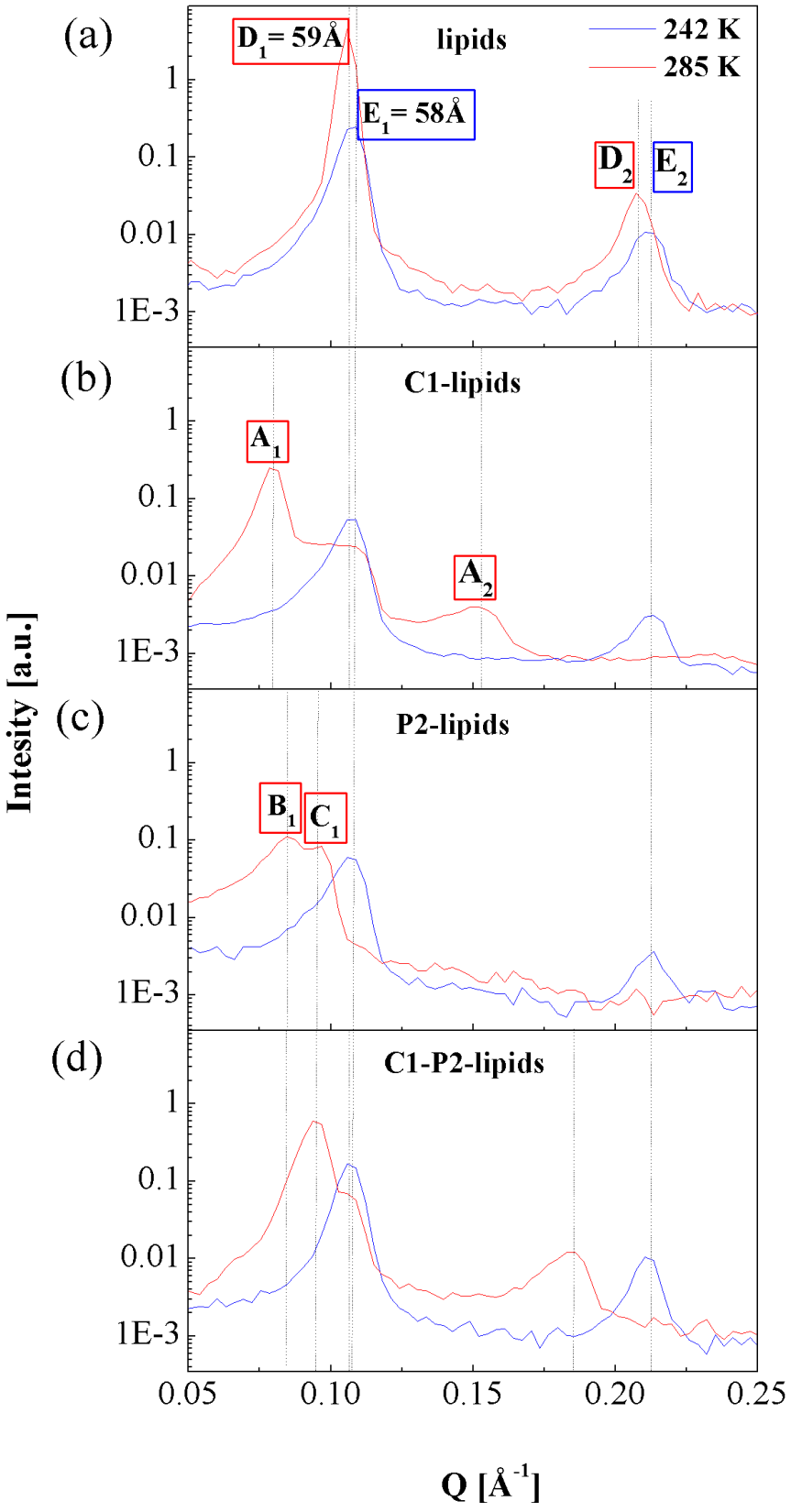

Figure 5.1: Diffraction patterns for lipids, C1-lipids, P2-lipids and C1-P2-lipids at 242 K (lipid gel phase, represented by the blue curve) and at 285 K (lipid liquid phase, represented by the red curve) achieved on D16. The index 1 indicates the first order of the Bragg peaks and the index 2 the second order, respectively.

In the gel phase all samples have the same repeat distance at $E_1 = 58\,\text{Å}$ (blue curve). Nevertheless, the Bragg peak is for the C1-lipids and for the P2-lipids less intense and broader than for the other samples, suggesting a more disordered structure. Furthermore, the intercept is higher, suggesting a less ordered membrane fraction with a large d-spacing (corresponding to low Q-values), which cannot be resolved here. MBP-C1 is known to be squeezed out of a bilayer in the gel phase, and preferentially binds to lipids in the liquid phase [28, 29, 30]. Thus, this domain could be associated with areas of squeezed out proteins. In contrast, for the C1-P2-sample this effect seems to be compensated by the association of the two proteins, since the Bragg peak resembles more the peak of the lipids with a smaller intercept. This could be caused by the stacking effect of MBP-C1 and P2 [59].
In the liquid phase, the C1-lipids and C1-P2-lipids show the same d-spacing as found for the lipids ($D_1 = 59\,\text{Å}$) and additional repeat distances, labeled as A_1, B_1 and C_1 (Figs. 5.1 b and 5.1 c), suggesting a formation of lipid domains with and without proteins in the liquid disordered phase. However, the P2-lipids exhibit two repeat distances in the liquid phase, which are larger than the $D_1 = 59\,\text{Å}$ of lipids (Fig. 5.1 c).
For the protein-free lipids a transient Bragg peak $G_1 = 0.118\,\text{Å}^{-1}$ (corresponding to 53 Å) was present in the phase transition temperature region of the lipids, which arose not before the anionic DOPS lipids also transformed into the liquid-disordered phase ($\approx 259\,\text{K}$) and was disappeared at the melting point of the ice (D_2O) within the bilayer, as measured with temperature scans. For membrane samples containing proteins, namely C1-lipids, P2-lipids and C1-P2-lipids, a similar structural behavior has been found, suggesting a common structural phase with a d-spacing of 53 Å in the temperature range of the lipid gel-to-liquid phase transitions.
In order to investigate the d-spacings of the membranes in the liquid phase in detail, Gaussian functions were used to fit the data obtained at 285 K (blue curves in Fig. 5.1), which is shown in Fig. 5.2 for the lipids (top left), the C1-lipid (top right), the P2-lipids (bottom left) and the C1-P2-lipids (bottom right). The first order Bragg peak of each sample was necessarily fitted by three Gaussians. The fit results are listed in Table 5.1, including the Q-values of the Bragg peaks, the corresponding repeat distances, the fraction of the membrane domains having this d-spacing and the FWHM of the Bragg peaks. The Gaussian fit for the Bragg peak of the lipids yields a repeat distance of $D_1 = 59.3\,\text{Å}$. This repeat distance has also been found for the C1-lipids and C1-P2-lipids, with fractions of 15.0 % and 7.3 %, respectively, indicating that these samples seem to exhibit a small fraction of membrane domains whose structure is not influenced by proteins. However, the P2-lipids do not show a repeat distance characteristic for the lipids, which reveals that there are no lipid domains uneffected by P2-proteins in the liquid phase.
For the C1-lipids (Fig. 5.2, top right), two other peaks have been found, one centered at $0.0795\,\text{Å}^{-1}$ (corresponding to a repeat distance of $A_1 = 79.0\,\text{Å}$) and the other at $0.0773\,\text{Å}^{-1}$ (corresponding to a repeat distance of $Z_1 = 81.3\,\text{Å}$). The repeat distance of 79.0 Å results in an inter bilayer spacing of 42 Å. Assuming that the height of a "C"-shaped MBP protein is 47 Å (see Section 1.2.1), the protein could fit between the bilayers, possibly

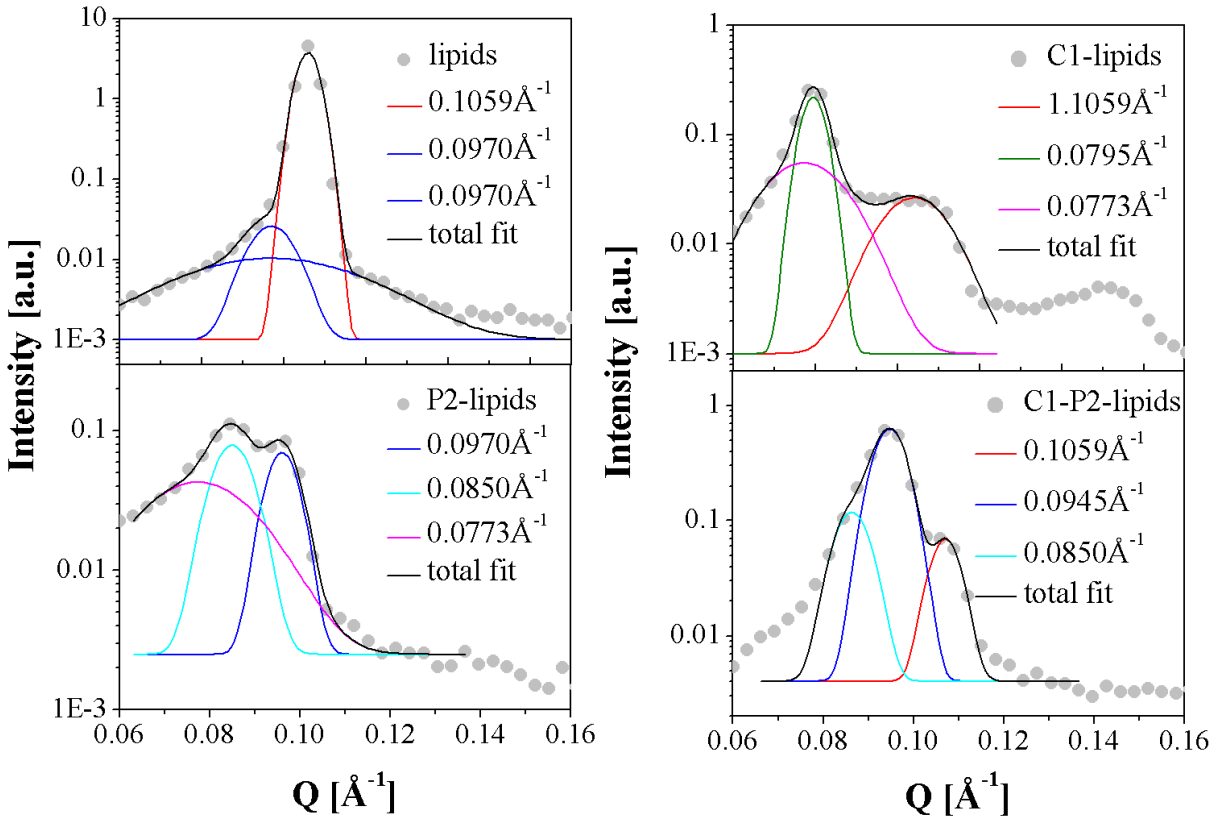

Figure 5.2: First order Bragg peaks at 285 K for lipids (top left), C1-lipids (top right), P2-lipids (bottom left) and C1-P2-lipids (bottom right). The data was fitted by three Gaussian functions, respectively.

Bragg peak [Å^{-1}]	0.1059 ± 0.0004	0.0970 ± 0.0004	0.0945 ± 0.0004	0.0850 ± 0.0004	0.0795 ± 0.0004	0.0773 ± 0.0004
repeat distance d [Å]	59.3 ± 0.1	65 ± 0.1	66.5 ± 0.1	74.0 ± 0.1	79.0 ± 0.1	81.3 ± 0.1
labeling	D_1	C_1	C_1	B_1	A_1	Z_1
lipids fraction [%]	96.8	1.9 ; 1.3				
FWHM [Å^{-1}]	0.005	0.04 ; 0.01				
C1-lipids fraction [%]	15.0 (24.0)				47.0 (76.0)	38
FWHM [Å^{-1}]	0.016				0.006	0.019
P2-lipids fraction [%]		22.1 (41.2)		31.6 (58.8)		46.3
FWHM [Å^{-1}]		0.007		0.009		0.02
C1-P2-lipids fraction [%]	7.3		78.0	14.9		< 0.7
FWHM [Å^{-1}]	0.006		0.0069	0.007		

Table 5.1: Results for the fitting of Gaussian functions to the first order Bragg peaks of the lipids, the C1-lipids, the P2-lipids and the C1-P2-lipids at 285 K. The Q-values of the Bragg peaks are given by the center of the Gaussians and the corresponding repeat distances d were calculated using Eq. 2.61. The fraction of the membrane domains with this repeat distance (given in %) were estimated by the ratio between the area of each Gaussian function and the total area of all Gaussian functions fitted to the data of one sample. Values in brackets (for C1-lipids and P2-lipids) are the fractions without considering the less ordered domain with Z_1. The FWHM is the full width at half maximum of each Gaussian, or rather of each Bragg peak.

partially penetrating (approximately 2 Å on each face) when binding to lipid headgroups. The Bragg peak centered at $0.0773\,\text{Å}^{-1}$ has a FWHM of $\approx 0.020\,\text{Å}^{-1}$, which is one order of magnitude larger than the FWHM of the two other peaks, with a high intercept. Hence, this large Bragg peak may indicate membrane domains with a repeat distance of 81.3 Å that are less ordered in directions parallel to the membrane plane, possibly containing squeezed out MBP-C1 proteins that are not associated to the ordered domains. However, the intercept of this Bragg peak is smaller than in the gel-phase, suggesting that less MBP-C1 proteins are present in this fraction. Since the Bragg peak characteristic for the lipids is also present, the C1-lipids seem to exhibit also membrane domains without MBP-C1 proteins. In Fig. 5.3 a membrane unit containing MBP-C1 is illustrated, considering the ideal case that the proteins are homogeneously distributed. The positive charge (shown in blue) of the protein is more or less continuously distributed on the protein surface. Since location of the less ordered domain with $Z_1 = 81.3$ Å within the membrane is not yet clear, it is not considered in the scheme.

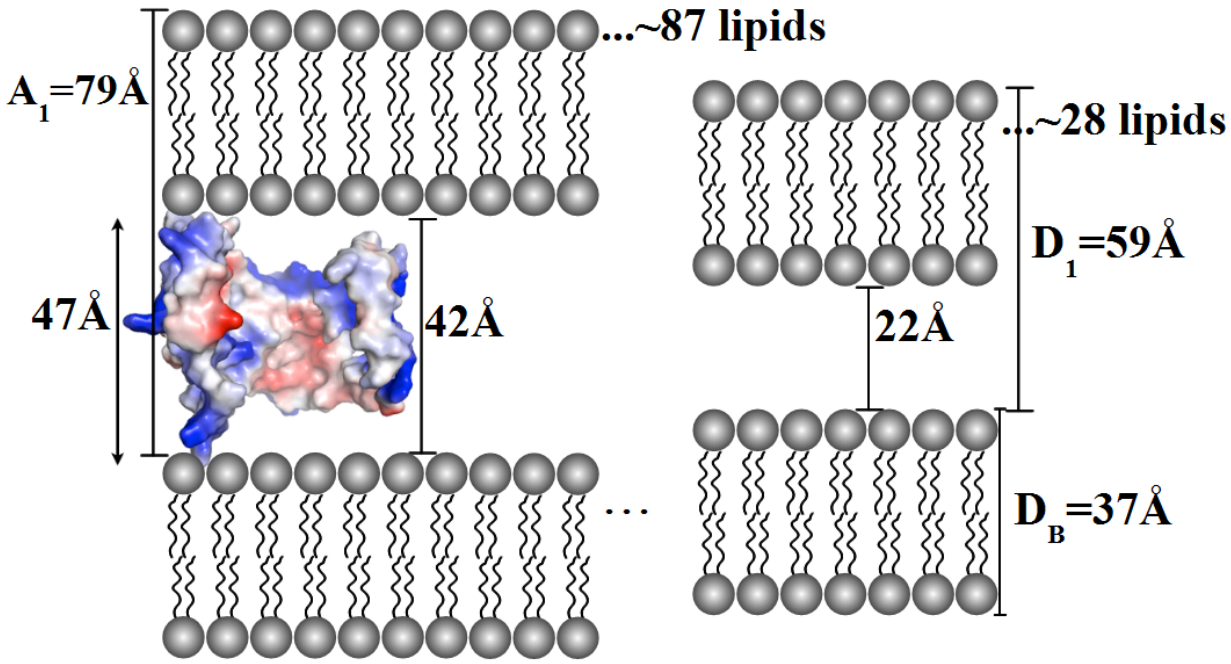

Figure 5.3: A schematic view of a membrane unit containing MBP-C1 proteins (C1-lipids): About 87 lipids per C1-molecule are affected by the protein, including the repeat distances of $A_1 = 79.0\,\text{Å}$, and about 28 lipids are unaffected (D_1), without considering the less ordered domain with the repeat distance $Z_1 = 81.3\,\text{Å}$. Positive charge is presented in blue and negative charge in red. Scale: $1\,\text{Å} : 0.7\,\text{mm}$.

For the P2-lipids, repeat distances of $B_1 = 74\,\text{Å}$ (corresponding to a Q-value of $0.085\,\text{Å}^{-1}$), $C_1 = 65\,\text{Å}$ ($0.097\,\text{Å}^{-1}$) and $Z_1 = 81.3\,\text{Å}$ ($0.0773\,\text{Å}^{-1}$) were identified, as illustrated in Fig. 5.2, bottom left. Similar to the C1-lipids, the peak centered at $0.0773\,\text{Å}^{-1}$ is very broad (FWHM of $0.032\,\text{Å}^{-1}$) with a high intercept (at low Q) and could be caused by less ordered domains containing P2 proteins. The inter bilayer spacings according to B_1 and C_1 are consequently 37 Å and 28 Å, respectively. The two occurring repeat distances could be explained in the following way: since the ligand binding site of P2 is situated inside the β-barrel (see Subsection 1.2.2), the lipids would have to enter the cavity when binding to the protein. Hence, the helical "lid" on the top of the β-barrel probably penetrates partially into the bilayer. With a height of the barrel of approximately 30 Å and a total height of the protein of 45 Å (measured with the software PyMOL), P2 is probably present in membrane domains with an inter bilayer spacing of 37 Å (or rather a repeat distance of $B_1 = 74\,\text{Å}$), oriented with its positively charged opposing sides in direction to the bilayers, respectively. Due to the charge distribution of P2, with two opposite highly positive charged regions separated by an almost neutral rim, the protein probably interacts strongly with two opposing membrane leaflets containing negatively charged lipids and thus a large membrane area could be influenced. Another possibility could be that P2 is situated in the membrane domains with an inter bilayer spacing of 28 Å (corresponding to $C_1 = 65\,\text{Å}$), but then the "lid" would have to penetrate completely into the membrane, nearly the half of the bilayer thickness, which is not very presumably. Assuming that the protein is located in domains with B_1, the adjacent domains near the proteins most likely exhibit a smaller spacing of 28 Å, where opposing headgroups show an intermediate distance between a headgroup distance including a protein (37 Å) and a headgroup distance of protein-free domains (21 Å), possibly due to a widening of the multilayers induced by P2. This coherency is shown in Fig. 5.4, without considering membrane domains with repeat distance Z_1.

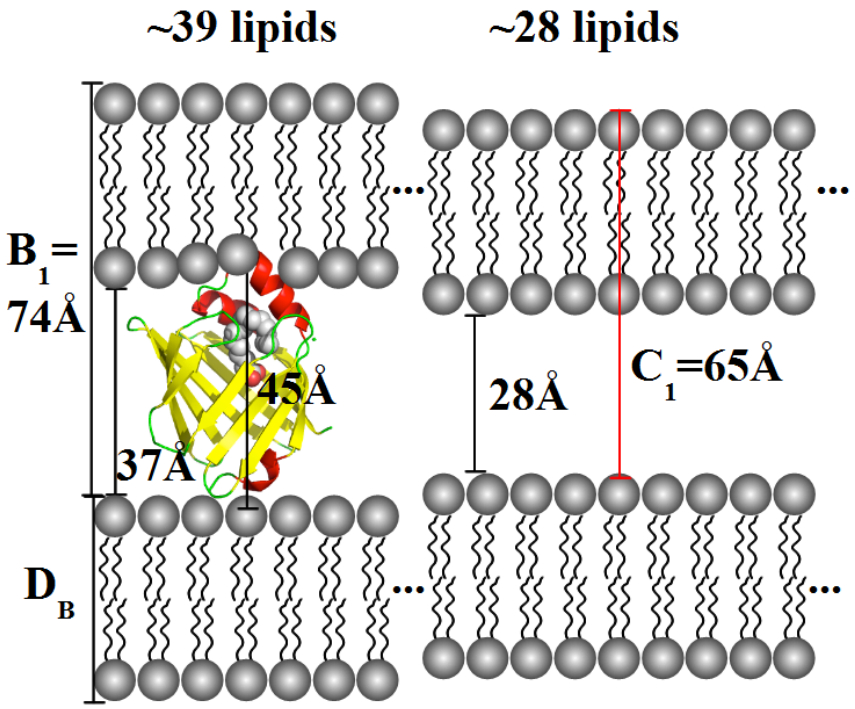

Figure 5.4: A schematic view of a membrane unit containing P2 proteins (P2-lipids): ≈ 39 lipids related to B_1 (protein-affected) and ≈ 28 lipids related to C_1 were calculated, without considering the less ordered fraction Z_1. Scale: $1\,\text{Å} : 0.7\,\text{mm}$.

Looking at the last sample, the C1-P2-lipids (Fig. 5.2, bottom right), three repeat distances, one for the lipids ($D_1 = 59.3$ Å) and two others at 74.0 Å and 66.5 Å were identified. A broad Bragg peak at $Z_1 = 81.3$ Å was also present, but at less than 0.7 %, indicating that almost no less ordered membrane domains exist, probably induced by the stacking effect of both MBP-C1 and P2. The peaks at 74 Å and 66.5 Å are most likely the d-spacings found for the P2-lipids, $B_1 = 74$ Å and $C_1 = 65$ Å. Since the C1-P2-lipid sample contains approximately 2.9 times more P2 molecules than MBP-C1 molecules (as calculated in the following), one could assume that three P2 proteins appear to associate with one MBP-C1 protein, respectively, and hence, the Bragg peaks found for P2-lipids dominate in this sample. The Bragg peak of the C1-lipids, $A_1 = 79$ Å, could not be identified in the fitting. The fraction of membrane domains with a d-spacing of B_1 is only 14.9 %, whereas the fraction of membrane domains with a d-spacing of C_1 is 78 %. This indicates that the intermediate interbilayer spacing due to a widening from the proteins is very large, which could be caused by assemblies of proteins, instead of single proteins well distributed through the whole membrane. The Bragg peak $D_1 = 59.31$ Å, characteristic for the lipids, is present at 7.3 % and suggests that the protein-assemblies are sufficiently far away from each other, so that the bilayers completely relax to their initial protein-free state. The related membrane domain is probably centered between two protein assemblies, as illustrated in Fig. 5.5.

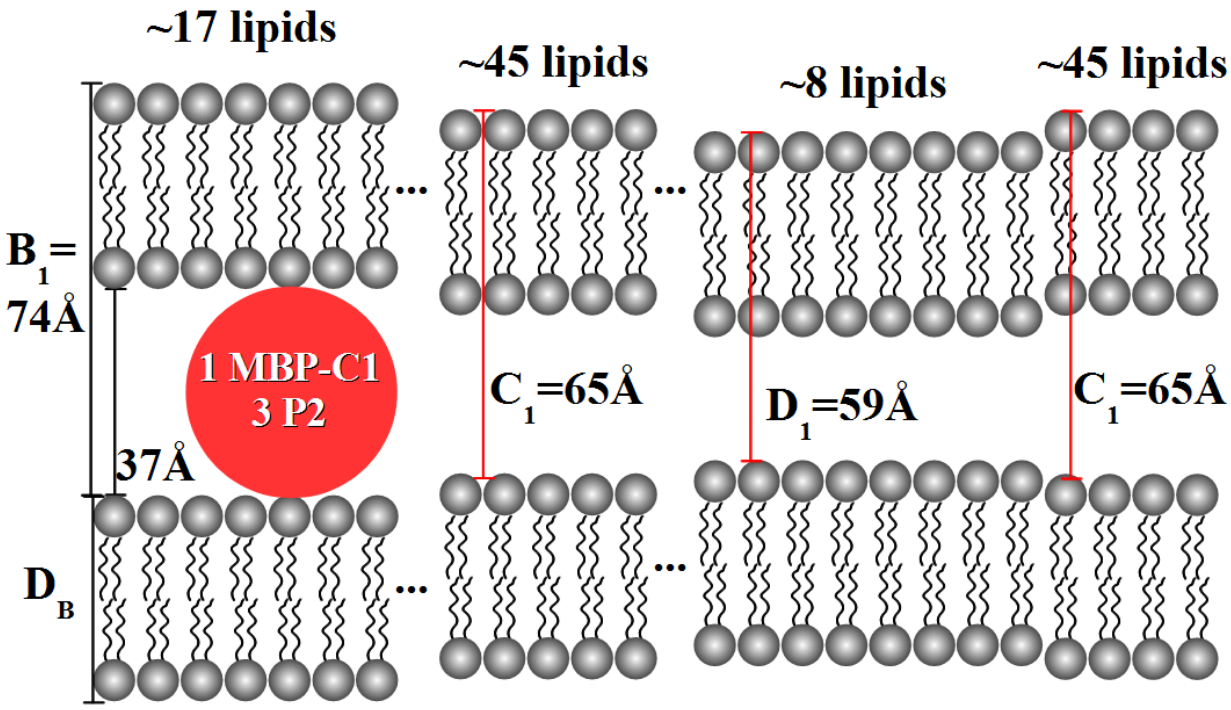

Figure 5.5: A schematic view of a membrane unit containing both MBP-C1 and P2 proteins (C1-P2-lipids): ≈ 17 lipids related to B_1 (protein-affected), ≈ 90 lipids related to C_1 and ≈ 8 protein-unaffected lipids, related to D_1, were calculated. The supposed protein-assembly of one MBP-C1 protein associated to three P2-proteins is not true to scale in this scheme. Scale: 1 Å : 0.7 mm.

To have a clearer picture about how the proteins are distributed in the membrane, the surface distribution of lipids bound to proteins and of protein-free lipids has been calculated for each sample and modeled schematically in a two dimensional plane for a monolayer. Therefore, the number of protein molecules n_{prot} was estimated following

$$n_{prot} = \frac{m}{MW} N_A, \tag{5.1}$$

where m is the protein mass in the sample, MW the molecular weight of the protein and N_A Avogadro's number. For the C1-P2-lipids, a protein assembly of three P2 proteins and one MBP-C1 protein was estimated, since approximately three times more P2 proteins are in the sample, compared to the number of MBP-C1 proteins. Hence, the number of those complexes is the same as the number of MBP-C1 molecules in a bilayer. The number of protein molecules per bilayer is

$$n_{prot}^{bi} = \frac{n_{prot}}{n_{bi}}, \tag{5.2}$$

where $n_{bi} = 19800$ is the number of bilayers in a sample (for calculations see Section 3.2). The total surface area of the membrane, given by the area of a wafer ($8.75\,10^{16}$ Å^2), divided by the number of protein molecules on a bilayer n_{prot}^{bi} gives the space for a protein in a bilayer (or rather on a monolayer), assuming the ideal case that the proteins are homogeneously distributed. The surface of MBP-C1, which is probably associated with the lipid heads, is approximately $A_{prot} = 2376$ Å, assuming that the protein lies flat in the bilayer, with the cavity of the "C"-shape parallel to the membrane plane (see Subsection 1.2.1). Since probably also lipids near the cavity are strongly affected by the protein, a circular surface is supposed, as shown in Fig. 5.6. The lipid-bound surface of P2 results

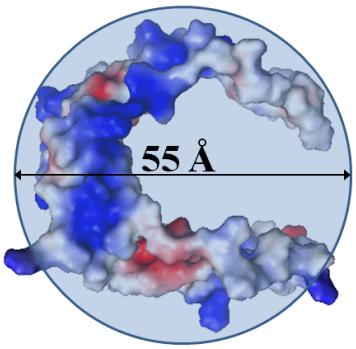

Figure 5.6: MBP surface associated with the lipid headgroups, assuming that also lipids near the cavity of the "C"-shape are affected by the protein.

in $A_{prot} = 600$ Å, assuming that P2 lies endwise in a bilayer with respect to the membrane plane (see Subsection 1.2.2). For the C1-P2-lipids, with a protein assembly of three P2 proteins and one MBP-C1 protein, it was assumed that the proteins arrange in a plane and not on top of each other, resulting in a surface of $A_{prot} = 3 \cdot 600$ Å $+ 2376$ Å. From

this, the distance between two proteins (or protein assemblies of three P2 proteins and one MBP-C1 protein for the C1-P2-lipids), including the protein, has been estimated, as well as the number of lipids n_{lip} fitting in this distance (assuming a diameter for a lipid head of $d_{lip} = 7.65\,\text{Å}$, which corresponds to a surface area of 46 Å [74]). The fraction of the surface with lipids bound to proteins, given by the ratio $A_{prot}\, n^{bi}_{prot}/(8.75\,10^{16}\,\text{Å}^2)$, is approximately 0.31% for C1-lipids, 0.23% for P2-lipids and 0.41% for C1-P2-lipids. For this purpose, the ideal case with perfectly isotropically distributed proteins was assumed. All values concerning those calculations are listed in Table 5.2. In Figs. 5.7 and 5.8, the

sample	C1-lipids	P2-lipids	C1-P2-lipids
n_{prot}	$2.22\,10^{15}$	$6.50\,10^{15}$	$8.72\,10^{15}$
n^{bi}_{prot}	$1.12\,10^{11}$	$3.28\,10^{11}$	$1.12\,10^{11}$
protein-space per bilayer [Å^2]	778983	266720	778983
A_{prot} [Å^2]	2376	600	4176
distance protein - protein [Å]	883	516	883
n_{lip}	115	67	115
fraction of surface with protein-bound lipids [%]	0.31	0.23	0.41

Table 5.2: Values concerning calculations for the surface distribution of protein-bound and -unbound lipids. n_{prot}: number of proteins per sample; n^{bi}_{prot}: number of proteins per bilayer; A_{prot}: lipid-bound surface area of proteins; protein-space per bilayer: space for one protein (for C1- and P2-lipids) and for a protein assembly of three P2 and one MBP-C1 (for C1-P2-lipids); n_{lip}: number of lipids between two proteins (or protein assemblies), including the first protein.

surface distribution of the lipid-bound proteins in a monolayer is schematically illustrated in a two dimensional plane for the C1-lipids and the C1-P2-lipids, respectively.

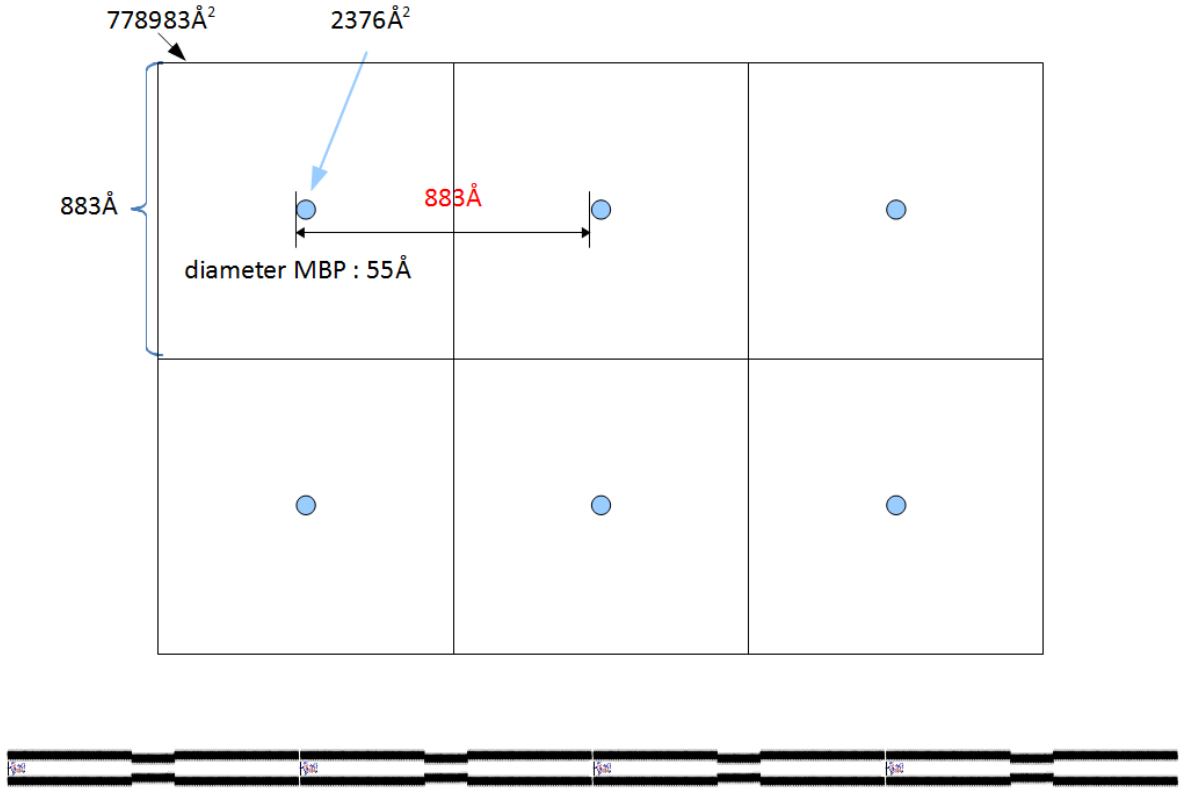

(a)

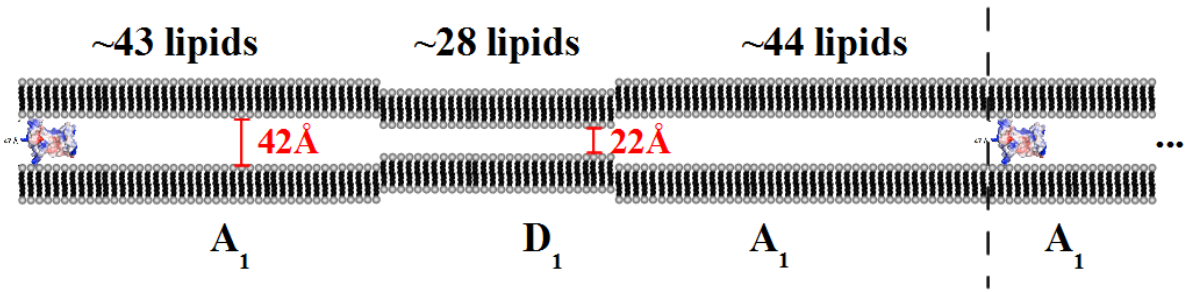

(b)

Figure 5.7: (a) Schematic illustration of the surface distribution of lipid-bound proteins in a monolayer for C1-lipids. The upper part shows a topview and the lower part a side view. (1 Å : 0.04 mm.) (b) Magnification of the side-view shown in (a), with a scale of 1 Å : 0.14 mm.

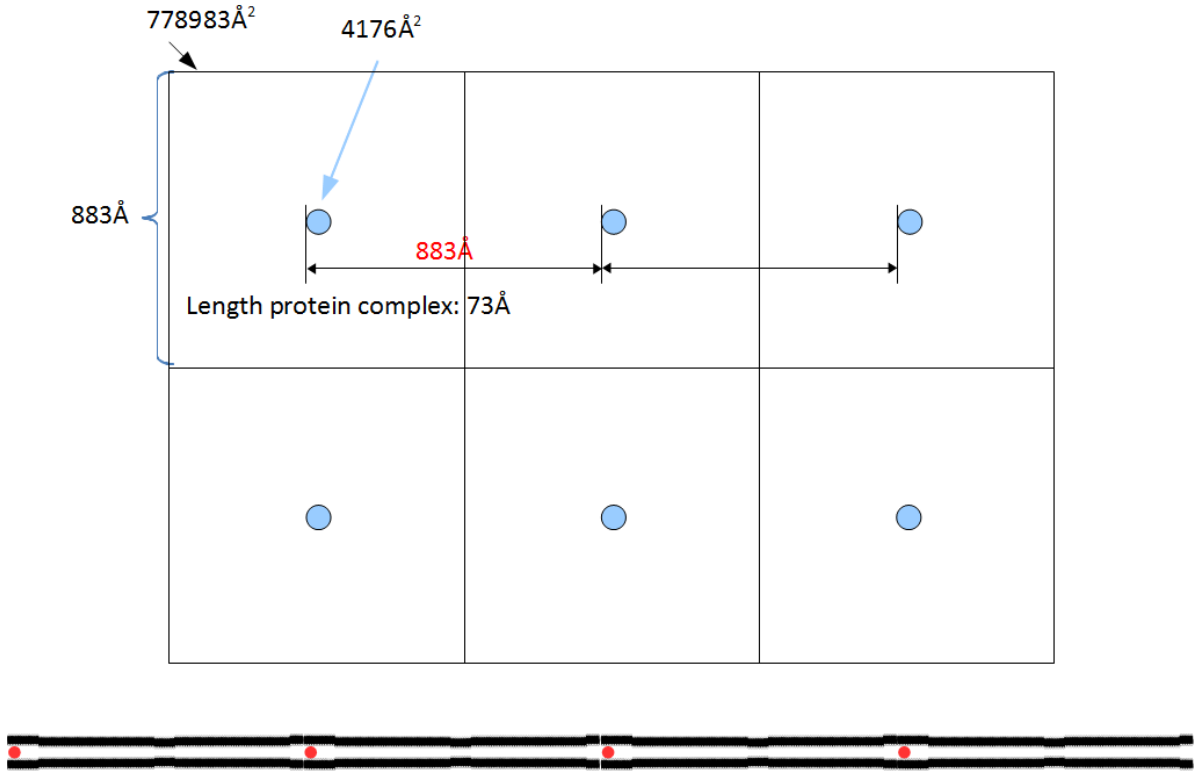

(a)

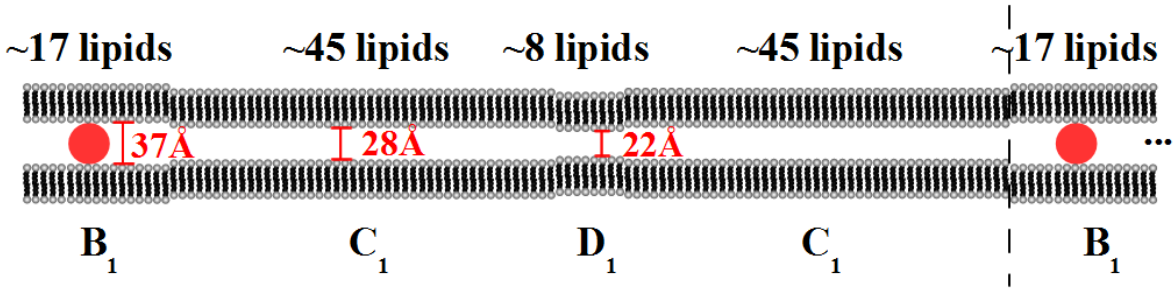

(b)

Figure 5.8: (a) Surface distribution of lipid-bound proteins in a monolayer for the C1-P2-lipids (1 Å : 0.04 mm.) with (b) a magnification of the side-view (1 Å : 0.14 mm).

For the P2-lipids, which exhibit three different d-spacings, $B_1 = 74\,\text{Å}$, $C_1 = 65\,\text{Å}$ and $Z_1 = 81\,\text{Å}$, there are three different possibilities for the location of the proteins. It was assumed that they are mainly situated in membrane domains with a d-spacing of C_1 and some proteins in less ordered domains (Z_1). The distance between two membrane-bound P2 proteins would be $\approx 516\,\text{Å}$, which is sufficient for approximately 67 lipids. Hence, the membrane probably cannot completely relax from a d-spacing of $B_1 = 74\,\text{Å}$ (for P2-bound lipid-domains) to its initial protein-free state (with $D_1 = 59\,\text{Å}$), but shows an intermediate repeat distance of $C_1 = 65\,\text{Å}$. Since these assumptions cannot be ensured with this diffraction study, a surface distribution of a monolayer with P2 proteins is not shown here.
With these two-dimensional illustrations, the origin of the Bragg peaks occurring in the liquid phase of the protein-membranes (C1-lipids, P2-lipids and C1-P2-lipids, see Fig. 5.1) is easier to understand. For the C1-lipids (Fig. 5.7), the space from one protein to the next, including the first protein (as illustrated in Fig. 5.7 a), is approximately 883 Å. This space, in which around 115 lipid molecules would fit, seems to be large enough for relaxation of the bilayers from a d-spacing of $A_1 = 79\,\text{Å}$ of the domain where the proteins are present, to their initial protein-free state with a d-spacing of $D_1 = 59\,\text{Å}$. Therefore, two Bragg peaks are visible, one representing the distribution of membrane domains bound to MBP-C1 proteins ($A_1 = 79\,\text{Å}$), and another the protein-free membrane domains ($D_1 = 59\,\text{Å}$), which are distributed in between. Here, it is assumed that proteins are homogeneously distributed in the membrane.
Assuming that the proteins in the C1-P2-lipids build assemblies of approximately three P2 proteins and one MBP-C1 protein, the distance between two protein assemblies (883 Å) is large enough for approximately 115 lipid molecules between each protein complex (one complex is here included), related to the C1-lipids (see Fig. 5.8). A Bragg peak at $D_1 = 59\,\text{Å}$ occurs, representing the membrane domains, which are not influenced by proteins and which are probably centered between two protein assemblies, and the Bragg peak at $B_1 = 74\,\text{Å}$ seems to describe the protein-bound membrane domains in between them. The d-spacing of $C_1 = 66.5\,\text{Å}$ probably represents adjacent membrane domains, showing a relaxing, intermediate interbilayer spacing. The MBP-C1 protein, associated with three P2 proteins, which interact strongly with negatively charged lipids due to their concentrated positive charge distribution, probably penetrates more into the bilayer than when present alone. Hence, the Bragg peak characteristic for C1-lipids ($A_1 = 79\,\text{Å}$) is not visible. Membrane domains of less order containing squeezed out proteins (Z_1) do not exist, which could be caused by the stacking effect of MBP-C1 and P2 together in a membrane. Regarding the fractions at which the Bragg peaks are present (Table 5.1), ≈ 17 lipids are related to B_1 (protein-affected), ≈ 90 lipids are related to C_1 and ≈ 8 lipids are related to D_1, when supposing a one-dimensional plane (Fig. 5.8 b). It has to be underlined that the hypothesis with protein assemblies of three P2 proteins and one MBP-C1 protein, homogeneously distributed in the membrane, is a possibility for the less complex case and cannot be guaranteed. Of course, the protein assemblies could also be distributed randomly and it is neither assured that every assembly contains four proteins, nor that all P2 proteins are always associated with one MBP-C1 protein.
Although the surface fractions of protein-bound lipids were estimated to only $\approx 0.31\%$ for

C1-lipids, $\approx 0.23\%$ for P2-lipids and $\approx 0.41\%$ for C1-P2-lipids (Table 5.2), the fractions of lipids influenced by the proteins are much larger, as shown in this section.

5.2 Influence on Dynamical Properties

To determine characteristic molecular motions of model myelin membranes influenced by MBP-C1 and P2 proteins, elastic temperature scans were performed on the backscattering spectrometer IN13 with the same experimental conditions as described in Section 4.2.
With very low concentrations of proteins in the membrane samples (less than 1% in weight) and D_2O as solvent, this EINS study gives information about the dynamics performed by the hydrogen atoms belonging to the lipids.
A description of data obtained for the lipids, without proteins, and the calculated MSDs $\langle u^2 \rangle(T)$, was given in Section 4.2. Observations on membranes containing MBP-C1 and P2 proteins will be compared to those results.
Fig. 5.9 shows the MSDs obtained for all samples in in-plane configuration (a) and in out-of-plane configuration (b). The dashed line represents the harmonic regime (region 1, see Section 4.2), in which hydrogens are vibrating harmonically around equilibrium positions. For data obtained for the in-plane configuration, this harmonic behavior occurs for $T \leq 160\,\mathrm{K}$. Anharmonic contributions, which were attributed to the rotation of methyl groups (CH_3 molecules) in the lipid chains (see Section 4.2), arise for $T \geq 160\,\mathrm{K}$ for all samples, apart from the C1-lipids, which behave harmonically up to $\approx 200\,\mathrm{K}$. In the anharmonic regime between approximately 200 K and 270 K, the MSDs of this sample are slightly smaller, indicating a less dynamic behavior. Thus, MBP-C1 seems to influence this transition. A further transition occurs at $\approx 250\,\mathrm{K}$ for all samples, which was attributed to the gel-to-liquid phase transition of the lipids DOPC ($T_c = 254\,\mathrm{K}$) and DOPS ($T_c = 259\,\mathrm{K}$), suggested by DSC measurements (Section 4.2). In the temperature range between $\approx 250\,\mathrm{K}$ and $\approx 270\,\mathrm{K}$ the gel-to-liquid phase transitions of the lipids occur and between 270 K and 280 K the melting of the surrounding D_2O takes place (at approximately 277 K), which could affect the membrane dynamics but which cannot be resolved due to the experimental protocol with large temperature steps. For $T \geq 280\,\mathrm{K}$ the dynamics are too far from the timescale defined by the instrumental resolution to be resolved, caused by the liquid D_2O.
In contrast, for data obtained in out-of-plane configuration, the lipids, the P2-lipids and the C1-P2-lipids show a harmonic behavior up to $\approx 200\,\mathrm{K}$ and the C1-lipids up to $\approx 220\,\mathrm{K}$. Between about 200 K and 270 K, the MSDs of the C1-lipids are smaller than for the lipids (inset in Fig. 5.9b). This suggests a reduction of membrane dynamics in a temperature region where the gel-to-liquid phase transitions of the lipids and the water melting occur, induced by the protein MBP-C1. This reduction in membrane flexibility lasts until the phase transitions are completed. Between the other samples (lipids, P2-lipids and C1-P2-lipids) there are no differences in the MSDs visible within the experimental uncertainty.
Compared to the structural properties of the membranes with MBP-C1 and P2 proteins, the obtained MSDs behave harmonically at low temperature for all samples, according to

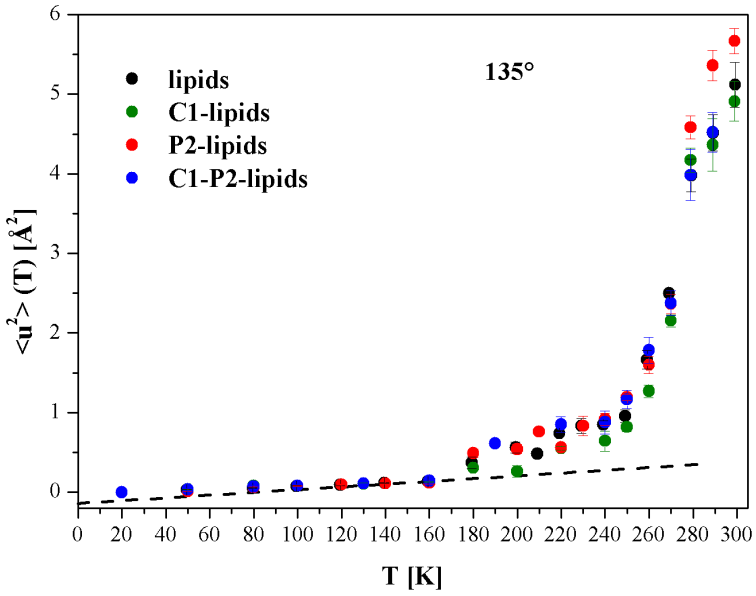

(a)

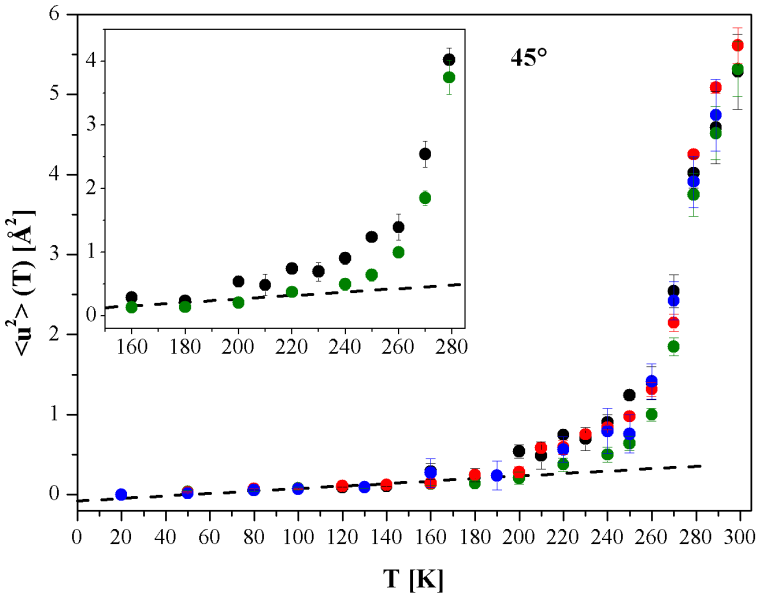

(b)

Figure 5.9: MSDs as a function of temperature for the lipids (black symbols), the C1-lipids (green symbols), the P2-lipids (red symbols) and the C1-P2-lipids (blue symbols) in in-plane (a) and out-of-plane configuration (b).The dashed line represents the regime at low temperature, in which the MSDs behave harmonically.

the same repeat distance of 59 Å in the gel phase of the lipids. It was shown that the methyl group rotation is significantly influenced by MBP-C1 proteins, arising at higher temperatures. This dynamical changes are not accompanied by structural changes in this temperature region. The reduction of the membrane dynamics between 200 K and 270 K induced by MBP-C1 , suggesting that the protein affects the temperature region of the lipid phase transitions, could be caused by the strong influences of the protein on the membrane structure (only 7 % of the membrane showed a repeat distance characteristic for the lipids). The diffraction measurements have shown that MBP-C1 penetrates about 2 Å at each side into the bilayer, which probably reduces the space for the lipids, resulting in decreased lipid motions. Structural changes induced by MBP-C1 and P2 proteins occurred in the liquid phase and the data was analyzed at ≈ 285 K. At this temperature the dynamics could not be resolved by IN13, due to the very high dynamics, which are too far from the timescale defined by the instrumental resolution to be visible in the accessible length-scale (see also Section 4.2).

QENS experiments were carried out on C1-lipids, P2-lipids and C1-P2-lipids, using the time-of-flight spectrometers IN5, Osiris and Neat with the same energy resolutions and Q-ranges as described in Section 4.2. Molecular motions occurring on different length-scales and on a very broad time domain were investigated, and will be compared to the lipids, in order to study the influence of myelin proteins on such molecular motions. The measurements and the data corrections were performed in an analogous manner as for the lipids (Section 4.2), namely at 230 K and 300 K, corresponding to the gel and to the liquid phase of the phospholipids, for the in-plane and for the out-of-plane configurations.
In order to describe membrane dynamics influenced by the myelin proteins, the same model functions as used for the lipids, $S^{300K}_{theo}(\vec{Q},\omega)$ (Eq. 2.46) for data obtained at 300 K, and $S^{230K}_{theo}(\vec{Q},\omega)$ (Eq. 2.47) for data obtained at 230 K, were applied to the quasielastic spectra. The fitting procedure can be found in Section 4.2. For the C1-lipids the fixing of the HWHM of the additional Lorentzian, Γ, to $2/\tau$ was not possible, since for the first Q-groups of Neat data smaller values for Γ were necessary.
Fig. 5.10 shows quasielastic spectra of all samples measured on IN5 at 300 K (upper panels) and 230 K (bottom panels) for in-plane configuration (left) and out-of plane configuration (right).

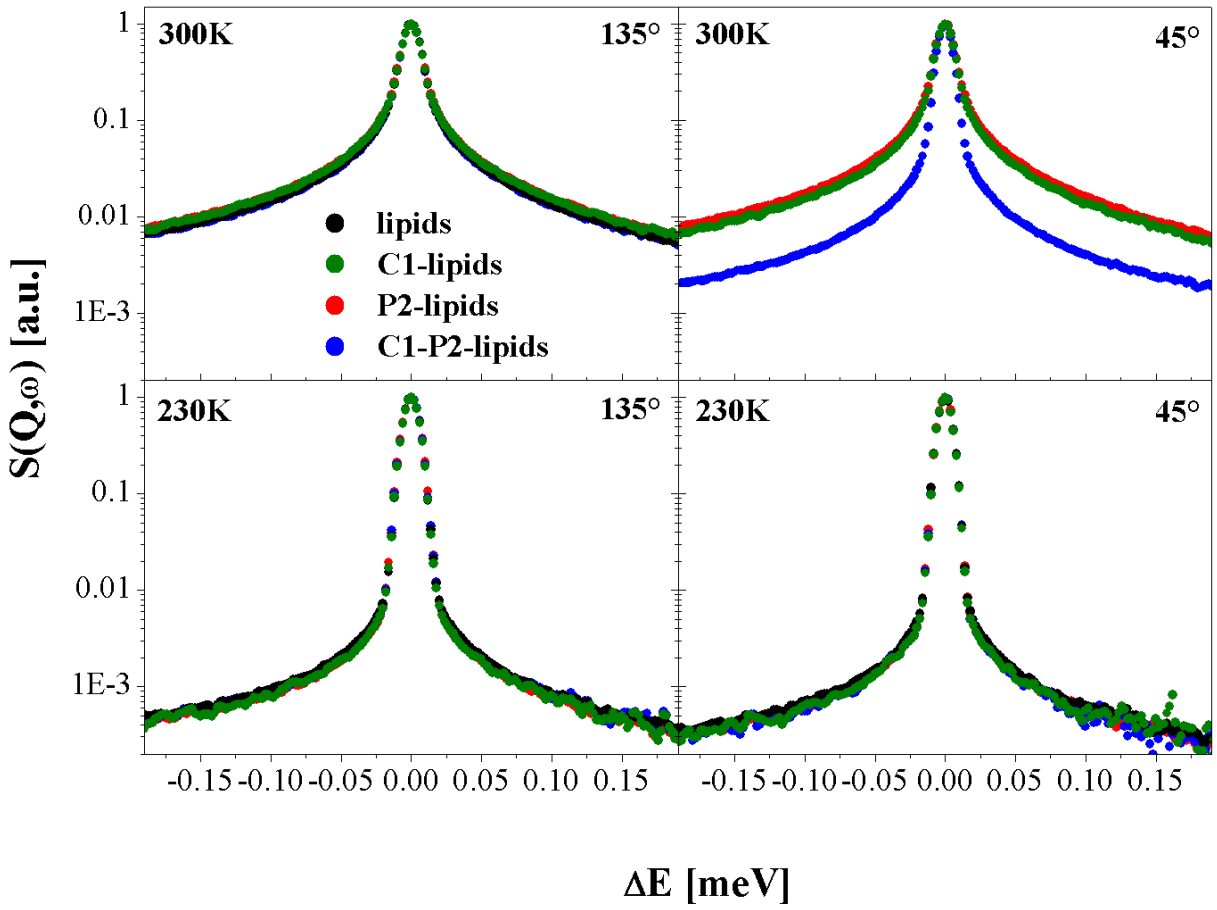

Figure 5.10: QENS spectra of lipids (black circles), C1-lipids (green circles), P2-lipids (red circles) and C1-P2-lipids (blue circles) measured on IN5. Data are shown for 300 K (top) and 230 K (bottom) for in-plane configuration (left) and out-of-plane configuration (right). The normalized intensities were integrated over the whole accessible Q-range.

The intensities are normalized and integrated over the whole accessible Q-range. It is clearly visible that the C1-P2-lipids (blue circles) show a smaller quasielastic contribution at 300 K with respect to the other samples, in the out-of-plane configuration, indicating a less dynamic membrane.
First of all, the resulting fitting parameters for data obtained in the ordered gel phase of the lipids, at 230 K, are shown in Table 5.3. It is obvious that the elastic contribution f of the

Sample 230 K	R_V [Å]	D_V [$\mathrm{cm}^2/\mathrm{s}\ 10^{-5}$]	R [Å]	τ [meV^{-1}]	f	$p_{V\otimes Rot}$
lipids, out-of-plane	6	0.10	1.1	6.65	0.91	0.10
C1-lipids, out-of-plane	9	0.06	1.1	1.07	0.89	0.11
P2-lipids, out-of-plane	3	0.33	1.6	6.60	0.96	0.04
C1-P2-lipids, out-of-plane	3	0.77	2.2	4.00	0.96	0.04
lipids, in-plane	3	0.68	1.2	2.03	0.92	0.08
C1-lipids, in-plane	9	0.02	2.0	9.35	0.92	0.09
P2-lipids, in-plane	6	0.02	1.0	10.00	0.79	0.21
C1-P2-lipids, in-plane	8	0.02	1.0	9.86	0.79	0.21

Table 5.3: Fitting parameters for data obtained at 230 K for the lipids, the C1-lipids, the P2-lipids and the C1-P2-lipids. The absolute errors are $\Delta R_V \approx \pm 1$ Å, $\Delta D_V \approx \pm 0.01\, 10^{-5}\mathrm{cm}^2/\mathrm{s}$, $\Delta R \approx \pm 0.5$ Å, $\Delta\tau \approx \pm 0.01\,\mathrm{meV}^{-1}$ and $\Delta f \approx \Delta p_{V\otimes Rot} \approx 0.05$.

scattering function is very high and the quasielastic contribution $p_{V\otimes Rot}$ is much smaller. Nevertheless, differences are observed within the small fraction of hydrogens undergoing molecular motions. With a diffusion constant of $D_{V1} = 0.06\, 10^{-5}\,\mathrm{cm}^2/\mathrm{s}$ for the C1-lipids in the out-of-plane configuration, the confined diffusion is slowed down, compared to the other samples at this configuration. The radius R_V of the confined diffusion is correspondingly larger. This agrees with the results obtained on IN13, which indicated that the membrane behaves harmonically up to higher temperatures, induced by MBP-C1, and thus influences methyl group rotation. In contrast, the correlation time τ is smaller for the C1-lipids in the out-of-plane configuration, indicating that rotation of the methylene groups with radii of rotation of ≈ 1.1 Å, as already found for the lipids (Section 4.2), is faster. For the in-plane configuration, no significant differences are observed for the two molecular motions.
In contrast, data obtained in the liquid phase, at 300 K, differ regarding the lipids and the lipids with proteins. As described in Section 4.2, the slow confined diffusion, described by Volino 1, was assigned to the upper part of the lipids, including the headgroups and the double bond of the vinyl group, and the fast confined diffusion, described by Volino 2, to the terminal part of the lipids, from the last methylene group until the double bond. Fig. 5.11 shows an example for the fitting of the model function to spectra obtained on IN5 at 300 K in the out-of-plane configuration for the lipids and for the C1-P2-lipids at $Q \approx 0.9\,\mathrm{Å}^{-1}$. The quasielastic broadening of the C1-P2-lipids is significantly smaller compared to the lipids, as already seen in the raw data. The elastic contribution, shown in

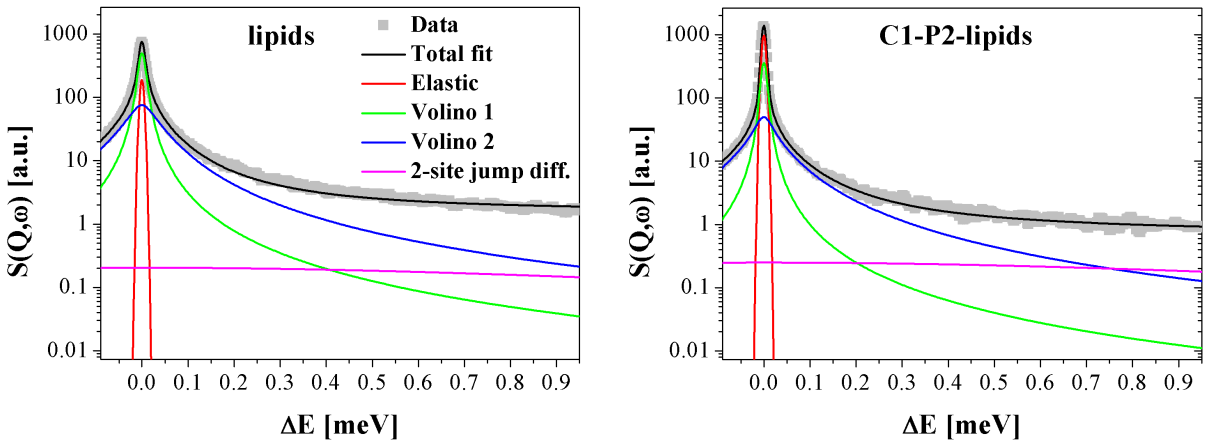

(a) (b)

Figure 5.11: Normalized QENS data obtained on IN5 for the lipids (left) and the C1-P2-lipids (right) in out-of-plane configuration at 300 K for $Q \approx 0.9\,\text{Å}^{-1}$.

red, is larger for the C1-P2-lipids than for the lipids.
The resulting fitting parameters, including the parameters obtained for the lipids for comparison, are listed in Tables 5.4 and 5.5. Fig. 5.12 illustrates schematically the fitting parameter f, which represents the contribution of immobile hydrogen atoms, obtained for IN5, Osiris and Neat. It is obvious that f is dominant for the C1-P2-lipid data obtained

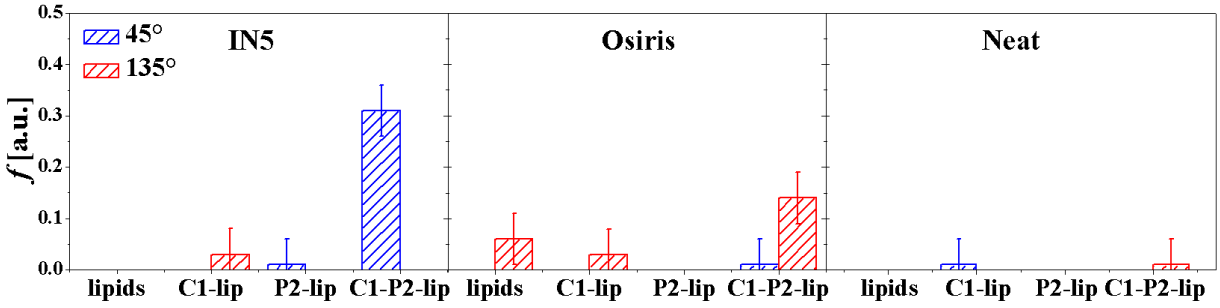

Figure 5.12: Fitting parameter f, indicating the fraction of immobile hydrogen atoms, obtained for IN5 (left), Osiris (middle) and Neat (right). The out-of-plane configuration is marked in blue and the in-plane configuration in red.

on IN5 for the out-of-plane configuration, indicating that the membrane dynamics are significantly reduced by MBP-C1 and P2 proteins. The large fraction of immobile hydrogen atoms indicates an enhanced rigidity induced by MBP-C1 and P2 proteins.
In Figs. 5.13 a and b the radii of confinement R_{V1} and the diffusion constants D_{V1}, described by Volino 1, are shown. Figs. 5.13 c and d represent the corresponding parameters R_{V2} and D_{V1} of Volino 2. As obtained for the lipids, the diffusion constant D_{V1} of hydrogen populations belonging to the upper part of the lipids is approximately one order of

Sample 300 K	R_{V1} [Å]	D_{V1} [$cm^2/s\ 10^{-5}$]	R_{V2} [Å]	D_{V2} [$cm^2/s\ 10^{-5}$]	d [Å]	τ [meV^{-1}]	Γ [meV]
lipids, out-of-plane	6	0.15	7	1.1	2.5	1.36	1.47
C1-lipids, out-of-plane	6	0.17	5	1.8	2.4	1.00	0.52
P2-lipids, out-of-plane	4	0.15	6	1.3	2.5	1.31	1.53
C1-P2-lipids, out-of-plane	6	0.09	4	1.7	2.3	1.32	1.52
lipids, in-plane	4	0.16	5	1.8	2.5	0.93	2.15
C1-lipids, in-plane	5	0.25	5	2.3	2.3	0.80	0.77
P2-lipids, in-plane	5	0.19	7	1.8	2.1	0.92	2.17
C1-P2-lipids, in-plane	4	0.19	6	1.3	2.2	1.32	1.51

Table 5.4: Fitting parameters for data obtained at 300 K with the following absolute errors: $\Delta D_{V1} \approx \pm 0.01\, 10^{-5} cm^2/s$, $\Delta D_{V2} \approx \pm 0.1\, 10^{-5} cm^2/s$, $\Delta R_{V1} \approx \Delta R_{V2} \approx \pm 1$ Å, $\Delta d \approx \pm 0.5$ Å, $\Delta\tau \approx \pm 0.01\, meV^{-1}$ and $\Delta\Gamma \approx \pm 0.05$ meV.

Sample 300 K	p_{V1}	p_{V2}	p_{Jump}	f	p_{Lor}
lipids, out-of-plane	0.49;0.45;0.03	0.40;0.40;0.44	0.11;0.15;0.53	0;0;0	0;0;0.09
C1-lipids, out-of-plane	0.53;0.52;0.08	0.42;0.41;0.43	0.05;0.08;0.49	0;0;0.01	0;0;0.27
P2-lipids, out-of-plane	0.49;0.40;0.04	0.48;0.51;0.46	0.02;0.10;0.50	0.01;0;0	0;0;0.08
C1-P2-lipids, out-of-plane	0.28;0.46;0	0.24;0.53;0.44	0.16;0.04;0.55	0.31;0.01;0	0;0;0.06
lipids in-plane	0.59;0.37;0.15	0.41;0.35;0.42	0;0.22;0.43	0;0.06;0	0;0;0.08
C1-lipids in-plane	0.52;0.51;0.10	0.37;0.34;0.43	0.08;0.13;0.48	0.03;0.03;0	0;0;0.31
P2-lipids in-plane	0.51;0.46;0.09	0.40;0.40;0.46	0.09;0.14;0.45	0;0;0	0;0;0.08
C1-P2-lipids in-plane	0.47;0.41;0.07	0.40;0.45;0.52	0.13;0.19;0.40	0;0.14;0.01	0;0;0.07

Table 5.5: Fitting parameters obtained for hydrogen populations p_{V1} , p_{V2}, p_{Jump} and f and for the fraction of the Lorentzian p_{Lor} for data measured at 300 K for all instruments. The absolute errors are ≈ 0.05 for all parameters. The first values are for parameters obtained for IN5, the second values for parameters obtained for Osiris and the third values for parameters obtained for Neat, respectively.

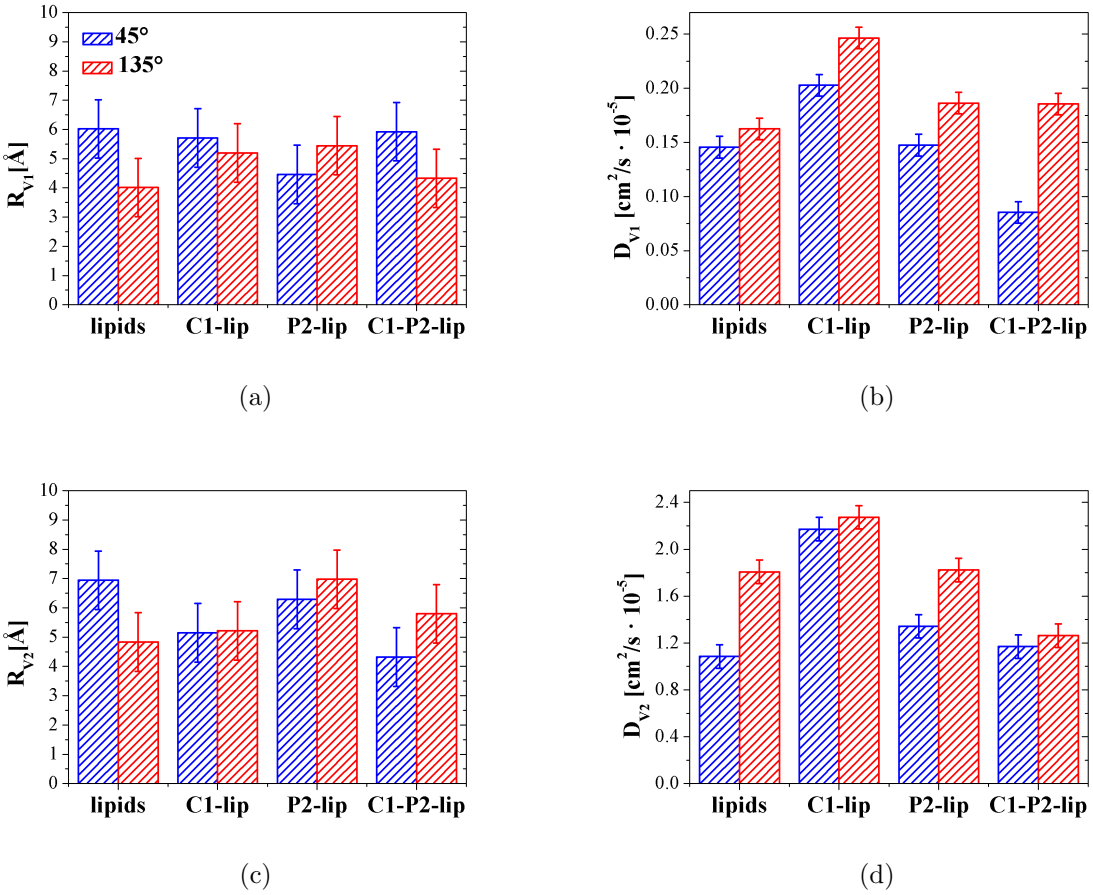

Figure 5.13: Radii of confinement R_{V1} (a) and diffusion constants D_{V1} (b), described by Volino 1 and R_{V2} (c) and diffusion constants D_{V2} (d), described by Volino 2. Blue bars: out-of-plane configuration; red bars: in-plane configuration.

magnitude smaller than the diffusion constant D_{V2} of populations belonging to the terminal part, for all membrane samples (Figs. 5.13 b and 5.13 d). Regarding the membrane orientations, the out-of-plane configuration (parallel to the lipid chains, blue bars in Fig. 5.13) and the in-plane configuration (perpendicular to the lipid chains, red bars), the confined diffusion is constantly faster in the in-plane configuration. This effect is seen in all samples and thus not influenced by MBP-C1 and P2 proteins.
For the radii of confinement R_{V1} and R_{V2}, values of approximately 5 Å were obtained for all samples (Figs. 5.13 a and 5.13 c), including the lipids (see Section 4.2).
For the population p_{Jump}, which was visible mainly on Neat, jump distances d between 2.1 Å and 2.5 Å were obtained, which can be attributed to 2-site jump diffusion of the hydrogen atoms belonging to CH_2 molecules in the lipid chains (Section 4.2). The jump distance does not seem to be influenced by MBP-C1 and P2 proteins. Hence, this population seems to be present in both protein-free membrane domains and in protein-lipid domains. However, the residence time τ is larger for the out-of-plane configuration than for the in-plane configuration, indicating slower jumps in the direction parallel to the lipid chains. For the C1-lipids, τ is smaller for both configurations compared to the other samples, which suggests that the methylene groups perform faster jumps, when MBP-C1 is present in the membrane.
It has to be remarked that with QENS, the average dynamics of all hydrogen atoms in the samples are investigated and described with this model. However, one cannot distinguish between membrane domains not influenced by MBP-C1 proteins and membrane domains in which the lipids remain unaffected. The diffraction data (Section 5.1) revealed that large quantities of the multilayers are influenced in terms of membrane structure (85 % for C1-lipids, 100 % for P2-lipids and 93 % for C1-P2-lipids), even if the surface area of protein-bound lipids is much less, with respect to the one of protein-free lipids (0.31 %, 0.23 % and 0.41 %).
By adding the P2 protein to the membrane, the diffusion coefficient of the slow diffusion D_{V1}, and of the fast diffusion D_{V2}, do not change significantly compared to the lipids, for both the in-plane and the out-of-plane configuration. A possible explanation for this could be the following: on the one hand, compared to the diffraction results (Section 5.1), the d-spacings found for the P2-lipids are indeed larger than for the lipids, which could enhance the lipid dynamics, but on the other hand, due to the electrostatic potential of P2, which has a positive charge distribution at the two opposing sides of the protein, interacting strongly with negatively charged lipids, this enhancement of the membrane dynamics is probably compensated. Additionally, the α-helical lid penetrating partially into the bilayer might reduce the lipid flexibility. Hence, no differences in the confined diffusions were obtained, with respect to the lipids.
When the MBP-C1 protein is present in the membrane, the slow diffusion of fraction p_{V1} is faster compared to the lipids, even more in the in-plane configuration. Regarding the diffusion of fraction p_{V2}, the diffusion coefficient is larger for both configurations. This effect could be due to the increase of the d-spacing ($A_1 = 79$ Å) caused by MBP-C1 proteins, penetrating ≈ 2 Å at each side into the bilayer, which accounts for ≈ 76 %, with respect to the protein-free lipids ($D_1 = 59$ Å). This increases the space for the lipid chains

in both directions, parallel and perpendicular to the membrane plane. Thus, the confined diffusions performed by hydrogen populations in the upper and in the lower part of the lipids, are enhanced for both configurations. Since the positive electrostatic potential of MBP-C1 is homogeneously distributed on the protein surface, but not concentrated on the lipid-bound protein area, the electrostatic interactions with the lipids are probably less than for P2 and a compensation of the enhanced flexibility might be excluded. The results are related to former studies on MBP bound to a reconstituted oriented membrane: Natali *et al.* [133, 31, 134] have shown with QENS experiments on IN16 and EINS experiments on IN13 that dynamics of a DMPA membrane are significantly enhanced by MBP, purified in the lipid-free form from mammalian CNS, above the gel to liquid phase transition, in particular in the out-of-plane direction. However, the protein concentration was with 5 % by weight much higher than in our case, which has to be considered for the interpretation. For the C1-P2 lipids, the fraction of immobile hydrogen atoms, f, as already shown in Fig. 5.12 (left), is dominant for data obtained on IN5 in the out-of-plane configuration. This suggests an enhanced rigidity of a given membrane motion induced by MBP-C1 and P2 proteins. In addition, the diffusion coefficient D_{V1} of the fraction p_{V1}, representing the population of the upper part of the lipids, is much smaller with respect to all other samples for this configuration. This indicates a reduction in diffusive motions of the upper part of the lipids for the out-of-plane configuration. These results are in agreement with AFM observations of Suresh *et al.* [59], which indicate that MBP-C1 and P2 synergistically increase membrane stacking. This stacking effect could be caused by an enhancement of the adhesiveness between bilayers due to MBP and P2. Since the C1-P2-lipids contain three times more P2 than MBP-C1 proteins, it was assumed that MBP-C1 and P2 molecules arrange in such a way that assemblies of three P2 proteins and one MBP-C1 protein are formed. The electrostatic potential of three P2 proteins together is much larger than for one P2 protein alone, and furthermore the MBP-C1 protein associated to those P2 proteins would have to penetrate deeply into the bilayer, as suggested with diffraction data. A less ordered membrane domain, containing proteins, with a d-spacing $Z_1 = 81\,\text{Å}$ was not present, indicating that all proteins are located in the more ordered domains, probably in those with a d-spacing of $C_1 = 66\,\text{Å}$. This supports the hypothesis that MBP-C1 and P2 act synergistically to induce membrane stacking. With the stacking effect and the much higher positive electrostatic potential of the protein assemblies, the reduction of the confined diffusion performed by hydrogens belonging to the upper part of the lipids, including headgroups and the chain up to the vinyl group, for the out-of-plane configuration, can be explained. On the one hand, the upper lipid parts are affected due to the deep penetration of MBP-C1 proteins and on the other hand they are affected by the strong electrostatic interactions with the P2 proteins. However, the diffusion constant D_{V1} in the in-plane configuration is of the same order of magnitude as for lipids, indicating that the restricted diffusion perpendicular to the lipid chains in not affected by the proteins. The diffusion constant D_{V2}, representing hydrogen atoms in the terminal part of the lipids, does not differ significantly to the one of the lipids in out-of-plane direction, but is smaller in the in-plane direction.

5.2.1 Conclusions

In order to investigate the influence of myelin proteins MBP-C1 and P2 on structure and dynamics of a model PNS-myelin membrane, neutron diffraction, EINS and QENS measurements have been performed.
The diffraction results reveal that in the lipid gel phase, all membranes exhibit the same repeat distance. Since the Bragg peaks at low Q for the C1-lipids and the P2-lipids are larger with a higher intercept, a less ordered membrane domain with a large d-spacing containing squeezed out proteins was suggested. This is in agreement with previous observations [28, 29, 30], indicating that MBP-C1 is squeezed out a bilayer in the gel phase, and preferentially binds to lipids in the liquid phase. These domains does not exist for the C1-P2-lipids, probably due to their stacking effect when present together in a bilayer. In the liquid phase of the lipids, the membrane structure is strongly affected by myelin proteins. Whereas the lipids have the same repeat distance as in the gel phase, for the C1-lipids and C1-P2-lipids only a small membrane fraction was found, which show a d-spacing characteristic for the lipids, suggesting that a large area is influenced by the proteins, although the protein-bound surface in the membranes is less than 1 %. Indeed, for the P2-lipids, a d-spacing characteristic for the lipids does not exist at all.
For the C1-lipids, a membrane fraction of 47 % shows a d-spacing of $A_1 = 79\,\text{Å}$ and a less ordered fraction of 38 % shows a d-spacing of $Z_1 = 81\,\text{Å}$, indicating that these domains are influenced by MBP-C1. The protein fits between the bilayers with a d-spacing of A_1, if penetrating partially into opposing bilayers ($\approx 2\,\text{Å}$ at each side). Regarding the protein distribution in the membrane, the space between two lipid-bound proteins would be large enough for a relaxation of the bilayers from a d-spacing of 79 Å (containing the protein) to an initial d-spacing for protein-free domains. The less ordered membrane fraction ($Z_1 = 81\,\text{Å}$) was suggested to contain squeezed out proteins, but less than in the gel-phase.
The P2-lipids exhibit two repeat distances of $B_1 = 74\,\text{Å}$ and $C_1 = 65\,\text{Å}$, which are larger than for the lipids and correspond to inter bilayer spacings of 37 Å and 28 Å. The first one probably contains the protein, with the α-helical "lid" penetrating partially into the bilayers, and the second seems to be an intermediate distance between membrane domains containing P2 proteins and protein-free domains, due to a widening of adjacent bilayers. The d-spacing of Z_1 was also present, indicating a less ordered membrane fraction with maybe squeezed out proteins. Regarding the ideal case of a homogeneous protein distribution in the membrane, the distance between lipid-bound proteins would not be sufficient for complete relaxation of the bilayers to their protein-free state.
For the C1-P2-lipids, approximately 7.3 % of the membrane have a repeat distance characteristic for the lipids. The two repeat distances found for P2-lipids also occur, but the distance for the C1-lipids was not visible. Assuming that three P2 proteins and one MBP-C1 protein arrange side by side in assemblies that are homogeneously distributed, the proteins are probably present in the membrane fraction with a d-spacing of C_1. The MBP-C1 proteins would have to penetrate deeply into opposing bilayers. Adjacent membrane fractions probably show an intermediate d-spacing of B_1, as seen for the P2-lipids. The distance between such protein assemblies would be large enough for relaxation of membrane

domains in between them with a d-spacing characteristic for the lipids. A less ordered domain was not present, probably due to the stacking effect of MBP-C1 and P2 proteins together.
Temperature scans revealed a similar structural behavior as previously found for the lipids: a common transient Bragg peak occurs after the gel-to-liquid phase transition temperatures of the lipids, which arose not before the anionic DOPS lipids also transformed into the liquid-disordered phase ($\approx 259\,\mathrm{K}$) and disappeared at the melting point of the ice (D_2O). This suggests a common structural phase for all samples.
EINS temperature scans on IN13 indicated that all membrane samples show a common harmonic behavior at low temperature. A transition to an anharmonic regime occurs for lipids, P2-lipids and C1-P2-lipids at $\approx 160\,\mathrm{K}$ for the in-plane and at $\approx 200\,\mathrm{K}$ for the out-of-plane configuration. However, for the C1-lipids, this transition appears at $\approx 200\,\mathrm{K}$ (in-plane) and at $\approx 220\,\mathrm{K}$ (out-of-plane). The transition from a harmonic to an anharmonic regime, which occurs below the phase transition of the lipids, could be attributed to rotation of the methyl groups (CH_3 molecules) in the lipid chains and in the proteins. Methyl group rotation was found to enter at approximately 150 K in the time windows of the instruments [118, 119, 120, 121, 122] and seems to be significantly influenced by MBP-C1 proteins. A further transition was found at $\approx 250\,\mathrm{K}$ for all samples and in both configurations. Comparing to DSC measurements, this transition seems to be caused by the gel-to-liquid phase transition of the lipids. The melting of the surrounding D_2O, which initiates at $\approx 277\,\mathrm{K}$ and could affect the membrane dynamics, could not be resolved, due to the experimental protocol with large temperature steps. For the C1-lipids, the MSD is smaller in a temperature range from $\approx 200\,\mathrm{K}$ to $\approx 270\,\mathrm{K}$, particularly in the out-of-plane configuration. This suggests a reduction in the membrane dynamics in the region encompassing the gel-to-liquid phase transitions of the lipids and the water melting point, induced by MBP-C1 proteins. Dynamics for $T > 280\,\mathrm{K}$ were outside the timescale of IN13 to be visible in the accessible Q-range.
The results of the QENS studies on IN5, Osiris and Neat, have revealed that membrane dynamics in myelin model membranes containing MBP-C1 and P2 proteins are performed by four different hydrogen populations, analogous to the lipids (Section 4.2): a fraction performing only vibrational motions, described by f, a fraction belonging to the upper part of the lipid molecules, from the headgroups until the vinyl group, and diffuses in a confined, spherical volume, represented by p_{V1}, a fraction belonging to the terminal part of the lipids that diffuses faster than p_{V1} in a confined volume described by p_{V2} and finally p_{Jump}, which is a population belonging to the methylene groups (CH_2) of the lipid chains, which undergoes 2-site jump diffusion. Both diffusive motions have been found to be faster in the in-plane configuration with radii of confinement of $\approx 5\,\text{Å}$ for all samples. The jump distance is not influenced by MBP-C1 and P2 proteins, and thus probably occurs in both protein-free lipid domains and in protein-lipid domains. However, the residence time τ is smaller for the C1-lipids for both configurations, suggesting faster jumps of the methylene groups when MBP-C1 is present in the membrane. Regarding the confined diffusive motions performed by the populations p_{V1} and p_{V2}, the P2 protein has no influence, which could be explained by our diffraction data and the electrostatic potential of P2: on the one

hand, the d-spacings characteristic for the P2-lipids are larger than the d-spacings found for the lipids, which probably induce more flexibility of the lipids. On the other hand, the positive electrostatic potential of P2, which is concentrated at the two opposing sites of the protein, probably compensates for this increase of the membrane dynamics, due to strong electrostatic protein-lipid interactions. In addition, the α-helical lid, which penetrates partially into the bilayer probably reduces the lipid flexibility. The MBP protein enhances the diffusive motions of fraction p_{V1} belonging to the upper part of the membrane for the in-plane configuration and diffusive motions performed by fraction p_{V2} belonging to the final lipid part, for both configurations. This could be explained by the structure of the C1-lipids, which shows a large fraction of a increased d-spacing, with respect to the lipids, induced by MBP-C1 proteins, penetrating into the bilayer. Thus, the lipids can be more flexible in all directions, resulting in increased diffusive motions for the whole lipid molecule (p_{V1} and p_{V2}) for both the in-plane and the out-of-plane configuration. A compensation of this enhanced flexibility caused by the electrostatic potential of MBP-C1, as suggested for the P2 proteins, might be excluded, since the positive net charge is quite homogeneously distributed, and not concentrated on the lipid-bound protein surfaces, as for P2. These results on MBP-C1 on the influence of lipid dynamics in the liquid phase are related to former neutron studies done by Natali *et al.* [133, 31, 134]. In contrast, for low temperature (230 K) MBP-C1 slows down diffusive motions of fraction $p_{V\otimes Rot}$ with a larger radius of confinement R_V for the out-of-plane configuration, corresponding to the results obtained on IN13, which indicated that the behavior of the MSDs remains harmonic up to higher temperatures and thus influences methyl group rotation. MBP-C1 and P2 proteins bound together to a reconstituted membrane have the most significant effect on membrane dynamics: the fraction of immobile hydrogen atoms is dominant for the out-of-plane direction, suggesting a reduction of given membrane dynamics. The diffusion coefficient D_{V1} of the fraction p_{V1} is reduced for the out-of-plane configuration, with respect to the other samples. This is probably first due to a synergistical stacking effect of both proteins on the membrane, which was suggested by Suresh *et al.* [59] and which was indicated by the absence of a less ordered membrane domain with squeezed out proteins, as shown with neutron diffraction. Secondly, the electrostatic interaction of a protein assembly containing three P2 proteins and one MBP-C1 protein with the bilayer is probably very strong. This interaction, caused by the positive charge distribution of three P2 proteins, which is concentrated on the opposing sides of the lipid-bound surfaces, probably reduces strongly the membrane dynamics occurring in the upper part of the lipids for the out-of-plane configuration. However, a clear picture of the arrangement of MBP-C1 and P2 proteins within the membrane is not yet available and is required for an accurate interpretation of the results on membrane dynamics.

In summary, these results give following information about the influence of the myelin-associated proteins MBP-C1 and P2 on the structure and dynamics of a model myelin membrane: (i) Neutron diffraction data revealed that below the phase transitions of the lipids DOPC (at $T \approx 254$ K) and DOPS (at $T \approx 259$ K), i. e. in the gel phase, all membrane sample have the same d-spacing and the C1-lipids and P2-lipids a less-ordered domain with squeezed out proteins, which is not the case for the C1-P2-lipids, probably

due to a stacking effect. However, the lipid phase transitions allowed the protein-bilayers to relax into an equilibrium state in which the MBP-C1 and P2 proteins were able to rearrange and affect the bilayer structure, even at low protein concentration. The C1-lipid and the C1-P2-lipid sample showed only a small membrane fraction, which remained unaffected by the proteins, whereas for the P2-lipid sample, these domains do not exist. (ii) EINS experiments identified a dynamical transition in DOPS-DOPC bilayers in the temperature region between 250 K and 270 K caused by the gel-to-liquid phase transitions of the lipids. It has been shown that MBP-C1 reduces dynamics in this temperature region, particularly in the out-of-plane configuration, parallel to the lipid chains. (iii) Finally, QENS data indicated that MBP-C1 and P2 together strongly influence the lipid dynamics in the liquid phase. In the disordered liquid phase, where the proteins are free to form domains and affect the membrane structure, large reductions are observed in the dynamics of the upper parts of the lipids in the out-of-plane configuration. In the gel-phase (230 K), MBP-C1 was found to reduce diffusive motions of the membrane, which confirms the EINS results. Together, these results support a model in which the myelin proteins MBP-C1 and P2 can associate and form domains in the membrane. The proteins promote adhesions between the bilayers, which is consistent with previous work of Suresh *et al.* [59], and thus reduce the dynamics of the membrane.

Chapter 6

Influence of MBP-C1 and MBP-C8 Proteins on the Structure and Dynamics of Model Myelin Membranes

In order to study diseased and healthy myelin, the influence of MBP-C8, a mutated form of the MBP protein, which has properties similar to the highly modified form seen in MS-patients, on the structure and the stability of model myelin membranes has been investigated. Therefore, neutron scattering experiments on reconstituted membranes containing MBP-C1 and MBP-C8 proteins, respectively, were performed and the results were compared to the observations of a protein-free membrane. The protein concentrations for the experiments described in this chapter, was increased 4-fold and 9-fold, and the results were compared to those of the C1-lipids (1-fold concentration, described in Chapter 5), in order to investigate also the influence of the protein amount on the membrane dynamics. For an accurate interpretation of the results, each data set (4-fold and 9-fold) will be compared to the protein-free lipids containing the same concentration of protein buffer. For detailed protein and buffer concentrations, see Table 3.1 in Chapter 3. The structure was investigated using neutron diffraction on D16 (ILL) on membranes containing the highest protein and buffer amount. In order to study the dynamics of those membranes as function of the temperature, EINS experiments have been performed on the backscattering spectrometer IN16. Quasielastic measurements on the time-of-flight spectrometers IN5 at two different energy resolutions allowed detailed analysis of molecular motions occurring in the phospholipid multilayers. Experiments on the time-of-flight spectrometer IN6 at the same energy resolution as the one on IN5 were also performed to guarantee the reproducibility of the data. First of all, results obtained for membranes containing 9-fold protein concentrations will be discussed and finally the results observed for membranes containing 1-fold, 4-fold and 9-fold protein concentrations will be compared.

6.1 Influence on Structural Properties

Neutron diffraction measurements on membranes with a 9-fold MBP-C1 concentration (sample 9f-C1-lipids) and with a 9-fold MBP-C8 concentration (sample 9f-C8-lipids), respectively, were carried out on D16 at the ILL (see also Subsection 3.3.4 about sample characterization).
Fig. 6.1 shows diffraction patterns as a function of Q at 300 K. The 9f-C1-lipid sample is represented by the green, the 9f-C8-lipid sample by the red curve and the C1-lipid sample, containing a 1-fold protein concentration is plotted in black for comparison. For the

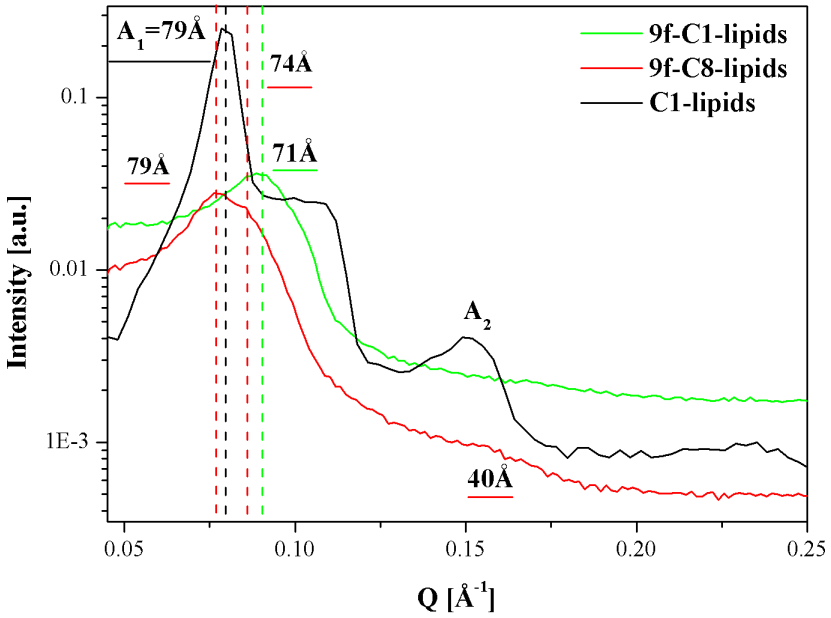

Figure 6.1: Diffraction patterns for the 9f-C1-lipids (green curve), the 9f-C8-lipids (red curve) and the C1-lipids (black curve) at 300 K.

9f-C8-lipids, the first order Bragg peak corresponding to a d-spacing of ≈ 79 Å, as well as the corresponding second order Bragg peak, were found, which is consistent with the repeat distance $A_1 = 79$ Å found for the C1-lipid sample in the liquid phase (see Section 5.1 and Table 5.1). A second peak seems to be present at ≈ 74 Å. However, the repeat distance found for the 9f-C1-lipids is shifted about -10 Å and an additional d-spacing is not present. Both samples do not exhibit the repeat distance $D_1 = 59$ Å characteristic of protein-free DOPS-DOPC lipid domains in the liquid phase, indicating that these domains do not exist. However, for the C1-lipids this repeat distance is clearly visible. It should be noted that the Bragg peaks found for 9f-C1-lipids and 9f-C8-lipids are quite broad, compared to the peak of the C1-lipids. Since the mosaicity, which is a characteristic parameter for the bilayer orientation perpendicular to the membrane plane, was nevertheless low ($\Delta\omega \approx 0.38^\circ$ for 9f-C1-lipids and $\Delta\omega \approx 0.40^\circ$ for 9f-C8-lipids, see Subsection 3.3.4), this broadening could indicate less order within the bilayers in the direction parallel to the

membrane plane or less ordered membrane fractions with larger d-spacings, suggested by the high intercept at low Q. A possible explanation could be firstly, the higher amount of protein buffer, since salts could give the lipids more freedom to move in the liquid phase or secondly, the higher amount of proteins in the membranes, inducing the absence of the d-spacing characteristic for the lipids as well as the higher intercept, which could indicate less ordered membrane fractions containing the excess proteins.

6.2 Influence on Dynamical Properties

In order to study the influence of MBP-proteins, particularly the role of the mutated form MBP-C8, on membrane dynamics, temperature dependent EINS measurements were performed on reconstituted membranes with, and without MBP-C1 and MBP-C8 proteins, using the backscattering spectrometer IN16 with the same experimental conditions as described in Section 4.2. Membrane samples containing a 9-fold protein and correspondingly a 9-fold protein-buffer concentration, the 9f-C1-lipids and the 9f-C8-lipids, were studied and the results were compared to the 9f-lipids. A description of the data analysis and the results obtained for the 9f-lipids, was given in Section 4.2. The results obtained for the 9f-C1-lipids and the 9f-C8-lipids will be compared to those results.
Fig. 6.2 (left) shows the normalized elastic intensities as a function of temperature, integrated over a Q-range from 0.45 Å^{-1} to 1.49 Å^{-1}, and the MSDs $\langle u^2 \rangle(T)$ (right), calculated as described in Section 4.2, for the in-plane configuration. Data obtained for the 9f-lipids

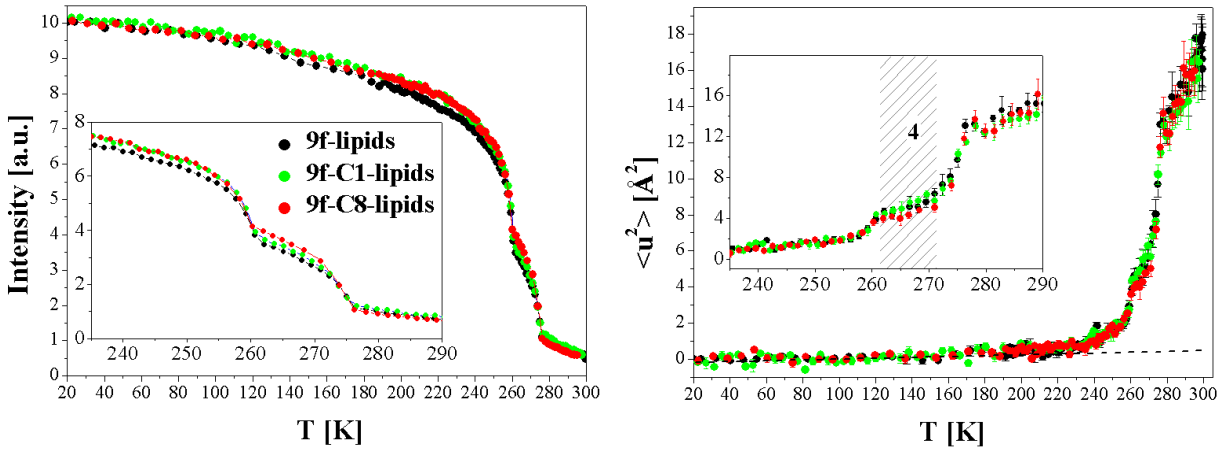

Figure 6.2: Normalized elastic intensities as a function of temperature, integrated over the whole accessible Q-range, for the in-plane configuration (left) and the MSDs as a function of temperature (right). The dashed line represents the regime at low temperature, in which the MSDs behave harmonically. Inset: magnification of the MSDs.

are shown in black, for the 9f-C1-lipids in green and for the 9f-C8-lipids in red. As already discussed in Section 4.2 for the temperature scan of the protein-free lipids (9f-lipids), the

MSDs $\langle u^2 \rangle(T)$ can be divided into six different regimes (1 to 6) (see Fig. 4.9 b in Section 4.2 for demonstration). In the low temperature region, from approximately 20 K to 160 K (regime 1, Fig. 6.2, right), all membranes show a harmonic behavior, resulting in MSDs that increase nearly linearly with Q^2 (illustrated by the dashed line). At $\approx$ 160 K, an kink occurs, which indicates a transition from a harmonic to an anharmonic region. This behavior was attributed to rotation of the methyl groups (CH_3 molecules) and is valid for all samples. In region 4, from $\approx$ 262 K to $\approx$ 271 K, where both lipids are in the liquid disordered phase, but the water is still in the crystalline phase, small differences between the membrane samples are visible, as shown in the inset of Fig. 6.2 (right): the MSDs of the 9f-C8-lipid sample are smaller, indicating a reduction of the membrane dynamics in a temperature region where the gel-to-liquid phase transitions of the lipids are completed, induced by MBP-C8 proteins. This reduction in membrane flexibility probably lasts at least until 271 K and probably until also the phase transition of the crystalline D_2O occurs at $T \approx 277$ K, which cannot be resolved due to the few number of data points between 271 K and 277 K. The MSDs obtained for the out-of-plane configuration show the same behavior, and are therefore not shown here. For $T \geq 280$ K the dynamics are too far from the timescale defined by the instrumental resolution to be visible, which is probably caused by the heavy water in the liquid phase. The Gaussian approximation was not valid for this highly dynamic temperature region.

In order to study the influence of the mutated form of the MBP protein, MBP-C8, on membrane dynamics, QENS experiments were performed on membranes containing MBP-C1 and MBP-C8 proteins at different protein-concentrations, namely on 4f-C1-lipids, 4f-C8-lipids, 9f-C1-lipids and 9f-C8-lipids. Firstly, results obtained for the 9f-samples will be compared to the 9f-lipids (Section 4.3) and secondly results for samples containing different protein concentrations will be compared among each other. Experiments were carried out, similar to the 4f-lipids and the 9f-lipids, on IN5, at the same energy resolutions (Δ E of $\approx 12\,\mu$eV and $75\,\mu$eV, FWHM) and at the same temperature (300 K).
The data was analyzed as described in Chapter 4, similarly as the data obtained for the lipids (lipids, 4f-lipids and 9f-lipids).
Fig. 6.3 shows QENS spectra of the 9f-lipids, the 9f-C1-lipids and the 9f-C8-lipids measured on IN5, normalized and integrated over the whole accessible $Q-$range.

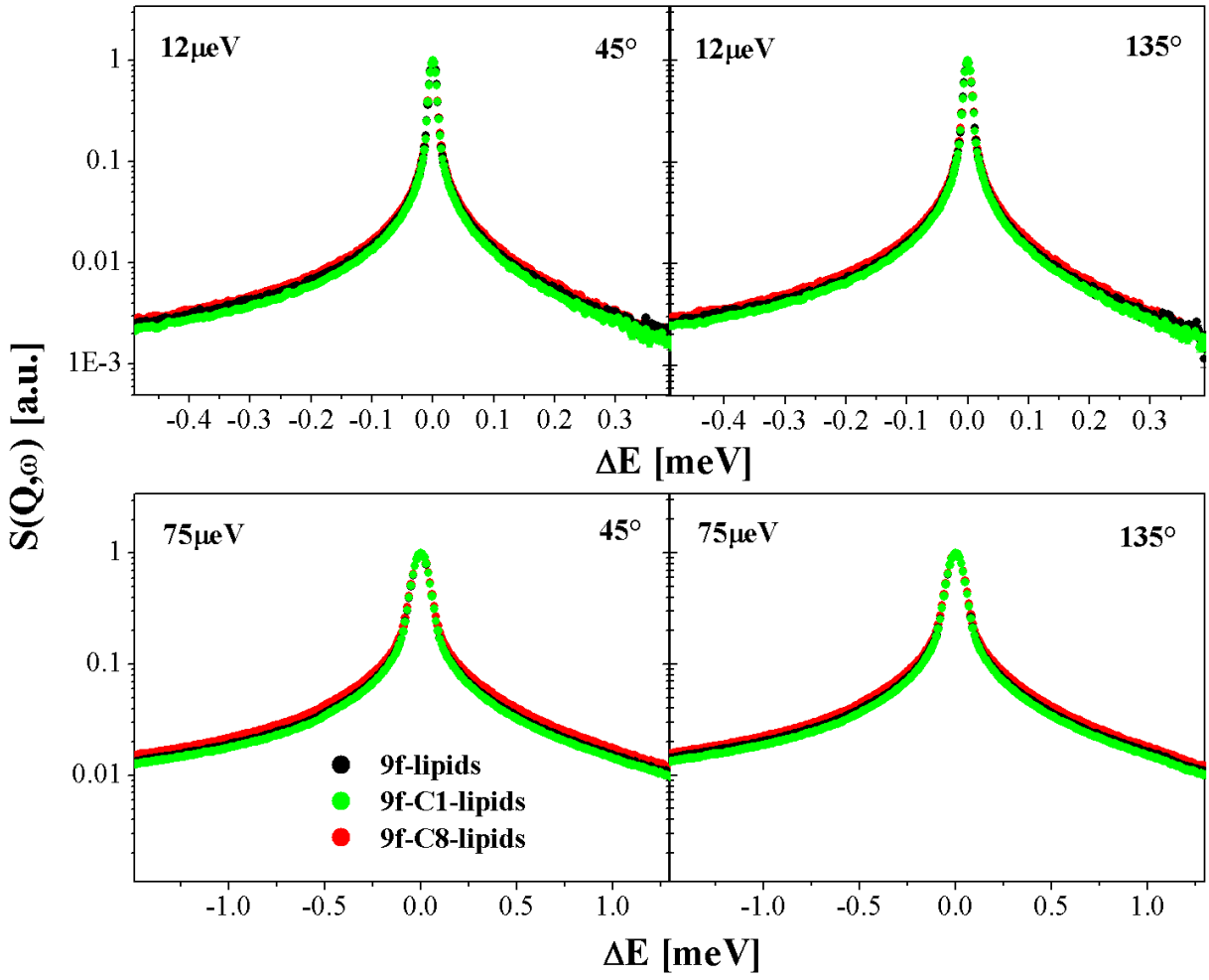

Figure 6.3: QENS spectra of 9f-lipids (black circles), 9f-C1-lipids (green circles) and 9f-C8-lipids (red circles) measured on IN5. Data are shown for $\Delta E \approx 12\,\mu eV$ (top) and $\Delta E \approx 75\,\mu eV$ (bottom) for out-of-plane configuration (left) and in-plane configuration (right). The normalized intensities were integrated over the whole accessible Q-range.

The upper panels show data obtained at $\Delta E \approx 12\,\mu eV$ and the bottom panels data obtained at $\Delta E \approx 75\,\mu eV$ for out-of-plane configuration (left) and in-plane configuration (right). From this first view of the data, without applying any model, the spectra of the 9f-C8-lipid sample (shown in red) seems to have the largest quasielastic broadening compared to the other samples, indicating enhanced molecular motions. However, the differences are very little, and comparing the spectra of each Q-group individually, instead of comparing the spectra summed over Q, would give more detailed information.
In Tables 6.1 and 6.2 the resulting fit parameters are listed. Fig. 6.4 illustrates schemat-

Sample	R_{V1} [Å]	D_{V1} [$cm^2/s\ 10^{-5}$]	R_{V2} [Å]	D_{V2} [$cm^2/s\ 10^{-5}$]	d [Å]	τ [meV^{-1}]	Γ [meV]
9f-lipids, out-of-plane	4	0.65	6	3.7	1.9	2.13	0.94
9f-C1-lipids, out-of-plane	4	0.57	5	3.4	1.9	2.09	0.96
9f-C8-lipids, out-of-plane	5	0.65	7	3.6	1.9	2.36	0.85
9f-lipids, in-plane	7	0.54	6	2.9	2.0	1.22	1.64
9f-C1-lipids, in-plane	4	0.67	8	3.7	1.9	2.06	0.93
9f-C8-lipids, in-plane	5	0.70	7	3.3	1.9	2.39	0.84

Table 6.1: Fitting parameters for data obtained on IN5 with energy resolutions of $\Delta E \approx 12\,\mu eV$ and $\Delta E \approx 75\,\mu eV$, with the following absolute errors: $\Delta D_{V1} \approx \pm 0.01\,10^{-5} cm^2/s$, $\Delta D_{V2} \approx \pm 0.1\,10^{-5} cm^2/s$, $\Delta R_{V1} \approx \Delta R_{V2} \approx \pm 1$ Å, $\Delta d \approx \pm 0.5$ Å, $\Delta\tau \approx \pm 0.01\,meV^{-1}$ and $\Delta\Gamma \approx \pm 0.05$ meV.

ically diffusion constants D_{V1} and D_{V2} and radii R_{V1} and R_{V2} of Volino 1 and Volino 2. As already observed for the lipids, the 4f-lipids and the 9f-lipids (Chapter 4), the diffusion constants D_{V1} are approximately one order of magnitude smaller than the diffusion constants D_{V2}. Referring to NMR studies and molecular dynamics simulations [129, 130, 131], as described in Chapter 4, the slower confined diffusion described by Volino 1, can be assigned to the upper part of the lipid chains, near the lipid headgroups, and the faster confined diffusion, modeled by Volino 2, to the final parts of the lipid chains. The radii of confinement, in which hydrogen atoms belonging to the initial part of the lipid chains, near the headgroups, diffuse, are approximately 4 Å, besides for the 9f-lipids with a large radius of $R_{V1} = (7 \pm 1)$ Å. However, the radii of confinement, in which hydrogens belonging to the final part of the lipid chains, diffuse, are slightly larger, ranging from approximately 5 Å to 8 Å. This could be caused by the higher flexibility of CH_2 molecules in the lipid chains with increasing their distance from the headgroups [129, 130, 131, 71]. However, the radii are in the same order of magnitude as found for MBP-C1 and P2 membranes (≈ 5 Å)

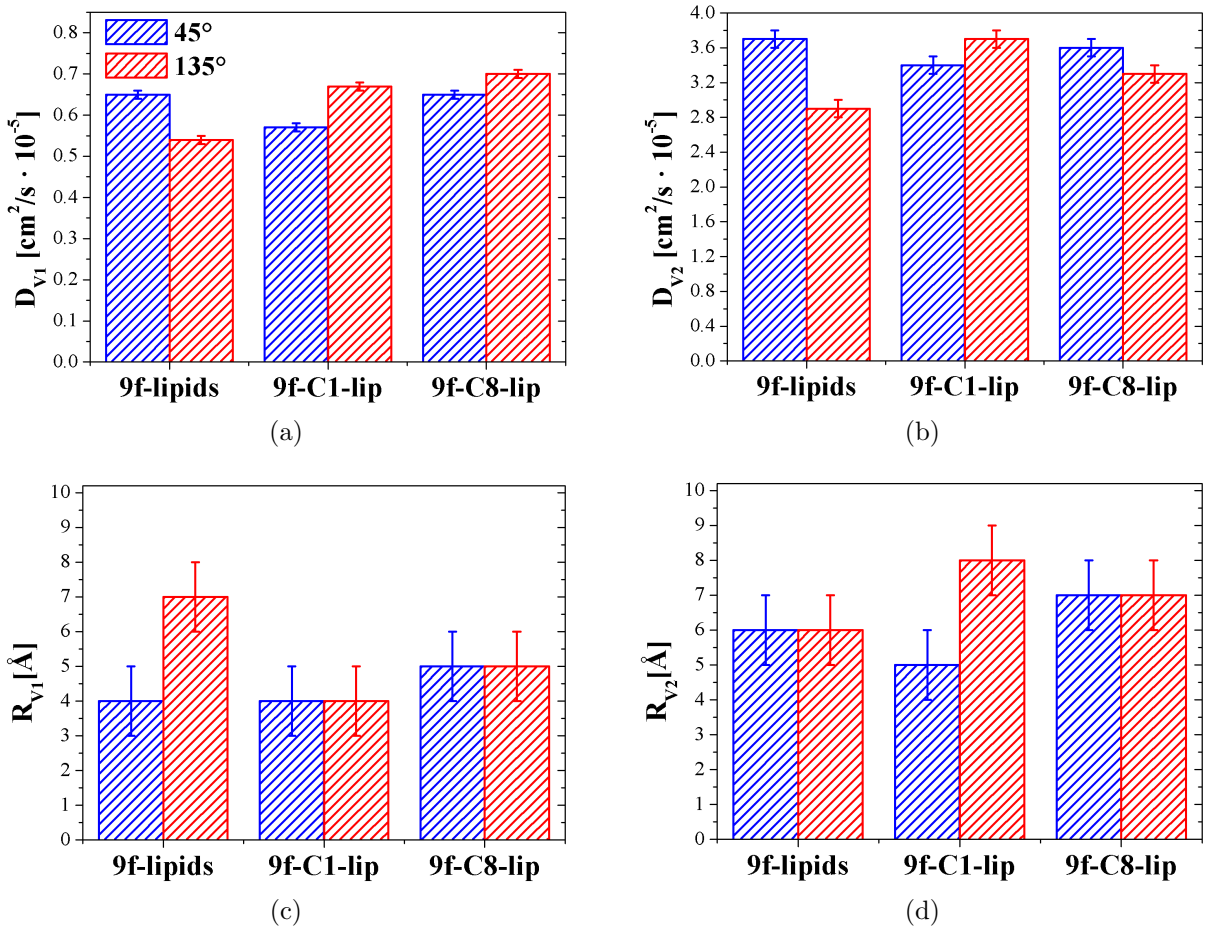

Figure 6.4: Diffusion constants D_{V1} of hydrogen population p_{V1}, described by Volino 1 (a), and D_{V2} of population p_{V2}, described by Volino 2 (b). The corresponding radii of confinement R_{V1} and R_{V2} are shown in panels (c) and (d). Parameters obtained for data in out-of-plane configuration are shown in blue and for data in in-plane configuration in red.

Sample	p_{V1}	p_{V2}	p_{Jump}	f	p_{Lor}
9f-lipids, out-of-plane	0.60 ; 0.52	0.20 ; 0.19	0.15 ; 0.21	0 ; 0	0 ; 0.09
9f-C1-lipids, out-of-plane	0.56 ; 0.50	0.22 ; 0.23	0.20 ; 0.21	0 ; 0	0 ; 0.06
9f-C8-lipids, out-of-plane	0.54 ; 0.50	0.24 ; 0.24	0.19 ; 0.19	0 ; 0	0 ; 0.09
9f-lipids, in-plane	0.44 ; 0.39	0.27 ; 0.28	0.23 ; 0.20	0 ; 0	0 ; 0.2
9f-C1-lipids, in-plane	0.58 ; 0.56	0.18 ; 0.22	0.20 ; 0.22	0 ; 0	0 ; 0.07
9f-C8-lipids, in-plane	0.53 ; 0.49	0.23 ; 0.23	0.20 ; 0.19	0 ; 0	0 ; 0.08

Table 6.2: Fitting parameters obtained for hydrogen populations p_{V1} , p_{V2}, p_{Jump} and f and for the fraction of the Lorentzian p_{Lor} for data obtained on IN5 with energy resolutions of $\Delta E \approx 12\,\mu eV$ and $\Delta E \approx 75\,\mu eV$. The absolute errors are ≈ 0.05 for all parameters. The first values are for parameters obtained at $12\,\mu eV$ and the second values for parameters obtained at $75\,\mu eV$, respectively.

and are consistent with the radii found with QENS studies and molecular simulations on liposomes [86, 128], as described in Section 5.2.

The resulting jump distances d of the 2-site jump diffusion, described by $S_{Jump}(\vec{Q},\omega)$, are approximately (2.0 ± 0.5) Å for all samples. Similar to MBP-C1 and P2 membranes, the fraction p_{Jump} can be attributed to 2-site jumps of hydrogens belonging to the methyl groups (CH_2) in the lipid chains, which remains unaffected by MBP proteins.

Regarding the membrane dynamics, described by Volino 1 and Volino 2, of the protein-free lipids and the lipids with MBP-C1 and with the mutated form MBP-C8, respectively, differences are observed. While the diffusion constants D_{V1} of Volino 1 do not differ significantly for the out-of-plane configuration, they differ slightly for the in-plane configuration: the fraction p_{V1} of the slow confined diffusion, occurring in the upper part of the lipid chains, is faster in the 9f-C1-lipid sample and in the 9f-C8-lipid sample than in the membrane sample without any proteins. Also the final part of the lipid chains, described by Volino 2, seems to be slightly more flexible for membranes containing MBP-C1 proteins, for the in-plane configuration. For the out-of-plane configuration, the diffusion constants are similar within the error bars. The increase of the confined diffusion induced by MBP-C1 was also observed for the C1-lipids, containing 1-fold protein concentration (see Section 5.2), and could be explained by the increase of the interbilayer space induced by the protein, penetrating into the bilayer.

By comparing the 9f-C1-lipid and the 9f-C8-lipid sample, the membrane dynamics described by both Volino 1 and Volino 2 are slightly enhanced by the mutant for the out-of-plane configuration. The differences are nevertheless not significant. The mutated form MBP-C8 has a less compact protein structure and its interactions with negatively charged lipids is disrupted, which results in a limited ability to maintain a compact myelin sheath [37, 38], which probably induces less stability and thus more membrane flexibility. Suresh *et al.* have shown that membrane stacking is induced by MBP-C8 at much higher concentrations as by MBP-C1 ($10.8\,\mu M$, or 9.08 wt%, for MBP-C8 and $1.8\,\mu M$, or 1.64 wt%, for MBP-C1), probably due to the reduction in charge in MBP-C8. Therefore, the post-

translational modifications could weaken the interactions of MBP-C8 with membranes. Since the amounts of the highly modified form seen in MS-patients, which has similar properties to MBP-C8, are not clear yet, further experiments, with membranes containing higher MBP-C8 protein concentrations should be performed, in order to study at which protein concentration membrane dynamics are significantly affected, compared to the influence of MBP-C1 on membrane flexibility.
Model membranes containing different MBP-C1- and MBP-C8-, and therefore buffer-, concentrations were measured with QENS. In the following, the fit results obtained with the model function $S^{300K}_{theo}(\vec{Q},\omega)$ (Eq. 2.46) for the C1-lipids, the 4f-C1-lipids and the 9f-C1-lipids are compared. Furthermore, the results for the 4f-C8-lipids and the 9f-C8-lipids are discussed. In Tables 6.3 and 6.4 the obtained fitting parameters are listed. The fraction f

Sample	R_{V1} [Å]	D_{V1} [cm^2/s 10^{-5}]	R_{V2} [Å]	D_{V2} [cm^2/s 10^{-5}]	d [Å]	τ [meV^{-1}]	Γ [meV]
C1-lipids, out-of-plane	6	0.17	5	1.8	2.4	1.00	0.52
4f-C1-lipids, out-of-plane	5	0.45	6	2.8	1.9	1.91	1.05
9f-C1-lipids, out-of-plane	4	0.57	5	3.4	1.9	2.09	0.96
C1-lipids, in-plane	5	0.25	5	2.3	2.3	0.80	0.77
4f-C1-lipids, in-plane	5	0.58	7	3.3	1.9	1.98	1.01
9f-C1-lipids, in-plane	4	0.67	8	3.7	1.9	2.06	0.93
4f-C8-lipids, out-of-plane	4	0.46	9	2.7	2.0	1.83	1.09
9f-C8-lipids, out-of-plane	5	0.65	7	3.6	1.9	2.36	0.85
4f-C8-lipids, in-plane	4	0.57	8	3.4	1.9	1.88	1.06
9f-C8-lipids, in-plane	5	0.70	7	3.3	1.9	2.39	0.84

Table 6.3: Fitting parameters for C1-lipids, 4f-C1-lipids, 9f-C1-lipids, 4f-C8-lipids and 9f-C8-lipids, with the following absolute errors: $\Delta D_{V1} \approx \pm 0.01\,10^{-5}$cm^2/s, $\Delta D_{V2} \approx \pm 0.1\,10^{-5}$cm^2/s, $\Delta R_{V1} \approx \Delta R_{V2} \approx \pm 1$ Å, $\Delta d \approx \pm 0.5$ Å and $\Delta\tau \approx \pm 0.01\,\text{meV}^{-1}$.

of immobile hydrogen atoms is zero for all samples, indicating highly dynamic membranes in the liquid phase of the lipids. The contribution of the 2-site jump diffusion p_{Jump} accounts for approximately 20 % for all samples. The fraction p_{V1} accounts for around 50 %

Sample	p_{V1}	p_{V2}	p_{Jump}	f	p_{Lor}
C1-lipids, out-of-plane	0.53;0.52;0.08	0.42;0.41;0.43	0.05;0.08;0.49	0;0;0.01	0;0;0.27
4f-C1-lipids, out-of-plane	0.49 ; 0.45	0.29 ; 0.31	0.19 ; 0.19	0 ; 0	0 ; 0.05
9f-C1-lipids, out-of-plane	0.56 ; 0.50	0.22 ; 0.23	0.20 ; 0.21	0 ; 0	0 ; 0.06
C1-lipids, in-plane	0.52;0.51;0.10	0.37;0.34;0.43	0.08;0.13;0.48	0.03;0.03;0	0 ;0;0.31
4f-C1-lipids, in-plane	0.52 ; 0.48	0.24 ; 0.25	0.21 ; 0.22	0 ; 0	0 ; 0.05
9f-C1-lipids, in-plane	0.58 ; 0.56	0.18 ; 0.22	0.20 ; 0.22	0 ; 0	0 ; 0.07
4f-C8-lipids, out-of-plane	0.57 ; 0.49	0.23 ; 0.27	0.16 ; 0.20	0 ; 0	0 ; 0.05
9f-C8-lipids, out-of-plane	0.54 ; 0.50	0.24 ; 0.24	0.19 ; 0.19	0 ; 0	0 ; 0.09
4f-C8-lipids, in-plane	0.56 ; 0.51	0.21 ; 0.23	0.19 ; 0.22	0 ; 0	0 ; 0.05
9f-C8-lipids, in-plane	0.53 ; 0.49	0.23 ; 0.23	0.20 ; 0.19	0 ; 0	0 ; 0.08

Table 6.4: Fitting parameters obtained for hydrogen populations p_{V1} , p_{V2}, p_{Jump} and f and for the fraction of the Lorentzian p_{Lor}. The absolute errors are ≈ 0.05 for all parameters. For the 4f-fold and 9f-samples, the first values are for parameters obtained on IN5 at ΔE $= 12\,\mu$eV and the second values for parameters obtained on IN5 at ΔE $= 75\,\mu$eV, respectively. For the 4f-C1-lipids, the first values are for parameters obtained for IN5 ($\Delta E = 12\,\mu$eV), the second values for parameters obtained for Osiris (ΔE $= 100\,\mu$eV) and the third values for parameters obtained for Neat (ΔE $= 216\,\mu$eV), respectively.

for all samples, whereas for the fraction p_{V2} differences are obtained: for the C1-lipids, this contribution accounts for $30 - 40\,\%$, but for the other samples for $20 - 30\,\%$, indicating that in the C1-sample, with the less MBP-C1 concentration, there are more hydrogens performing confined diffusion in the upper part of the lipids. As mentioned above, the jump distances d of the 2-site jump diffusion component, as well as the radii of the confined diffusions, were found to be independent of any proteins and protein buffer and the same for all samples. However, the residence time τ increases with increasing the protein concentration of MBP-C1 and MBP-C8, respectively, indicating faster 2-site jumps of the methylene molecules. Great interest lies in the diffusion constants D_{V1} and D_{V2} of Volino 1 and Volino 2, respectively, which is illustrated in Fig. 6.5 for membranes containing MBP-C1 proteins and MBP-C8 proteins, respectively, at different protein-concentrations. As obtained for the lipids, the 4f-lipids and the 9f-lipids (see Section 4.3), both diffusion constants of the confined diffusions performed by hydrogen populations p_{V1} and p_{V2}, obtained for the in-plane and for the out-of-plane orientation, increase with higher protein concentration, or rather higher protein-buffer concentration. The question arises, if these observations are caused by the increasing protein- or the increasing buffer concentration. Therefore, the absolute difference of the diffusion constants for the lipids with proteins with respect to the diffusion constants for the lipids with the same protein buffer concentration were calculated, following

$$dD_V^{C1-lip} = D_V^{C1-lip} - D_V^{lipids}, \tag{6.1}$$

$$dD_V^{4f-C1-lip} = D_V^{4f-C1-lip} - D_V^{4f-lipids} \tag{6.2}$$

and

$$dD_V^{9f-C1-lip} = D_V^{9f-C1-lip} - D_V^{9f-lipids}, \tag{6.3}$$

for the lipids with different MBP-C1 concentrations. The same was calculated for the 4f-C8-lipids and the 9f-C8-lipids. Further, the relative increase of the diffusion constants (in %) for the lipids with proteins with respect to the diffusion constants for the corresponding lipids (containing the same protein buffer concentration) were calculated, with $\frac{dD_V^{prot}}{D_V^{buff}}$, where dD_V^{prot} is the absolute difference of the diffusion constant for the lipids with MBP-C1 and MBP-C8, respectively, at a certain concentration, and D_V^{buff} the diffusion constant of the corresponding lipids, containing the same concentration of protein buffer. The results are listed in Table 6.5.

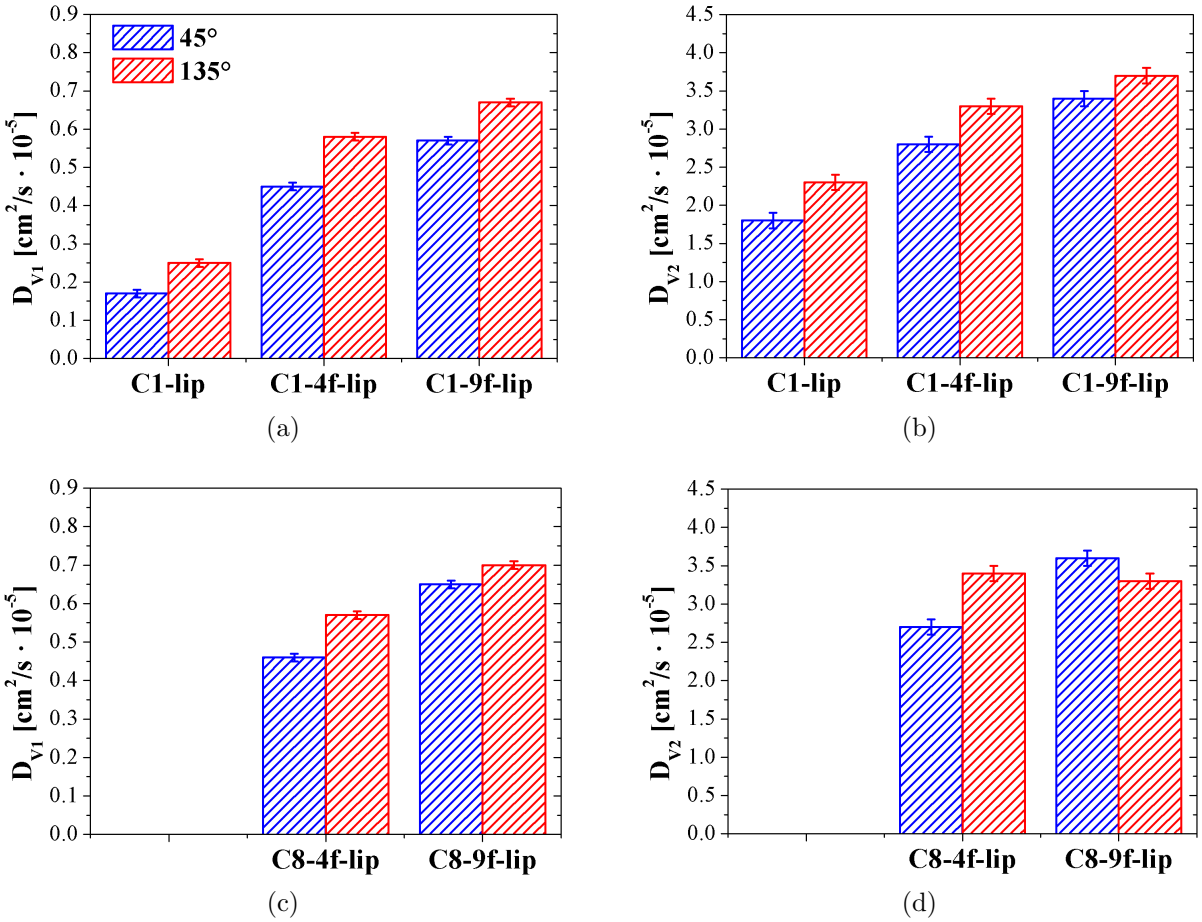

Figure 6.5: Diffusion constants D_{V1} (left) and D_{V2} (right) of hydrogen populations p_{V1} and p_{V2}, respectively, described by Volino 1 and by Volino 2, for membranes containing different amounts of MBP-C1 proteins and corresponding protein buffer concentrations (top), and for membranes containing different amounts of MBP-C8 proteins and protein buffer concentrations (bottom). Parameters obtained for data in out-of-plane configuration are shown in blue and for data in in-plane configuration in red.

Sample	dD_{V1} [$\mathrm{cm}^2/\mathrm{s}\ 10^{-5}$]	dD_{V2} [$\mathrm{cm}^2/\mathrm{s}\ 10^{-5}$]	$dD_{V1}^{prot}\ /\ D_{V1}^{buff}$ [%]	$dD_{V2}^{prot}\ /\ D_{V2}^{buff}$ [%]
C1-lipids, out-of-plane	0.02	0.7	13 ± 10	64 ± 19
4f-C1-lipids, out-of-plane	0.01	-0.3	2 ± 3	−10 ± 5
9f-C1-lipids, out-of-plane	-0.08	-0.3	−12 ± 2	8 ± 4
C1-lipids, in-plane	0.09	0.5	56 ± 12	28 ± 9
4f-C1-lipids, in-plane	0.10	0.3	21 ± 3	10 ± 5
9f-C1-lipids, in-plane	0.13	0.8	24 ± 3	28 ± 6
4f-C8-lipids, out-of-plane	0.02	-0.4	5 ± 3	−13 ± 5
9f-C8-lipids, out-of-plane	0	-0.1	0	−3 ± 4
4f-C8-lipids, in-plane	0.09	0.4	19 ± 3	13 ± 5
9f-C8-lipids, in-plane	0.16	0.4	30 ± 3	14 ± 5

Table 6.5: dD_{V1} and dD_{V2}: absolute differences of the diffusion constants for the lipids with proteins with respect to the diffusion constants for the lipids with the same protein buffer concentration with absolute errors of $\Delta dD_{V1} \approx \pm 0.014\,10^{-5}\mathrm{cm}^2/\mathrm{s}$ and $\Delta dD_{V2} \approx \pm 0.14\,10^{-5}\mathrm{cm}^2/\mathrm{s}$. $dD_{V1}^{prot}\ /\ D_{V1}^{buff}$ and $dD_{V2}^{prot}\ /\ D_{V2}^{buff}$: relative differences of the diffusion constants for the lipids with proteins with respect to the diffusion constants for the corresponding lipids (containing the same protein buffer concentration).

For schematic illustrations, the relative differences in the diffusion constants are illustrated in Fig. 6.6 for all samples. For the C1-lipids, the relative difference between the diffusion constants D_{V1} and D_{V2} and the diffusion constants of the corresponding lipids, is large, even approximately 60 % for D_{V1} in the in-plane configuration and for D_{V2} in the out-of-plane configuration. Hence, the influence of MBP-C1 at a 1-fold concentration on diffusive motions of the membrane is significantly strong. For the 4f-C1-lipids, this effect is less, but D_{V1} is nevertheless about $\approx 20\,\%$ increased for the out-of-plane configuration, with respect to the 4f-lipids. Regarding D_{V2}, the differences are still positive for the in-plane configuration, but for the out-of-plane configuration D_{V2} is larger for the 4f-lipids than for the 4f-C1-lipids. For the 9f-lipids, an effect of the proteins is observed only for the out-of-plane configuration, at $\approx 30\,\%$. The relative differences for the 4f-C8-lipids and 9f-C8-lipids are also only relevant for the out-of-plane configuration, and are relatively small or even negative for the in-plane configuration. It seems that MBP-C1 has the largest effect on the diffusion constants, when present at the lowest protein concentration. The influence of the protein on the difference of the diffusion constants seems to be reduced by increasing the protein concentration. Comparing the differences between membranes with MBP-C1 and the mutant, MBP-C8, there are no significant differences within the error bars. Thus, eliminating the buffer contribution, membranes containing MBP-C1 proteins and membranes containing MBP-C8 proteins show approximately the same properties of the dynamics investigated in this work.

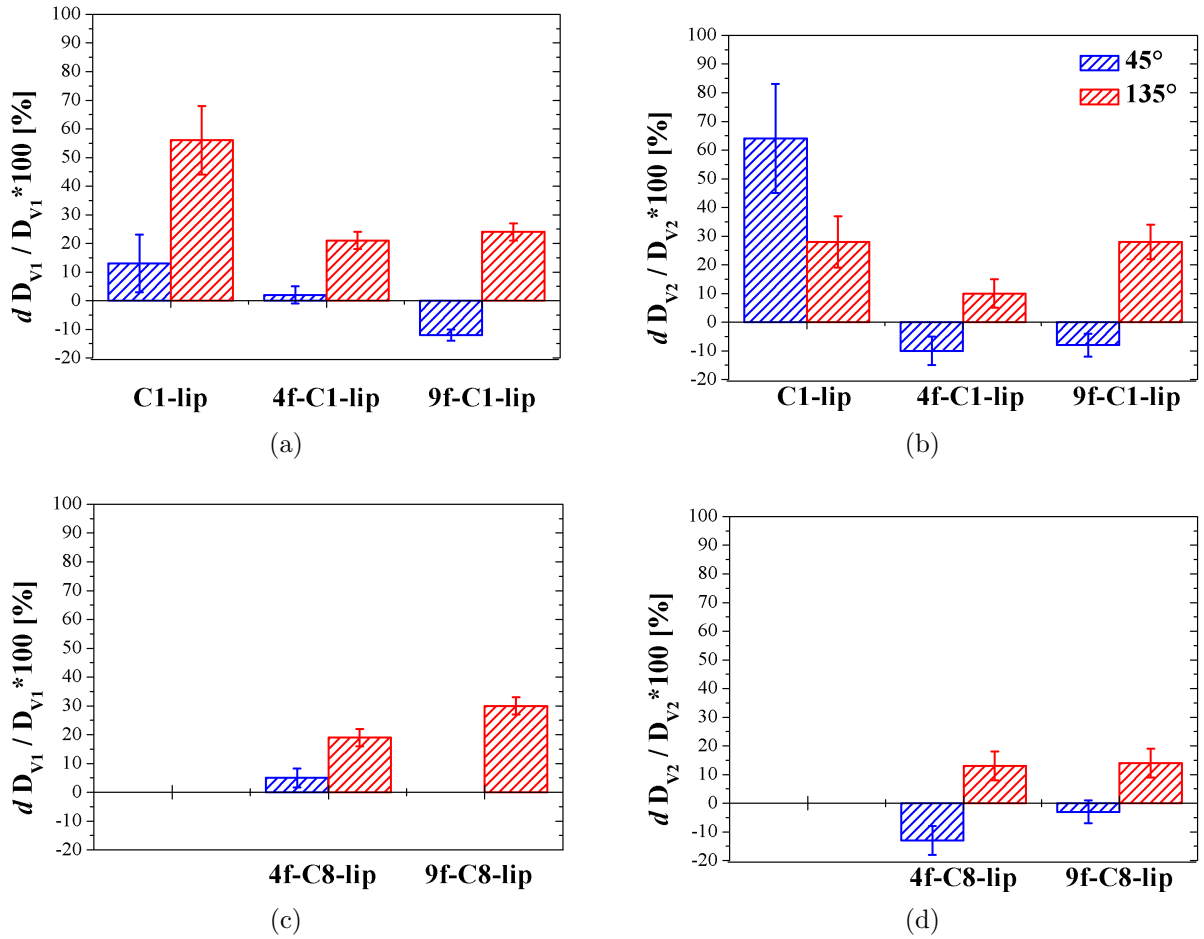

Figure 6.6: Relative differences in the diffusion constants D_{V1} and D_{V2} for membranes containing MBP-C1 and MBP-C8 proteins, with respect to lipids containing the corresponding buffer amount for the out-of-plane configuration (red) and the in-plane configuration (blue).

6.3 Conclusions

In order to investigate the structure and dynamics of diseased and healthy myelin, neutron diffraction, EINS and QENS measurements were performed on reconstituted myelin membranes containing MBP-C1 proteins and the mutated form MBP-C8, respectively, and the observations were compared to the results obtained for protein-free membranes. To study also the influence of higher protein concentrations than used previously, experiments were performed on membranes containing 4-fold and 9-fold protein amounts.
The diffraction results reveal that the 9f-C8-lipids exhibit a repeat distance corresponding to the Bragg peak $A_1 = 79\,\text{Å}$ found for the C1-lipids in the liquid phase. However, the repeat distance of the 9f-C1-lipids was shifted about $\approx -10\,\text{Å}$. Protein-free membrane domains, as present in the samples with a 1-fold protein concentration, do not exist, but the intercept at low Q-values is relatively high, indicating that less ordered membrane fractions exist, containing squeezed out proteins, which could be due to the higher protein concentration.
The elastic temperature scans on 9f-C1-lipids and 9f-C8-lipids on IN16 indicated that a first transition from the harmonic regime to an anharmonic regime occurs at $\approx 160\,\text{K}$ for both samples, as also found for the lipids, and was attributed to rotation of the methyl groups (CH_3 molecules) in the lipid chains. In a temperature region from $\approx 262\,\text{K}$ and $271\,\text{K}$, where the water is crystalline, but the lipids have already transformed into the liquid disordered phase, the 9f-C8-lipids have shown smaller MSDs, with respect to the other samples. This indicated a reduction of the membrane dynamics, induced by MBP-C8, in this temperature regime.
For the QENS measurements performed on IN5 on the 9f-lipids, the 9f-C1-lipids and the 9f-C8-lipids, the same model as found for the lipids (Chapter 4), the C1-lipids, the P2-lipids and the C1-P2-lipids (Chapter 5), has been adopted to interpretate the data. The distance of the 2-site-jump diffusion, attributed to the methylene molecules in the lipid chains was found to be independent of any protein or buffer concentrations. However, the residence time τ increases with increasing the protein concentration of MBP-C1 and MBP-C8, respectively, indicating faster 2-site jumps of the methylene molecules. The radii of the confined diffusions were $\approx 4\,\text{Å}$ for the upper part of the lipids, for all samples, besides for the 9f-lipids in the in-plane configuration, showing a radius of $R_{V1} = 7 \pm 1\,\text{Å}$. For the lower part of the lipids, radii ranging from $5\,\text{Å}$ to $8\,\text{Å}$ were found for all samples. The diffusion constant D_{V1} was found to be larger for the 9f-C1-lipids and the 9f-C8-lipids in the in-plane configuration, indicating enhanced membrane dynamics for the upper part of the lipids, as found for the C1-lipids (see Section 5.2).

The QENS results on membranes containing different MBP-C1 and MBP-C8 concentrations indicated that both diffusion constants, D_{V1} and D_{V2}, increase with higher protein, and therefore buffer, concentrations. Calculating the relative difference between the diffusion constants of the membranes with proteins and of the membranes containing the corresponding protein buffer amount, revealed that MBP-C1 significantly enhance the diffusion constants, when present at the lowest protein concentration (C1-lipids). The influence of MBP-C1 on the confined diffusions seems to be reduced by increasing the protein concentration.

Conclusions and Perspectives

In this work, the influence of the myelin proteins MBP-C1, MBP-C8 and P2, on the structure and dynamics of reconstituted model myelin membranes was investigated with neutron scattering techniques. The purpose of the study was to better understand the role of the complex myelin membrane in autoimmune degenerative diseases, such as MS or Guillain-Barré syndrome. Measurements on model membranes, made of a binary mixture of anionic DOPS and neutral DOPC lipids, containing MBP-C1 (the least modified form of the various MBP isomers) and P2, allowed the investigation of PNS myelin. The composition of anionic and neutral lipids was used to mimic the negatively charged inner leaflets of the bilayers in myelin, where MBP-C1, MBP-C8 and P2 are located. Experiments on membranes including MBP-C1 and the mutated form MBP-C8 (which is similar to the highly modified form seen in MS-patients) permitted the study of the influence of the mutant on the membrane structure and stability.

To investigate the structure of the model membranes, neutron diffraction measurements were performed, while the dynamical properties of the membranes were studied with EINS temperature scans, ranging from 20 K to 300 K, in order to cover the phase transition temperatures of the lipids. QENS experiments gave detailed information about molecular motions occurring in the membranes in the gel and liquid phases. The success of these experiments and the reliability of the results are depended on the quality of the samples. Hence, detailed sample characterization was performed with a range of biophysical techniques, including dynamic light scattering (DLS), sucrose gradient centrifugation, differential scanning calorimetry (DSC) and neutron diffraction.

The first aim of this study was to characterize the behavior of a protein-free membrane, so that the results could be used as a reference for the protein-containing samples. Diffraction measurements showed that structural changes occur after the temperature region of the gel-to-liquid lipid phase transitions ($T_c = 254$ K for DOPC and $T_c = 259$ K for DOPS, as obtained by DSC), when the hydration water was still crystalline, but that in both the gel and the liquid phase the membrane has the same interbilayer d-spacing. Three Bragg peaks characteristic for hexagonal ice were found, which suggested the presence of bulk heavy water in the nearly fully hydrated bilayers (95 % humidity).
EINS temperature scans were performed to study the membrane dynamics, indicating a transition from a harmonic to an anharmonic temperature regime that could be assigned

to methyl group rotations in the lipid chains and in the proteins entering the experimental time-window of the instrument. This was followed by further transitions at the phase transition temperatures of the lipids and the heavy water.
To study the specific dynamic behavior in more detail, QENS studies were performed. Four different hydrogen populations were identified in the liquid phase: (i) a fraction that undergoes only vibrational motions and appears immobile within the experimental resolution, (ii and iii) two populations that diffuse in a confined spherical volume and belong to the upper and terminal parts of the lipids, respectively, and (iv) a hydrogen fraction belonging to methylene groups and that undergoes 2-site jump diffusion. For the gel phase, a slightly different model was adopted: fraction (i) was found to account for $\approx 90\,\%$, while a smaller population performing both confined diffusion and isotropic rotation, was assigned to the methylene groups.

Having characterized the structure and dynamics of a protein-free membrane, the second aim of the study was to understand the influence of the myelin proteins MBP-C1 and P2 on the membrane structure and dynamics. Diffraction measurements revealed that, in the gel phase, protein-containing membranes exhibit the same d-spacing as the lipids, suggesting they have minimal effect on the structure. In contrast, in the liquid phase, the proteins were shown to significantly increase the interbilayer distances. A model was suggested, in which MBP-C1 widens the interbilayer space and penetrates $\approx 2\,\text{Å}$ into opposing bilayers. P2-containing membranes were found to exhibit, two widened membrane fractions. The larger spacing is suggested to contain P2, penetrating partially into the bilayer. In combination, MBP-C1 and P2 result in the same d-spacings as P2 alone. Due to a threefold excess of P2 proteins with respect to MBP-C1 proteins, it was assumed that, in the ideal case, three P2 molecules and one MBP-C1 molecule arrange side by side in the membrane plane building assemblies. The electrostatic potential of the three P2 proteins, with two highly positively charged opposed regions, would be strong, and the MBP-C1 protein would have to penetrate deeply into the bilayer. When MBP-C1 and P2 included in a membrane separately, each protein was shown to induce an additional, less ordered, membrane fraction with a large d-spacing, particularly in the gel phase, consistent with proteins being squeezed out [30]. This was absent when added together, suggesting that the proteins can act synergistically to increase bilayer stacking [59].
Regarding the effect of the proteins on membrane dynamics, it was identified, with EINS measurements, that MBP-C1 significantly reduces global lipid motions in the gel phase. Firstly, the methyl group rotation arose at $20 - 40\,\text{K}$ higher temperatures than for the other samples. Secondly, the membrane dynamics in the temperature region including the phase transitions of the lipids and the heavy water were reduced. QENS results supported this conclusion, showing that MBP-C1 slowed down the diffusive motions with a larger radius of confinement in the gel phase. In contrast, in the liquid phase, MBP-C1 was found to enhance the diffusive motions of the lipids, which is in agreement with the structural properties: due to the widening of the interbilayer spacing induced by MBP-C1, which penetrates into the bilayer, the lipids were suggested to be more flexible, resulting in increased diffusive motions. Unlike MBP-C1, P2 did not appear to significantly affect

the diffusive motions of the lipids. This was explained by the compensating structural and electrostatic properties of P2: although an increase in interbilayer spacing is observed, which could increase flexibility, the positive electrostatic potential of P2, which is concentrated at the two opposing sides of the protein, probably compensates for the enhancement of the dynamics, due to strong stabilizing electrostatic protein-lipid interactions. By far the most significant effect on the membrane dynamics in the liquid phase was induced by MBP-C1 and P2 together, as indicated by a dominant fraction of immobile hydrogen atoms. Furthermore, the diffusion constant of the hydrogen population belonging to the upper part of the lipids was found to be reduced. This coherency is consistent with the previously proposed synergistic stacking effect of multilayers induced by MBP-C1 and P2, which was previously suggested by Suresh *et al.* [59]. This is also consistent with the proposed association of MBP-C1 and P2 based on the neutron diffraction data, with a very strong electrostatic interaction between protein assemblies and lipids caused by the positive charge distribution of three P2 proteins, concentrated on the opposing sides, at the lipid-bound surfaces.

The third aim of this work was the investigation of the influence of the effects of the modified form MBP-C8, on the structure and dynamics of a reconstituted membrane. Interestingly, no significant differences in the dynamics and structure of the membrane, when compared to MBP-C1, were observed in the QENS experiments. Further experiments, with membranes containing higher MBP-C8 protein concentrations should be performed, in order to study at which protein concentration membrane dynamics are significantly affected, compared to the influence of MBP-C1 on membrane flexibility. The amounts of the highly modified form of MBP seen in MS-patients, which has similar properties to MBP-C8, are not clear yet, but it is well-known that MBP-C8 has a less compact protein structure and its interactions with negatively charged lipids are disrupted, which results in a limited ability to maintain a compact myelin sheath [37, 38].

In summary, these results propose a model in which the myelin-specific proteins MBP-C1 and P2 associate within the interbilayer space of a reconsituted myelin membrane and influence large membrane fractions. These proteins are suggested to promote adhesion between the bilayers, caused by electrostatic interactions and a synergistic stacking effect of both proteins and thus reduce membrane dynamics. This is likely to play an important role in the formation of compacted PNS myelin.

In further work, it would be useful to perform neutron reflectometry or small angle scattering on reconstituted membranes as investigated in this work, containing deuterated lipids, in order to get a clearer picture about the location of the proteins within the membrane. Since very little is known about the interplay of MBP-C1 and P2 in a bilayer, particularly the interaction between them, molecular dynamic simulations on bilayers containing MBP-C1 and P2 would be very helpful. In order to investigate the structure and dynamics of more complex model myelin membranes, that are step by step closer to natural compact myelin, a gradual addition of further myelin proteins is planned. Cholesterol, which

represents $\approx 50\,\%$ of the total lipid fraction (regarding the molecular weight of the lipids) in myelin and is essential for myelin assembly, could also be added, in order to study its influence on membrane stability. Selected deuteration of membrane components will be useful to define the contribution of single components to the global membrane dynamics.
This work is partially continued by another PhD project, dealing with the structure-function relationship in myelin proteins, particularly in P2 and CNPase, which is a myelin specific enzyme for which the physiological function is unknown. For P2, the interest lies in the effects of a mutation of the functionally relevant hinge-region, located at the α-helical protein lid, on protein dynamics. This mutation, called P38G, results in differences in membrane and lipid binding properties. For CNPase, the influence of mutations on protein dynamics will be studied. For this purpose, neutron scattering experiments are planned on the wild type proteins and on the mutated forms, in order to study the influence of the mutants on the protein dynamics. To further investigate the effect of hydration, the samples will be measured as highly pure dry and fully hydrated powders.
Furthermore, experiments on natural tissue of diseased and healthy myelin are planned to better understand the role of myelin in degenerative diseases. For this purpose, the dynamics of different sections of the CNS (such as the optical nerve, the cerebellum and the spinal cord) extracted from different post-mortem animal species suffering, or not, of neurological diseases, will be studied using neutron scattering techniques.

Conclusions et Perspectives

Dans ce travail, l'influence des protéines de la myéline MBP-C1, MBP-C8 et P2 sur la structure et la dynamique des membranes reconstituées de la myéline, a été étudiée par diffusion neutronique. Ces protéines périphériques, localisées dans la gaine de myéline compacte, ont été choisies pour étudier le rôle de la membrane complexe de la myéline dans les maladies auto-immunes et dégénératives telles que la sclérose en plaques ou le syndrome de Guillain-Barré. Des mesures sur les membranes modèles composées d'un mélange binaire de lipides DOPS (anionique) et DOPC (neutre), contenant MBP-C1 (la forme la moins modifiée des isomères de MBP) et P2, ont permis l'étude de la myéline du SNP. La composition des lipides anioniques et neutres a été utilisée afin d'imiter les feuillets internes des bicouches de la myéline, lesquelles sont chargées négativement. Des expériences sur les membranes avec MBP-C1 et du mutant MBP-C8 (qui a des propriétés similaires à la forme modifiée vue dans les malades de sclérose en plaques) a permis l'étude de l'influence du mutant sur la structure et la stabilité de la membrane.

Pour l'étude de la structure de la membrane, des expériences de diffraction neutronique ont été effectuées alors que ses propriétés dynamiques ont été étudiées par balayage élastique en température allant 20 K à 300 K afin de couvrir les transitions de phase des lipides. Des expériences de diffusion quasi-élastique de neutrons ont donné une information détaillée sur les mouvements moléculaires présents dans la membrane dans la phase de gel ainsi que dans la phase liquide. Des échantillons très bien caractérisés étaient indispensables pour assurer le succès des expériences et la fiabilité des résultats. Par conséquent, la caractérisation détaillée des échantillons a été une composante essentielle de ce travail. Plusieurs techniques biophysiques ont été utilisées, telles que la diffusion de la lumière (DLS: dynamic light scattering), la centrifugation en gradient de sucre, la calorimétrie différentielle à balayage (DSC: differential scanning calorimetry) et la diffraction neutronique.

Le premier objectif de cette étude était de caractériser l'attitude d'une membrane sans protéine, pour utiliser les résultats comme référence pour les échantillons contenant des protéines. Les expériences de la diffraction de neutrons ont montré que des changements structuraux apparaissent après le domaine de température des transitions de phase des lipides ($T_c = 254\,\mathrm{K}$ pour DOPC et $T_c = 259\,\mathrm{K}$ pour DOPS, obtenu par DSC), mais que dans la phase de gel et liquide, la membrane a la même distance répétée. Trois pics de Bragg caractéristiques pour la glace hexagonale ont été trouvés, qui indiquent la présence

de l'eau lourde en vrac dans les bicouches presque totalement hydratées (humidité de 95 %). Des balayages élastiques en température ont été effectués pour étudier la dynamique de la membrane, indiquant une transition d'un domaine de température harmonique à non harmonique, qui pourrait être due aux rotations de groupes méthyliques dans les chaînes de lipides et dans les protéines, entrant dans la fenêtre de temps expérimentale de l'instrument. Ce phénomène est suivi par d'autres transitions aux températures de la transition de phase des lipides et de l'eau lourde.
Pour étudier le comportement dynamique spécifique plus en détail, des expériences de diffusion quasi-élastique de neutrons ont été effectuées. Quatre populations d'hydrogènes ont été identifiées dans la phase liquide: (i) une fraction qui subit seulement des mouvements vibratoires, (ii et iii) deux populations qui diffusent dans un volume sphérique confiné et qui fait partie de la partie haute et terminale des lipides, et (iv) une fraction d'hydrogène qui fait partie des groupes méthylènes et subit une diffusion de saut de deux cotés. Pour la phase de gel, un modèle légèrement différent a été adopté: la fraction (i) s'est avérée compter pour environ 90 %, lorsqu'une population plus petite effectuant une diffusion confinée et une rotation isotropique, a été attribuée aux groupes méthylènes.

Après avoir analysé la structure et la dynamique d'une membrane sans protéine, le deuxième objet de cette étude était de comprendre l'influence des protéines de myéline MBP-C1 et P2 sur la structure et la dynamique de la membrane. Les expériences par diffraction de neutrons ont révélé, dans la phase de gel, que les membranes avec protéines montrent les même propriétés structurales que les lipides sans protéine. En revanche, dans la phase liquide la structure de la membrane est fortement affectée par les protéines. Un modèle a été proposé: Le MBP-C1 élargit l'espace entre les bicouches et pénètre d'environ 2 Å dans les couches opposées. Pour la membrane contenant des protéines P2, deux élargissements différents de la membrane ont été trouvés. Il a été proposé que l'élargissement le plus important était dû à la protéine qui pénètre partiellement dans la bicouche. Lorsque les protéines MBP-C1 et P2 sont ensemble dans une membrane, on constate des élargissements similaires à ceux observés pour P2 seule. Pour un nombre trois fois plus important de protéines P2 comparé aux protéines MBP-C1, il a été proposé que dans le cas idéal, trois molécules P2 et une molécule MBP-C1 s'arrangent côte à côte dans le plan de la membrane pour construire des assemblages. Le fort potentiel électrostatique des trois molécules P2 contenant deux régions opposées très chargées positivement forcerait les protéines MBP-C1 à pénétrer profondément dans la bicouche. Lorsque MBP-C1 et P2 sont insérées séparément dans une membrane elles induisent une phase supplémentaire présentant un espacement moins homogène mais plus large, en particulier dans la phase de gel, suggérant que certaines molécules ont été éjectées [30], effet qui n'a pas été observé lorsque les deux protéines sont insérées ensemble. Ceci a été expliqué par un effet de synergie sur l'empilement induit par les protéines MBP-C1 et P2 [59].
Concernant l'effet des protéines sur la dynamique de la membrane, il a été identifié avec EINS, que MBP-C1 réduit significativement les mouvements globaux de lipides dans la phase de gel. La rotation de groupes de méthyle apparaît à des températures plus élevées de $20 - 40$ K que pour les autres échantillons. En plus, la dynamique de la membrane

dans un domaine de température des transitions de phase des lipides et de la fusion de l'eau lourde ont été réduits. Des expériences de diffusion quasi-élastique ont appuyé cette conclusion en montrant que MBP-C1 ralentit les mouvements de diffusion avec un rayon de confinement plus grand dans la phase de gel. Par contre, dans la phase liquide, MBP-C1 a été trouvé de augmenter les mouvements diffusives des lipides, qui est en accord avec les propriétés structurales: grâce à un élargissement de l'espace entre les bicouches induit par MBP-C1, qui pénètre dans le bicouche, les lipides ont supposé d'être plus souples. Contrairement à MBP-C1, P2 ne semble pas affecter les mouvements de diffusion des lipides. Ceci a été expliqué par les propriétés structurales et électrostatiques compensatrices de P2: Bien qu'une augmentation de l'espace entre les bicouches a été observée, ce qui pourrait augmenter la flexibilité, le potentiel électrostatique positif de P2, qui est concentré sur les deux côtés opposés de la protéine, compense probablement l'augmentation de dynamique, grâce aux fortes interactions électrostatiques stabilisantes de protéines avec les lipides. L'effet le plus important sur la dynamique de la membrane a été induit par MBP-C1 et P2 ensemble, indiqué par une fraction majeure d'hydrogènes immobiles. Par ailleurs, la constante de diffusion de la population hydrogène, appartenant à la partie haute des lipides, s'est trouvé être réduit. Ceci est consistant avec l'effet de synergie sur l'empilement de multi-couches induit par MBP-C1 et P2, proposé par Suresh *et al.* [59]. Ceci est également consistant avec l'association proposée de MBP-C1 et P2, basée sur les données de la diffraction de neutrons, avec une interaction électrostatique très forte entre les protéines et les lipides. Cette interaction est très forte grâce à la distribution de charge positive de trois protéines P2, qui est concentrée aux côtés opposés des surfaces liées aux lipides.

Le troisième objet de ce travail était l'étude de l'influence des effets de la forme modifiée (MBP-C8) sur la structure et la dynamique d'une membrane reconstituée. Il est intéressant de remarquer qu'en comparaison avec MBP-C1, aucune différence significative sur la dynamique et la structure de membrane n'a été observée avec la diffusion de neutron quasi-élastique. Les expériences complémentaires sur les membranes contenant des concentrations de protéine MBP-C8 plus élevées devraient être effectuées, afin d'étudier à quelle concentration la dynamique est affectée de façon significative, comparé à l'influence de MBP-C1 sur la flexibilité de la membrane. Les quantités de la forme hautement modifiée, MBP-C8, vue dans les malades de sclérose en plaques, qui a des propriétés similaires à MBP-C8, ne sont pas encore claires, mais il est bien connu que MBP-C8 a une structure de protéine moins compacte et que ses interactions avec les lipides chargés négativement sont perturbées, ce qui conduit à une capacité limitée de maintenir une gaine de myéline compacte [37, 38].

En résumé, ces résultats induisent un modèle dans lequel les protéines de myéline MBP-C1 et P2 s'associent dans l'espace entre les bi-couches d'une membrane reconstituée et influencent de larges fractions de la membrane. On suppose fortement que ces protéines favorisent l'adhésion entre les bi-couches, grâce à un effet de synergie sur l'empilement induit par les deux protéines et donc réduisent la dynamique de la membrane. Ce phénomène joue prob-

ablement un rôle important dans la formation de la myéline compacte du SNP.

Dans le futures travaux il sera utile d'effectuer des expériences par réflectométrie de neutrons ou par diffusion aux petits angles sur les membranes reconstituées telles que celles étudiées dans ces travaux, mais contenant des lipides deutérés afin d'avoir une idée claire de la localisation des protéines dans les bicouches. Etant donne que peu de choses sont connues a propos des effets réciproques entre les protéines MBP-C1, P2 et les bicouches, des simulations par dynamique moléculaire seraient très utiles. Pour étudier la structure et la dynamique de membranes myéline complexe se rapprochant peu a peu de la myéline compacte naturelle, un ajout graduel d'autres protéines de la myéline est prévu. Le cholestérol, qui représente environ la moitié du total des lipides (concernant le poids moléculaire) dans la myéline et qui est essentiel pour sa structure, pourrait aussi être ajouté afin d'étudier son influence sur la stabilité de la membrane. Des deutérations sélectives des membranes seront utiles pour définir les contributions de composants individuels sur l'ensemble de la dynamique de la membrane.
Ce travail est partiellement prolonge par un autre projet de thèse de doctorat portant sur la relation fonction-structure dans les protéines de la myéline, en particulier dans P2 et CNPase . CNPase est une enzyme spécifique de la myéline pour laquelle la fonction physiologique est inconnue. Pour le P2 l'intérêt est d'étudier les effets de la mutation de la région charnière fonctionnellement importante, localisée sur le couvercle de l'hélice α de la protéine, sur la dynamique. Cette mutation, appelée P38G, a pour résultat des différences dans les liaisons lipidiques dans la membrane. Pour CNPase, l'influence des mutations sur la dynamique des protéines sera étudié. Des expériences par diffusion de neutrons sont programmées sur la protéine de type sauvage ainsi que sur la forme mutante afin d'en déduire l'influence de la mutation sur la dynamique de la protéine. Les effets de l'hydratation seront étudiés sur des échantillons poudre secs et totalement hydratés.
Par ailleurs, des expériences sur des tissus naturels de myéline morts et en bonne santé sont prévues pour comprendre le rôle de la myéline sur les maladies dégénératives. A cette fin, la dynamique de différentes parties du CNS tels que le nerf optique, le cervelet et la moelle épinière extraits post-mortem de différentes espèces animales souffrant ou non de maladies neuro-dégénératives seront étudiées par diffusion de neutrons.

Appendix

In the following, two articles I contributed to are listed.

A.1 Dynamic Properties of a Reconstituted Myelin Sheath

The following article about dynamical properties of a reconstituted myelin sheath, investigated on IN13 (ILL), was published in the proceedings of the XIII European Conference on the Spectroscopy of Biological Molecules, in Palermo, Italy, from 28th August to 2nd September 2009. The results, described in this article, were presented with a poster, for which I won a poster prize.

Spectroscopy 24 (2010) 585–592
DOI 10.3233/SPE-2010-0479
IOS Press

Dynamic properties of a reconstituted myelin sheath

W. Knoll [a,b], F. Natali [c,*], J. Peters [a,b,d], R. Nanekar [e], C. Wang [e] and P. Kursula [e]
[a] *University Joseph Fourier, Grenoble, France*
[b] *Institut Laue-Langevin, Grenoble, France*
[c] *CNR-IOM, OGG, c/o Institut Laue-Langevin, Grenoble, France*
[d] *Institut de Biologie Structurale, Grenoble, France*
[e] *Department of Biochemistry, University of Oulu, Oulu, Finland*

Abstract. Myelin is a multilamellar membrane which, wrapping the nerve axons, increases the efficiency of nervous signal transmission. Indeed, the molecular components of the myelin sheath interact tightly with each other and molecules on the axonal surface to drive myelination, to keep both myelin and the axon intact, and to transduce signals from myelin to the axon and vice versa. Myelin is strongly affected in human demyelinating diseases in both the central and peripheral nervous system (CNS and PNS, respectively). Despite the presence of a well-defined set of myelin-specific proteins, little is known about the structure and the dynamics of these proteins, their interactions with the membrane and their influence on myelin stability. We present here the first neutron scattering results on the dynamics of the myelin sheath in PNS and of the interaction between its constituents. Specifically, the human P2 protein is shown to stabilize the lipid membrane upon binding to it.

Keywords: Membrane dynamics, neutron scattering, myelin

1. Introduction

Biological membranes serve diverse basic functions in eukaryotic and prokaryotic cells, regulating the exchange of matter, energy and information with the surrounding environment. In a functional sense, proteins obviously play a pertinent role in many of these functions. Yet, their lateral organization within membranes is often highly dynamic, causing their transient localization in different lipid environments that may affect protein structure, their oligomerization and, thereby, function.

Myelin is the lipid-rich, multilamellar membrane responsible for the speed-up of the nerve impulse conduction in vertebrates (up to 100 m/s in a healthy person). Myelin is destroyed by autoimmune processes in human demyelinating diseases, including multiple sclerosis (MS) in CNS and peripheral neuropathies (PN) in PNS. MS is characterized by patches of demyelination [10] that can be scattered throughout the white matter of the CNS, but are usually localized in the brain stem, periventricular areas, the optic nerve and the cervical spinal cord. These multiple scars (or scleroses) cause symptoms specific to the interrupted signals.

The biochemical composition of myelin includes only a few major proteins [19]; two proteins, the proteolipid protein (PLP) and the myelin basic protein (MBP) account for 80% of the total CNS myelin protein. CNS and PNS myelin differ in their protein constituents. MBP is also an abundant component

*Corresponding author: Dr. F. Natali, CNR-IOM, c/o Institut Laue-Langevin, BP 1566, rue Jules Horowitz, 38042 Grenoble Cedex 9, France. Tel.: +33 4 76 20 70 71; Fax: +33 4 76 20 76 88; E-mail: natali@ill.fr.

of PNS myelin [11], where it colocalizes with another myelin-specific protein, P2. The P2 protein, while missing in CNS, represents 1–15% of the total myelin protein in the PNS.

MBP is essential for the formation of CNS myelin, able to interact with a wide range of ligands, often polyanionic in nature [2]. Due to its high charge and low overall hydrophobicity, there is significant intramolecular electrostatic repulsion in MBP; this results in MBP being an extended, intrinsically unstructured protein in solution [12,21].

P2 is a small folded protein with a high homology to members of the fatty acid binding protein family [7,18]. It is expressed in the cytoplasmic face of compact myelin in the PNS [9,27], and its lipid-binding activity suggests it may serve important functions in generating and maintaining the unique lipid composition of myelin [28]. P2 is possibly one of the autoantigens in the human disorder Guillain–Barre syndrome [14,15], an autoimmune disease of the PNS.

Although the main subject of myelin research often concerns its proteins, dynamic changes in protein–lipid interactions and lipid-based membrane microdomains also have a role in the etiology of MS and PN. Detailed knowledge of the fine structure and dynamics of myelin at the level of lateral membrane domain composition, and lipid–protein interactions within such domains, is imperative for understanding the unknown pathogenic mechanisms of demyelination.

Biochemical and structural studies on myelin flourished during the 1970s and 1980s [3–6,16,26,29], and correlations have been observed between myelin structural modifications [13,22] and some common neurological degenerative events of pathological nature in humans. In this context, wide angle X-ray diffraction studies [5] revealed that the lipid phase transition temperature of MS myelin is 20°C lower than that of normal myelin, indicating differences in the structural organization of the bilayer.

Dynamic properties are of great importance at the molecular level of biology and the marked temperature dependence of the activity of biomolecules reflects their thermal mobility. Dynamic events in biomolecular systems occur on a very large time-scale, ranging from femtoseconds to nearly seconds. Within this broad interval, motions occurring in the pico- to nano-second time-scale are of particular interest and relevance, since they cover the transition region from 'discrete' local excitations of small molecular subunits to slower processes involving collective motions of massive parts of macromolecular assemblies. This time window is well covered by inelastic and quasielastic neutron scattering, These techniques can, therefore, play a relevant role in improving the understanding of molecular motions which affect the functionality of biomolecules.

We have demonstrated, during the last five years [8,23–25], the power of the neutron scattering technique as an optimal probe for the dynamics of the myelin sheath and its components. Our studies so far focused on the effect of MBP on the global membrane dynamics of ordered dimyristoyl L-a-phosphatidic acid (DMPA) assemblies, simulating the myelin sheath in the CNS. The study covered the lipid gel (phase α) to liquid (phase β) phase transition ($T_{\alpha\rightarrow\beta} = 320$ K). Strong anisotropy in the dynamic behaviour depended on the membrane composition, and MBP was found to strongly enhance the out-of-plane mobility of the lipid molecules in the liquid phase. In this study, we now address the PNS system, and effects of both MBP and P2 on liposome membranes are investigated.

2. Materials and methods

2.1. Protein purification

Details of the protein purification protocols will be published elsewhere. In brief, His-tagged human P2 was expressed in *E. coli* and purified using immobilized metal ion affinity chromatography. The His-

tag was cleaved off with recombinant TEV protease and purification was completed by gel filtration. The recombinant His-tagged C1 and C8 isoforms of murine 18.5 kDa MBP were expressed in *E. coli* and purified by slight modifications of previously published procedures [1]. All protein samples were lyophilized prior to shipment to the neutron source and final sample preparation.

2.2. Sample preparation and characterization

1,2-dimyristoyl-*sn*-glycero-3-phosphate (DMPA), 1,2-dioleoyl-*sn*-glycero-3-phosphocholine (DOPC) and 1,2-dioleoyl-*sn*-glycero-3-phospho-L-serine (DOPS) were purchased as dry powders from Lipoid Company (Germany). After dissolving the lipids in chloroform and subsequent drying with nitrogen gas, they were solubilised in D_2O. By extruding the lipid solution through a 100 nm pore sized membrane, using the *Avanti® Mini-Extruder*, unilamellar vesicles were prepared. To compare liposomes of DMPA and DOPS + DOPC with these liposomes mixed with the MBP or P2 proteins, the proteins were added to one part of the lipid solution before the extrusion. The hydrodynamic radius (R_h) of the liposomes, with and without proteins, was estimated by dynamic light scattering (DLS). The experiments were carried out at the EMBL outstation in Grenoble using the *ALV CGS-3 Compact Goniometer*. The obtained correlation intensities were normalized to the measurement of a standard for which toluene is typically used. The suitable lipid concentration for DLS measurement was found to be of 0.001 mg/ml. Dust particles were removed by using a filter with 20 μm pores.

2.3. Neutron scattering experiment

Incoherent elastic neutron scattering measurements as a function of temperature were performed on the thermal ($\lambda = 2.23$ Å) high-energy resolution backscattering spectrometer IN13 (Institut Laue-Langevin, Grenoble, France), characterized by a very large momentum transfer range ($0.2 < Q < 4.9$ Å^{-1}) with a good and nearly Q-independent energy resolution (8 μeV FWHM). IN13, therefore, allows accessing the space and time windows of 1–6 Å and 0.1 ns respectively.

The elastic scattering intensities ($I_{el}(Q) = S(Q, \omega = 0)$), properly corrected for the empty sample holder signal, were normalized with respect to a vanadium scan (typically used as a standard), to compensate for spurious background contributions and detector efficiency. The sample mass and thickness were suitably chosen to optimize the compromise between good signal-to-noise ratio and multiple scattering contributions. For this purpose, a transmission of approximately 90% was guaranteed using 100 mg of powder per sample allocated in 1.5 mm thick aluminum sample holders.

3. Results and discussion

The temperature region ($278 < T < 313$ K) was chosen in order to (1) avoid any Bragg reflections arising from ice assigned to free water molecules in- and outside the liposome ($T > 273$ K) and (2) prevent P2 from denaturation ($T < 320$ K). In order to investigate how the membrane dynamics are affected by the presence of P2 in both the gel and liquid lipidic phase (which would allow us a direct comparison to our previous study in CNS), two different liposome compositions were chosen. The DMPA artificial membrane shows a lipid $L_\alpha \rightarrow L_\beta$ phase transition at $T = 320$ K. Thus, in the whole $273 < T < 315$ K region, DMPA is in the gel phase. On the other hand, two-component liposomes, made of a mixture of neutral (DOPC) and charged (DOPS) lipids, at 1:1 w/w ratio, were chosen to investigate the liquid

lipid phase. Indeed, both DOPC and DOPS show a lipid $L_\alpha \rightarrow L_\beta$ phase transition well below room temperature (DOPC: $T_{\alpha\rightarrow\beta} = 253$ K; DOPS: $T_{\alpha\rightarrow\beta} = 264$ K). Thus, the mixed lipid compound is in the liquid phase in the entire T range investigated here.

While DMPA was chosen to compare results in PNS to our previous investigation in CNS [23–25], the neutral-charged mixture was chosen to better represent the lipid composition in myelin. The chosen P2 concentration (1.25% of the total sample mass) allows neglecting the scattering arising from the protein (5% at maximum of the total scattering signal). Thus, any differences in the neutron response can be unambiguously assigned to changes in membrane dynamics induced by the presence of the P2 protein.

In Fig. 1, we report the incoherent elastic intensity of DMPA liposomes vs. the square of momentum transfer. The fast decrease of the intensity observed for all the temperatures investigated is a clear sign of enhanced dynamics that may count also for some additional quasi-elastic components to the elastic scattering. In particular, two main effects may contribute to the QENS additional terms: (1) confined water inside the liposomes, and (2) liposome diffusion in the heavy water medium. D_2O was chosen as solvent, indeed, to minimize the first contribution to the total scattering intensity. However, while free water outside the liposomes does not participate in our signal since it counts as flat background in the energy window explored here, the heavy water molecules inside the liposomes may include at least two different populations: free (at the center of the liposomes) and bound (closer to the lipid polar heads of the internal leaflet) molecules. The latter may give rise to a quasi-elastic contribution, which can fall within the energy resolution of the experiment, thus affecting the correct interpretation of the elastic data, since it results in a spurious decrease of the elastic intensity. Thus, bound water molecules have to be taken into account for a correct data interpretation. Also liposome diffusion has to be properly

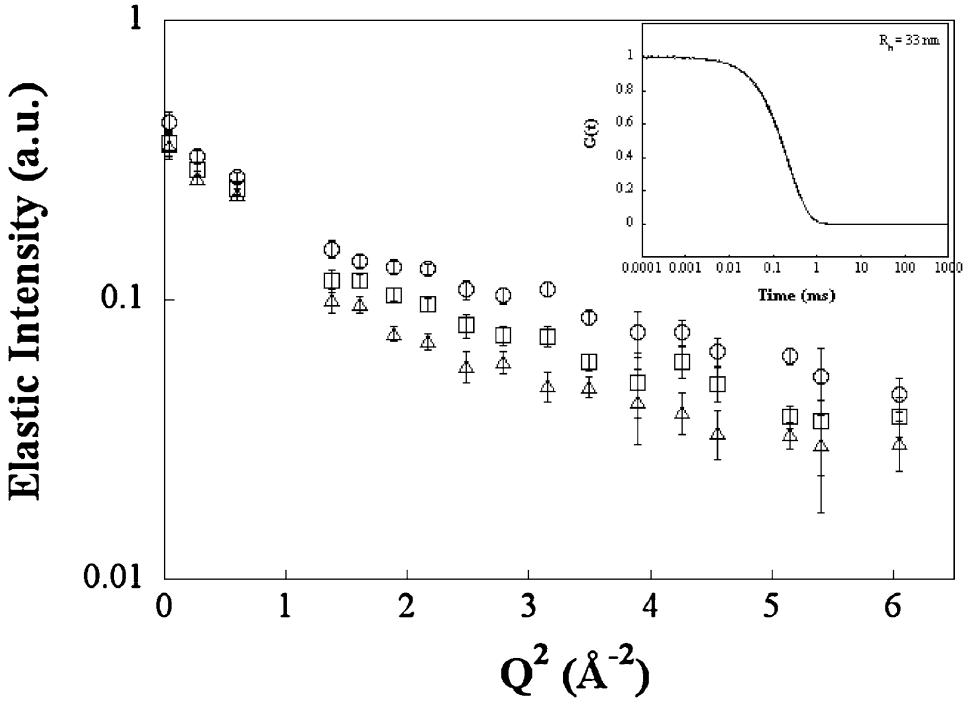

Fig. 1. Normalized elastic intensity of DMPA liposomes vs. T. For clarity, only 3 temperatures are shown (circles: 277 K; squares: 287 K; triangles: 297 K). Insert: experimental DLS correlation functions of DMPA liposomes measured before and after the neutron experiments (continuous and dotted lines, respectively).

considered, since at the used lipid concentration (50 mg/ml), the system has to be considered as crowded, thus speeding down the lipid diffusion constant to values observable on IN13. To identify and quantify all the different contributions to our elastic data, further QENS experiments are planned on several complementary instruments, allowing us to span a wide energy range (1–100 μeV).

In order to check the quality of the sample we systematically performed DLS measurements before and after the neutron experiments. In the insert of Fig. 1, we report, as an example, the experimental time dependent correlation function $G(t)$ of DMPA liposomes measured before and after the neutron experiments. The two curves overlap perfectly and can be fitted using a single and narrow liposome population of hydrodynamic radius $R_{\mathrm{h}} = 33$ nm and a very low polidispersity ($p = 0.98$).

The proper protein-liposome binding is currently checked by gel electrophoresis using a sucrose gradient protocol [17].

The influence of the composition of the two protein-free liposome samples used in this work (DMPA and DOPC + DOPS) is shown in Fig. 2, where the integrated elastic intensities are reported as a function of the explored T range. In order to gain in statistics, data have been binned over the interesting Q region where the non-zero intensities are still appreciable ($Q^2 \leqslant 6$ Å^{-2}). A remarkable difference is observed, supporting a damping of membrane dynamics in the DMPA system. This may be assigned to the different lipid phases explored by the two types of liposomes in the measured T region. As expected, indeed, the liquid phase at which DOPC + DOPS liposomes are trapped reflects much higher lipid motion. However, a contribution from a different behavior of the dynamics of the confined water molecules inside the liposomes cannot be excluded, due to a difference in the charge distribution on the lipid inner surface; the neutral DOPC lipids behave as spacers, probably causing a change in the lipid polar head-water molecules interactions.

The mean square displacements (MSD) extracted for the protein-free and P2-bound liposomes are reported in Fig. 3. All data on MBP bound liposomes are here only briefly commented and not shown, even

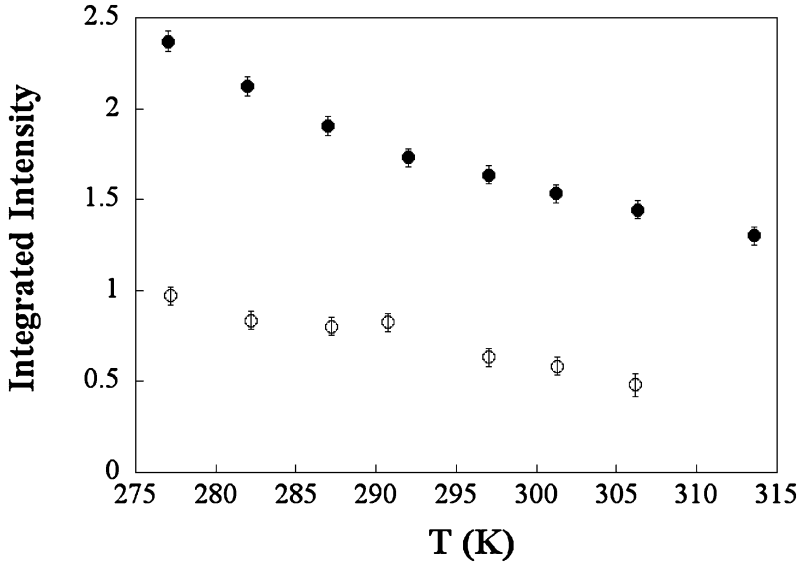

Fig. 2. Comparison of temperature dependence of the normalized elastic intensity of mono and bi-component liposomes. To gain in statistics, data are integrated over the Q^2 region up to 6 Å^{-2} (DMPA: filled symbols; DOPC + DOPS: empty symbols).

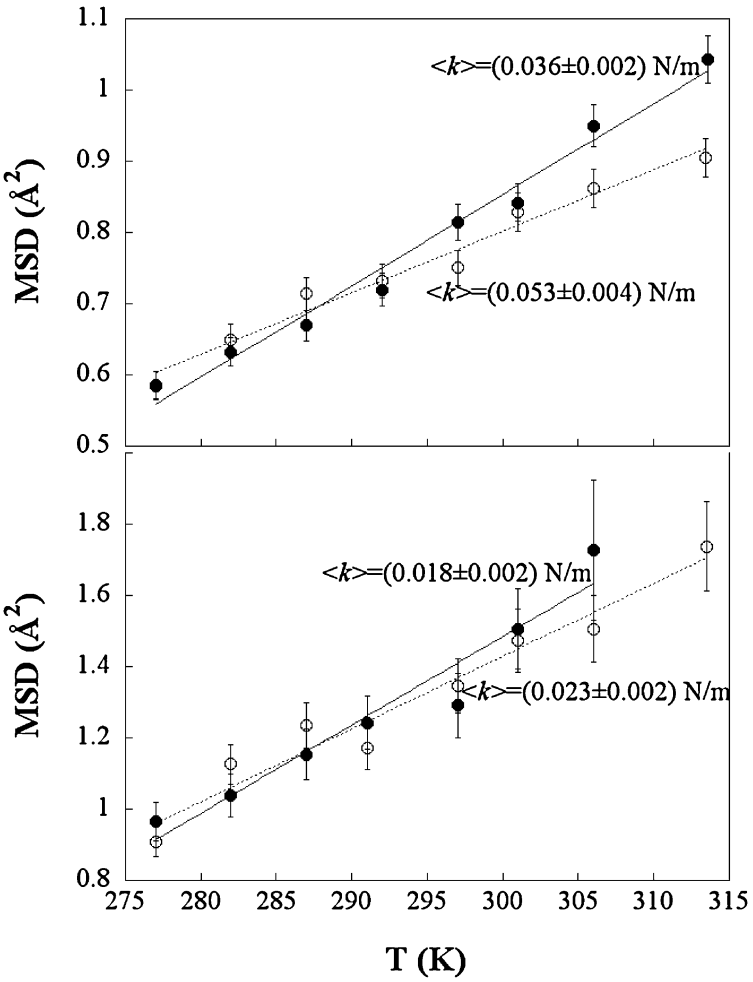

Fig. 3. Temperature dependence of the mean square displacements of proteolipid complexes compared to their respective liposomes. Upper panel: DMPA complexes; lower panel: DOPC + DOPS complexes. Empty symbols: liposomes with P2; filled circles: protein-free liposomes. The k force constants, estimated using the force constant model, are also reported.

though in perfect agreement to previous results [23–25], because of the poor sample quality suggested by significant changes in the DLS spectra as a function of time. The MSD values have been calculated from the slope of the elastic intensity vs. Q^2, in the low Q limit, where the Gaussian approximation is valid. The MSD count for both harmonic and anharmonic contributions of the all proton dynamics. A detailed description of the MSD extraction protocol may be found elsewhere [20]. The binding of P2 to the liposomes shows the same effect on the two lipocomplexes studied here: P2 is found to enhance the membrane stability, reducing the lipid dynamics. Using the free constant model successfully introduced by Zaccai in 2000 [30], the effective force constants (k parameters) have been estimated for our compounds (Fig. 3). The k constants are an indirect measure of the stability of a system; higher k values refer to a more rigid system, confirming the property of P2 to enhance the membrane stability, which may play a key role in proper nerve impulse transmission.

4. Conclusions

P2 is a highly abundant protein of the PNS myelin membrane, with putative roles in the formation and homeostasis of myelin; the relationships between the structure, function, and dynamics of P2 have, however, been poorly characterized. The results presented here strongly suggest a stabilizing effect induced by the P2 protein on the membrane dynamics, independently from the liposome composition (in particular from the net charge density of the liposomes) and from the lipidic phase transition in which the liposomes are trapped (gel phase in DMPA and liquid phase in DOPC + DOPS). One possible physical explanation for the observed higher rigidity may account for the recent observation (data not yet published) by molecular dynamics simulation, of the partial disposition of the P2 protein inside the lipid bilayer and on its surface, affecting in such a way both in plane and out-of-plane lipid motions.

In the near future, QENS experiments are planned to get better insight into the properties exerted by P2, in particular to map selectively the different lipid motions, which may be affected by the lipid–protein interaction. Complementary elastic experiments will also soon be performed on the same liposome compositions, where the free water molecules will be removed by promoting oriented multibilayer formation, followed by drying treatment, in order to extend the study of the DOPC + DOPS liposomes below room temperature, i.e., in the gel phase. This will allow us to discriminate between net charge density, lipid phase and chemical lipid composition contributions. Taken together, our results elucidate the functional properties of a quantitatively major component of vertebrate PNS myelin.

Acknowledgements

We would like to express our gratitude to Mrs. Iulia Blesneac, Ms. Niina Torniainen and Ms. Viivi Majava for their help in sample preparation and characterization. This work has been supported by the Academy of Finland and the Sigrid Juselius Foundation (Finland).

References

[1] I.R. Bates, P. Matharu, N. Ishiyama, D. Rochon, D.D. Wood, E. Polverini, M.A. Moscarello, N.J. Viner and G. Harauz, Characterization of a recombinant murine 18.5-kDa myelin basic protein, *Protein Expr. Purif.* **20** (2000), 285–299.
[2] J.M. Boggs, Myelin basic protein: a multifunctional protein, *Cell. Mol. Life Sci.* **63** (2006), 1945–1961.
[3] C. Brunner, H. Lassmann, T.V. Waehneldt, J.M. Matthieu and C. Linington, Differential ultrastructural localization of myelin basic protein, myelin/oligodendroglial glycoprotein, and 2′,3′-cyclic nucleotide 3′-phosphodiesterase in the CNS of adult rats, *J. Neurochem.* **52** (1989), 296–304.
[4] D.L. Caspar and D.A. Kirschner, Myelin membrane structure at 10 Å resolution, *Nat. New Biol.* **19** (1971), 46–52.
[5] L.S. Chia, J.E. Thompson and M.A. Moscarello, Alteration of lipid-phase behavior in multiple sclerosis myelin revealed by wide-angle X-ray diffraction, *Proc. Natl. Acad. Sci. USA* **81** (1984), 1871–1874.
[6] L.S. Chia, J.E. Thompson and M.A. Moscarello, X-ray diffraction evidence for myelin disorder in brain from humans with Alzheimer's disease, *Biochim. Biophys. Acta* **775** (1984), 308–331.
[7] A. Chmurzynska, The multigene family of fatty acid-binding proteins (FABPs): function, structure and polymorphism, *J. Appl. Genet.* **47** (2006), 39–48.
[8] A. Deriu and F. Natali, Recent neutron investigation on biomolecular dynamics: from model systems towards complex macromolecular machines, *J. Neutron Research* **10** (2002), 115–122.
[9] E.H. Eylar, I. Szymanska, A. Ishaque, J. Ramwani and S. Dubiski, Localization of the P2 protein in peripheral nerve myelin, *J. Immunol.* **124** (1980), 1086–1092.
[10] R.J. Franklin, Why does remyelination fail in multiple sclerosis?, *Nat. Rev. Neurosci.* **3** (2002), 705–771.
[11] B. Garbay, A.M. Heape, F. Sargueil and C. Cassagne, Myelin synthesis in the peripheral nervous system, *Prog. Neurobiol.* **61** (2000), 267–304.

[12] G. Harauz, N. Ishiyama, C.M. Hill, I.R. Bates, D.S. Libich and C. Farès, Myelin basic protein-diverse conformational states of an intrinsically unstructured protein and its roles in myelin assembly and multiple sclerosis, *Micron* **35** (2004), 503–542.
[13] A. Hirano, S.D. Cook, J.N. Whitaker, P.C. Dowling and M.R. Murray, Fine structural aspects of demyelination *in vitro*. The effects of Guillain–Barré serum, *J. Neuropathol. Exp. Neurol.* **30** (1971), 249–265.
[14] R.A. Hughes and D.R. Cornblath, Guillain–Barre syndrome, *Lancet* **366** (2005), 1653–1666.
[15] R.A. Hughes, R.D. Hadden, N.A. Gregson and K.J. Smith, Pathogenesis of Guillain–Barre syndrome, *J. Neuroimmunol.* **100** (1999), 74–97.
[16] D.A. Kirschner and A.L. Ganser, Compact myelin exists in the absence of basic protein in the shiverer mutant mouse, *Nature* **283** (1980), 207–210.
[17] J. Knol, Membrane reconstitution and functional analysis of a sugar transport system, PhD dissertation, University of Groningen, Groningen, 1999.
[18] P. Kursula, Structural properties of proteins specific to the myelin sheath, *Amino Acids* **34** (2008), 175–185.
[19] C. Laule, I.M. Vavasour, S.H. Kolind, D.K. Li, T.L. Traboulsee, G.R. Moore and A.L. MacKay, Magnetic resonance imaging of myelin, *Neurotherapeutics* **4** (2007), 460–484.
[20] U. Lehnert, V. Reat, M. Weik, G. Zaccaï and C. Pfister, Thermal motions in bacteriorhodopsin at different hydration levels studied by neutron scattering: correlation with kinetics and light-induced conformational changes, *Biophys. J.* **75** (1998), 1945–1952.
[21] V. Majava, C. Wang, M. Myllykoski, S.M. Kangas, S.U. Kang, N. Hayashi, P. Baumgärtel, A.M. Heape, G. Lubec and P. Kursula, Structural analysis of the complex between calmodulin and full-length myelin basic protein, an intrinsically disordered molecule, *Amino Acids* **39** (2010), 59–71.
[22] E.B. Masurovsky, M.B. Bunge and R.P. Bunge, Cytological studies of organotypic cultures of rat dorsal root ganglia following X-irradiation *in vitro*. II. Changes in Schwann cells, myelin sheaths, and nerve fibers, *J. Cell Biol.* **32** (1967), 497–518.
[23] F. Natali, A. Gliozzi, R. Rolandi, P. Cavatorta and A. Deriu, Myelin basic protein reduces molecular motions in DMPA, an elastic neutron scattering study, *Appl. Phys. A* **74** (2002), 1582–1584.
[24] F. Natali, A. Relini, A. Gliozzi, R. Rolandi, P. Cavatorta, A. Deriu, A. Fasano and P. Riccio, Protein-membrane interaction: effect of myelin basic protein on the dynamics of oriented lipids, *Chem. Phys.* **292** (2003), 455–464.
[25] F. Natali, A. Relini, A. Gliozzi, R. Rolandi, P. Cavatorta, A. Deriu, A. Fasano and P. Riccio, The influence of the lipid–protein interaction on the membrane dynamics, *Physica B* **350** (2004), E623–E626.
[26] P. Riccio, A. Tsugita, A. Bobba, F. Vilbois and E. Quagliariello, A new protein of the brain myelin: isolation and chemical characterization, *Biochem. Biophys. Res. Commun.* **127** (1985), 484–492.
[27] B.D. Trapp, M. Dubois-Dalcq and R.H. Quarles, Ultrastructural localization of P2 protein in actively myelinating rat Schwann cells, *J. Neurochem.* **43** (1984), 944–948.
[28] K. Uyemura, K. Yoshimura, M. Suzuki and K. Kitamura, Lipid binding activities of the P2 protein in peripheral nerve myelin, *Neurochem. Res.* **9** (1984), 1509–1514.
[29] C.R. Worthington and T.J. McIntosh, Direct determination of the lamellar structure of peripheral nerve myelin at moderate resolution (7A), *Biophys. J.* **14** (1974), 703–729.
[30] G. Zaccai, How soft is a protein? A protein dynamics force constant measured by neutron scattering, *Science* **288** (2000), 1604–1607.

A.2 Down to Atomic Scale: Neutrons Probe the Brain

The following article deals with quasielastic neutron scattering on bovine brain tissue. For this work, I contributed to the performance of the experiments. Since this article is under progress, only the abstract is presented here.

Title: Down to atomic scale: neutrons probe the brain

Authors:

F. Natali[1,2*], Y. Gerelli[2], C. Stelletta[3], J. Peters[2,4,5], W. Knoll[2,4], D. Hansul[6], J. Ollivier[2]

Affiliations:

[1] CNR-IOM, OGG, c/o Institut Laue-Langevin,6 rue Jules Horowitz, 38042 Grenoble Cedex 9, France

[2] Institut Laue-Langevin, 6 rue Jules Horowitz, 38042 Grenoble Cedex 9, France

[3] Department of Animal Medicine, Production and Health, University of Padova, Viale dell'Università 16, 35020 Agripolis, Legnaro (Padova), Italy

[4] University Joseph Fourier, BP 53, 38041 Grenoble Cedex 9, France

[5] Institut de Biologie Structurale J. P. Ebel, 41 rue Jules Horowitz, 38027 Grenoble Cedex 1, France

[6] Department of Physics, University of Würzburg, Sanderring 2, 97070 Würzburg, Germany

[*]To whom correspondence should be addressed. E-mail: natali@ill.fr

Abstract:

From the elementary building blocks of the cell (proteins, membranes etc) to bacteria and *in vivo* cells, neutrons have proven to be unique in pinpointing proton dynamics at atomic scale in biological compounds regardless of the macromolecular complexity involved. In this paper water diffusion in different brain areas is, for the first time, spotlighted at the scale experiencing macromolecular separation using neutron spectroscopy. The results are relevant for improving the modeling of the physics driving intra- and extra-cellular water diffusion in brain, with evident benefit for the diffusion magnetic resonance imaging technique, nowadays widely used to diagnose, at the micron scale, brain diseases such as ischemia and tumors.

Once Sentence Summary:

Neutrons reveal water diffusion at atomic scale in intra- and extra-cellular media of brain matter.

Bibliography

[1] R.H. Quarles, W.B. Macklin, and P. Morell. Myelin formation, structure, and biochemistry, in basic neurochemistry: molecular, cellular and medical aspects. *Academic Press Elsevier, New York*, pages 51–71, 2006.

[2] C.M. Taylor, C.B. Marta, R. Bansal, and S.E. Pfeiffer. *Myelin Biology and Disorders*, chapter The Transport, Assembly and Function of Myelin Lipids. Elsevier Academic Press, San Diego, CA, 2004.

[3] R. Virchow. Über das ausgebreitete Vorkommen einer dem Nervenmark analogen Substanz in den tierischen Geweben. *Virchows Archiv für Pathologische Anatomie*, **6**:562, 1854.

[4] P. Morell. *Myelin*. Plenum Press, New York, 1984.

[5] W.T. Norton, and S.E. Poduslo. Myelination in rat brain: method of myelin isolation. *Journal of Neurochemistry*, **21**(4):749–757, 1973.

[6] G.W. Brady, N.S. Murthy, D.B. Fein, D.D. Wood, and M.A. Moscarello. The effect of basic myelin protein on multilayer membrane formation. *Biophysical Journal*, **34**:345–350, 1981.

[7] D. A. Kirschner, A. L. Ganser, and D. L. D. Caspar. *Myelin*, chapter Diffraction Studies of Molecular Organization and Membrane Interactions in Myelin. Plenum Press, New York, 2004.

[8] M. De Felici, R. Felici, C. Ferrero, A. Tartari, M. Gambaccini, and S. Finet. Structural characterization of the human cerebral myelin sheath by small angle X-Ray scattering. *Physics in Medicine and Biology*, **53**:5675, 2008.

[9] S. Greenfield, S. Brostoff, E.H. Eylar, and P. Morell. Protein composition of myelin of the peripheral nervous system. *Journal of Neurochemistry*, **20**(4):1207–1216, 1973.

[10] C. Laule, I.M. Vavasour, S.H. Kolind, D.K.B. Li, T.L. Traboulsee, G.R. Moore, and A.L. MacKay. Magnetic resonance imaging of myelin. *Neurotherapeutics*, **4**(3):460–484, 2007.

[11] H. Webster. The geometry of peripheral myelin sheaths during their formation and growth in rat sciatic nerves. *The Journal of Cell Biology*, **48**:348–367, 1971.

[12] N. Baumann, and D. Pham-Dinh. Biology of oligodendrocyte and myelin in the mammalian central nervous system. *Physiological Reviews*, **81**(2):871–927, 2001.

[13] J.M. Boggs, G. Rangaraj, W. Gao, and Y.-M. Heng. Effect of phosphorylation of myelin basic protein by MAPK on its interactions with actin and actin binding to a lipid membrane in vitro. *Biochemistry*, **45**:391–401, 2006.

[14] A. Peters. Observations on the connexions between myelin sheaths and glial cells in the optic nerves of young rats. *Journal of Anatomy*, **98**(1):125–134, 1964.

[15] B.D. Trapp, and G.J. Kidd. *Myelin Biology and Disorders*, chapter Structure of the Myelinated Axon. Elsevier Academic Press, San Diego, CA, 2004.

[16] B. Ferguson, M.K. Matyszak, M.M. Esiri, and V.H. Perry. Axonal damage in acute multiple sclerosis lesions. *Brain*, **120**(3):393–399, 1997.

[17] J.A. Benjamins, and P. Morell. Proteins of myelin and their metabolism. *Neurochemical Research*, **3**:137–174, 1978.

[18] P. Riccio, L. Masotti, P. Cavatorta, A. De Santis, D. Juretic, A. Bobba, J. Pasquali-Ronchetti, and E. Quagliariello. Myelin basic protein ability to organize lipid bilayers: structural transition in bilayers of lisophosphatidylcholine micelles. *Biochemical and Biophysical Research Communications*, **134**(1):313–319, 1986.

[19] C. Readhead, B. Popkoa, N. Takahashia, H.D. Shinea, R.A. Saavedraa, R.L. Sidmana, and L. Hooda. Expression of a myelin basic protein gene in transgenic shiverer mice: correction of the dysmyelinating phenotype. *Cell*, **48**:703–712, 1987.

[20] I.R. Bates, P. Matharu, N. Ishiyama, D. Rochon, D.D. Wood, E. Polverini, M.A. Moscarello, N.J. Viner, and G. Harauz. Characterization of a recombinant murine 18.5-kDa myelin basic protein. *Protein Expression and Purification*, **20**:285–299, 2000.

[21] I.R. Bates, and G. Harauz. Molecular dynamics exposes α-helices in myelin basic protein. *Journal of Molecular Modeling*, **9**:290–297, 2003.

[22] G. Harauz, V. Ladizhansky, and J.M. Boggs. Structural polymorphism and multifunctionality of myelin basic protein. *Biochemistry*, **48**:8094–8104, 2009.

[23] J.M. Boggs, M.A. Moscarello, and D. Papahadjopoulos. *Lipid-protein interactions: Vol 2: Structural Organization of Myelin - Role of Lipid-Protein Interactions Determined in Model Systems*. Wiley-Interscience, New York, 1982.

[24] M.B. Sankaram, P.J. Brophy, and D. Marsh. Selectivity of interaction of phospholipids with bovine spinal cord myelin basic protein studied by spin-label electron spin resonance. *Biochemistry*, **28**:9699–9707, 1989.

[25] Y. Min, K. Kristiansen, J.M. Boggs, C Husted, J.A. Zasadzinski, and J. Israelachvili. Interaction forces and adhesion of supported myelin lipid bilayers modulated by myelin basic protein. *PNAS*, **106**(9):3154–3159, 2009.

[26] E. Polverini, S. Arisi, P. Cavatorta, T. Berzina, L. Cristofolini, A. Fasano, P. Riccio, and M.P. Fontana. Interaction of myelin basic protein with phospholipid monolayers: mechanism of protein penetration. *Langmuir*, 19:872–877, 2003.

[27] J. Sedzik, A.E. Blaurock, and M. Höchli. Lipid/myelin basic protein multilayers - a model for the cytoplasmic space in central nervous system myelin. *Journal of Molecular Biology*, **174**:385–409, 1984.

[28] R.G. Oliveira, and B. Maggio. Compositional domain immiscibility in whole myelin monolayers at the air-water interface and langmuir-blodgett films. *Biochimica et Biophysica Acta*, **1561**:238–250, 2002.

[29] C.M. Rosetti, and B. Maggio. Protein-induced surface structuring in myelin membrane monolayers. *Biophysical Journal*, **93**:4254–4267, 2007.

[30] C.M. Rosetti, B. Maggio, and R.G. Oliveira. The self-organization of lipids and proteins of myelin at the membrane interface. Molecular factors underlying the microheterogeneity of domain segregation. *Biochimica et Biophysica Acta*, **1778**:1665–1675, 2008.

[31] F. Natalia, A. Relini, A. Gliozzi, R. Rolandi, P. Cavatorta, A. Deriu, A. Fasano, and P. Riccio. Protein-membrane interaction: effect of myelin basic protein on the dynamics of oriented lipids. *Chemical Physics*, **292**:455–464, 2003.

[32] V. Majava, M.V. Petoukhov, N. Hayashi, P. Pirilä, D.I. Svergun, and P. Kursula. Interaction between the C-terminal region of human myelin basic protein and calmodulin: analysis of complex formation and solution structure. *BMC Structural Biology 2008, 8:10*, **8**(10):1–18, 2008.

[33] M.A. Moscarello, D.D. Wood, C. Ackerley, and C. Boulias. Myelin in multiple sclerosis is developmentally immature. *The Journal of Clinical Investigation*, **94**:146–154, 1994.

[34] C.M.D. Hill, and G. Harauz. Charge effects modulate actin assembly by classic myelin basic protein isoforms. *Biochemical and Biophysical Research Communications*, **329**:362–369, 2005.

[35] `http://www.ncbi.nlm.nih.gov/protein/69885049?report=fasta&log$=seqview`.

[36] D.R. Beniac, D.D. Wood, N. Palaniyar, F.P. Ottensmeyer, M.A. Moscarello, and G. Harauz. Marburg's variant of multiple sclerosis correlates with a less compact structure of myelin basic protein. *Molecular Cell Biology Research Communications*, **1**:48–51, 1999.

[37] J.M. Boggs, G. Rangaraj, K.M. Koshy, C. Ackerley, D.D. Wood, and M.A. Moscarello. Highly deiminated isoform of myelin basic protein from multiple sclerosis brain causes fragmentation of lipid vesicles. *Journal of Neuroscience Research*, **57**:529–535, 1999.

[38] D.R. Beniac, D.D. Wood, N. Palaniyar, P. Ottensmeyer, M.A. Moscarello, and G. Harauz. Cryoelectron microscopy of protein-lipid complexes of human myelin basic protein charge isomers differing in degree of citrullination. *Journal of Structural Biology*, **129**(1):80–95, 2000.

[39] J.K. Kim, F.G. Mastronardi, D.D. Wood, D.M. Lubman, R. Zand, and M.A. Moscarello. Multiple sclerosis - an important role for post-translational modifications of myelin basic protein in pathogenesis. *Molecular & Cellular Proteomics*, **2**:453–462, 2003.

[40] Z. Spyranti, T. Tselios, G. Deraos, J. Matsoukas, G.A. Spyroulias. NMR structural elucidation of myelin basic protein epitope 83-99 implicated in multiple sclerosis. *Amino Acids*, **38**:929–936, 2010.

[41] R. E. Martenson. *Myelin: Biology and Chemistry.* CRC Press, Boca Raton, Fla, 1992.

[42] G. Harauz, N. Ishiyamaa, C.M.D. Hilla, I.R. Batesa, D.S. Libicha, and C. Farès. Myelin basic protein - diverse conformational states of an intrinsically unstructured protein and its roles in myelin assembly and multiple sclerosis. *Micron*, **35**:503–542, 2004.

[43] V. Majava, C. Wang, M. Myllykoski, S.M. Kangas, S.U. Kang, N. Hayashi, P. Baumgärtel, A.M. Heape, G. Lubec, and P. Kursula. Structural analysis of the complex between calmodulin and full-length myelin basic protein, an intrinsically disordered molecule. *Amino Acids*, **39**:59–71, 2010.

[44] C. Wang, U. Neugebauer, J. Brück, M. Myllykoski, P. Baumgärtel, J. Popp, and P. Kursula. Charge isomers of myelin basic protein: structure and interactions with membranes, nucleotide analogues, and calmodulin. *PLoS ONE*, **6**(5):e19915, 2011.

[45] E. Polverini, A. Fasano, F. Zito, P. Riccio, and P. Cavatorta. Conformation of bovine myelin basic protein purified with bound lipids. *European Biophysics Journal*, **28**:351–355, 1999.

[46] H. Haas, M. Torrielli, R. Steitz, P. Cavatorta, R. Sorbi, A. Fasano, P. Riccio, and A. Gliozzi. Myelin model membranes on solid substrates. *Thin Solid Films*, **327-329**:627–631, 1998.

[47] G. L. Stoner. Predicted folding of β-structure in myelin basic protein. *Journal of Neurochemistry*, **43**(2):433–447, 1984.

[48] R.E. Martenson. Possible hydrophobic region in myelin basic protein consisting of an orthogonally packed β-sheet. *Journal of Neurochemistry*, **46**(5):1612–1622, 1986.

[49] D.R. Beniac, M.D. Luckevich, G.J. Czarnota, T.A. Tompkins, R.A. Ridsdale, F.P. Ottensmeyer, M.A. Moscarello, and G. Harauz. Three-dimensional structure of myelin basic protein. I. reconstruction via angular reconstitution of randomly oriented single particles. *The Journal of Biological Chemistry*, **272**(7):4261–4268, 1997.

[50] R.A. Ridsdale, D.R. Beniac, T.A. Tompkins, M.A. Moscarello, and G. Harauz. Three-dimensional structure of myelin basic protein. II. molecular modeling and considerations of predicted structures in multiple sclerosis. *The Journal of Biological Chemistry*, **272**(7):4269–4275, 1997.

[51] I.R. Bates, J.B. Feix, J.M. Boggs, and G. Harauz. An immunodominant epitope of myelin basic protein is an amphipathic α-helix. *The Journal of Biological Chemistry*, **279**:5757–5764, 2004.

[52] E. Polverini, E.P. Coll, D.P. Tieleman, and G. Harauz. Conformational choreography of a molecular switch region in myelin basic protein-molecular dynamics shows induced folding and secondary structure type conversion upon threonyl phosphorylation in both aqueous and membrane-associated environments. *Biochimica et Biophysica Acta (BBA)-Biomembranes*, **1808**(3):674–683, 2011.

[53] H. Haas, C.L.P. Oliveira, I.L. Torriani, E. Polverini, A. Fasano, G. Carlone, P. Cavatorta, and P. Riccio. Small angle X-Ray scattering from lipid-bound myelin basic protein in solution. *Biophysical Journal*, **86**:455–460, 2004.

[54] P. Morell, R.H. Quarles, and W.T. Norton. *Myelin Formation, Structure and Biochemistry.* in Basic Neurochemistry, New York: Raven: 117-143, 1994.

[55] B.D. Trapp, M. Dubois-Dalcq, and R.H. Quarles. Ultrastructural localization of P2 protein in actively myelinating rat schwann cells. *Journal of Neurochemistry*, **43**(4):944–948, 1984.

[56] E. Polverini, M. Fornabaio, A. Fasano, G. Carlone, P. Riccio, P.Cavatorta. The pH-dependent unfolding mechanism of P2 myelin protein: an experimental and computational study. *Journal of Structural Biology*, **153**:253–263, 2006.

[57] J. Sedzik, A.E. Blaurock, and M. Höchli. Reconstituted P2/myelin-lipid multilayers. *Journal of Neurochemistry*, **45**(3):844–852, 1985.

[58] W. Knoll, F. Natali, J. Peters, R. Nanekar, C. Wang, and P. Kursula. Dynamic properties of a reconstituted myelin sheath. *Spectroscopy*, **24**(6):585–592, 2010.

[59] S. Suresh, C. Wang, R. Nanekar, P. Kursula, and J.M. Edwardson. Myelin basic protein and myelin protein P2 act synergistically to cause stacking of lipid bilayers. *Biochemistry*, **49**:3456–3463, 2010.

[60] R.A.C. Hughes, R.D.M. Hadden, N.A. Gregson, and K.J. Smith. Pathogenesis of Guillain-Barré syndrome. *Journal of Neuroimmunology*, **100**:74–97, 1999.

[61] R.A.C Hughes, and D.R. Cornblath. Guillain-Barré syndrome. *Lancet*, **366**:1653–1666, 2005.

[62] A. Chmurzynska. The multigene family of fatty acid-binding proteins (FABPs): function, structure and polymorphism. *Journal of Applied Genetics*, **47**(1):39–48, 2006.

[63] T.A. Jones, T. Bergfors, J. Sedzik, and T. Unge. The three-dimensional structure of P2 myelin protein. *The EMBO Journal*, **7**(6):1597–1604, 1988.

[64] P. Riccio, F. Zito, A. Fasano, G.M. Liuzzi, F. Lolli, E. Polverini, and P. Cavatorta. Purification of bovine P2 myelin protein with bound lipids. *NeuroReport*, **9**:2769–2773, 1998.

[65] R.A. Steele, D.A. Emmert, J. Kao, M.E. Hodsdon, C. Frieden, and D.P. Cistola. The three-dimensional structure of a helix-less variant of intestinal fatty acid-binding protein. *Protein Science*, **7**:1332–1339, 1998.

[66] J. Sedzik, G. Carlone, A. Fasano, G.M. Liuzzi, and P. Riccio. Crystals of P2 myelin in lipid-bound form. *Journal of Structural Biology*, **142**:292–300, 2003.

[67] D. Bitounis, R. Fanciullino, A. Iliadis, and J. Ciccolini. Optimizing druggability through liposomal formulations: new approaches to an old concept. *ISRN Pharmaceutics*, **2012**, 2012.

[68] J.F. Nagle, S. Tristram-Nagle. Structure of lipid bilayers. *Biochimica et Biophysica Acta*, **1469**:159–195, 2000.

[69] `http://64.150.176.19/index.php?option=com_content&view=article&id=612&Itemid=238&catnumber=840035`.

[70] `http://64.150.176.19/index.php?option=com_content&view=article&id=231&Itemid=207&catnumber=850375`.

[71] M. Trapp, T. Gutberlet, F. Juranyi, T. Unruh, B. Demé, M. Tehei, and J. Peters. Hydration dependent studies of highly aligned multilayer lipid membranes by neutron scattering. *The Journal of Chemical Physics*, **133**:164505, 2010.

[72] P. Berntsen, C. Svanberg, and J. Swenson. Interplay between hydration water and headgroup dynamics in lipid bilayers. *The Journal of Physical Chemistry B*, **115**:1825–1832, 2011.

[73] H. I. Petrache, S. Tristram-Nagle, K. Gawrisch, D. Harries, V.A. Parsegian, and J.F. Nagle. Structure and fluctuations of charged phosphatidylserine bilayers in the absence of salt. *Biophysical Journal Volume*, **86**:1574–1586, 2004.

[74] G. Cevc. *Phospholipids Handbook*. Marcel Dekker, 1993.

[75] J. Chadwick. The existence of a neutron. *Proceedings of the Royal Society of London. Series A*, **136**(830):692–708, 1932.

[76] J. Chadwick. Possible existence of a neutron. *Nature*, **129**(3252):312, 1932.

[77] M. Bée. *Quasielastic Neutron Scattering*. Adam Hilger, 1988.

[78] L.G. Squires. *Introduction to the Theory of Thermal Neutron Scattering*. Dover Publications Inc., 1978.

[79] L.v. Hove. Correlation in space and time and born approximation scattering in systems of interacting particles. *Physical Review*, **95**(1):249–262, 1954.

[80] A.-J. Dianoux, G. Lander. *Neutron Data Booklet*. Institut Laue-Langevin, 2001.

[81] J.C. Smith. Protein dynamics: comparison of simulations with inelastic neutron scattering experiments. *Quarterly Reviews of Biophysics*, **24**(3):227–291, 1991.

[82] W. Doster. The dynamical transition of proteins, concepts and misconceptions. *European Biophysics Journal*, **37**(5):591–602, 2008.

[83] V. Réat, G. Zaccai, M. Ferrand, and C. Pfister. *Biological Macromolecular Dynamcis, Proceedings of a Workshop on Inelastic and Quasielastic Neutron Scattering in Biology*, chapter Functional Dynamics in Purple Membranes. 1997.

[84] A. Guinier, G. Fournet, C.B. Walker, G.H. and Vineyard. Small-angle scattering of X-Rays. *Physics Today*, **9**:38, 1956.

[85] T. Springer. *Quasielastic Neutronscattering for the Investigation of Diffuse Motions in Solids and Liquids*. Springer, Berlin, Heidelberg, New York, 1972.

[86] Y. Gerelli, V.G. Sakai, J. Ollivier, and A. Deriu. Conformational and segmental dynamics in lipid-based vesicles. *Soft Matter*, **7**(8):3929–3935, 2011.

[87] F. James, and M. Winkler. Minuit users guide. *CERN, Geneva*, 2004.

[88] F. Volino, and A.J. Dianoux. Neutron incoherent scattering law for diffusion in a potential of spherical symmetry: general formalism and application to diffusion inside a sphere. *Molecular Physics*, **41**(2):271–279, 1980.

[89] V.F. Sears. Cold neutron scattering by homonuclear diatomic liquid: 2 hindered rotation. *Canadian Journal of Physics*, **44**:1999, 1966.

[90] http://nmi3.eu.

[91] H. Maier-Leibnitz, and I. Springer. The use of neutron optical devices on beam-hole experiments. *Journal of Nuclear Energy. Parts A/B. Reactor Science and Technology*, **17**(4-5):217–225, 1963.

[92] http://www.isis.stfc.ac.uk/about-isis/how-isis-works6313.html.

[93] http://www.ill.eu/instruments-support/instruments-groups/instruments/in13.

[94] http://www.ill.eu/instruments-support/instruments-groups/instruments/in16.

[95] http://www.ill.eu/instruments-support/instruments-groups/instruments/in5.

[96] http://www.ill.eu/instruments-support/instruments-groups/instruments/in6.

[97] http://berlinpro.org/media/media/grossgeraete/nutzerdienst/neutronen/instrumente/inst/bensc_v3.pdf.

[98] M. T. F. Telling and K. H. Anderson. *The Osiris User Guide*. ISIS Facility Rutherford Appleton Laboratory, 2008.

[99] M.T.F. Telling and K.H. Andersen. Spectroscopic characteristics of the OSIRIS near-backscattering crystal analyser spectrometer on the ISIS pulsed neutron source. *Physical Chemistry Chemical Physics*, 7:1255–1261, 2005.

[100] http://www.isis.stfc.ac.uk/instruments/osiris.

[101] http://www.ill.eu/instruments-support/instruments-groups/instruments/d16.

[102] I.R. Bates, D.S. Libich, D.D. Wood, M.A. Moscarello, and G. Harauz. An Arg/Lys → Gln mutant of recombinant murine myelin basic protein as a mimic of the deiminated form implicated in multiple sclerosis. *Protein Expression and Purification*, 25:330–341, 2002.

[103] M. Hammarström, E.A. Woestenenk, N. Hellgren, T. Härd, and H. Berglund. Effect of N-terminal solubility enhancing fusion proteins on yield of purified target protein. *Journal of Structural and Functional Genomics*, **7**:1–14, 2006.

[104] V. Majava, E. Polverini, A. Mazzini, R. Nanekar, W. Knoll, J. Peters, F. Natali, P. Baumgärtel, I. Kursula, and P. Kursula. Structural and functional characterization of human peripheral nervous system myelin protein P2. *PLoS ONE*, **5**:e10300, 2010.

[105] F. W. Studier. Protein production by auto-induction in high-density shaking cultures. *Protein Expression and Purification*, **41**(1):207–234, 2005.

[106] Bronstein, Semendjajew, Musiol, and Mühlig. *Taschenbuch der Mathematik*. Verlag Harri Deutsch, 2001.

[107] Malvern Instruments. Dynamic light scattering: an introduction in 30 minutes. 1999.

[108] A. Rath, M. Glibowicka, V.G. Nadeau, G. Chen, and C.M. Deber. Detergent binding explains anomalous SDS-PAGE migration of membrane proteins. *PNAS*, **106**(6):1760–1765, 2009.

[109] H.-J. Flammersheim G. Höhne, W. Hemminger. *Differential Scanning Calorimetry*. Springer, Berlin, 2003.

[110] C. D. Hodgman. *Handbook of Chemistry and Physics*. Chemical Rubber Publishing Company, 1952.

[111] T.C. Hansen, M.M. Koza, and W.F. Kuhs. Formation and annealing of cubic ice: I. modelling of stacking faults. *Journal of Physics: Condensed Matter*, **20**:285104, 2008.

[112] T.C. Hansen, M.M. Koza, P. Lindner, and W.F. Kuhs. Formation and annealing of cubic ice: II. kinetic study. *Journal of Physics: Condensed Matter*, **20**:285105, 2008.

[113] L. Bosio, G.P. Johari, and J. Teixeira. X-Ray study of high-density amorphous water. *Physical Review Letters*, **56**(5):460–463, 1986.

[114] V.F. Petrenko, and R.W. Withworth. *Physics of Ice*. Oxford University Press, 1999.

[115] `http://www.ill.eu/instruments-support/computing-for-science/cs-software/all-software/lamp`.

[116] W. Doster, S. Cusack, and W. Petry. Dynamical transition of myoglobin revealed by inelastic neutron scattering. *Nature*, **337**:754–756, 1989.

[117] G. Zaccai. How soft is a protein? A protein dynamics force constant measured by neutron scattering. *Science*, **288**(5471):1604–1607, 2000.

[118] K. Wood, M. Plazanet, F. Gabel, B. Kessler, D. Oesterhelt, D.J. Tobias, G. Zaccai, and M. Weik. Coupling of protein and hydration-water dynamics in biological membranes. *PNAS*, **104**(46):18049–18054, 2007.

[119] M. Weik, U. Lehnert, G. and Zaccai. Liquid-like water confined in stacks of biological membranes at 200K and its relation to protein dynamics. *Biophysical Journal*, **89**(5):3639–3646, 2005.

[120] K. Wood, D.J. Tobias, B. Kessler, F. Gabel, D. Oesterhelt, F.A.A. Mulder, G. Zaccai, and M. Weik. The low-temperature inflection observed in neutron scattering measurements of proteins is due to methyl rotation: direct evidence using isotope labeling and molecular dynamics simulations. *Journal of the American Chemical Society*, **132**(14):4990–4991, 2010.

[121] G. Schiro, C. Caronna, F. Natali, and A. Cupane. Direct evidence of the amino acid side chain and backbone contributions to protein anharmonicity. *Journal of the American Chemical Society*, **132**(4):1371–1376, 2010.

[122] J.H. Roh, V.N. Novikov, R.B. Gregory, J.E. Curtis, Z. Chowdhuri, and A.P. Sokolov. Onsets of anharmonicity in protein dynamics. *Physical Review Letters*, **95**(3):38101, 2005.

[123] `http://www.isis.stfc.ac.uk/instruments/iris/data-analysis`.

[124] J. Fitter, B. Rufflé, and R.E. Lechner. FITMO: NEAT software package.

[125] W. Pfeiffer, T. Henkel, E. Sackmann, W. Knoll, and D. Richter. Local dynamics of lipid bilayers studied by incoherent quasi-elastic neutron scattering. *Europhysics Letters*, **8**(2):201–206, 1989.

[126] J. Swenson, F. Kargl, P. Berntsen, and C. Svanberg. Solvent and lipid dynamics of hydrated lipid bilayers by incoherent quasielastic neutron scattering. *The Journal of Chemical Physics*, **129**:045101, 2008.

[127] J. Fitter, R.E. Lechner, G. Buldt, and N.A. Dencher. Internal molecular motions of bacteriorhodopsin: hydration-induced flexibility studied by quasielastic incoherent neutron scattering using oriented purple membranes. *PNAS*, **93**(15):7600–7605, 1996.

[128] M. Doxastakis, V.G. Sakai, S. Ohtake, J.K. Maranas, and J.J. De Pablo. A molecular view of melting in anhydrous phospholipidic membranes. *Biophysical Journal*, **92**(1):147–161, 2007.

[129] M.F. Brown, J. Seelig, and U. Häberlen. Structural dynamics in phospholipid bilayers from deuterium spin-lattice relaxation time measurements. *The Journal of Chemical Physics*, **70**:5045–5053, 1979.

[130] M.C. Pitman, F. Suits, K. Gawrisch, and S.E. Feller. Molecular dynamics investigation of dynamical properties of phosphatidylethanolamine lipid bilayers. *The Journal of Chemical Physics*, **122**:244715, 2005.

[131] D.P. Tieleman, S.J. Marrink, and H.J.C. Berendsen. A computer perspective of membranes: molecular dynamics studies of lipid bilayer systems. *Biochimica et Biophysica Acta-Reviews On Biomembranes*, **1331**(3):235–270, 1997.

[132] S.A. Pandit, D. Bostick, and M.L. Berkowitz. Molecular dynamics simulation of a dipalmitoylphosphatidylcholine bilayer with NaCl. *Biophysical Journal*, **84**(6):3743–3750, 2003.

[133] F. Natali, A. Gliozzi, R. Rolandi, A. Relini, P. Cavatorta, A. Deriu, A. Fasano, and P. Riccio. Changes in the anisotropy of oriented membrane dynamics induced by myelin basic protein. *Applied Physics A*, **74**:S1582–S1584, 2002.

[134] F. Natalia, A. Relinib, A. Gliozzi, R. Rolandi, P. Cavatorta, A. Deriu, A. Fasano, and P. Riccio. The influence of the lipid-protein interaction on the membrane dynamics. *Physica B*, **350**:e623–e626, 2004.

Résumé

La gaine de myéline joue un rôle essentiel dans l'efficacité de la conduction électrique des impulsions nerveuses dans le système nerveux central et le système nerveux périphérique. Afin de mieux comprendre le rôle de la myéline dans les maladies auto-immunes qui affectent le système nerveux, l'influence des protéines MBP-C1, MBP-C8 (une forme mutante) et P2 sur la structure de la membrane a été étudiée par diffraction neutronique, et sur sa dynamique par diffusion neutronique élastique incohérente (EINS) et diffusion neutronique quasi-élastique (QENS).
Les expériences ont révélé que des changements de structure se produisent dans les membranes de myéline modèles dans la région de température couvrant les transitions de phase des lipides. Par des mesures de diffraction neutronique, on a observé que les protéines MBP-C1 et P2 affectent profondément la structure des membranes de myéline reconstituées, révélant des changements importants dans la bicouche de la phase liquide.
Une variété de comportements dynamiques fonctions de la température sont également observés par EINS dans le modèle des membranes de myéline: une transition entre un régime harmonique vers un régime non harmonique en raison des rotations du groupe de méthyle est suivie par d'autres transitions induites par la transition de phase gel-liquide de la bicouche et de la fusion de l'eau d'hydratation. MBP-C1 s'avère réduire la dynamique de la membrane, augmentant la température à partir de laquelle la première transition se produit et réduisant la dynamique dans la phase de gel. Ces résultats sont en adéquation avec les mesures par QENS qui montrent une réduction de la dynamique de la membrane dans la phase de gel induite par MBP-C1. Au contraire, dans la phase liquide, MBP-C1 s'avère accroître les mouvements de diffusion observés par QENS, ce qui est consistant avec l'observation des changements de la structure bicouche induits par MBP-C1 dans la phase liquide: en raison de l'élargissement de l'espace à l'intérieur de la bicouche, causé par la protéine MBP-C1 qui pénètre dans la bicouche, les lipides pourraient avoir augmenté leur degré de liberté.
Aucune différence significative sur les mouvements observés de la membrane entre les effets de MBP-C1 et sa forme modifiée MBP-C8 associée à de multiples scléroses n'a été observée dans cette étude.
Par ailleurs, on a démontré que les protéines MBP-C1 et P2 agissent de façon fortement synergique et il se pourrait qu'elles s'associent à l'intérieur de la membrane. Leur capacité à réduire la dynamique de la membrane dans la phase liquide est considérablement accrue quand les deux protéines sont présentes. Un modèle est proposé dans lequel les protéines associées influencent des grandes parties de la membrane en améliorant l'adhésion entre les bicouches par leurs fortes interactions électrostatiques et par un effet de synergie sur leur empilement.

Mots clefs: système nerveux central et périphérique, myéline, protéines de la myéline MBP-C1, MBP-C8 et P2, diffusion neutronique, dynamiques de la membrane

Summary

The myelin sheath is essential for efficient electrical conduction of nerve impulses in the central and in the peripheral nervous system. To gain insight into the role of myelin, in autoimmune diseases that affect the nervous system, the influence of the myelin protein MBP-C1, a mutated form MBP-C8, and P2 on the membrane structure was investigated using neutron diffraction and on the membrane dynamics using incoherent elastic (EINS) and quasielastic neutron scattering (QENS).
The experiments revealed that structural changes occur in the model myelin membranes across the temperature region covering the lipid phase transitions. The myelin proteins MBP-C1 and P2 are shown to strongly affect the structure of the model myelin membranes, shown by neutron diffraction measurements revealing significant changes in the bilayer spacing in the liquid phase.
A range of distinct dynamical behaviours are observed by EINS in the model myelin membranes as a function of temperature: a first transition from a harmonic to an anharmonic temperature regime, assigned to methyl group rotations, is followed by further transitions induced by the gel-liquid phase transition of the bilayer and melting of the hydration water. MBP-C1 is shown to reduce the dynamics of the membrane, increasing the temperature at which the first transition occurs, and reducing the dynamics in the gel phase. These results were in agreement with quasielastic neutron scattering measurements, which showed a reduction of confined diffusive motions of the membrane in the gel phase induced by MBP-C1. In contrast, in the liquid phase, MBP-C1 was found to enhance diffusive motions, revealed with QENS, which is consistent with the observed changes to the bilayer structure that are induced by MBP-C1 in the liquid phase: due to the widening of the interbilayer space caused by MBP-C1, which penetrates into the bilayer, the lipids may have increased their conformational freedom.
Any significant difference between the effects of MBP-C1 and its modified form MBP-C8, which is associated with multiple sclerosis, on motions of the membrane, investigated by QENS, were not identified in this study.
It was demonstrated that both proteins MBP-C1 and P2 act in a highly synergistic manner and may associate within the membrane. Their ability to reduce the membrane dynamics in the liquid phase is considerably enhanced when both proteins are present. A model is proposed in which the associated proteins influence large fractions of the membranes by promoting adhesion between the bilayers through their strong electrostatic interactions and by their synergistic stacking effect.

Key words: central and peripheral nervous system, myelin, myelin proteins MBP-C1, MBP-C8 and P2, neutron scattering, membrane dynamics